

kassel
university
press



High Pressure Synthesis of Novel Hard Materials: Spinel- Si_3N_4 and Derivates

Marcus Rolf Schwarz

Dem Fachbereich Material- und Geowissenschaften der Technischen Universität Darmstadt zur Erlangung des Grades eines Doktor Ingenieur (Dr.-Ing.) vorgelegte Dissertation von Dipl.-Ing. Marcus Schwarz aus Offenbach am Main.

Referent: Prof. Dr. R. Riedel
Koreferent: Prof. Dr. H. Fueß

Tag der Einreichung	14. 10 2003
Tag der mündlichen Prüfung	11. 11 2003

Bibliografische Information Der Deutschen Bibliothek
Die Deutsche Bibliothek verzeichnet diese Publikation in der Deutschen Nationalbibliografie; detaillierte bibliografische Daten sind im Internet über <http://dnb.ddb.de> abrufbar

Zugl.: Darmstadt, Univ., Diss. 2003
D 17
ISBN 3-89958-104-0
URN urn:nbn:de:0002-1045

© 2005, kassel university press GmbH, Kassel
www.upress.uni-kassel.de

Umschlaggestaltung: 5 Büro für Gestaltung, Kassel
Druck und Verarbeitung: Unidruckerei der Universität Kassel
Printed in Germany

Necessity and Limits of (Materials) Science and Technology

²⁰ Now no blacksmith could be found in all the land of Israel, for the Philistines said, "Otherwise the Hebrews will make swords or spears." So all Israel went down to the Philistines, each to sharpen his plowshare, his mattock, his axe, and his hoe. ²¹ The charge was two-thirds of a shekel for the plowshares, the mattocks, the forks, and the axes, and to fix the hoes.

1. Samuel 13.

¹ Surely there is a mine for silver And a place where they refine gold.

² Iron is taken from the dust, And copper is smelted from rock. ³ Man puts an end to darkness, And to the farthest limit he searches out the rock in gloom and deep shadow.

...

⁴ He sinks a shaft far from habitation, Forgotten by the foot; They hang and swing to and fro far from men. ⁵ The earth, from it comes food And underneath it is turned up as fire. ⁶ Its rocks are the source of sapphires, And its dust contains gold.

...

¹⁰ He hews out channels through the rocks, And his eye sees anything precious. ¹¹ He dams up the streams from flowing, And what is hidden he brings out to the light.

...

¹² But where can wisdom be found?

And where is the place of understanding?

¹³ Man does not know its value, Nor is it found in the land of the living.

¹⁵ Pure gold cannot be given in exchange for it, Nor can silver be weighed as its price.

¹⁴ The deep says, 'It is not in me'; And the sea says, 'It is not with me.'

²¹ Thus it is hidden from the eyes of all living

...

²³ God understands its way, And He knows its place.

²⁵ When He imparted weight to the wind And meted out the waters by measure,

²⁶ When He set a limit for the rain And a course for the thunderbolt, ²⁷ Then

He saw it and declared it; He established it and also searched it out.

...

²⁸ And to man He said, "Behold, the fear of the Lord, that is wisdom; And to depart from evil is understanding."

after Job 28., ~800 b.C.

Contents

1	Introduction & Motivation: Synthetic Hard Materials	1
1.1	Historical Aspects on Hard Materials	2
1.2	High-Pressure-Derived Synthetic Hard Materials	3
1.3	The Search for New Superhard Materials	4
1.4	Principles of Hardness	6
1.4.1	Phenomenological Definition of Hardness	6
1.4.2	Intrinsically Hard Materials	6
1.4.3	Extrinsically Hard Materials	10
1.5	Application-Relevant Properties	13
1.5.1	Hot Hardness and Creep Resistance	13
1.5.2	Thermal Stability	14
1.5.3	Tribochemical and Oxidation Stability	15
1.5.4	Toughness and Wear Resistance	16
1.5.5	Coefficient of Thermal Expansion	17
1.5.6	Thermal Conductivity	18
2	Experimental Techniques	19
2.1	High Pressure Techniques	19
2.1.1	The Diamond Anvil Cell, DAC	20
	Working Principle	20
	Experimental Set-up	21
2.1.2	The Multianvil Press, MAP	23
	Working Principle	23
	The Octahedral Pressure Cell	26

Temperature Measurement	30
Pressure Calibration	30
Procedure of a HP/HT-Experiment	31
Methods of Sample Recovery and Preparation	32
2.1.3 The Flyer Plate Technique	34
Working Principle	34
Experimental Set-up	34
2.2 Micromechanical Characterization	37
2.2.1 Conventional Hardness Testing	37
Vickers hardness	37
Knoop hardness	38
H/E ratio from Knoop Hardness Measurement	38
Indentation Size Effect and Normalized Hardness	38
2.2.2 Indentation Fracture Toughness	41
after Anstis	43
after Shetty	44
2.2.3 Hardness Testing Devices	46
2.2.4 Testing Procedure	47
2.2.5 Example: Standard Reference Material SRM 2100	48
2.2.6 Load-Depth Sensing Indentation Technique	55
Limitations of the Technique	59
2.3 Vibrational Spectroscopy	62
Micro-Raman Spectroscopy	62
Infrared Spectroscopy	63
2.4 Electron Microscopy and Microanalysis	63
Sample Preparation: Plasma Etching	63
Scanning Electron Microscopy, HR-SEM	64
Electron Probe Microanalysis, EPMA	64
Transmission Electron Microscopy, HR-TEM	64
2.5 X-ray Diffractometry	65
2.5.1 Diffractometers	65
2.5.2 Special XRD Sample Preparation	66
2.6 Bulk Analyses	67
2.6.1 Archimedian Density	67

2.6.2	Combustion Elemental Analysis	67
3	Spinel-Si_3N_4	69
3.1	Discovery of Spinel- Si_3N_4	69
3.1.1	Synthesis of γ - Si_3N_4 in a Diamond Anvil Cell	73
	Experimental Procedure	73
3.1.2	TEM Sample Characterisation	74
3.1.3	γ - Si_3N_4 and the Spinel Structure	75
3.2	Group 4, 13 & 14 Element HP-Nitrides	82
3.3	Multianvil Press Synthesis of γ - Si_3N_4	84
3.3.1	Choice of starting materials	84
3.3.2	Sample preparation and HP/HT-experiments	86
3.3.3	Sample recovery	87
3.3.4	Further Syntheses of γ - Si_3N_4 reported in Literature	89
3.4	Sample Characterisation	91
	Electron beam methods: SEM, TEM and EPMA	91
	Raman and Infrared Spectroscopy	99
3.5	Rietveld Structure Analysis of γ - Si_3N_4	100
3.5.1	Structural Comparison I: Anion Parameter	105
3.5.2	Structural Comparison II: Group 13- and 14-Nitrides	107
	The Group 14 Element Nitrides	108
3.6	Phase Relationships of γ - Si_3N_4	112
3.6.1	A First p-T Diagram of Si_3N_4	112
3.6.2	Theoretical Predictions of post-spinel Si_3N_4 -phases	117
3.7	The first dense γ - Si_3N_4 -based ceramic	119
3.7.1	Experimental Procedure	120
3.7.2	Sample recovery and preparation	121
3.7.3	Characterization: Results and Discussion	123
	XRD and Rietveld structure refinement	123
	Microstructure	125
	Microprobe Analyses	130
	Transmission Electron Microscopy	131
3.8	Properties of γ - Si_3N_4	134
3.8.1	Hardness	134

Nanoindentation Studies on Precursor-derived γ -Si ₃ N ₄	134
Hardness Studies Reported in Literature	137
Micromechanical Characterization of Sample SN13	139
Instrumented Hardness Testing	144
3.8.2 Elastic Moduli	147
Theoretical Predictions reported in Literature	147
Determination of the Bulk Modulus B_0 reported in Literature	148
Indentation Moduli E_r , E_{IT} and Shear Modulus G_0	152
3.8.3 G_0 of γ -Si ₃ N ₄ : Current Status of Knowledge	158
3.8.4 Indentation Toughness	163
3.8.5 Note on Properties of γ -Ge ₃ N ₄ and γ -Sn ₃ N ₄	170
3.8.6 Thermal and Oxidation Stability of γ -Si ₃ N ₄	171
3.8.7 Coefficient of Thermal Expansion	173
Experimental Procedure	174
Results and Discussion	174
3.8.8 Specific Heat and Thermal Conductivity	180
3.8.9 Vibrational Properties of γ -Si ₃ N ₄ , γ -Ge ₃ N ₄ and γ -Sn ₃ N ₄	182
3.8.10 Electronic Properties	186
3.9 High Pressure Shock Synthesis of γ -Si ₃ N ₄	189
3.9.1 Motivation	189
3.9.2 Shock Conditions for γ -Si ₃ N ₄ -Synthesis	190
3.9.3 Starting Materials and Sample Preparation	192
3.9.4 Experiment and Sample Recovery	192
3.9.5 FP-SN1: Characterization of Shock-Derived γ -Si ₃ N ₄	194
Scanning Electron Microscopy, SEM	194
X-ray Diffraction and Phase Analysis	196
Transmission Electron Microscopy, TEM	198
3.9.6 Resumé	200
4 Spinel-Sialons	201
4.1 Introduction	201
4.1.1 Prominent Sialon Phases	202
4.2 HP/HT-Studies of Sialons in Literature	204
4.3 Multianvil Press Synthesis of γ -Sialons	205

4.3.1	Choice of Starting Materials	205
4.3.2	Synthesis of β -Sialon Starting Materials	205
4.3.3	Characterisation of β -Sialons	206
	X-Ray Diffraction	206
	Chemical Composition	207
	Archimedian Density	211
	Microstructure of β -Sialons	211
4.3.4	Sample Preparation and HP/HT-Experiments	214
4.3.5	Sample Recovery, Preparation and First Investigations	216
4.4	X-Ray Diffraction Studies	221
4.4.1	Data Acquisition and Phase Identification	221
4.4.2	Lattice Parameter	225
4.4.3	Rietveld Structure Analysis of γ -Si ₂ AlON ₃	228
4.5	Microstructural Characterization	235
4.5.1	Grain Size and Morphology of γ -Sialons	235
4.5.2	Reactions between Sialon and the HP/HT-Environment	236
4.6	Micromechanical Properties	239
4.6.1	Sample Preparation, Testing Methods & Procedure	239
4.6.2	Results: Electron Microscopy of Indentations	242
4.6.3	Hardness Testing Results	242
4.6.4	Indentation Modulus	246
4.6.5	Indentation Fracture Toughness	249
4.7	Electronic Properties	252
4.8	Phase Stability Aspects	255
4.8.1	Resumé: Formation and Stability of γ -Sialon	261
Zusammenfassung		263
Bibliography		273
Danksagung		299
Curriculum Vitae		301
Keyword Index		303

Contents

1 Introduction & Motivation: Synthetic Hard Materials

The scope of this dissertation was to explore the newly discovered cubic spinel modification of silicon nitride (γ -Si₃N₄). It includes the synthesis of γ -Si₃N₄ specimen via different high-pressure–high-temperature (HP/HT) techniques in order to assess basic structural, physical (and chemical) properties. Special attention is paid to the potential of γ -Si₃N₄ as a *hard material*. Own measurements as well as results of other researchers on this quickly growing field of spinel nitrides are presented and will be discussed. In the course of the investigations, a first set of oxide nitride derivatives of γ -Si₃N₄ within the system Si–Al–O–N and related multinary systems was discovered and characterized. The acquired data should enable to evaluate the suitability of these materials as cutting materials, abrasives or in other structural or functional applications. Below, the importance of synthetic hard materials will be outlined in a brief historical review. The concept of the HP/HT approach to produce highly condensed materials with superior properties will be considered on the basis of the *physics of hardness* in subsequent sections. The additional prerequisites for “*useful*” hard materials will be treated at the end of this first chapter.

1.1 Historical Aspects on Hard Materials

Removing material from a workpiece in order to shape it was and is one of the most important manufacturing techniques of mankind — from the stone age until the present day. However, whilst chipping off pieces of flintstone to make a new tool was a very timeconsuming process and relied on the individual hunter-gatherer, the industry of the 19th and 20th century was able to ship out an ever-increasing tonnage of tools and goods that were produced in various steps of cutting, turning, drilling, sawing and lathing. The basic demands on the materials used to perform these actions have not changed much: Their properties should be superior — or at least equal — to those of the material to be removed. In most cases, *mechanical* properties such as hardness, fracture toughness and closely related features like abrasion resistance are requested. In many hard materials, these are accompanied by a high thermal conductivity and resistance to heat. It was the lack of the latter that spurred the development of synthetic hard materials: Before 1900 the most suitable cutting material was carbon steel (99% Fe/1% C), the strength and wear resistance of which is not very high and deteriorate rapidly at high temperatures that are easily created at a cutting edge with increasing speed. The industrial revolution in the 20th century required more rapid metal cutting operations, resulting in higher temperatures at the cutting edge of the tool. A solution was found by alloying the steel with hard carbide particles, leading to the development of cemented tungsten carbide (“*hard metal*”) in the mid 1920s. The first industrial production of a synthetic hard material however, was started in 1894, when EDWARD G. ACHESON established the *Carborundum Company* in Monongahela City, Pennsylvania, to produce grinding wheels, whet stones, knife sharpeners, and powdered abrasives from *silicon carbide* (SiC). Acheson himself invented the electrothermal synthesis of SiC from clay and carbon in 1893 [1]. The so called “*Carborundum*” ended

The information contained in this section was acquired from the following internet sites:

- www.nhf.nl/E/index.html,
- www.secotools.se/company/secohist.shtml, www.carbo.com,
- <http://web.mit.edu/invent/www/inventorsA-H/acheson.html>,
- www.chemheritage.org/EducationalServices/chemach/eei/ega.html

the search for a highly effective and durable abrasive required for the mass production manufacturing of precision-ground, interchangeable metal parts. Prior to the invention of *Acheson's process*, SiC had been synthesized by Berzelius [2] in 1824 and Despretz [3] 1849 in small quantities. Because of its extremely rare occurrence as a natural mineral (*Moissanite*) in some meteorites, it can be said to be the *first synthetic hard material* of widespread industrial importance.

1.2 High-Pressure-Derived Synthetic Hard Materials

As many others before and after him, E.G. Acheson originally intended to produce synthetic diamond when he discovered his electrothermal route to SiC. It should take almost exactly 60 years and the development of a sophisticated HP/HT technology, until the “*philosopher's stone*” of modern times had been found: Between 1953 and 1954, two independent teams of scientists from ASEA in Sweden and General Electric in USA were successful in converting **graphite to diamond**. Interestingly, this could not have happened without the preceding development of cemented tungsten carbide, for it was the only material to sustain the extreme forces associated with the creation of such high pressures. As we will see in Section 2.1.2, WC-Co cermets today are still a material of choice in high pressure environments.

Synthetic diamond made the supply for industrial diamonds in principle independent from natural resources, and — in fact, less than 10% of all diamond used for industrial purposes nowadays comes from natural deposits [4]. While industrial diamond works excellently in interaction with stone and concrete, glass, ceramics, tungsten carbides, precious and nonferrous metals, it fails almost entirely in the biggest market segment of the metalworking industry: Under most machining conditions, tribochemical reactions restrain diamond from becoming an effective cutting material for steel and ferrous alloys. Therefore, synthetically produced *cubic boron nitride*, *c*-BN, was introduced to the market in the 1960s [4]. As diamond, *c*-BN is formed via a dissolution–precipitation process using a *solvent catalyst* and applying HP/HT conditions. Being known as the second hardest material for a long time, *c*-BN does not chemically interact with iron

and has a higher thermal stability than diamond. Cutting tools from *c*-BN are considered as the best state-of-the-art material for finish and interrupted cutting of hardened steel, gray, and ductile cast iron [5].

1.3 The Search for New Superhard Materials

Despite its outstanding performance, *c*-BN has several shortcomings: In contrary to the diamond synthesis, where transition metals like Ni and Co serve als solvent catalysts, *c*-BN requires alkali or alkaline-earth metals or their nitrides (i.e. Mg, Ca, Li₃N, Mg₃N₂, Ca₃N₂). These substances are hygroscopic and sensitive to oxygen, which necessitates the HP/HT treatment and preliminary preparations to be carried out under inert conditions. Moreover, while single- and polycrystalline diamond is almost equal in hardness, part of the high intrinsic mechanical properties of *c*-BN is lost in polycrystalline compacts due to the lack of appropriate binding phases [6]. Therefore, an industrial demand for new hard and superhard* materials remains. Of particular interest would be a single material system whose properties could be tailored to a broad range of applications. This is the sense, in which DAVID M. TETER suggests a change of focus in the search for new superhard materials: The aim should be “*to locate materials **more useful** than diamond, rather than **harder** than diamond*” [8]. Also STAN VEPŘEK in his review article *The search for novel, superhard materials* [9] points out that “*hardness is only one of many other properties such a material has to meet*” and summarizes the most important demands with …

... *high hot hardness and toughness (up to ≥ 800 °C), oxidation resistance, chemical stability and a low coefficient of friction against the material to be machined ... and low thermal conductivity ...*

These additional properties will be discussed in more detail in Section 1.5 on page 13 of this chapter. In their above mentioned articles, both, Teter and Vepřek refer to the ‘*harder-than-diamond fever*’ which appeared to be a major driving force for the hard materials research in the 1990s. This ‘fever’ originated from theoretical predictions that a three-dimensional network of carbon and nitrogen

**superhard* usually denotes materials with an indentation hardness ≥ 40 GPa, some authors use the term “*ultrahard*” for still higher hardness ≥ 70 GPa [7]

could be *less compressible* than diamond [10, 11, 12]. One or the other postulated crystal structure of *carbon(IV)nitride* (C_3N_4) was hence believed to be possibly also *harder* than diamond. The author suspects that many researchers, including his own person, attempting to synthesize this substance, were at least partially guided by the lure to break down another barrier in nature rather than having rational objectives concerning better materials: Successful synthesis of ‘*the*’ C_3N_4 would have had a similar meaning to science like moving faster than light or reaching absolute zero. In his article however, Teter reminds the science community that the *shear modulus* G_0 rather than *compressibility* κ (or *bulk modulus* B_0) of a solid is a good predictor for its hardness. A fact that should not be surprising, because while solids and fluids both have compressibilities, the presence of a finite (and static) shear modulus is exactly what makes a solid.* Hence, the higher G_0 , the more ‘solid-like’ or the harder the material. Teter assembled data from over thousand hardness measurements of various materials, plotted them against the respective shear moduli and demonstrated that this simple rule holds up to the hardest materials [8]. According to their predicted shear moduli, all postulated C_3N_4 -polymorphs had to be declassed to *even below* *c*-BN. Recently osmium has been shown to be less compressible than diamond [13] — but of course this noble metal is much softer. A single-phase bulk material harder than diamond would have to surpass $G_0(\text{diamond}) = 535 \text{ GPa}$, which is by far the most extreme value known. The reasons why diamond is still ranking above all other single-phase solids leads us to the next section, dedicated to *Principles of Hardness*. It will also provide us with *design concepts* and *evaluation criteria* for novel synthetic hard materials. For further information on C_3N_4 , the interested reader is referred to recent review articles, e.g. those published by MALKOW [14] or KROKE and SCHWARZ [15].

*Formulating the criterion for a solid via a finite shear *strength* τ_{crit} is equivalent, as G_0 characterizes the elastic response of the material until τ_{crit} is reached.

1.4 Principles of Hardness

1.4.1 Phenomenological Definition of Hardness

The term *hardness* is easily appreciated and understood by almost everybody, however, even scientists may hesitate if they are asked to precisely *define* its meaning: Contrary to properties like elastic modulus, fracture strength or toughness, hardness lacks a single and unique mathematical model on which basis it could be described. Instead, each specification of a certain hardness test defines a “*hardness*” of its own — a fact that led TETER to the statement that “*as many kinds of hardness exist as there are ways of testing it*” [8]. Accordingly, only a general definition, that more or less explicitly addresses these testing manners, can be given as follows:

Hardness is the resistance offered by a given material to external mechanical action looking to scratch, abrade, indent or in any other way permanently affect its surface [16].

It is interesting to note that in this sense, hardness is considered a *surface property*, although — as we will see in the following two sections — the fundamental features that give rise to hardness are almost entirely associated with *volume*.

1.4.2 Intrinsically Hard Materials: Definition of Hardness at the Atomic Scale

Any macroscopic scratching, abrasion or deformation originates from reversible (= *elastic*) and non-reversible (=“*plastic*”) deformations at the microscopic level of a material. Thus, in order to be hard, the atomic configuration of this material should cause the amplitudes of these deformations to be small and their energetic barriers to be high. By this sense, five fundamental features that determine hardness at the atomic scale (“*intrinsic hardness*”) may be identified.

- (a) the magnitude of the bond energy, ϵ_b^0 ('*bond strength*')
- (b) the equilibrium distance between adjacent atoms, d_0 ('*bond length*')
- (c) the *angular* dependence of bond energy $\partial\epsilon_b/\partial\phi_i$ ('*bond bending*')
- (d) the average coordination number \bar{N}_c
- (e) the number of free atomic coordinates N_f

From these five, many other features common among hard solids can be derived:

The '*bond strength*' ϵ_b^0 shall be understood as the amount of energy, necessary to separate two adjacent atoms. This '*bond breaking*' may be accomplished by either thermal vibration, collision with energetic particles (including photons) or mechanical loading. This definition already suffices to understand that materials which exhibit a high bond strength are likely to have high melting- and boiling points and will exhibit a certain resistance against being torn apart.

External forces, seeking to stretch or compress the bond will have to be of the same order of magnitude as the first derivative $\partial\epsilon_b/\partial d$. The rigidity of the bond, also called *radial force constant* (k_r), is proportional to the second derivative, i.e. to the *curvature* of the interatomic potential. Radial or *central* forces represent the strongest interaction within a solid. They increase towards higher ϵ_b^0 and smaller d_0 and are comparatively independent of the electronic nature of the chemical bonding. Ionic as well as metallic or covalent materials can possess high bond energies and small atomic distances and therefore may have the same high k_r s. These materials will be most likely formed from atoms with high valency or ionic charge and small size, which is especially fulfilled by the elements within the second and third period within the '*p-block*' of the periodic table: B, C, N, O, Al, Si and P. The *macroscopic stiffness* of the material, as e.g. expressed by its Young's modulus (E_Y) or the volume elastic modulus (synonymously named *modulus of compression* or *bulk modulus* B_0) are proportional to the k_r s. The actual magnitude of B_0 and E_Y however depends on how directly macroscopic forces are transferred into axial stretching or compression of bonds, i.e. the bonding topology of the solid.

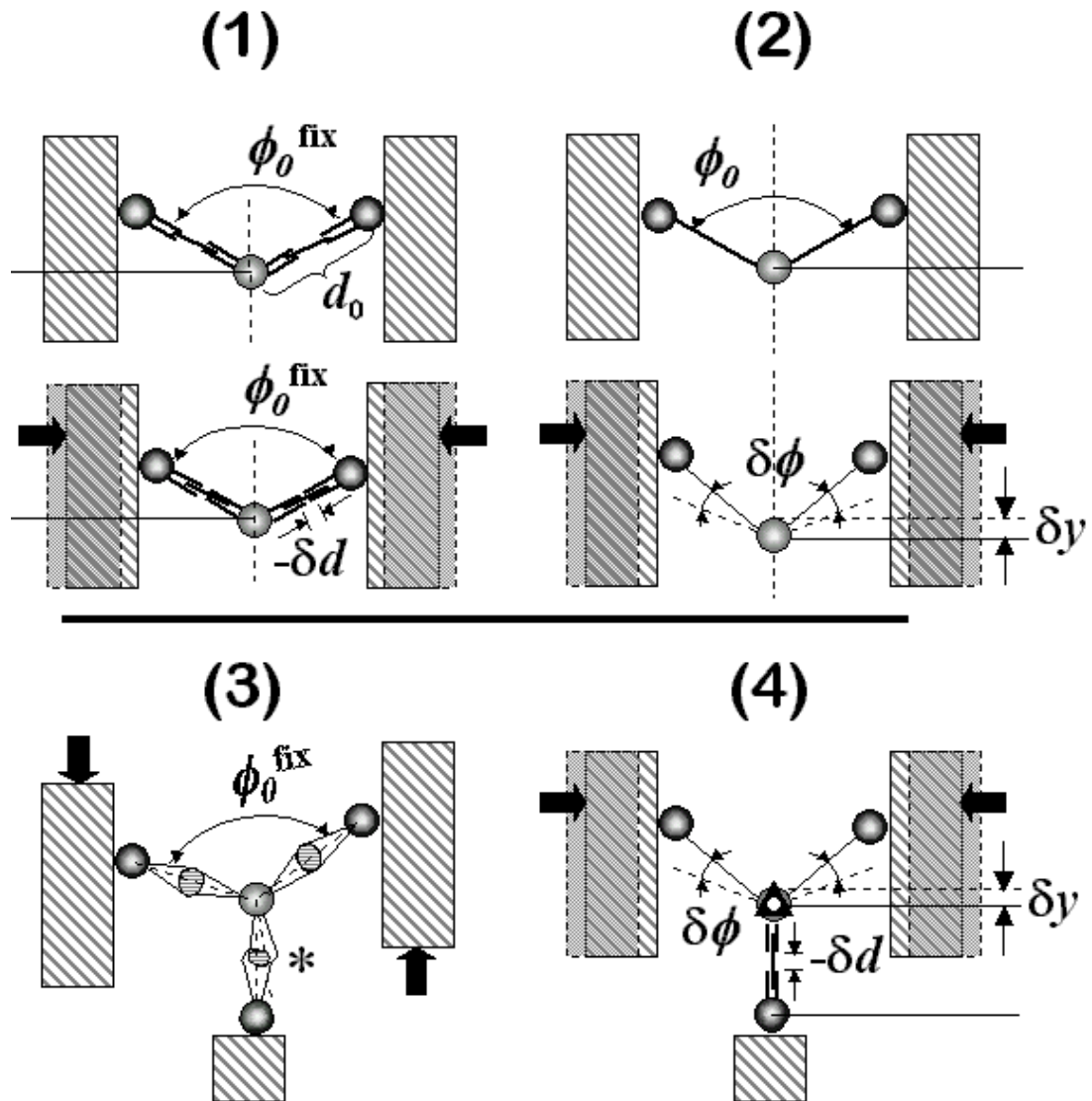


Figure 1.1: Simplified models to demonstrate the influence of the angular rigidity and coordination number on the deformation behavior of solids: (1) rigid angles facilitate axial loading of the bonds; (2) The bond angle ϕ changes, but bond distance can remain unchanged; (3) 'Bond bending': The angles between the hybrid orbitals of an individual atom cannot change, the apparent 'bending' of the bond is accomplished by a decrease in the overlap with an adjacent atom (after [17]); (4) High symmetry (here, a threefold axis at the central atom perpendicular to the paper plane) facilitates axial loading of the bonds, resulting in a higher overall stiffness.

Angular dependence of the bond energy, $\partial\epsilon_b/\partial\phi$, is directly associated with the covalent bonding type. The “*angular forces*” are highest for extremely directional electron distributions such as *sp*-bonds and decrease towards a more spherical distribution of the electron density, thus resulting in a sequence *sp* (linear) $>$ *sp*² (planar) $>$ *sp*³ (tetrahedral) $>$ *d*²*sp*³ (octahedral)). The magnitude of the angular forces is always lower than that of the radial forces. In solids the simultaneous increase in coordination number N_c outweighs this decrease (see below) and the directionality of the bonds plays an important role for the hardness. As indicated in Figure 1.1, rigid bond angles ϕ_0 in (1) facilitate axial deformation δd of the bonds instead of internal displacements δy in (2). Therefore, of two materials with equal bond stiffness k_r , the one that possesses the higher angular force constants k_ϕ will deform less because of a more direct loading of the bonds.* This is the reason why strong solids like diamond and *c*-BN are found to be highly covalent. Fig. 1.1 (3) shows that the angles between the hybrid orbitals as such behave rigid, while the ‘bond bending’ is accomplished by a decrease of their overlap (*, after Harrison, [17]).

Finally, comparison between (1),(2) and (3), (4) shows the influence of the coordination number N_c and the number of structural parameters N_f . In (3) and (4) a third atom has been added to the environment of the central atom. Its coordination number N_c has been increased from 2 to 3 and in the initial state, the symmetry of the central site is also increased from a mirror plane perpendicular to the paper (dotted vertical line in (1) and (2)) to a threefold rotation axis perpendicular to it. The solid block at the bottom shall indicate that this additional atom itself is bound to further atoms so that its position is fixed. In this configuration, an axial compression of the bonds $-\delta d$ is already enforced by geometry, even if k_ϕ is small. At the same time, the threefold symmetry of the central atom is broken, both in compression (4) and shear (3). In contrary, the symmetry of the central atom in (1) and (2) is unaffected by the deformation, as it remains on the mirror plane. This means that its vertical position along this axis is not fixed by symmetry, so that $N_f = 1$ (in the 2D case). In this planar model, increase of the coordination number and geometrical fixation (expressed by a low number of free parameters N_f) happen to coincide with one another.

*The two constants k_r and k_ϕ refer to a simple valence force field, where the mixed force constants k_{rr} , $k_{r\phi}$ etc. are assumed to be zero [18]

This must not be the case in three dimensional crystals. It can be however noted in general that solids with highly symmetric atom positions exhibit an additional resistance against deformation.

The Role of High-Pressure in the Synthesis of Hard Matter Because many solids consist of several atomic species with different coordination numbers, the average coordination per formula unit \bar{N}_c appears to be the most appropriate figure of merit. An increase in \bar{N}_c in most cases is — paradoxically — associated with an *increase* in bond length* but nevertheless leads to a strong net increase of the bulk modulus B_0 [20]. Often the resistance to shear deformation, i.e. shear modulus G_0 and critical shear stress τ_{crit} are simultaneously increased, leading to a higher hardness. This property enhancement due to the increase of \bar{N}_c is the main effect utilized in the high pressure synthesis of hard materials. According to LE CHATELIER's principle, the application of pressure enforces the formation of a state with smaller specific volume. In most cases,[†] the system facilitates this densification by an increase of \bar{N}_c .

1.4.3 Extrinsically Hard Materials: Definition of Hardness at the Microscale

From the atomic principles of hardness considered in the previous section it follows that solids that have high bond energies and incorporate small interatomic distances together with highly directional (= covalent) bonds in a symmetrical, three-dimensionally crosslinked network fulfil all requirements to be extremely hard and strong. It was further noted that pressure provides a helpful tool to synthesize new materials that obey these criteria using lower condensed phases as precursor — which is essentially the task of this thesis.

It is a long known fact however, that even the hardest among these yield at loads

*The so called “*pressure-distance paradox*” [19] exists only at first sight: The smallest possible size of the first coordination sphere around a central atom is determined by the constituting atoms ‘touching’ one another, i.e. the edge length of the polyhedron is determined by the radii sum of two adjacent nearest neighbors. Thus, if N_c — the number of ‘corners’ of the polyhedron — is increased and the size of the constituting atoms remains approximately constant, the size of the entire coordination sphere and hence also the distance to the central atom — the bond length d — are also increased.

[†]An exception is e.g. the olivine–spinel transformation: These minerals have different volumes but essentially the same \bar{N}_c [21].

which are orders of magnitude smaller than what can be expected from the atomic principles. A number of defects and mechanisms within the real structure of materials have been identified to be responsible for this. The most important are multiplication and *movement of dislocations* or other slip events like *grain boundary gliding* and *brittle fracture*. Generations of scientists and engineers have been successfully improving the load-bearing capability of metals, ceramics and other materials, mainly by increasing the energetic barriers required to activate and drive these failure mechanisms. These improvements were usually in the range of several 10% with respect to the starting situation. One widely-used principle for example is *fine grain hardening* based on the so-called “*Hall-Petch effect*” [22, 23]. In polycrystalline materials with submicron grain sizes, an increase in hardness and strength is observed with a further decrease of grain size D . This is because upon shear loading, dislocations of equal sign move at the same slip plane and queue in front of an obstacle, e.g. a grain boundary. The shear stress exerted on the obstacle is $\tau_1 = \tau \cdot n$ where τ the external stress and n the number of dislocations within the “pile-up” [24]. Thus, n acts as stress multiplication factor and the material yields when τ_1 becomes so large that further dislocations are initiated in an adjacent grain ($\tau_1 = \tau_{crit}$). Due to their own repulsive stress field, the dislocations in the pile-up are separated by certain distances with respect to one another and hence their number n is limited by the size of the crystallite D . Consequently, smaller D lead to a lower stress concentration at grain boundaries and higher strength. A crystallite smaller than a certain critical size should not contain any dislocations [25]. At these length scales however, the volume fraction of the more disordered and hence ‘softer’ material at the grain boundaries has grown so large that slip between individual grains leads to a softening, which is called the “*inverse Hall-Petch effect*” [26]. As the practical strength and hardness of materials was already noted to be *orders of magnitude* from their theoretical limit, the two- four- or sixfold increase of mechanical properties by *simultaneously* circumventing *all* these mechanisms appears not impossible. Starting from a material with a decent hardness of 20 GPa this should include the option to actually *surpass even the hardness of diamond*. This possibility was recognized early, but remained limited to studies on layered heterostructures with limited applicability for a long time (see [27, 9] and references therein). Starting in the middle of the 1990ies, some groups were able to deposit heteroepitactical thin films with

interlayer spacings below the threshold for dislocation activity [27]. Not much later, isotropic polycrystalline films were successfully synthesized, consisting of a nanocrystalline (*nc*-) component—usually the nitride, carbide or boride of a transition metal Ti, Zr, Hf, Cr, V or Ta—and an amorphous (*a*-) intergranular phase, e.g. Si_3N_4 , or BN. This means that both phases fulfil the abovementioned five criteria for “*intrinsic hardness*”. However, the key to what VEPŘEK denoted as “*extrinsic hardness*” [9] was to find phase combinations with a pronounced miscibility gap that form strong interfaces to prevent grain boundary sliding and do not show any coarsening (Ostwald ripening), neither during their synthesis nor at temperatures that occur under the attempted working conditions [28, 29]. Meanwhile the knowledge on the mechanical properties and thermal stability of these coatings has gained considerably [30, 31, 7]. In 2001 VEPŘEK and colleagues presented a *nc*-TiN/*a*- Si_3N_4 /*a*- TiSi_2 thin film with a plastic hardness of 140 GPa (*nc*-diamond gave 105 GPa) [32] and similar coatings with a high thermal stability up to 1100 °C [29]. First commercial applications based on these coatings emerged.* Finding a route to ultrahard *bulk* materials of this type holds potential to become a major scientific breakthrough.

*see <http://www.shm-cz.cz/a/company.htm>

1.5 Application-Relevant Properties of Hard Materials

As stated in Section 1.3 on page 4, high hardness and stiffness is by far not the only requirement for a “useful” material to be employed in an abrasive or structural application. The relative importance of these additional properties will of course largely depend on the particular application and, may even vary with the process parameters *within* this application. For example, in the performance of a cutting tool insert, creep and chemical resistance become increasingly important at higher cutting speeds. In the following, these ‘key properties’ will be shortly explained and reference values be given.

1.5.1 Hot Hardness and Creep Resistance

Abrasive action, which is one of the most important applications for these hard materials, does always imply frictional heating. In metal cutting, additional heat is dissipated at the cutting edge due to the high plastic strain rates of the metallic workpiece. Both the temperature and productivity increase with cutting speed: materials with high hot hardness can maximize productivity by permitting higher cutting speeds. High speed cutting tool tips can encounter temperatures of 1000 °C or higher.

A decrease in hardness at high temperatures is a common feature of all solids without any exception to hard and superhard materials. It arises mainly from the thermal activation of additional deformation mechanisms, especially cross slip of dislocations but also creep via grain boundary and lattice diffusion or even viscous flow. The effect can be very dramatic: At ~ 600 °C *c*-BN is said to have lost approximately 50% of its original hardness which then is equal to that of α -Si₃N₄. The hardness of diamond drops with some delay, but above 1100 °C (and inert atmosphere provided) boron carbide becomes the hardest known material.* This is because the crystal structures of α -Si₃N₄ and B₄C are less symmetric than that of the cubic zincblende solids diamond and *c*-BN and hence provide a smaller number of possible directions for thermally activated dislocation slip.

Spinel compounds that are subject of this thesis are of cubic symmetry like dia-

*see R. Telle, “Boride and carbide ceramics” in [33], Ch. 4, Page 255

mond and *c*-BN. Conventional oxide spinels are known to have two slip systems, namely one being the same as with diamond-like solids $\frac{1}{2}\{111\}\langle110\rangle$ plus at least one *additional* system $\frac{1}{2}\{110\}\langle110\rangle$, in some cases also $\frac{1}{2}\{100\}\langle110\rangle$ [34]. It is reasonable to expect the same preferred slip directions and planes to be active in spinel nitrides and hence their hot hardness is not likely to be extreme. It may nevertheless be competitive with other ceramic materials, as it will benefit from the high initial hardness value. Moreover, as indicated previously, even excellent intrinsic properties could be lost due to interfacial effects such as the local structure and the presence of secondary phases at the grain boundaries. In [20], HAINES et al. point out that dense compacts of novel high-pressure derived materials like stishovite can be obtained directly from low-density starting materials and hence would be free of binder and impurities that may deteriorate their intrinsic properties. This has been achieved recently by fabrication of phase-pure “translucent” *c*-BN qualities [35, 36] and was also demonstrated for spinel- Si_3N_4 (cf. Section 3.3.4 on page 89) and especially for spinel sialons (Chapter 4) that are both subject of this thesis.

A determination of the hot hardness requires sophisticated equipment and was not attempted during this work.

1.5.2 Thermal Stability

All the high pressure derived hard materials, with diamond and *c*-BN among them, are metastable at ambient pressure. Not only during the actual performance as a tool, but also during compaction treatments necessary to form the tool from a powdery source material in the first place, these materials may be subjected to high temperatures. Thus, the importance of a high “metastability” or thermal stability, i.e. the temperature where decomposition or back-transformation to the low pressure polymorphs occurs, can barely be underestimated. Here, stishovite and the cottunite phase of TiO_2 provide sad examples: Both phases exhibit high hardness values of 33 GPa and even 36.8–40.7 GPa, respectively. Furthermore, being pure oxides, they should reveal 100% resistance against oxidation. Alas, *r*- SiO_2 starts to amorphize at $\sim 650\text{ }^\circ\text{C}$ [37]. The hardness measurements of *cottunite*- TiO_2 were only possible after the material had

been decompressed at the temperature of liquid nitrogen, 77 K, and was kept at 157 K throughout the entire hardness testing [38]. Decompression below 25 GPa at ambient temperature caused the phase to transform into a lower density TiO_2 polymorph. The two superhard materials in use, diamond and *c*-BN exhibit a much higher thermal stability. The rate of graphitization of diamond is reported to become significant above 1500 °C [39] and the $c\text{-BN} \rightleftharpoons h\text{-BN}$ equilibrium was found to be located at \sim 1400 °C [40], further substantiated by annealing studies of pure *c*-BN by AKAISHI et al. [35]. However, these temperatures are valid only for inert atmosphere. As we shall see in the next section, chemical reactions during frictional interactions and the ubiquitous presence of oxygen within the vast majority of working environments will pose much more strenuous limitations.

1.5.3 Tribocatalytic and Oxidation Stability

Facing the severe conditions at the dynamic contact e.g. between a metallic work-piece and a cutting tool tip, both the thermal stability of the hard material alone and the resistance against abrasive wear and plastic deformation, given by a high hot hardness and microfracture toughness, are not enough for an overall good performance of a hard material, as a further limitation is set by tribocatalytic interactions and oxidation. These chemical reactions are especially threatening in modern machining applications, such as surface finishing hardened steel (in order to save the final grinding operation) and high speed cutting for increased productivity, where very intense heating occurs. Moreover, these operations are now being preferentially performed *without* liquid coolants or lubrication for environmental and cost-efficiency reasons, so that oxygen in the air will have direct access to the interaction zone. Even under lubricated conditions, chemical interactions due to the cracking of the carbon backbone of the employed oil has to be considered [41]. Like diamond, silicon carbide has been early recognized to be unsuitable for the machining of ferrous alloys, because it forms iron silicide and iron carbide in contact with the workpiece. Boron carbide, commonly represented by the formula B_4C provided with a high hardness around 35 GPa suffers from increased oxidation above 450 °C [9]. Even for *c*-BN, currently the best suited cutting material for hard turning of steel, several mechanisms of chemical wear have been proposed (see [42] and references therein).

Silicon nitride and sialon based ceramics are unsuitable for hardened steel but can be used for machining of cast iron. High temperature studies of Si_3N_4 /steel interaction couples revealed dissociation of Si_3N_4 and diffusion of Si into the iron between 700 and 1100 °C, followed by N diffusion (instead of N_2 formation) at still higher temperatures [43, 44]. This demonstrates a basic thermodynamic limitation for silicon based ceramics. The rate of this process may however be limited by appropriate additives. In this regard it is interesting to note that sialons perform up to 5 times better than β - Si_3N_4 ceramics when cutting nickel superalloys [42] — probably also due to a better chemical stability. In the above-mentioned experiments with interaction couples [44], the sintering additives of the Si_3N_4 ceramic, Al_2O_3 and MgO were found to be immobile. They formed small particles that were dispersed within the ceramic side of the interdiffusion layer. The exceptional chemical stability of pure Al_2O_3 against iron is well known and aluminum oxide ceramics were among the first employed for cutting applications [45]. However, fine-grained pure Al_2O_3 is hard but not creep resistant, $\text{Al}_2\text{O}_3 + 30\%$ $\text{Ti}(\text{CN})$ is harder than 20 GPa but brittle and Al_2O_3 toughened with 20% SiC -whiskers suffers from decreased chemical stability [45]. It seems however to be possible to utilize the inertness of Al_2O_3 for nitride ceramics by incorporating appropriate amounts of this element. For example, a high aluminum content was found to be beneficial for the stability of hard TiAlN PVD-coatings on cutting tools. It is believed that Al diffuses to the surface and forms a highly resistant thin film of amorphous Al_2O_3 [46]. Moreover, co-sputtering Si and Y into the crystalline TiAlN-layer led to an enhanced oxidation resistance [46]: After exposure to oxygen at 750 °C for 30 min, the material with a net composition $(\text{Ti}_{0.38}\text{Al}_{0.50}\text{Y}_{0.10}\text{Si}_{0.10})\text{N}$ developed an only 50 nm thick oxide layer as compared to pure $(\text{Ti}_{0.4}\text{Al}_{0.6})\text{N}$ that had 1.8 μm [46].

1.5.4 Toughness and Wear Resistance

Hard materials are, due to their inherent disability for plastic deformation, prone to brittle failure. In (purely) load-bearing structural applications of these materials, for example turbine blades, valves or bearings, the macroscopic fracture toughness that is associated with the propagation of large cracks leading to catastrophic failure of the *entire* part is the most important feature. In cutting tool

applications this parameter is also important, especially in intermittent cut where high mechanical and thermal stresses arise from the repeated impact upon the workpiece. However, as the primary loading of the material occurs in compression and shear, macroscopic toughness is less critical. Here, the performance of the material is determined by the resistance against *microscopic* fracture events such as grain pullout due to abrasive impact of carbide particles, e.g. while processing hard (ferrous) alloys. In these cases the otherwise more resistant coarse grained materials proved to be outperformed by materials with submicron grain sizes [45].

Because of the strongly localized stress fields around the indenter, conventional microhardness testing proved to be a convenient means to study fracture at these small length scales [47]. Hence, apart from being the only *applicable* method because of the small sample sizes, the indentation toughness method used to characterize the novel high pressure phases of this thesis, is also believed to yield the *more relevant* information to evaluate their potential for future applications.

1.5.5 Coefficient of Thermal Expansion

Thermal lattice expansion, usually described by the linear coefficient of thermal expansion, α_{th} [$10^{-6} \times K^{-1}$], is a thermomechanical property that becomes in particular important, when either a composite, a joint between two different materials or a coating on a substrate are subjected to changes in temperature. A misfit between the thermal expansion coefficients in these materials may cause cracking and delamination due to induced stress fields. In the case of very steep temperature gradients, fracture may also occur in brittle single-component materials (*thermal shock*) as a consequence of the volume difference between the hot and cold part of the shocked body. Again using the example of a cutting tool, where large and fluctuating temperature differences between the cutting tip region and the bulk may occur, materials with small expansion coefficients are preferred. In other cases however, also larger α_{th} values would be desirable, e.g. to match the expansion of a substrate or backing material.

In the course of this work, the thermal expansion coefficient was determined in the case of the cubic silicon nitride. This is reported in Chapter 3, on page 173 of this thesis. In conformity with data from other researchers, the thermal expansion of $\gamma\text{-Si}_3\text{N}_4$ was found to be larger than that of the low pressure modifications.

1.5.6 Thermal Conductivity

While for many of the aforementioned properties, novel materials are sought to have the highest (hardness, fracture toughness, thermal stability) or lowest (coefficient of friction, thermal expansion) values, there is no such clear preference in the thermal conductivity λ_{th} of cutting materials. Instead, this property is usually tailored to adapt the heat fluxes that occur in the respective cutting application and/or to attain a high resistance against thermal shock. It has been shown e.g. that a *low* λ_{th} of hard ceramic PVD-coatings on cutting tools had a positive effect on the tool life, by rejecting more of the heat into the chip [46]. A good example for the ambiguous influence of the thermal conductivity in the case of *bulk* cutting materials is provided by DAWSON (see [42] and references therein): In turning hardened steel with *c*-BN-based cutting tools, a higher life-span was found for tools with a lower *c*-BN fraction and hence *lower* thermal conductivity (45 W/mK instead of 100 W/mK). This was at least partially explained by an increase in the thermally induced softening of the workpiece metal resulting in a reduction of the abrasive attack and the thermal load on the tool. On the other hand, the heat is not entirely restricted to the chip and the workpiece surface can also experience thermal damage. Consequently, the best surface quality was obtained using the well-conducting *high* *c*-BN content tools — however, at the expense of reduced tool life.

Considering these examples, a hard material the λ_{th} of which could be tuned within a wide range without affecting its mechanical properties would be very desirable.

2 Experimental Techniques

2.1 High Pressure Techniques

In Section 1.4.2 of the previous chapter, the approach of this work, synthesizing novel hard materials by conversion of low-condensed starting materials that consist of light *p*-elements into dense extended phases has been explained. This is always associated with an increase of the average coordination number \bar{N}_c within the solid, which usually requires high pressures in the range of 10^9 Pa = GPa. In most cases also heating has to be applied in order to overcome kinetic barriers. There are two basic principles according to which pressure can be applied: The term “*static pressure*” refers to devices which allow subjecting a sample to pressure for virtually unlimited time, while “*dynamic pressure*” means that a sample is under pressure for fractions of a second only under the effect of *shock waves*. For the underlying synthesis experiments, two static and one dynamic HP/HT-methods have been used:

- Static high-pressure devices:
 - diamond anvil cell (DAC)
 - multianvil press (MAP)
- Dynamic high-pressure methods:
 - flyer-plate technique (FP)

In the following, these methods will be introduced in general, followed by details concerning pressure and temperature calibration, their actual design in the experiments, including the development of special sample environments. A general overview of high-pressure techniques in chemical synthesis is given by KROKE [48].

2.1.1 The Diamond Anvil Cell, DAC

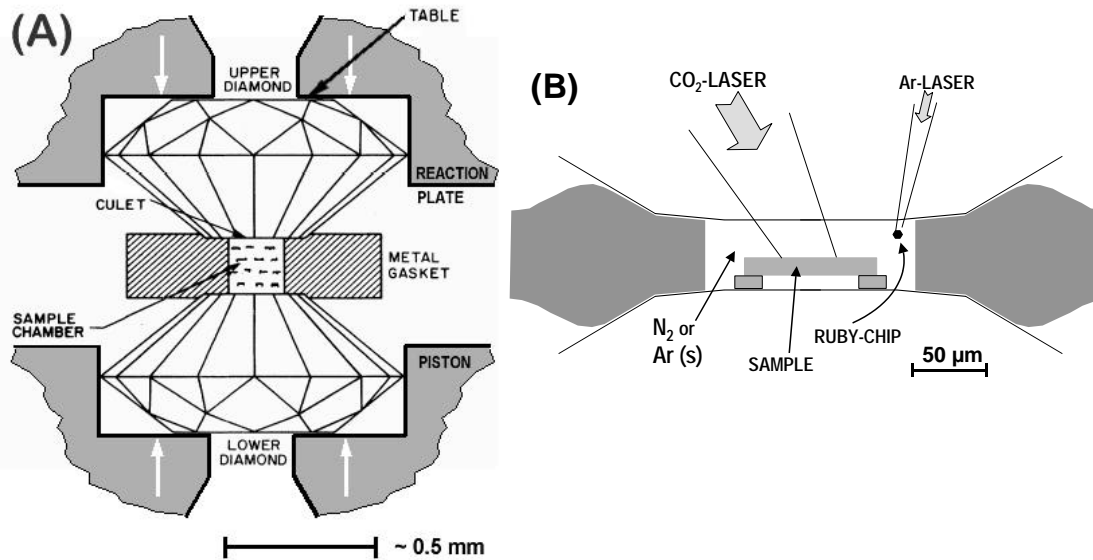


Figure 2.1: (A) Schematic representation of a diamond anvil cell (DAC); (B) Schematic cross section through the DAC sample chamber: Assembly for laser heating experiments. After Zerr, Serghiou and Boehler [49].

Working Principle

The function of a DAC is easily anticipated from Fig. 2.1 (A), showing the core part of this high-pressure device. A cylindrical sample volume, confined between two flat parallel culets of opposed diamond anvils and a metal gasket, is subjected to a pressure buildup, when the anvils are forced together. In most cases, the sample is not in direct contact to the anvils, but embedded in a pressure medium (inert gases, organic liquids, alkaline halides e.g. NaCl, KBr) which has low shear strength and thus creates quasi-hydrostatic conditions. The anvils are usually selected from brilliant-cut diamonds of gem quality and have to satisfy additional requirements such as very low luminescence for light scattering studies. The optical transparency of diamond is a great surplus to its exceptional compressive strength which we already elucidated in Section 1.4.2. It enables the user of a DAC to study a number of optical properties *“in situ”*, i.e. under sustained pressure, and to have visual control of the sample at all pressures. Also the pressure calibration is performed optically, via the pressure dependency of

the ruby fluorescence (see [50], pages 69–70). In the present case, the sample was furthermore heated optically, by focusing a CO₂-laser beam through one of the diamond anvils (Fig. 2.1 (B)). The availability and cost of large diamond crystals sets a limit to the volume of the sample chamber, resulting in typical sample dimensions of 70 × 70 × 15 μm [49].

The gasket, apart from providing containment for the pressure medium, extrudes around the diamonds and acts as a supporting ring, preventing failure of the anvils due to concentration of stresses at the edge of the anvil faces. It is prepared by drilling a hole (~ 150 μm in diameter) at the center of the indentation made by the anvil faces on a metal foil. Various types of stainless steels are used for standard gasketing. For in situ X-ray studies or to achieve extremely high pressures, metals with low absorption or high yield strength and low compressibility such as Be or Re, W and Os are being used, respectively.

Variations in the DAC arise from different ways in which the force-generating and the anvil-alignment mechanisms can be designed. In a comprehensive review article from 1983, JAYARAMAN presents five different design concepts [50]. Many modifications and intermediate forms of these may have emerged since then.

Actual Design of the Employed DAC and Experimental Set-up

Cell Design The DACs used for the underlying experiments have been developed by BOEHLER [51]. They are based on the Syassen-Holzapfel-type loading mechanism ([50], page 68) and were especially tailored for use in both X-ray and optical apparatus.

Sample Preparation The samples, having approximately the abovementioned dimensions, were introduced into the DAC under an optical microscope. They were separated from the highly thermal conducting diamond anvils by either placing them between two thin discs of sodium chloride, which then also acted as solid pressure medium, or by suspending them over the lower diamond using even smaller pieces of alkali halide (see Fig. 2.1 (B)). In the latter case, the DAC was successively filled with Ar using a gas loading device. Prior to gas loading and closing the cell, micron-sized ruby chips—to be used as pressure calibrants—were distributed within the sample volume at some distance to the sample.

Pressure Calibration The ruby fluorescence scale is the most commonly used pressure gauge for DAC-experiments. The R lines of the Cr^{3+} -ions in Al_2O_3 shift linearly by $0.365 \text{ nm} \cdot \text{GPa}^{-1}$. Deviations in the linearity were found to be negligible up to 20 GPa. Above this pressure, a small positive correction may be applied. Further details can be found in Ref. [52] The measurements were carried out at room temperature. The increase in pressure due to the heating was found to be less than 2% of the average pressure value, when the volume ratio between sample and pressure medium was kept below 1:10 (see [49] and references therein).

Sample Heating and Temperature Calibration Heating of the sample was performed with a CO_2 -laser (Melles Griot, 150 W). The spot size of the laser-beam could be varied via an optical system and the laser power was controlled with a feedback stabilisation to minimize the temperature fluctuations to approximately 5% of the average temperature. The temperature itself was estimated by fitting the emission spectrum of the sample to the Planck formula under the assumption of a greybody emission behavior. The experimental set-up for the laser heating experiments is shown in Ref. [49], which also provides further details concerning uncertainties in temperature and pressure determination.

In Situ Raman Spectroscopy The Raman spectra were excited with the 457.9 nm line of an argon ion laser with about 10–20 mW of power at an incident angle of 25° focused to a $15 \mu\text{m}$ spot on the sample. The spectra were analyzed using an ISA U1000 double monochromator with a photon counting detection system with a Spex 1402 double monochromator with a CCD (carged coupled device) detector.

2.1.2 The Multianvil Press, MAP

Working Principle

DACs are the most prominent representatives of Bridgman high-pressure devices, which are in general characterized by the two opposed anvils. Force is applied uniaxially via these anvils and therefore, isostaticity solely relies on the low shear strength of the employed pressure medium. In multianvil devices, isostatic conditions are already anticipated via *multidirectional* mechanical loading. In the past, multianvil devices with complicated geometries including multidirectional *force generation* have been constructed. In contrary, the working principle of the two-stage 6–8 type (split-sphere) multianvil apparatus used for the present studies, includes an effective geometrical redistribution of a *uniaxially* applied force. This force can be provided by a commercial hydraulic press which may be one reason for the popularity of this method. Throughout the entire document, the abbreviation **MAP** solely addresses this 6–8 type device. A good overview on the MAP-technique is given by RUBIE [53].

Pressure assembly The numbers 6 and 8 refer to the numbers of anvils which are used to redistribute the uniaxial force into a multidirectional compressive stress. A schematic sketch of this assembly is shown in Figure 2.1.2 on the next page: Two **guide blocks** (1) are attached to the pistons of a hydraulic press. Each guide block contains a spherical cavity in which **3 outer anvils** (2) with the shape of a sectioned sphere are seated, respectively. Thus, there is a total number of **6 outer anvils** forming the first stage of the high-pressure assembly. In other concepts, the outer anvils resemble a split cylinder instead of a sphere (“Walker-Type” MAP). The second stage consists of **8 cube-shaped inner anvils** (3), usually made of WC/Co alloy* (‘WC-cubes’).

These cubes have truncated corners and are arranged to form a bigger cube, as indicated by the fat lines (in the figure, only the top and the bottom WC-cube are shown, the 6 peripheral cubes are omitted for clarity). At the innermost part of the multianvil assembly, the pressure medium (4) that contains the sample is

*At the Bayerisches Geoinstitut, Toshiba Grade “F” and WiDia “THM-U” grade WC-cubes are used. Cubes from polycrystalline diamond or *c*-BN has been successfully employed for more extreme conditions in other high-pressure laboratories. (V.L. Solozhenko, personal communication)

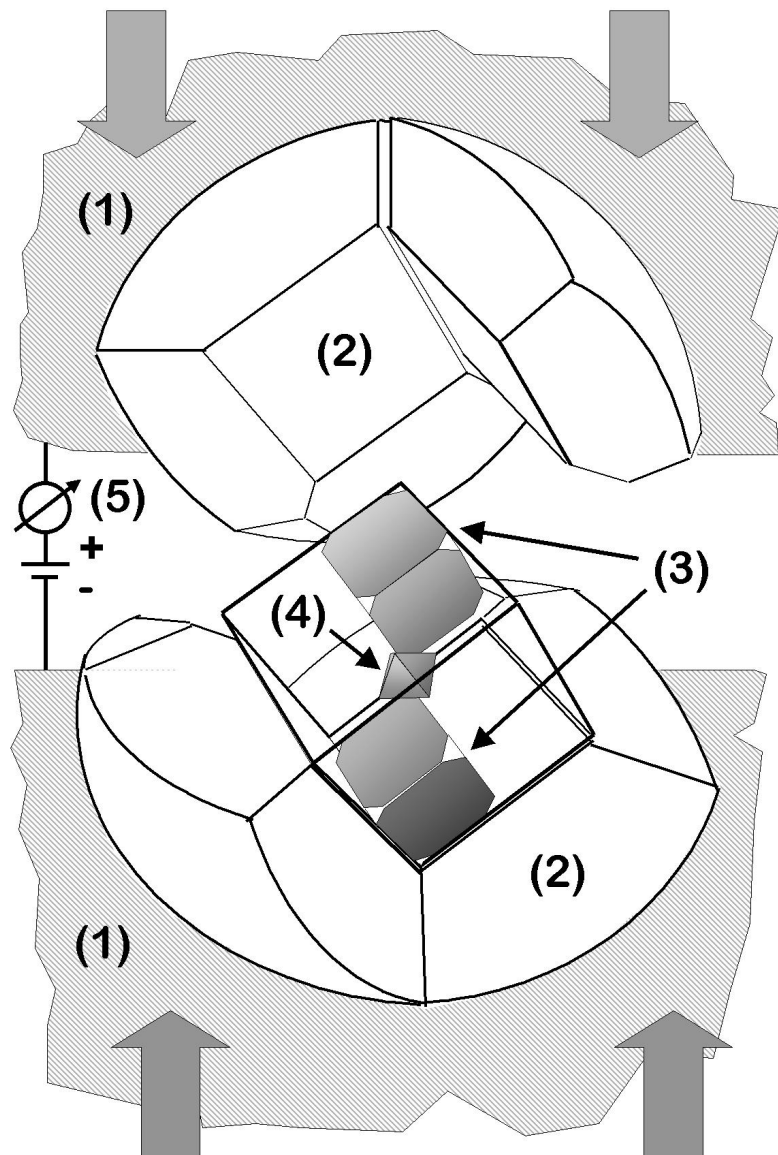


Figure 2.2: Crossectional view into the pressure assembly of a split-sphere 6–8 multianvil apparatus:

- (1) metal guide blocks
- (2) hardened steel outer anvils
- (3) tungsten carbide inner anvils (2 of 8 shown)
- (4) octahedral pressure cell ('MgO-octahedron')
- (5) adjustable power supply (sample heating)

located. It consists of a deformable ceramic which has the shape of an octahedron, hereafter named *octahedral pressure cell* or ‘*MgO-octahedron*’. The internal assemblage of the pressure cell is explained in the following section. Each face of the octahedron is in contact to the triangular facet of a truncated WC-cube-corner. The octahedron is larger than the void being formed by the truncated corners of the 8 WC-cubes and hence gaps exist between them. These gaps are diminished, as the guide blocks are driven together and the outer anvils force the WC-cubes to move uniformly towards the center, approaching one another. The MgO-octahedron in the center is compressed which creates a quasi-hydrostatic stress in its interior. As the applicable load is limited by the capacity of the hydraulic press, higher pressures can be only achieved with smaller truncations on the WC-cubes, i.e. the same force is transduced through smaller effective areas. This leads also to smaller octahedra and hence smaller sample dimensions. The pressure assemblies are specified by the edge length of the octahedra (‘*octahedron size*’) and the length of the triangular facets at the truncated cube corners. The latter is denoted as **truncated edge length (TEL)**. Three differently sized pressure assemblies were used in the underlying experiments. They are defined in Table 2.1.

	octahedron size Assembly	TEL [mm]	pressure range [GPa]
10M	10	4.0	17–21
14M	14	8.0	11–16
18M	18	11.0	4–10

Table 2.1: Specification of the three pressure assemblies that were used in the multianvil experiments

Gasketing The inward movement of the WC-cubes causes material from the corners of the octahedron to flow into the gaps between them—an intended effect that diminishes the shear stresses in the center of the octahedron. However, the extrusion must be limited by additional gaskets in order to keep up the pressure for a longer time. The gaskets must be thermally stable and exhibit an appropriate shear strength: On the one hand they must be capable to flow in

order to constantly reduce shear stresses, on the other hand they must be strong enough to bear the high stress gradient between the interior of the pressure cell and the empty gap between the anvils. The easy-to-machine silicate mineral pyrophyllite proved to be a good material for this purpose.*

Electrical heating By using gaskets and taking additional precautions, not only the direct mechanical contact but also short circuit between the anvils is prevented. Moreover, as the upper and the lower guide block are designed to never touch during an experiment, currents of sometimes up to 100 A can be easily sent through the axial WC-carbide cubes to heat the interior of the pressure cell, as symbolized by feature (5) in Figure 2.1.2. Temperatures in the range of 3100 K, albeit not simultaneously with the maximum pressure of \sim 26 GPa, can be achieved [53]. The materials used for the resistance heating will be treated within the next section.

The Octahedral Pressure Cell

As mentioned above, the force of the uniaxial press is concentrated upon a pressure medium in the center of the 6-8 multianvil assembly. It has the shape of an octahedron and does not only contain the sample, but also a resistive heater (the ‘furnace’) and a device for temperature control—usually a thermocouple. Pressure cells containing additional sensors for in situ measurement of properties like electrical conductivity or sound velocity have been designed and are also frequently used at the BGI. However, for the ‘simple’ synthesis experiments subject to this thesis, a basic set-up shown in Figure 2.3 was sufficient. In the course of the investigations, some modifications in order to minimize oxidation and to maximize the volume of the sample were made. These will be treated further below.

General set-up In general, the **octahedron main body (O1)** consists of a porous magnesium oxide ceramic, doped with 5% Cr_2O_3 . An also porous **zirconia tube (O3)** with its low thermal conductivity is used to reduce heat losses. Zirconia is considerably harder than MgO ; therefore, additional **MgO-**

*e.g. StenauTM (formerly Rosenthal ceramics) machinable ceramic, used in unfired state

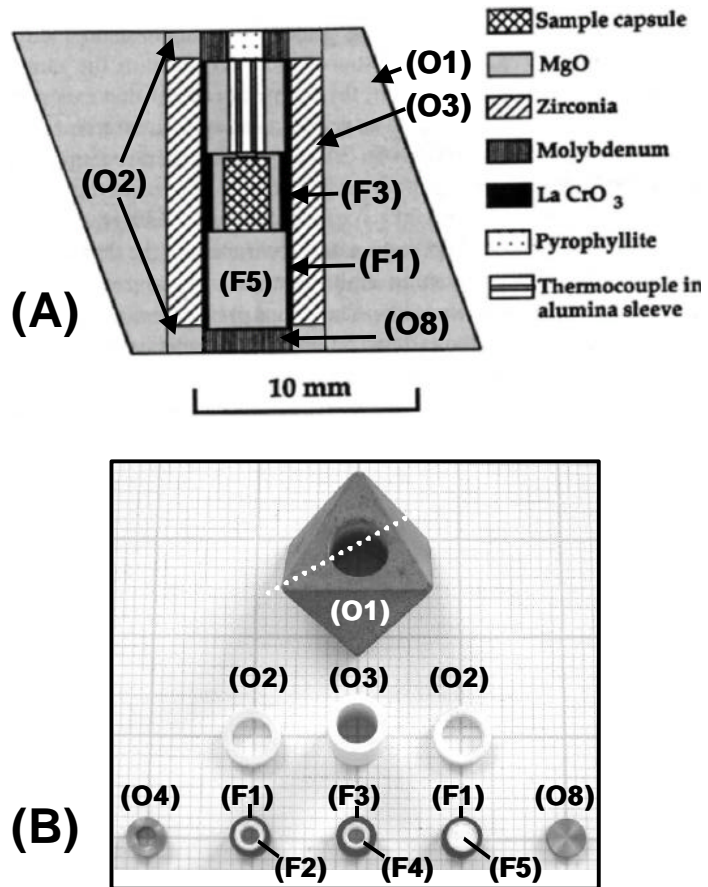


Figure 2.3: (A) Crossectional view of the interior of an octahedral pressure cell ('MgO-octahedron') in the standard configuration taken from [53]. (B) Main parts of the MgO-octahedron before the assembly. The intersecting plane shown in (A) is indicated by the white dotted line.

rings (**O2**) are used for the small assemblies 10M and 14M in order to prevent damage of the WC-cubes. They can be omitted for the large 18M assembly, because the relative extrusion during the experiments is much smaller. The next layer towards the center of the octahedron is formed by the electrically conducting **furnace parts** (**F1**) and (**F3**). In the 18M and 14M assemblies, the furnace is “stepped” with the wall thickness of (**F3**) at the center being thicker in order to minimize the thermal gradients along the sample length. The furnace of the 10M assembly is a single straight tube, because of its small dimensions. Transformation to diamond limits utilisation of graphite as heater material to ~ 10 GPa. Above this pressure and for all experiments reported in this work, lanthanum chromate, La₂CrO₃, was used. Parts from the refractory metal molybdenum,

(O4) and **(O8)**, provide electrical connection between the furnace and the axial WC-Co cubes which are in turn connected to the guide blocks (recall Fig. 2.1.2). The sample and the thermocouple unit are electrically insulated against the furnace by means of **(F2)** and **(F4)**—tubes of pure sintered MgO. A cylindrical spacer **(F5)** that is made of the same material completes the assembly.

Sample encapsulation Powdered samples were filled into noble metal capsules enabling their tight pre-compaction by means of a hardened steel plunger and a small hammer. In order to diminish contamination with oxygen and/or moisture, this was done in either a glovebag (earlier experiments) or a glovebox. The capsules were first formed by rolling several layers of Re or Pt foil around a plunger with appropriate diameter, folding one end and forging it into flat bottom by means of the plunger and a die ('*Method I*'). Later, seamless Pt-tubing* was cut to the appropriate length and arc-welded close at one end, leaving only one side open. In this latter case, the Pt was thereafter annealed in flowing Ar at 1000 °C in order to remove any trace of absorbed oxygen. The material also retained full ductility and could be easily hammered close at the second end after the powdered sample material had been filled in ('*Method II*'). *Welding* also the second end of the capsule proved not to be beneficial, because residual sample powder adhering at the Pt surface prevented the formation of a proper weld seam. In the case of SN13 (Table 3.1 on page 72 the sialons (Chapter 4) the sample cylinders of sintered ceramic were either also wrapped into Pt foil (H1401 and HP-SialXX_I, XX = 20...42, series, see Table 4.3 on page 217) or directly inserted into the furnace, partially even without MgO capsule ((F4), Fig. 2.3 on the preceding page). For the last series (HP-SialXX_III), hot isostatically pressed hexagonal boron nitride (HIP-*h*-BN)[†] was used as encapsulation material. HIP-*h*-BN is a very soft ceramic and can be easily turned on a lathe. Under the HP/HT conditions of the MAP-experiment it is converted into the ultrahard *c*-BN, thus providing an excellent diffusion barrier. Starting from capsules that were simply substituting the MgO-part (F4), longer *h*-BNcapsules to accommodate more sample material were employed in later experiments, however at the

*The precious metals division of the Heraeus company, Hanau, Germany, and Mrs. Cordula Koehler in particular, are gratefully acknowledged for the support of this work, substantiated in *i*) the donation of custom-made Pt-tubing *ii*) providing a second charge at preferential price.

[†]"HDBN", Henze Special Ceramics, Kempten, Germany

cost of a less homogeneous temperature distribution, because the length of the MgO buffer piece (**F5**) had to be reduced (Figure 2.4). For some samples, further precautions against oxidation were taken:

- (1) **Triple encapsulation:** The innermost Pt-capsule was secondly inserted in a molybdenum capsule that had also been made by abovementioned *Method I* and then into the *h*-BN.
- (2) **Inert atmosphere:** In order to exclude air from the initial porosity of the Mg-octahedron, the semi-finished pressure cell was heated at 900 °C under flowing argon, the sample was inserted inside the glovebox and the whole assembly was sealed in an air-tight vessel for transportation. Thereby exposure time to air was thereby reduced to the last half hour before pressurisation.

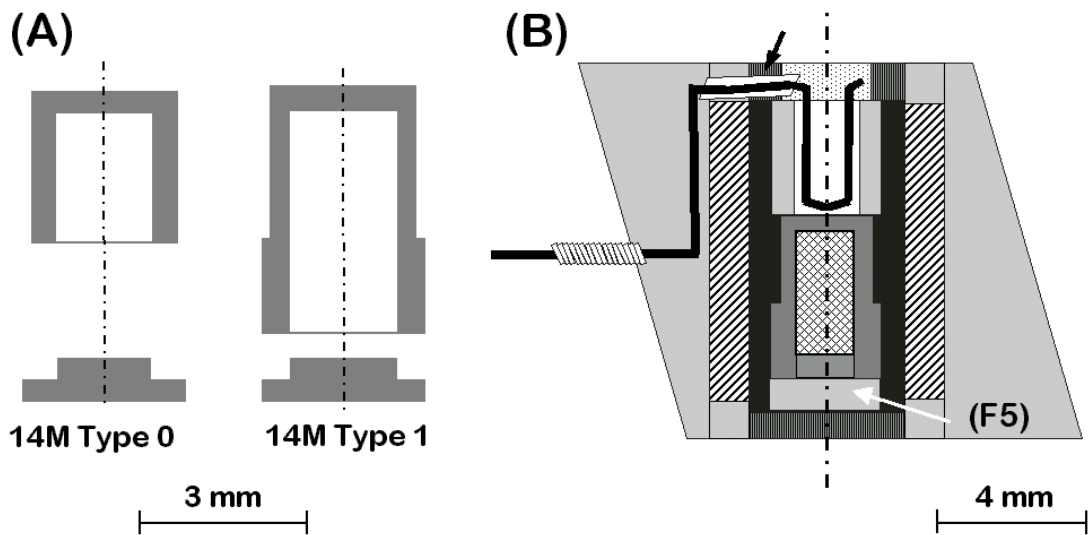


Figure 2.4: (A): Crossectional view of different BN-capsule designs. (B): Crossection of a 14M octahedron with a Type 1 BN-capsule. Note that the length of the MgO-spacer (F5) is diminished with respect to the standard configuration shown in Fig. 2.3 on page 27

Thermocouple The thermocouple is inserted coaxially with respect the bore of the octahedron main body and the junction is in direct contact to the sample capsule. The two thermocouple wires are guided through the molybdenum rings and the octahedron main body (as indicated by the arrow in Fig. 2.4 B) and

finally leave the high pressure region via the pyrophyllite gaskets and the gaps between the WC-Co cubes in opposed directions. In all experiments W3%Re–W25%Re thermocouples were used and the junction was formed mechanically without welding.

Temperature Measurement

The major uncertainty in temperature determination arises from the thermal gradient along the sample length. This means that the temperature measured at the contact point between sample and thermocouple can considerably differ from the temperature experienced by the sample material at the interface to (F5). WALTER and coworkers [54] found that the temperature distribution within a sample is highly dependent on the specifications of the assembly and the furnace configuration in particular. Using standard cell configurations with multiple thermocouples as well as diopside–enstatite mineral assemblages, the composition of which depends on temperature, they found following gradients away from the furnace midlines:

- 18M stepped LaCrO_3 furnace: $-50 \text{ }^{\circ}\text{C}/\text{mm}$
- 14M stepped LaCrO_3 furnace: $-70 \text{ }^{\circ}\text{C}/\text{mm}$
- 10M straight LaCrO_3 furnace: $-200 \text{ }^{\circ}\text{C}/\text{mm}$

No efforts were undertaken to measure the thermal gradients for the present cases. They may be comparable to those of Walter et al., where short capsules and the regular (F5) pieces (MgO) were employed. Especially long samples with BN-encapsulation, such as shown in Fig. 2.4 (B) will experience larger gradients. Nevertheless, throughout the entire thesis, the nominal temperatures as read from the thermocouple at the specific experiments are given. Also, no correction to compensate the high-pressure effect on the thermocouple was made.

Pressure Calibration

The experimental pressure values for the MAP-experiments given throughout the entire thesis refer to the *maximum nominal targeted pressure* applied during an experiment (cf. Figure 2.5 on page 32). They are denoted with ' p_{\max} ' and rely

on the pressure calibrations carried out by the Bayerisches Geoinstitut: For each press and each assembly (10, 14 or 18M) a sample-pressure-versus-hydraulic-oil-pressure curve was established in multiple high-pressure runs, using known phase transformations for example the I-II and III-V transition of Bi and I-II transition in Pb at room temperature. At elevated temperatures, the pressure can be different and is calibrated via known equilibria, such as quartz–coesite, coesite–stishovite, and α – γ transformations in Mg_2SiO_4 [53]. Rubie notes that uncertainties in the absolute pressure cannot be estimated, because no such scale has been established. Relative uncertainties in pressure calibrations were commonly stated to be $\pm 5\%$ or ± 0.5 GPa, but in reality could well be larger depending on the starting material used in the calibration experiments and the sample volume [53].

Procedure of a HP/HT-Experiment

A typical MAP-experiment is conducted as follows: The octahedral pressure cell containing the sample is built into the 8 WC-cubes outside the press. This assembly is fixed to give one large cube (indicated by the bold black lines on page 24) by gluing glassfiber-epoxy sheets on each side. This ‘big cube’ is then inserted into the MAP and compressed to the nominal targeted pressure p_{max} within the time t_{raise}^p , usually 3 h. p_{max} is then kept for the time t_{hold}^p , during which the heating can be conducted. The general p – T history of a multianvil HP/HT-experiment and the other relevant experimental parameters are explained in Figure 2.5. After the sample has been heated at T_{max} for a duration t_{hold}^T , it is quenched by switching off the heating power. The massive high pressure assembly represents an efficient heat sink and the sample usually attains a temperature ≤ 200 °C in about 10 s, corresponding to average quenching rates between -400 and -500 K/s. The depressurization has to be done very slowly in order to release the large elastic energy stored within the WC-cubes and the other mechanical parts. With about 18 h, it takes the major time of a high pressure run. A too fast pressure release may cause the WC-anvils to burst due to internal stresses—sometimes even after they have been taken out of the press. Safety goggles are therefore compulsory while handling them.

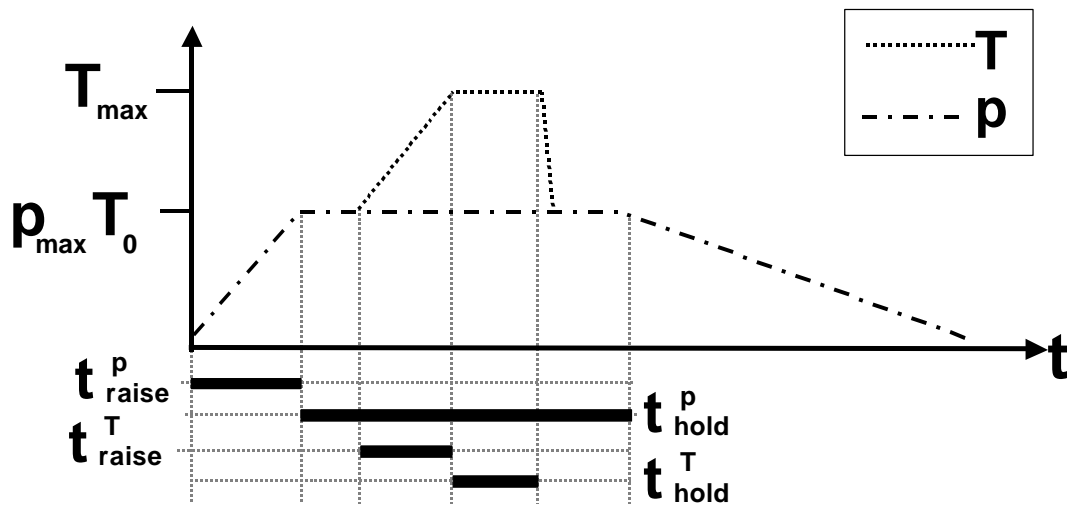


Figure 2.5: Definition of the experimental parameters in the course of a multianvil HP/HT-experiment

Methods of Sample Recovery and Preparation

As mentioned above, the octahedral pressure cell has an initial porosity of 30%. During the early stages of the compression, it is therefore subjected to considerable densification, thereby creating a self-alignment of the anvils and an equalized stress distribution throughout the sample. A comparison between the initial and the final size of a 14M octahedron is shown in Figure 2.6 on the next page. It is clear that the recovered octahedron is considerably stronger than the initial material. Recovered octahedra from the early experiments (on both γ - Si_3N_4 and sialon) were simply broken using nippers or a hammer to reveal the sample capsule. In the course of the investigations, more sophisticated methods to retain also spatial information on the sample environment and facilitate sample preparation for various characterization methods were developed. In particular, a diamond wire saw* turned out to be a powerful tool for this purpose. Whole octahedra, but also recovered sample capsules were hot-glued onto a porous ceramic substrate and then could be cut and sliced. Small portions of a single sample could be thus prepared out of the bulk (Fig. 2.7).

*well Diamantdrahtsägen GmbH, Luzenbergstr. 82, D-68305 Mannheim, Germany;
<http://www.welldiamondwiresaws.com>

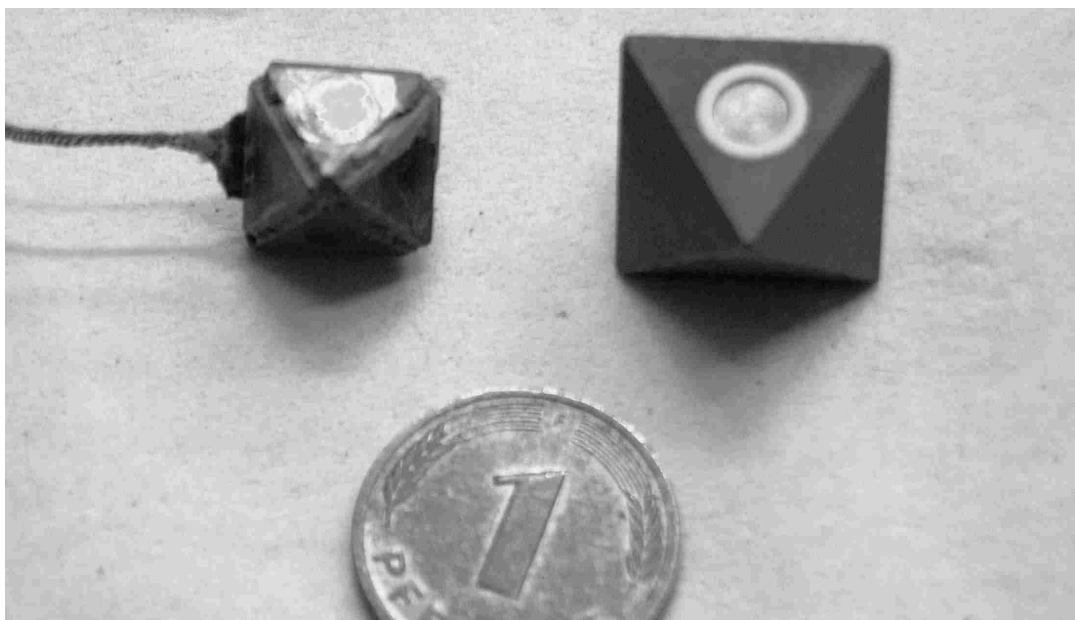


Figure 2.6: Size of a 14M octahedral pressure cell before and after an experiment

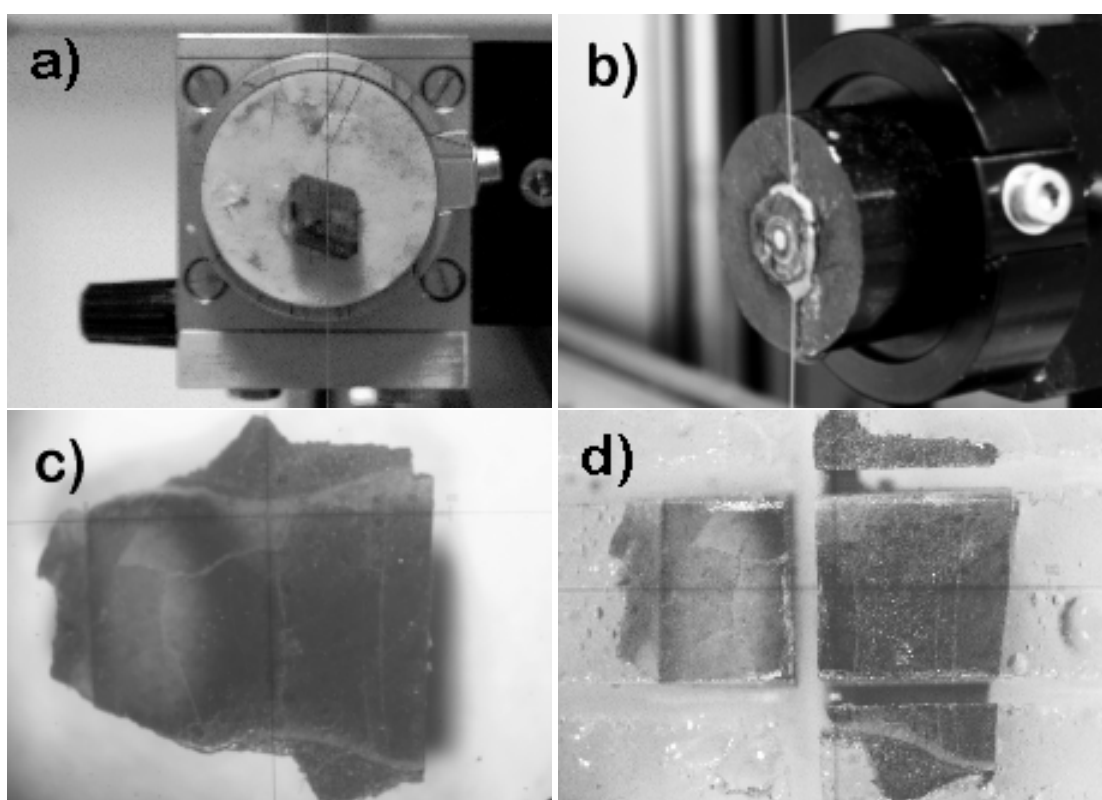


Figure 2.7: Examples for MAP-sample preparation using a diamond wire saw: a) Radial cutting of an octahedron; b) Slicing octahedron perpendicular to sample axis; c) and d) Extracting a small sample portion

2.1.3 Dynamic HP/HT-Experiments: Flyer Plate Technique

Working Principle

A planar compressive shock wave is created by the hypervelocity impact of a flat projectile (“*flyer plate*”) onto a sample material. The velocities are in the order of km/s and the flyer plate can be accelerated using explosive charges, light-gas or propellant guns, intense laser pulses or electromagnetic fields [55]. The shock pressure and duration can be adjusted via the velocity and the mass, i.e. thickness d and density ϱ of the flyer-plate (Fig. 2.8 on the facing page A). The pressure of the leading shock wave is released by a following wave with tensile stress components. This “*rarefaction wave*” can disrupt or even pulverize the sample, which therefore has to be enclosed in a ductile encapsulation in cases where the shocked sample is to be recovered for further analysis (→ “*shock recovery experiments*”). In another type of experiments that are concerned with the direct shock response of a material (e.g. Hugoniot*-measurements) and facilitate *in situ* diagnosis techniques with high time resolution, the sample cannot be encapsulated. It is atomized by the rarefaction waves and usually not recovered.

Experimental Set-up

The shock experiments were carried out at the *Fraunhofer-Institut für Kurzzeit-dynamik, Ernst-Mach-Institut* (EMI) in Efringen Kirchen, Germany,[†] using an explosively driven flyer plate setup as shown in Figure 2.8 (A) [56]. It consists basically of two units, a shock-generating and a recovery system. The shock-generating unit is comprised of an high explosive charge, shaped to create a planar detonation front that accelerates the millimeter-thick metal flyer plate. The shock generator and the attached flyer plate rests upon the recovery unit, kept at a distance of about 10 mm by means of a spacer ring. This distance is already sufficient for the acceleration of the flyer plate to its maximum velocity. The recovery system is assembled from two massive steel blocks that act as momentum traps. The cylindrical recovery container made from ARMCO iron (an almost pure iron with very low carbon content) is inserted into a bore in the upper steel block. It contains a disc-shaped sample or sample capsule. The design allows complete recovery of relatively large samples (diameters of 10–20 mm and thickness up to several millimeters).

^{*}Hugoniot (curve) = adiabate of a material under dynamic loading

[†]Many thanks to Dr. Ulrich Hornemann and his coworkers

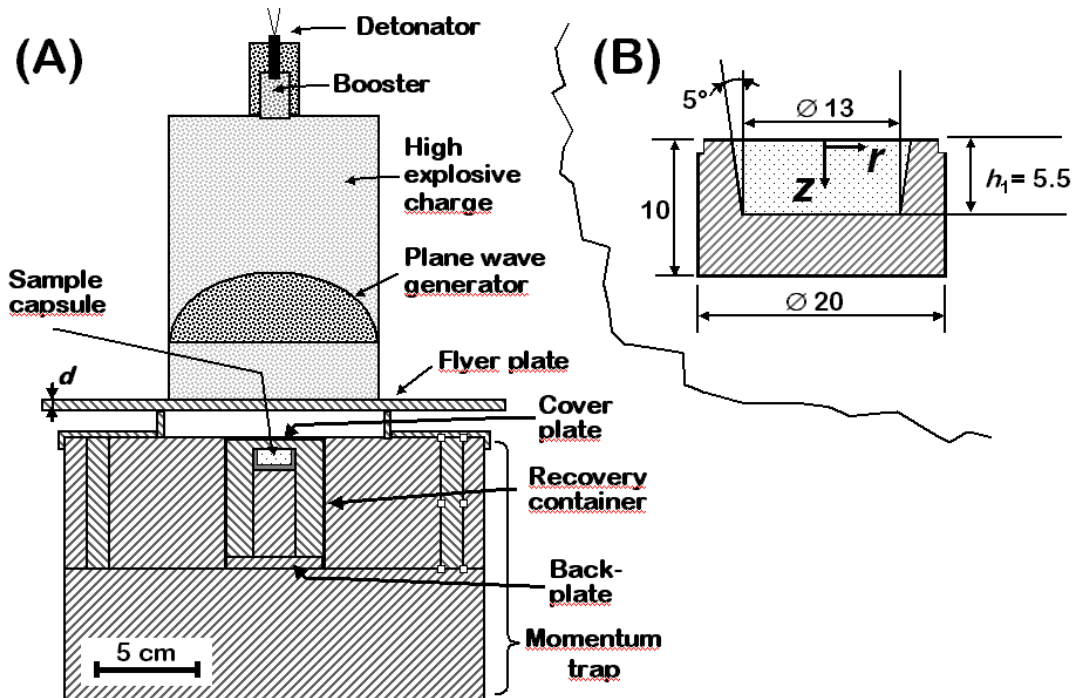


Figure 2.8: (A) Cross-sectional view through an explosively driven flyer plate apparatus used for the shock experiments on Si_3N_4 . **(B)** Sketch of the corresponding sample capsules. All measures in [mm], material: Copper.

Sample Encapsulation For the shockwave synthesis of $\gamma\text{-Si}_3\text{N}_4$, copper capsules with dimensions shown in Figure 2.8 (B) were used. Copper has a high thermal conductivity to accomplish a rapid post-shock quenching. Moreover, the moisture-sensitive starting material could be sealed air-tight for transportation by soldering a copper lid onto the filled capsules in an atmosphere of argon. The sample consists of a mixture of the starting material with a large excess of additive (in the present case 80–90 wt.% of Cu powder were used) acting as a pressure medium and to accomplish both, high temperatures and high quenching rates during and after compression, respectively: Intense heat is created due to the very large deformation rates at the contact points of the copper granules (so-called “hot spots”). After passage of the shock wave, the heat is absorbed by the cooler interior of the Cu particles, leading to an equilibrated temperature. The element copper has been proven to be a suitable additive in the shock synthesis of diamond, $c\text{-BN}$ and other nitride materials (see [55] and references therein), because it exhibits high ductility and forms neither carbides nor nitrides.

Pressure, Temperature and Shock Duration According to the relatively thick samples ($h_1 = 5.5$ mm) a single shock event without multiple reflection of the shock wave at the sample–container interfaces was to be expected [56]. The initial pressure amplitude \hat{p}_0 of the shock wave was calculated using the Hugoniot data for ARMCO iron (the cover plate) and porous copper (the additive) and assuming the influence of the remaining 10 wt.% of sample material to be small. The given estimate of \hat{p}_0 strictly is valid only directly below the cover plate shortly after the shock wave has entered the sample (i.e. . $\hat{p}_0(z = 0)$). The pressure of the first wave \hat{p}_0 decreases as it runs through the porous sample mixture. In cases where the thickness h_1 is sufficiently small, multiple reflections at the front and backside of the sample occur, leading to an equilibrated pressure \hat{p}_{eq} that depends only on impact velocity and the Hugoniots of the flyer plate and encapsulation materials (“*impedance match method*”, see [55] and references therein). In either case, the shock (\hat{T}) and postshock temperatures are mainly determined by energy dissipation due to the plastic flow of the Cu additive and the heat capacity of the mixture. They therefore rely on the initial density ϱ_0 and $\hat{p}(z)$. In the present case T was not exactly known, but there are indications for a post-shock phase transformation $\gamma\text{-Si}_3\text{N}_4 \rightarrow \beta\text{-Si}_3\text{N}_4$ which means that T and hence \hat{T} could have been well above 1200 °C (see the Sections on the thermal stability of $\gamma\text{-Si}_3\text{N}_4$ 3.8.6 on page 171 and the results of the shock synthesis experiments 3.9 on page 189). The shock duration is mainly determined by the thickness d of the flyer plate. Thin plates yield higher \hat{p} but shorter durations, that are thus varying between 1 μs at $\hat{p} = 20$ GPa and 0.1–0.2 μs at $\hat{p} = 100$ GPa.

2.2 Micromechanical Characterization

2.2.1 Conventional Hardness Testing

Hardness testing of ceramics and other hard materials is usually accomplished using sharp or “*pointed*” indenters such as the Vickers or the Knoop pyramid, in contrary to the steel and diamond balls that are common for soft and ductile materials, polymers and metals, for which the Rockwell and Brinell tests have been established. These are all standard testing techniques and details can be found e.g. in [57], or at the internet sites

<http://www.metallography.com/amp/micro.htm> and
<http://www.metallography.com/ceramics/ceramics.htm>

All hardness readings will be given in SI-units [GPa] and were derived using the formulas given below. The determination of the indentation fracture toughness and the depth-sensing hardness measurement technique which yields information on the plastic and elastic material behavior will be treated in more detail. The latter especially with respect to their limited applicability for superhard and ultrahard materials.

Vickers hardness

$$HV_P = 1854.4 \cdot \frac{P}{\langle 2a \rangle^2} = 2 \sin(\psi) \cdot \frac{gL}{\langle 2a \rangle^2} \quad (2.1)$$

HV_L	[GPa]	Vickers hardness (at load L [kg])
P	[N]	indentation load (weight force)
L	[kg]	indentation load
g	[m/s ²]	gravitational acceleration (9.80665 m/s ²)
$\langle 2a \rangle$	[μm]	average indentation diagonal
2ψ	[°] / [rad]	apex-angle of Vickers pyramid (136°)

Knoop hardness

$$HK_L = 14229 \cdot \frac{P}{b^2} \quad (2.2)$$

HK_L [GPa] Knoop hardness (at load L [kg])

P [N] indentation load (weight force)

b [μm] remanent long indentation diagonal

H/E ratio from Knoop Hardness Measurement

A simple method to estimate the elasticity of a material in terms of its hardness-to-modulus ratio (H/E) has been proposed by MARSHALL, NOMA and EVANS (MNE) [58]. It is based on the elastic recovery of the in-surface dimensions of a Knoop indentation upon load removal. MNE make the assumption that because of the large difference of the indentation diagonals a and b , the recovery of the long diagonal is almost negligible ($b \approx b^*$). The difference between the ideal a^*/b^* -ratio imposed by the rigid diamond indenter and the recovered imprint gives an estimate for the elastic recovery:

$$\frac{a}{b^*} \approx \frac{a}{b} = \frac{a^*}{b^*} - \alpha \cdot \left(\frac{H}{E} \right)_{\text{MNE}} \quad (2.3)$$

a^*, b^* [μm] short and long diagonal at load

a^*/b^* [–] $\approx 1/7.11$ (ideal Knoop geometry)

a, b [μm] remanent short and long indentation diagonal

α [–] empirical dimensionless constant ($= 0.45$)

$(H/E)_{\text{MNE}}$ [–] hardness-to-modulus ratio after MNE

Indentation Size Effect and Normalized Hardness

Especially in the case of brittle (ceramic) materials, the measured hardness is known to increase rapidly as the size of the indentation decreases below 10–20 μm (see [59] and references therein). This phenomenon, commonly denoted as indentation size effect (ISE), at the same time implies load-dependency of

the hardness towards small loads and complicates quantification and comparison between different materials. In order to account for this effect, it is common to measure the hardness over a whole range of loads. According to an energy-balance relationship first established by BERNHARDT and FRÖHLICH et al. (see [60] and references therein) the work, or energy, of indentation can be expressed as

$$Ph \propto Pd = c_1 d^2 + c_2 d^3 \quad (2.4)$$

The product Ph refers to the external work performed by the indenter (force \times displacement, both directed normal to the indented surface). It is directly linked to Pd via the indenter geometry function. Pd in turn can be directly measured from the resultant indentation size ($d = \langle 2a \rangle$ for Vickers and b for Knoop indents). Within this model, this external work is dissipated by compression of the indentation volume ($\simeq d^3$) and area-related ($\simeq d^2$) processes, such as creation of new surface area, or friction at the indenter/material interface, or the formation of microcracks. The constants c_1 and c_2 establish the proportionality and incorporate the indenter geometry. Dividing Eqn. 2.4 by d^2 yields Equation 2.5, from which a so called “*load-independent hardness*” can be obtained by linear regression of a P/d versus d plot of the hardness data:

$$P/d = c_1 + c_2 d \quad \text{with} \quad (2.5)$$

$$HV_n = 1.8544 \cdot g \cdot c_2 \quad (2.6)$$

$$HK_n = 14.229 \cdot g \cdot c_2 \quad (2.7)$$

P	[N]	indentation load (weight force)
d	[μm]	indent size, $\equiv b$ for Knoop and $\langle 2a \rangle$ for Vickers
c_1	[N/ μm]	‘load size coefficient’
c_2	[N/ μm^2]	“load-independent” parameter
HV_n	[GPa]	normalized Vickers hardness
HK_n	[GPa]	normalized Knoop hardness
g	[m/s 2]	gravitational acceleration (9.80665 m/s 2)

2 Experimental Techniques

The reciprocal of the ‘load size coefficient’ $1/c_1$ gives the deviation from the ‘ideal’ indentation size with decreasing or increasing load, and may be expressed in units of μm per g of load change.

KAJI et al. point out that the hardness values obtained by this procedure do not represent an illegitimate extrapolation of the hardness data into the high-load range, because it is determined from the slope c_2 of a trend line that is drawn between existing data points [61]. The analysis is most suitable for data obtained at low indentation loads and hence complies well with the present investigations, where only a *limited number of small specimen* was available.

Quinn and Quinn [60] found a discrete transition between microplastic deformation at small loads and gross fracture at high loads. They stress that the transition point can easily be overseen in logarithmic or otherwise normalized hardness-versus-load plots. However, the corresponding critical loads P_c at which this transition occurs were found to be quite high, ranging from 50 to more than 100 N for advanced ceramics Al_2O_3 , Si_3N_4 and γ -alon* [60]. The loads applied in the present studies were all below P_c . The extensive cracking that occurs above P_c is to be distinguished from the moderate-sized cracks that regularly accompany hardness impressions and were used for toughness determination (see Sect. 2.2.2 below).

Other recent investigations also suggest that the linear dependency between P/d and d is only an approximation and the ‘constants’ c_1 and c_2 could themselves contain higher order dependencies of d [62]. Hence, rather than being really “load independent”, the hardness values HK_n or HV_n determined in this work shall be understood in terms of a ‘normalized hardness’ that serves the purpose of comparing the microdeformation properties of different materials using a single number. This should be valid as long as the corresponding hardness data has been obtained within the same load range and will be discussed in the respective sections.

*see Section 4.1.1 on page 202

2.2.2 Indentation Fracture Toughness

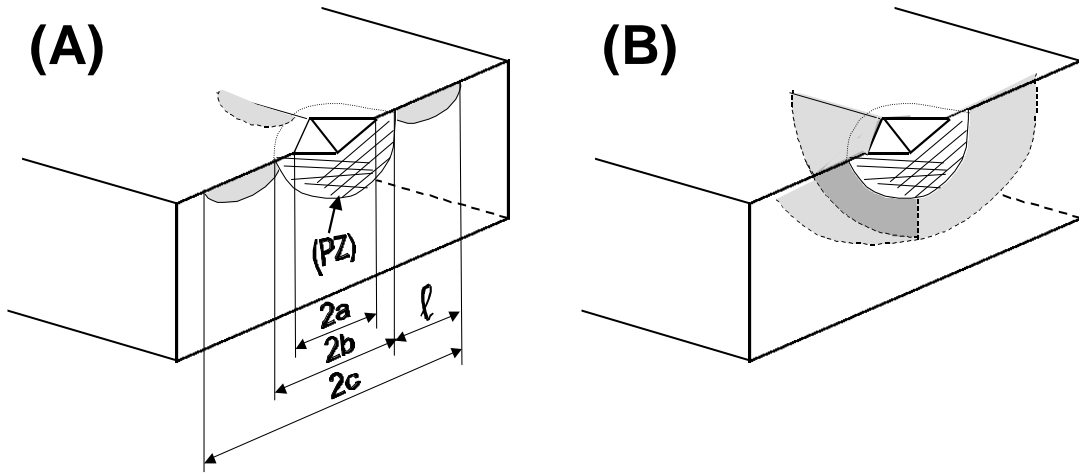


Figure 2.9: Two different crack systems associated with Vickers indentations in brittle materials. The features in (A) are denoted as follows: (PZ) plastic Zone; $2a$ indentation diagonal; $2b$ plastic zone width; c crack radius; l crack length.

Indentation Cracking In brittle elastic solids such as ceramics, other hard materials, and glasses, the stress field introduced by an impinging indenter cannot be released via dislocation-mediated/plastic deformation alone. If the applied load surpasses the elastic limit of the material, various crack systems can form in the vicinity of the indent. The specific geometry of these cracks depends on the indenter type and the indented material. The sequence of crack formation and crack extension is a function of the applied load. A comprehensive review on this issue is given by COOK and PHARR [47]. Cone-shaped cracks with a circular surface trace usually develop under the action of blunt indenters like Rockwell spheres or a flat punch. For stresses below the elastic-plastic limit of the material these cracks can be quantitatively described with good agreement to the Hertzian contact model [63, 64, 47]. Most devices for the measurement of hard materials are equipped with “sharp” indenters like the Vickers pyramid or the Knoop geometry—these were also used in the present case. Depending on the material and load, sharp indenters produce different cracking patterns, the two most prominent of which are shown in Figure 2.9. Above a critical load, four (independent) cracks nucleate directly at or close to the corners of the indenta-

tion and extend radially into the material. If these cracks remain shallow and do not merge in the depth of the sample (Fig. 2.9 A), they are named radial or “*Palmqvist cracks*” after their discoverer PALMQVIST [65]. So called “*half-penny*” cracks can result from the merger of radials at higher loads and/or other mechanisms [47]. A significant feature of half-pennies is the existence of a subsurface crack *below* the plastic zone (PZ) of the impression (2.9 B).

Toughness Determination A large variety of approaches has been made to estimate fracture resistance from the cracks associated with indentations [47], but it was also Palmqvist who established an *empirical* relation between the crack length ℓ (see Fig. 2.9 A) and the indentation load P . The proportionality constant was a measure for the “**toughness**” of the material [66, 67]. This was adopted by many workers leading to an appreciable number of *analytical* solutions for both, radial and half-penny crack geometries. They differ mainly in the underlying model to calculate the effective stress field that is acting on the cracks and represent always a simplification with respect to the true stress conditions within the material. **The proportionality constant between applied load and the stress field is often derived empirically, by fitting experimental data of one or more different materials.** One of the most widely cited model is that after **Lawn, Evans and Marshall (LEM)** [68]. The LEM model is based on the assumption that the volume that is displaced by the indenter is accommodated by the plastic zone (PZ) which behaves like an expanding spherical cavity in a linear elastic medium. The residual stresses in the material result from the misfit between the PZ and the surrounding matrix. The LEM model predicts a characteristic relation between the applied load P and the crack radius c that has the form

$$c = \chi P^{2/3} \quad (2.8)$$

The proportionality constant χ depends on the properties of the indented material (hardness, elastic modulus, and fracture toughness). Although Eqn. (2.8) was derived for the median crack geometry, this relationship was also found to be obeyed in the materials subject to this thesis, where a Palmqvist geometry is assumed. The Palmqvist crack system has been shown dominant under regular

hardness testing conditions for a large variety of materials, ranging from SiC to NaCl [47]. The validity of this assumption is proved by applying the $\frac{c}{a} < 3.5$ criterion provided by Niihara et al. [69].

Indentation Fracture Toughness after Anstis et al.

The method provided by Anstis et al. [70] is based on the LEM model. In its present formulation the procedure is suited to determine a value for the so-called “indentation fracture toughness” ($K_{\text{IC-IF}}$) corresponding to large cracks. This means that the result should be comparable to a K_{IC} measured from macroscopic samples, e.g. via 4-point bending test on a single edge notched beam (SENB).

$$K_{\text{IC-IF}} = \xi \left(\frac{E}{H} \right)^{\frac{1}{2}} \cdot \chi^{-3/2} \quad (2.9)$$

where χ is derived by fitting the measured indentation data to

$$c = \chi(P - P_0)^{2/3} \quad (2.10)$$

$K_{\text{IC-IF}}$	[MPa m ^{1/2}]	indentation fracture toughness
P	[N]	indentation load (weight force)
P_0	[N]	threshold load (for crack initiation)
c	[μm]	crack radius (see Fig. 2.9)
χ	[$\text{mN}^{-2/3}$]	fit parameter
ξ	[-]	geometry factor (= 0.016, Ref. [70])
E/H	[-]	modulus-to-hardness ratio

For Equation (2.9), the modulus-to-hardness ratio E/H is required. It can be obtained from the measurement of Knoop hardness indents by applying the method of Marshall, Noma and Evans, previously described on page 38 or approximated by the Young’s modulus and the normalized hardness (cf. Equations 2.11 and 2.12 on the following page, respectively).

$$E/H \approx 1.4229 \cdot \frac{1.8544}{2} \cdot \left(\frac{H}{E} \right)_{MNE}^{-1} \quad (2.11)$$

$$E/H \approx \frac{1.8544}{2} \cdot \frac{E_Y}{HV_n} \quad (2.12)$$

$(H/E)_{MNE}$ [-] hardness-to-modulus ratio after MNE

E_Y [GPa] Young's modulus

HV_n [GPa] normalized Vickers hardness

The factors 1.8544 and 1.4229 are the geometry constants for the Vickers and Knoop indenter, respectively. The former is to be applied in both equations due to the fact that Anstis et al. used the *projected* area of the hardness indent ($A_{proj} = \langle 2a \rangle^2$) to derive the constitutive equations for the residual stress field acting on the cracks. By introduction of the factor 1.4229 in Equation (2.11), a better agreement between the two methods was obtained (see Section 2.2.5). It is meant to account for the fact that $(H/E)_{MNE}$ is determined from a *Knoop indent*, while the toughness measurements are based on *Vickers* indentations.

Indentation Fracture Toughness after Shetty

The formulation provided by Shetty [71], in its final form, does not include the elastic modulus E_Y . This is advantageous for unknown and not well characterized materials, such as the newly synthesized spinels. The method is defined for the Palmqvist crack geometry and was originally developed for hard metal (WC-Co alloys). In a comparative study of different fracture toughness methods applied to Si_3N_4 ceramics, DUSZA found that especially the Shetty formula shows good correlation between $K_{\text{IC-IF}}$ and the values obtained by the standard single-edge notch beam test (SENB) [72]. In contrary to the aforementioned 'Anstis method', where a *single* $K_{\text{IC-IF}}$ -value is obtained *from the whole data set*, the Shetty formula will be applied to *every single indentation*. It may therefore be suitable to probe the dependence of $K_{\text{IC-IF}}$ on the crack length. A dependence of toughness on crack length is in general called crack resistance curve or "R-curve" of the material. R-curve behavior is associated with microstructural toughening mechanisms like crack deflection and crack bridging.

$$K_{\text{IC-IF}} = \beta \cdot \sqrt{\frac{HV \cdot P}{4 \cdot \langle \ell \rangle}} \quad (2.13)$$

$K_{\text{IC-IF}}$	[MPa m ^{1/2}]	indentation fracture toughness
β	[-]	dimensionless constant = 0.0856 (Shetty: 0.0889 [71])
HV	[Pa]	Vickers hardness according to Eqn. (2.1)
P	[N]	indentation load (weight force)
$\langle \ell \rangle$	[μm]	averaged crack length ($\approx c - a$; Fig. 2.9)

The dimensionless geometry factor β can be explicitly written as

$$\beta = \frac{\left(\frac{1}{\pi} \tan \psi\right)^{1/2}}{3(1 - \nu^2)(\sqrt{2}\pi \tan \psi)^{1/3}} \quad (2.14)$$

ν	[-]	Poisson's ratio (assumption: $\nu = 0.22$)
2ψ	[°] / [rad]	apex-angle of Vickers pyramid (136°)

Here, the term $(\frac{1}{\pi} \tan \psi)^{1/2}$ stems from the insertion of the Vickers hardness formula (Equation (2.1) on page 37). This was omitted within the formula originally published, but if it is not included into the calculation, β acquires the value 0.15752 and not the 0.0889 given by Shetty [71]. The remaining discrepancy between the result for β using Eqn. 2.14 and this latter value (a factor of 1.039) remains somehow mysterious. It is however negligible in comparison to the error introduced by the determination of the crack length $\langle \ell \rangle$. This error has contributions as follows:

- (a) no exact location for surface crack tips (even if HR-SEM is used)
- (b) the subsurface extension of the Palmqvist cracks
- (c) deviations from the ideal crack geometry, e.g. curved or missing surface traces of the radial cracks
- (d) omitting the plastic zone width $2b$ ($\Leftrightarrow \ell \approx c - a$, see Fig. 2.9)

The same is valid for the tacit assumption that the Poisson's ratio of the investigated materials is equal to that of hard metal (WC-Co alloy, $\nu = 0.22$) used in the original work: None of the subsequent publications, where the Shetty formula is applied to the indentation toughness of ceramics seems to take this into consideration. However, calculating β with the most extreme values for ν , i.e. $\nu = 0.07$ for diamond and $\nu = 0.33$ for a ductile metal, the resulting value differs by 4.6% and 6.8% from the published value of β and hence will also be of small influence compared to the other uncertainties listed above.

2.2.3 Hardness Testing Devices

- **Tester A:** LECO M-400 G2 hardness tester; load range: 1 g ... 0.1, 0.2, 0.5, 1.0, 2.0 kg; Vickers diamond indenter. The tester is equipped with a CCD-camera and a monitor for semiautomatic measurement of the indentation diagonals. Lenses with magnifications of $10\times$ and $55\times$ are available. The maximum magnification for the image at the monitor is $1660\times$, at which most of the indentations were measured.
- **Tester B:** Model 38160, Knoop diamond indenter, Karl Frank GmbH, Weinheim Birkenau, Germany. Load range: 0.2, 0.3, 0.5, 1 ... 10 kg.
- **Tester C:** Automated load-depth sensing indentometer, FISCHERSCOPE 100, HELMUT FISCHER GmbH + Co KG, Sindelfingen-Maichingen, Germany, <http://www.helmut-fischer.de>.

Load range: 100–1000 mN. Fischerscope 100 uses linear extrapolation of the unloading curve between 100 and 80 % of the maximum applied load P_{max} to determine the corrected indentation depth h_{corr} as suggested by Doerner and Nix [73] (see Sect. 2.2.6 on page 57). In every case, before and after the measurement the calibration of the Fischerscope was checked (measurement of silicon standard Si(111), hardness always 10 ± 0.2 GPa). The hardness was also determined for the same indentations, measuring the indentation diagonals at the sample surface by means of a calibrated SEM. A photolithographic mask with an exact spacing of metallic lines was used as calibration standard.

All investigations were performed by Dr. Pavla Karvankova at the Institute for Chemistry of Inorganic Materials, Technical University of Munich. My grateful acknowledgements to her and to Prof. Dr. Vepřek for a very fruitful e-mail correspondence adding up to a very valuable contribution to this work.

2.2.4 Testing Procedure

All hardness measurements were made at ambient atmosphere and the dwelling time at peak load was 10 s for **Testers A, B and D**. Hardness impressions and — where possible — crack lengths, from **Testers A** and **B** were first measured using the optical system of **Tester A**. This was often followed by measurements with the Philips XL30 (HR)-SEM (see Section 2.4 on page 63), using the built-in measurement function. The hardness reading obtained by electron microscopy depends on the distance between sample and the objective lens of the electron gun. It was calibrated by focussing on the unindented sample surface in the vicinity of each impression. Specimen tilt to enhance the contrast of the hardness indents against the sample surface was compensated automatically. There was however no external length standard available, as in the case of **Tester C**.

2.2.5 Example: Hardness of Toughness of Standard Reference Material SRM 2100

In order to increase the comparability of the (conventional) hardness and fracture toughness data, determined within this thesis, a standard **reference material** (SRM) of the U.S. NATIONAL INSTITUTE OF STANDARDS AND TECHNOLOGY (NIST) was tested, using the aforementioned techniques and equipment.* SRM 2100 is a β - Si_3N_4 ceramic material with a certified fracture toughness of $K_{\text{IC}} = 4.57 \pm 0.23$.† Its Young's modulus was measured 312 GPa using the impulse excitation method [74].

The material was tested with a Vickers indenter at loads up to 10 kg using **Tester A** and **Tester B**. Indentation diagonals $\langle 2a \rangle$ and crack lengths $\langle 2c \rangle$ were first measured optically at $10\times$ and $55\times$ magnification, respectively, using the video system of **Tester A**. This was followed by carbon coating and a third measurement with the HR-SEM. Vickers hardness, normalized Vickers hardness and the indentation fracture toughness according to the method of Anstis and Shetty were determined.

Normalized Hardness Figure 2.10 shows the measured hardness data plotted according to the previously described procedure for the normalized hardness, HV_n . Regression analysis was performed for each single set of data obtained from the three different measurement methods. All regression lines except one are omitted for clarity. The results of the regression analyzes are shown in Table 2.2.

The HV_n -values obtained from optical measurements are all between 14.5 and 15 GPa indicating sufficient agreement between the indentation sizes of **Tester A** and **Tester B** and between the indentation sizes as measured at $10\times$ and $55\times$ magnification. The values obtained from SEM measurement are significantly higher, which may be attributed to the fact that the SEM was not calibrated. Hence, only the average of the optical measurements $HV_n = 14.8$ GPa will be used

*I gratefully acknowledge A. Kounga and the group for *Inorganic Non-Metallic Materials* of Prof. J. Rödel for providing me with a SRM 2100 specimen

†<http://patapsco.nist.gov/srmcatalog/certificates/2100.pdf>

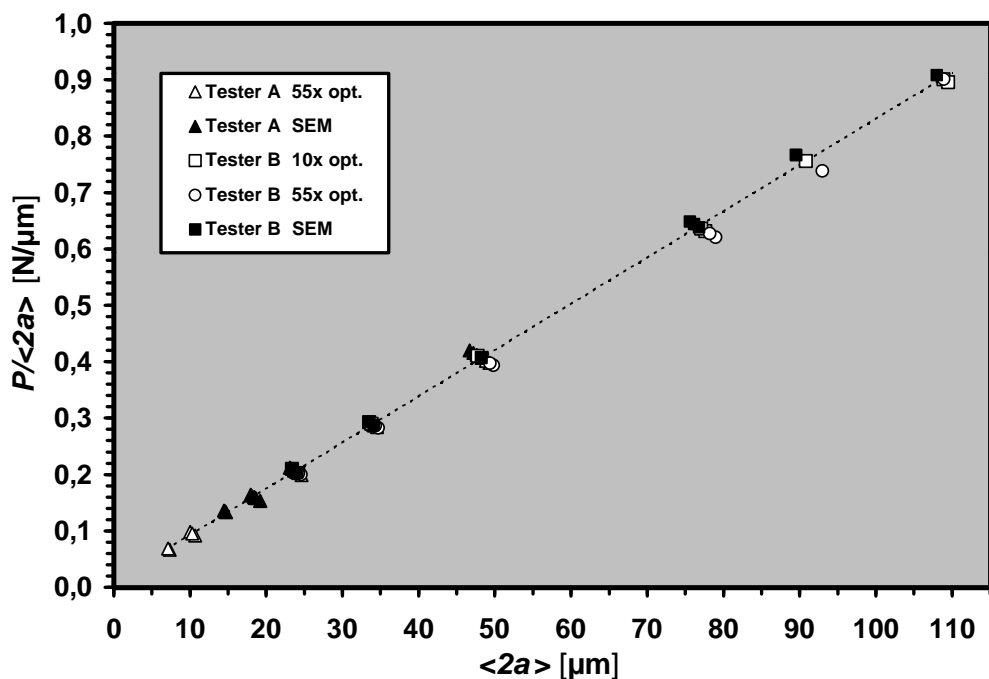


Figure 2.10: Plot for normalized hardness of NIST standard reference material SRM 2100, with the data from different measurements indicated. One regression line is shown as an example.

SRM 2100	Method	Tester A	Tester B	Average
HV_n [GPa]	opt. 10×	—	14.95	14.8
	opt. 55×	14.58	14.76	
	SEM	15.87	15.50	
ISE [$\mu\text{m/g}$] $(= 1/c_1)$	opt. 10×	—	0.57	1.0*
	opt. 55×	0.74	6.25	
	SEM	2.94	1.89	

* regression of entire data

Table 2.2: Normalized (“load independent”) Vickers hardness values and ‘indentation size coefficients’, as obtained by linear regression of hardness-vs.-load data.

further, e.g. for the determination of K_{IC-IF} after Anstis et al. The indentation size coefficient of the $55\times$ measurement of **Tester B** is unusually high, while the remaining values are in the same order of magnitude, for the optical and the SEM measurement, respectively. Regression of the whole data gives an average value of $1.0 \mu\text{m/g}$.

Knoop Hardness and H/E Ratios For Knoop hardness testing, only four indentations at 10 and 12 kg load were made, yielding HK values of $12.1 \pm 0.2 \text{ GPa}$ and $12.5 \pm 0.2 \text{ GPa}$ for the optical ($55\times$) and SEM measurement respectively. A $(H/E)_{MNE}$ ratio of 0.07 ± 0.004 was obtained using Equation (2.3). This value is based on the optical measurement. The corresponding values from the SEM measurement were smaller, varying between 0.044 and 0.066. This is because the image contrast of the SEM does not allow to resolve the fine edges of the long diagonal so that all b were measured shorter than those obtained from the optical system. The H/E obtained from the Young's modulus and the optical HV_n -value is 0.047. For the indentation fracture toughness determination, both values have to be scaled according to Equation (2.11) and (2.12), respectively:

H/E	Value	Scaling factor	Scaled	'Type'
$(H/E)_{MNE}$	0.070	$2/(1.8544 \cdot 1.4229)$	0.053	(1)
HV_n/E_Y	0.047	$2/1.8544$	0.050	(2)

Table 2.3: Hardness-to-modulus ratios of SRM 2100

Indentation Fracture Toughness In order to check if SRM 2100 obeys the $c - P$ dependency predicted by the LEM-Model (recall Sect. 2.2.2) the measured crack lengths and indentation diagonals of the hardness imprints were plotted against the load, as shown in Figure 2.11. As indicated by the hatched line in Figure 2.11, the $\langle c \rangle$ values could indeed be fitted to equation 2.10, in spite of the fact that all c/a ratios were in the range of 1.2–2.4, which is well below the $c/a < 3.5$ limit for half penny cracks (cf. Sect. 2.2.2 on page 42). The values obtained from the **Tester B** $10\times$ measurements show some irregularities and were omitted in the following analyzes. The results for the fracture toughness determination after Anstis et al. are listed in Table 2.4.

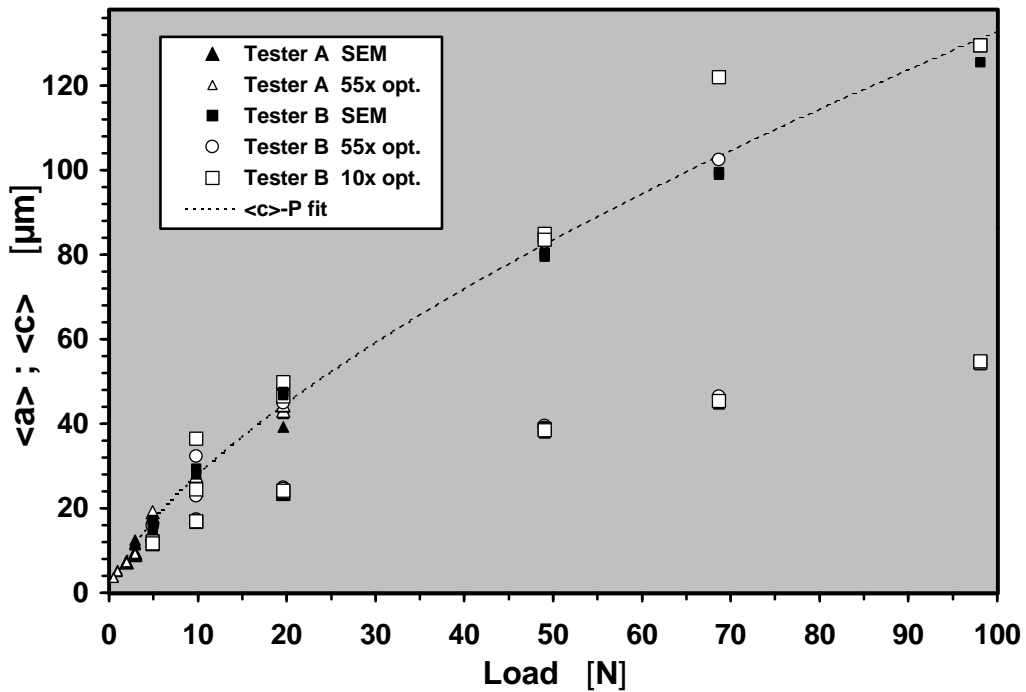


Figure 2.11: Plot of crack length and indentation diagonal versus load of NIST standard reference material SRM 2100.

Data	P_0	χ	$K_{IC-IF}^{(1)}$	$K_{IC-IF}^{(2)}$
Source	[N]	[$\mu\text{m N}^{-2/3}$]	[MPa $\text{m}^{1/2}$]	[MPa $\text{m}^{1/2}$]
optical	—	6.13	4.57	4.67
	0.36	6.18	4.52	4.61
SEM	—	5.93	4.81	4.90
	0.23	5.96	4.77	4.87
all*	—	6.02	4.70	4.80
	0.27	6.05	4.67	4.76

(1),(2) see Table 2.3 on the preceding page; * without Tester B 10x data

Table 2.4: Indentation fracture toughness values of SRM 2100 according to the 'Anstis procedure'

As indicated by bold script in Table 2.4, fitting of optical indentation data yields the best agreement to the certified reference value of $K_{IC} = 4.57 \pm 0.23 \text{ MPa m}^{1/2}$. The value is exactly met for the fit result where the threshold load for crack initiation P_0 was set to zero and the scaled H/E -ratio from the Knoop indentation, $(H/E)_{MNE}$, was used. This single result does however not allow to deduce a general superiority of this particular choice of parameters. Especially the geometry constant of the Knoop indenter as scaling factor for H/E would have to be verified by testing a larger number of different materials.

For the SEM-measured data, K_{IC-IF} -values are higher than the reference, which resembles the same trend as in the hardness measurements. Obviously, $\langle a \rangle$ and $\langle c \rangle$ have both been measured somewhat too short.

Up to this stage of the investigation, the results were obtained from the entire set of indentations. Applying loads up to 10 kg and higher renders no problem for the macroscopic SRM 2100 bending bars, but for the HP/HT-derived samples — the true subject of this study — would be almost impossible: Most of these samples had volumes smaller than 1 mm³ and loads exceeding 5 kg or even 2 kg would cause severe fracture and yield unreadable indentations and crack systems. In order to check, if the result obtained from the ‘Anstis method’ will still provide an estimate for the *macroscopic* fracture toughness if only data from small indentation loads (and consequently shorter cracks) is available, the fitting procedure was repeated under successive reduction of data, first omitting the 10 kg (= 98 N) impressions, then those obtained at 7 kg (= 68.7 N) and so on. The resulting χ values were converted into the corresponding indentation fracture toughness and plotted against the maximum crack length $\langle \ell \rangle$ up to which each fit was performed (Figure 2.12 on the facing page). The graph shows that the determined indentation fracture toughness stays close to 4.5 MPa m^{1/2}, even if only crack systems with $\langle \ell \rangle \leq 40 \mu\text{m}$, corresponding to 35% of $\langle \ell \rangle_{max}$ (the largest crack length measured in this study) were included. Below this value, the number of data points becomes too small to obtain a meaningful fit result, which is most evident by the fact that the threshold load for crack initiation P_0 turns negative. This analysis has been performed on the optical data.

In Figure 2.13 on page 54 the individual fracture toughness values of each in-

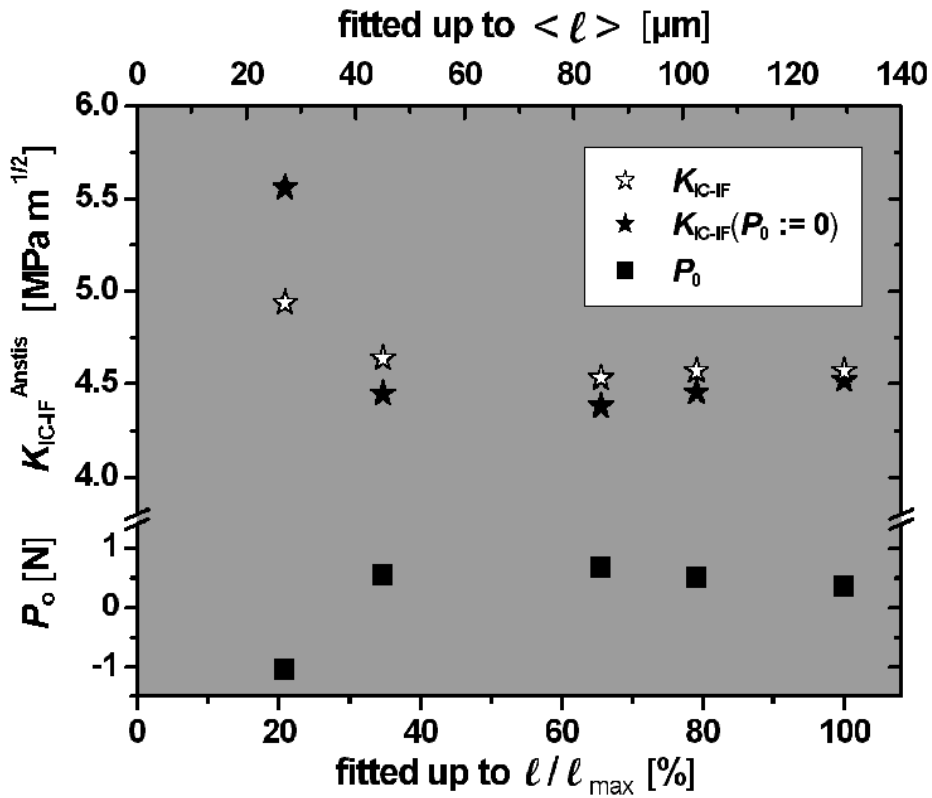


Figure 2.12: Indentation fracture toughness as obtained by fitting a subsequently smaller set of the (optically measured) data, plotted against the maximum crack length that was included in the fit.

indentation calculated via the Shetty formula are plotted against the average crack length $\langle \ell \rangle$. The hatched lines indicate the certified reference value and the upper and lower deviation, respectively. It can be seen that also this method produces good agreement to the reference value, if applied to ‘long’ cracks. The indentation fracture toughness decreases with decreasing crack length which is typical for materials that exhibit crack-tip shielding due to microstructural toughening (R-curve behavior). Again the values obtained from SEM-measurement are somewhat higher. From the development of K_{IC-IF} with $\langle \ell \rangle$ it can be deduced that the crack tip toughness K_0 of SRM 2100 must be below $3 \text{ MPa m}^{1/2}$ and that the bridging zone is almost fully developed at a crack length of about $80 \mu\text{m}$. This latter deduction is however based on the knowledge of the reference K_{IC} value which represents the toughness plateau. More indentations at higher loads

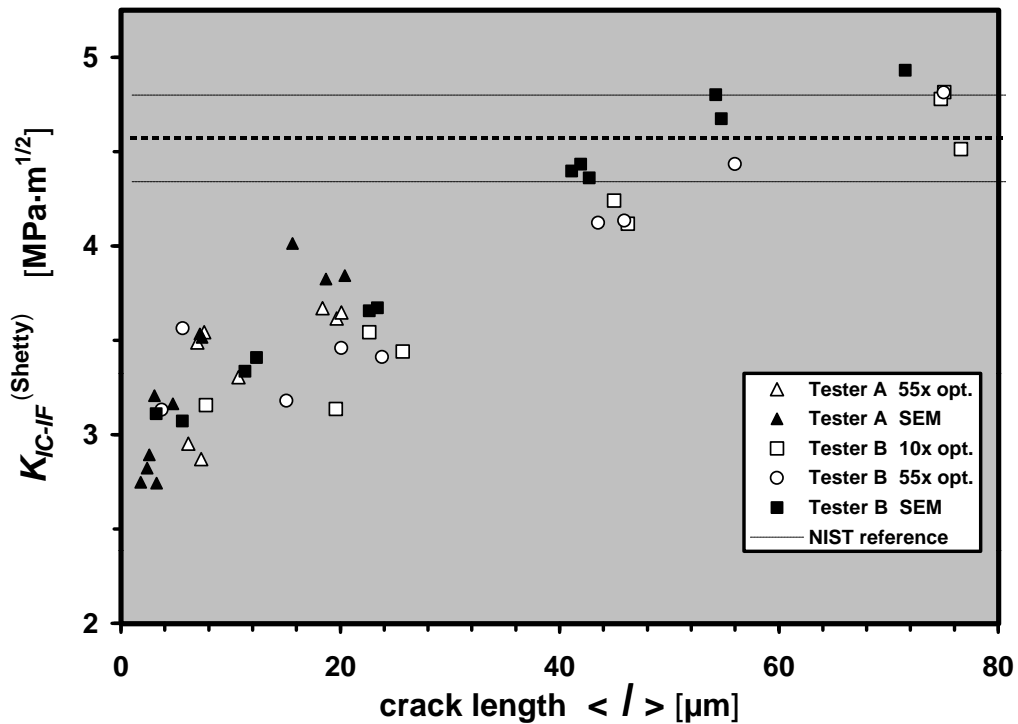


Figure 2.13: Indentation fracture toughness (R-curve?) of SRM 2100 calculated for each indentation according to the Shetty formula (Eqn. (2.13) on page 45).

would have to be made in order to prove if the toughness indeed remains constant for $\langle l \rangle \geq 80 \mu\text{m}$. Because of aforementioned reasons, this is not feasible for the HP/HT-derived materials which are the main subject of this thesis. Further investigation was hence also not attempted in the case of SRM 2100.

In conclusion, the two employed methods have been shown to yield useful and partially complementary results from indentation fracture data. The single K_{IC-IF} value derived by the Anstis method agrees well with macroscopically measured toughness values, even for data measured from low load indentations. The formula provided by Shetty et al. is useful to probe the R-curve behavior of the material under investigation. The results obtained by optical measurement showed the best accuracy with respect to the reference value, while the SEM-derived measures somewhat overestimated the properties of the tested material.

2.2.6 Load-Depth Sensing Indentation Technique and Nanoindentation

In the aforementioned traditional hardness tests, hardness readings are obtained from the dimension of the *remanent impression after the load has been removed*. The primary information that can be gained by these methods corresponds to the *plastic* behavior of the material. In contrary, in depth-sensing hardness testing — also called “*instrumented hardness testing*”— the applied force and the indenter displacement are recorded over a full loading–unloading cycle. This facilitates a full determination of the *elastic*-plastic properties and the corresponding work of plastic deformation that is absorbed during this cycle. Friction and time dependent phenomena such as creep may also be studied and in many cases repeated loading-unloading cycles are performed. The instrumented hardness testing is subject to standards such as DIN 50359 [75] and ISO/DIS 14577 [76]. With the development of the atomic probing techniques like STM* and AFM† in the last two decades, the so called “*nanoindentation*” has gained considerable importance. This technique represents a miniaturization of the depth-sensing hardness measurement and is capable to apply very small loads of a few mN with lateral and vertical resolution in the nanometer scale, thus enabling to study the mechanical behavior of single grains or even molecules. Some hardness studies on γ -Si₃N₄ reported in literature were carried out with this technique and are mentioned in Section 3.8.1 on page 134. The basic principles of nanoindentation are very similar to those of the regular depth-sensing hardness testing which uses loads of (multiple) hundred mN and will be considered in more detail below. The corresponding results in this thesis were obtained with **Testers C** and **D** (recall Sect. 2.2.3 on page 46).

In Figure 2.14 a schematic load-versus-displacement plot (A) and a sketch of the indenter/surface contact at various stages of the indentation cycle (B) are shown. Loading and unloading curves in (A) are indicated by arrows. The area enclosed by the two curves corresponds to the work of plastic deformation W_{pl} . If creep is present in the material, h_{max} will have increased by δh_{creep} when the unloading cycle starts. Creep is usually negligible for hard covalent materials

*scanning tunneling microscopy

†atomic force microscopy

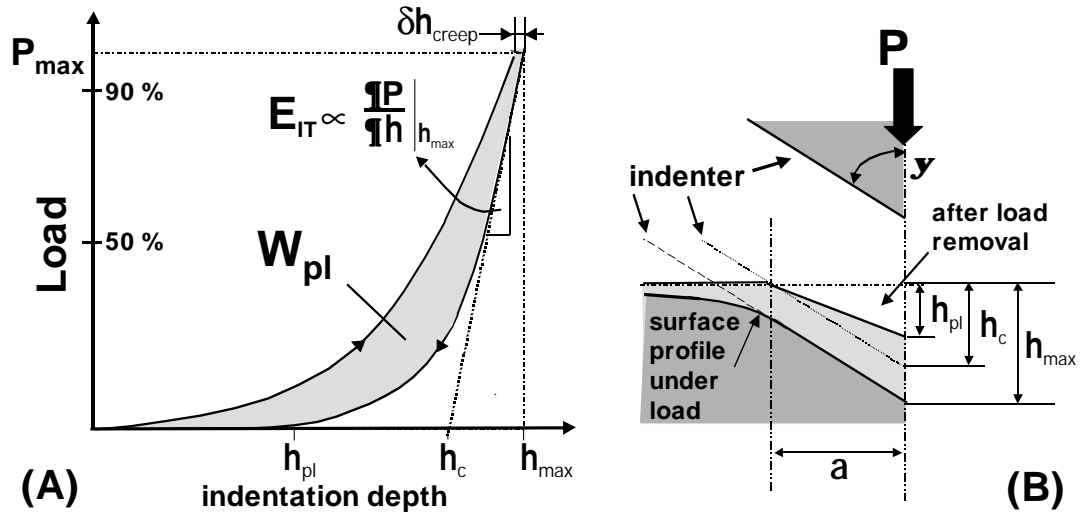


Figure 2.14: (A) Load-versus-displacement diagram of a depth-sensing hardness measurement; (B) Schematic representation of the indentation process.

as those investigated in the present case. The “Universal Hardness” (HU) — also called Martens hardness (HM)[77] — corresponds to the deformation of the material under full load P_{max} , i.e. it is including elastic and plastic contributions. HU converges to a final value of 22–24 GPa, if both indenter and the tested surface consist of diamond or a comparable ultrahard material [78]. The plastic hardness HU_{pl} is defined by the remaining size of the impression after the load has been removed and the elastic recovery of the material has pushed the indenter back to position h_{pl} . HU_{pl} is therefore comparable, *however not necessarily identical** to the results obtained by conventional hardness tests. For the *ideal** Vickers geometry, HU and HU_{pl} can be calculated according to Equations (2.15) and (2.16).

Universal Hardness

$$HU, HU_{pl} = \frac{P_{max}}{A_c(h_i)} \approx \frac{P_{max}}{26430 \cdot h_i^2} \quad (\text{Vickers geometry}) \quad (2.15)$$

$$A_c(h_i) = \frac{4 \sin \psi}{\cos^2 \psi} \cdot h_i^2 \quad \text{where } h_i = h_{max}, h_{pl} \quad (2.16)$$

*see discussion below

HU	[GPa]	universal hardness
HU_{pl}	[GPa]	plastic hardness
P_{max}	[N]	maximum applied load (see Fig. 2.14 A)
$A_c(h_i)$	[μm^2]	area function for sample/indenter contact area
h_{max}	[μm]	indenter displacement at P_{max}
h_{pl}	[μm]	depth of remanent indentation
2ψ	[$^\circ$] / [rad]	apex-angle of Vickers pyramid (136°)

Reduced Modulus and Indentation Modulus While the loading curve shown in Fig. 2.14 resembles plastic *and* elastic response of the indented material, the recovery of the material upon unloading can be assumed as almost purely elastic.* From the slope of the first part of the unloading curve a so called “*reduced modulus*” E_r can be derived.

$$E_r = \sqrt{\frac{\pi}{4} \cdot \frac{1}{A_c} \cdot \frac{\partial P}{\partial h}} \quad (2.17)$$

The concept of the reduced modulus was adopted from the analytical solutions of the Hertzian contact problem [63, 64], where the axial distance between *the centers* of two approaching elastic spheres (“*distance of mutual approach*”) is derived from the composite compliance C the reciprocal of which gives E_r :

$$C = \frac{1}{E_r} = \frac{1 - \nu_1^2}{E_1} + \frac{1 - \nu_2^2}{E_2} \quad (2.18)$$

Here, either of the quantities E_1 , ν_1 and E_2 , ν_2 may refer to the (Young) elastic modulus and Poisson’s ratio of the smaller sphere (the ‘indenter’) and the larger sphere (the tested material), respectively. This means that the indenter is treated as elastic and *non rigid*.† Insertion of (2.17) in (2.18) and implementing the parameters of the force-displacement curve and the Vickers indenter geometry

*Especially for plastic materials like metals, OLIVER and PHARR [79] found that the shape of the unloading curve is not the same for the first few repetitions of the loading-unloading cycle *at the same indentation*. This was attributed to work hardening and densification effects and the authors recommend to use the data for the determination of the elastic moduli only after the unloading behavior has become constant after several repetitions.

†Accounting for the elastic deformation of the diamond indenter in load-depth sensing hardness studies via this equation was recently offend as an “*arbitrary amendment*” by CHAUDHRI [80]. He stressed that a generalized analytical solution so far has only been found for *ideally*

gives an expression for the so-called “*indentation modulus*” E_{IT} :

$$E_{IT} = E_1 = (1 - \nu^2) \cdot \left[\frac{4 \tan \psi \cdot h_c (h_{max} - h_c)}{P_{max} \sqrt{\pi}} - \frac{1 - \nu_i^2}{E_i} \right]^{-1} \quad (2.19)$$

E_{IT}	[GPa]	indentation elastic modulus
E_i	[GPa]	elastic modulus of indenter (diamond: 1141 GPa)
ν	[-]	Poisson’s ratio of sample material
ν_i	[-]	Poisson’s ratio of indenter (diamond: 0.07)
2ψ	[°] / [rad]	apex-angle of Vickers pyramid (136°)
h_c, h_{max}	[μm]	see Fig. 2.14
P_{max}	[N]	maximum applied indentation load

According to DOERNER and NIX [73] the corresponding parameter h_c is obtained by *linear* extrapolation to $P = 0$ (hatched line) while OLIVER and PHARR [79] established a *power law fit* $P(h) = A \cdot (h - h_p)^m$ to describe the unloading curve. E_r is then obtained by differentiation of the fitted function. This has become the standard procedure to derive elastic constants from indentation data and it may also be used to determine HU and HU_{pl} . However, it has been shown to yield less trustable results for both hardness and modulus, if the tested material is very hard ($HU_{pl} \sim 35$ GPa)[†].

If the indented material is elastically isotropic, E_{IT} is commonly assumed to be identical to the Young’s modulus E_Y . E_{IT} can be calculated if the Poisson ratio of the material ν is known. It may be derived from another elastic constant

stiff axisymmetric indenters [81]. Moreover, these solutions were derived for the displacement of the *indenter tip* into the indented material, whereas the Hertzian solution describes the “*distance of mutual approach*”. According to Chaudhri, this standard method of data analysis should only be used for sufficiently soft materials, where the indenter could be indeed regarded as stiff and $(1 - \nu_i^2)/E_i$ is set to zero.

[†]see e.g. [82, 78]

that has been determined independently by using the well known relations of elastic theory, e.g.:

$$E_Y = \frac{9BG}{3B + G} \quad (2.20)$$

$$\nu = \left(\frac{1}{2}\right) \left(\frac{3B - 2G}{3B + G}\right) \quad (2.21)$$

E_Y [GPa] (Young's) elastic modulus

G [GPa] shear modulus

B [GPa] bulk modulus

ν [-] Poisson's ratio

There is common agreement that in the case of textured materials or single crystals, the interpretation $E_{IT} \simeq E_Y$ is problematic: The elastic response of the material will depend on *all* intrinsic elastic constants and the orientation of the indenter with respect to the crystallographic directions.

More recently, there have been some general concerns about the accuracy and applicability of this standard method for the analysis and interpretation of load-penetration data, even when the tested material behaves isotropic. These will be briefly explained within the next section.

Limitations of the Load-Depth Sensing Indentation Technique

The results of the load-depth sensing indentation testing procedure, HU , HU_{pl} and E_{IT} can be obscured by several artifacts. Moreover, there may also be general limitation to the technique, all of which will be briefly explained in the following. First it is to note that because of the quadratic dependency between $A_c(h)$ and h , there is a large leverage for the relative error of HU . E.g. at an indentation depth of 0.5 μm and an error δh of only $\pm 0.05 \mu\text{m}$ ($= \pm 50 \text{ nm}$), the discrepancy will be as high as 20%. Deviations from the ideal indenter geometry are to be especially expected for small indentation depths $< 6 \mu\text{m}$ and the area function

$A_c(h)$ is to be corrected accordingly [79, 76]. Possible reasons for these deviations are surface roughness and the finite radius of the indenter tip. In the latter case, more accurate approximations for $A_c(h)$ may be found by either directly measuring the indenter tip radius, e.g. with an electron microscope, or measuring the dimensions of a series of impressions with different h_{max} , preferentially in a soft material with low elastic recovery [79]. Other methods based on iterated indentation–correction procedures [79] or the hardness of standard materials [73] have been proposed. These methods were also found to be helpful in order to correct for the elastic deformation of the testing machine.

In recent publications [78, 83] Vepřek et al. reminded the scientific community that even if these aforementioned problems are addressed carefully and corresponding corrections are made according to the state of the art, erroneous hardness readings may be obtained. In the case of materials with extreme hardness, Vepřek even pleads for a different *interpretation* of indentation moduli E_{IT} or E_r .

One phenomenon that was also observed in the testing of samples SN13 and HP-Sial40-II (see Sections 3.8.1 and 4.6.4, respectively) stems from the fact that the indenter penetration h cannot be measured directly, but is determined from the indenter displacement of the testing machine. In the case of the employed testing devices, **Tester C** (Fisherscope 100) and **Tester D**...

“...a massive ring with a diameter of several millimeters that is pressed towards the sample to be measured with a large force (50 N in the case of Fisherscope 100) in order to stabilize the sample prior to the approach of the diamond indenter to its surface. This results in a lift-up of the surface of the sample being measured against the approaching indenter (Figure 2.15) The elastic part of that deformation occurs instantaneously whereas the anelastic one is delayed. When the half time of the time delayed deformation is comparable with the time which the indenter needs to approach the surface and perform the indentation measurement, the apparent indentation depth registered by the instrument will be smaller than the real indentation depth with respect to the surface of the sample.”[83]

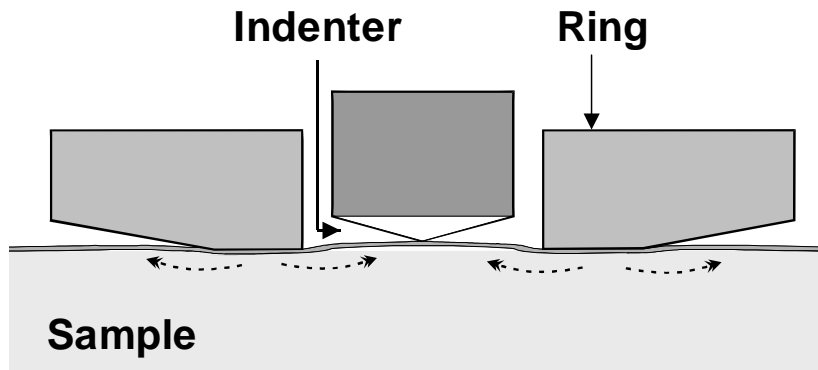


Figure 2.15: Schematic illustration of the effect of anelastic response during the indentation measurement (after Vepřek)

Owing to the aforementioned quadratic dependency between h and A_c , this can lead to absurd values for HU_{pl} (as high as 500 GPa). Checking the size of the remanent impression by means of a calibrated SEM gave correct hardness values.

Another problem stems from influences of the applied contact pressure — that is in the order of HU_{pl} — on the properties of both, the indenter and the indented material. This may have serious implications for the instrumented indentation technique and especially for the common interpretation of the indentation modulus E_{IT} .

In this regard it is to be noted that OLIVER and PHARR within their often cited work on the determination of the elastic modulus from load-depth sensing data [79] found the largest discrepancy between their experimental result and the literature value for the Young's modulus E_Y for the hardest material: Sapphire. They attributed this to the fact the elastic response of the indented single crystal would be a complex function of its five elastic constants and hence difficult to compare with the isotropic average.

VEPŘEK et al. addressed the problem of the non-rigid diamond indenter by means of finite element (FEM) simulations and found considerable deformation of the indenter tip when impinging a superhard composite [83].

Upon load release, both, the sample surface and the diamond will be subject to elastic recovery. Therefore, the general assumption that the indenter/substrate contact area A_c remains constant between h_{max} and h_c (recall Fig. 2.14 (B)) is not valid and may lead to erroneous values for HU , HU_{pl} and E_{IT} . In a related study, Vepřek et al. investigated the common observation that the value of E_{IT} is often found to be smaller than the Young's Modulus E_Y measured by alternative methods [78], but falls within the ambient pressure shear modulus G_0 and the bulk modulus B_0 of the material. Arguing that because E_{IT} is obtained from the first part of the unloading curve, i.e. under the contact pressure of the impinging indenter which can be considerable for hard materials, it was concluded that a more appropriate interpretation of E_{IT} — at least for very hard materials — would be a *pressure enhanced shear modulus* G rather than the Young's modulus E_Y . Currently, this theory seems to lack a theoretical fundament, but is nevertheless of considerable brisance, because many works would have to be re-evaluated if it indeed was proved to be true. The conventional interpretations of the load-depth sensing indentation results, as set out in the sections preceding this paragraph, will be therefore discussed under reserve of these latest developments.

2.3 Vibrational Spectroscopy

Micro-Raman Spectroscopy

- **Raman A:** Dilor Labram confocal spectrometer equipped with a 20 mW HeNe laser 632.817 nm, 300 mm focal length spectrograph with 1800 g/mm grating, and a Peltier cooled CCD detector. Measurements were conducted in backscattering geometry under an Olympus optical microscope with 100 \times objective using a 600–700 nm confocal hole. Total acquisition times were on the order of 300–600 s. Facility of the BGI.
- **Raman B:** Ar-ion laser ($\lambda=457.9$ nm, 2020-05S, Spectra-Physics, San Jose, CA); double spectrometer (SPEX 1402, Spex Industries, Metuchen, NJ) with a charge coupled device detector (LN/CCD-1100 FB, Princeton Instruments, Trenton, NJ, lateral resolution ~ 20 μm). Facility of the high pressure group of the Max-Planck-Institut für Chemie, Mainz.

Infrared Spectroscopy

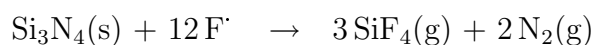
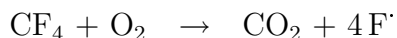
Perkin-Elmer 1750 FT-IR spectrometer. Three sample preparation methods:

- (1) Conventional KBr-method: Sample/KBr-mixture prepared and pressed in air and measured in transmission.
- (2) ‘Thin film method’: A small portion of the pulverized sample is suspended in methanol and dropped a single crystal KBr platelet. Prior to measurement, the platelet is stored for some 10 minutes in a dry-box to evaporate the solvent.
- (3) ‘Golden Gate method’: The so called “*Golden Gate*” *Diamond ATR Accessory* is an insert for the FT-IR spectrometer, provided by ThermoNicolet. The sample can be a powder, liquid or foil and is pressed against a type IIa diamond surface in a similar configuration like a DAC. An optic guides the infrared radiation through the diamond. The radiation reflected at the diamond/sample interface is detected. It is diminished in the intensity of those frequencies coupling to the vibrational modes of the sample. The samples can be loaded in air or under argon.

2.4 Electron Microscopy and Microanalysis

Sample Preparation: Plasma Etching

Working Principle The employed plasma etching process is especially selective for non-oxide silicon ceramics and was applied to the polished specimen after the hardness indentation testing in order to enhance the surface contrast for SEM-investigations. Reactive fluorine radicals are created by an RF plasma discharge in a CF_4/O_2 gas mixture. Reaction with Si_3N_4 leaves only volatile species:



Si–O bonds, e.g. within the intergranular phase of a Si_3N_4 ceramic, are chemically more inert and have smaller etching rates. Hence, the plasma etching

2 Experimental Techniques

process creates a surface topology, where oxidic portions of the sample are embossed over the remaining nitride material and can be directly visualized in the secondary electron (SE) imaging mode of the SEM.

Experimental Procedure The etching was performed with a Polaron Plasma Barrel Etcher, Type PT7100. Only a certain part of the specimen was exposed to the plasma, the remainder, including the polymeric embedding matrix was covered with aluminum foil or self-adhesive PTFE-film. The CF_4/O_2 volume flow ratio was 1:4, etching time between 4 and 10 min at a total pressure of 4 mbar. The plasma input power was adjusted to 40–60 W.

(High-Resolution) Scanning Electron Microscopy, HR-SEM

SEM and HR-SEM was performed on a Philips XL30 FEG with a lateral resolution of 1 nm, equipped with an energy dispersive X-ray analysis (EDX) detector

Electron Probe Microanalysis, EPMA

Cameca SX-50. Measurements at 20 kV and 20 nA for all elements. Mappings at 20 kV, 49 nA, beam-scan mode, 256×256 data points, step size $\sim 0.4 \mu\text{m}$ Detectors: TAP for Al, 30 s/data point; PET for Si, 30 s/data point; and PC1 for N and O, 60 s/data point for each element.

Analytical standards for quantitative analysis: Silica SiO_2 for Si, *c*-BN for N, aluminum metal for Al.

(High-Resolution) Transmission Electron Microscopy, HR-TEM

Philips CM20UT microscope, equipped with an energy dispersive X-ray analysis (EDX) detector (HPGe, NORAN-system Voyager).

2.5 X-ray Diffractometry

2.5.1 Diffractometers

- **Diffractometer A:** Rigaku fine focus diffractometer in reflexion geometry with a position sensitive detector (PDS) covering an angular range from 20–130° 2θ and CrK α radiation ($\lambda_1 = 2.289620 \text{ \AA}$, $\lambda_2 = 2.293520 \text{ \AA}$, intensity ratio $I_1/I_2 = 0.5$). The incident beam was collimated to 0.1 mm diameter. (Facility of the Bayerisches Geoistitut, Bayreuth, Germany)
- **Diffractometer B:** Stoe STADI-P with a curved position-sensitive detector, CuK α_1 radiation ($\lambda = 1.54056 \text{ \AA}$, curved Ge (111) monochromator). (TU-Darmstadt, Dept. of Materials Science, Structure Research Group)
- **Diffractometer C:** Stoe STADI-P with a position-sensitive detector covering 6°, CoK α_1 radiation ($\lambda = 1.78896 \text{ \AA}$, curved Ge (111) monochromator) (TU-Darmstadt, Dept. of Materials Science, Structure Research Group)
- **Diffractometer D:** Gandolfi camera with fine-focus rotating anode (GX21, Enraf-Nonius) and flat imaging plate ($23 \times 25 \text{ cm}$) for detection of two-dimensional diffraction patterns. Distance from sample: 119 mm. 2-D patterns are digitized using an imaging analyzer (BAS-1800II, Fuji Film) with a spatial resolution of 50 μm . (Facility of the Max-Plack Institut for Chemistry, High Pressure Group, Mainz, Germany.) To obtain a standard one-dimensional diffraction pattern, the intensities are integrated along the azimuthal direction. The thus obtained data can be further processed to emulate the Debye-Scherrer geometry [84].

2.5.2 Special XRD Sample Preparation

Preparing powder samples from hard bulk materials—the synthesis of which is a declared aim of this work—can lead to contamination due to less harder grinding media. E.g. an agate mortar or even one made of corundum ceramic may be eroded during the grinding process. If the mortar and the sample material have common elements, this can lead to ambiguous diffraction results. For example, doubts were raised on first results on a spinel-Si–Al–O–N material, presented at a conference. The powder diffractogram showed strong additional reflexions of quartz. In subsequent investigations, these impurities could be clearly traced to the debris of the agate mortar (cf. Section 4.4.1, page 222). In order to circumvent any further difficulties, two methods for XRD (and TEM) sample preparation were developed:

- a) powderisation by use of an diamond-tipped grinder
- b) sectioning the sample into thin slices

For a), the sample was immersed in 2-propanol and abraded with a handheld electrical grinder equipped with a daimanted toolbit. The resulting suspension of powdered sample was then transferred to either a copper grid for TEM studies, to the thin polymer film on a conventional flat sample holder for powder XRD, or dried to be filled in a capillary. The toolbit contains small diamond grains embedded in a electrolytically deposited Ni matrix. Diamond splinters were occasionally found during TEM studies but were apparently much too less to appear in any of the X-ray patterns.

Method b) proved to be especially advantageous where only small amounts of sample (as such obtained from an MAP-experiment) were available. Thin slices were cut by means of a diamond wire saw (recall Section 2.1.2 on page 32). Containing only light elements such as Si, Al, N and O, the absorption of these specimen was small enough to allow direct transmission X-ray measurements. In order to minimize the scattering background or to investigate certain regions of the specimen exclusively, the samples were mounted on a lead mask with 1–2 mm aperture instead of the regular polymer film within the XRD flat sample holder. In contrary to powderized material, spatially distributed features like chemical

gradients and microstructure remained intact and the samples could be subjected to further characterisation like SEM and hardness-testing after being X-rayed.

2.6 Bulk Analyses

2.6.1 Archimedian Density

The measurements were performed with an electronic balance, equipped with a Sartorius YDK 01 set for archimedian density determination. Prior to measurement, the samples were boiled in distilled water for several hours. The dry weight of the samples was then determined after several hours heating at 120 °C. The densities were corrected for the buoyancy of the specimen and the sample basket, during the dry- and the wet-measurement, respectively, using allowance factors according to the users manual.

2.6.2 Combustion Elemental Analysis

- (1) N/O-tester type TC-436 (LECO Corporation, St. Joseph, Michigan USA)
- (2) Commercial analysis by *Mikroanalytisches Labor Pascher*,
Remagen-Bandorf, Germany

2 Experimental Techniques

3 Spinel- Si_3N_4 : The High-Pressure Polymorph of Silicon Nitride

3.1 Discovery of Spinel- Si_3N_4

The third polymorph of Si_3N_4 with a spinel structure was discovered 1998 by a cooperation between the Dispersed Solids and Structure Research Groups at the Technische Universität Darmstadt, the High Pressure Mineral Physics Group at the Max-Planck-Institut für Chemie in Mainz and Dr. Peter Kroll, currently at RWTH Aachen. Interestingly, in spite of the close vicinity and exchange between the researchers, spinel- Si_3N_4 was synthesized independently, yet almost simultaneously, in two different series of high pressure DAC experiments. The series carried out by Andreas Zerr is the one being predominantly documented in a first joint publication [85].

Nomenclature As the spinel-type belongs to the cubic system, it was initially given the symbol $c\text{-Si}_3\text{N}_4$. The connotation to the most commonly used symbol for high-pressure boron nitride, $c\text{-BN}$ ^{*} was intended and “ $c\text{-Si}_3\text{N}_4$ ” was adopted in subsequent publications (see e.g. [86, 87, 88]). In the original works on the almost simultaneously discovered spinel nitrides of the heavier group 14 elements Ge and Sn (see Section 3.2 on page 82), LEINENWEBER et al. used the prefix γ - for Ge_3N_4 [89], whereas SCOTTI et al. omitted the allocation of a

^{*} $c\text{-BN}$ is not the only high pressure polymorph of boron nitride: Analogous to the existence of carbon in a cubic (*diamond*) and a hexagonal modification (*lonsdaleite*), there is a wurtzite-type $w\text{-BN}$, whilst the structure type of $c\text{-BN}$ is sphalerite

prefix at all [90]. The nomenclature γ - M_3N_4 was also used in a highlight article on the group 14 element spinel nitrides by W. SCHNICK [91, 92] and at least two other review articles [6, 93]. As the spinel modifications of many oxides and oxide nitrides are traditionally indicated by γ (e.g. γ - Al_2O_3 , γ - Fe_2O_3 , γ -alon), this appears to be more systematic. Consequently, this convention will be used preferentially throughout this thesis. It should be noted however, that we initially hesitated to use the symbol γ because of an unconfirmed report on the synthesis of a tetragonal silicon nitride back in 1986 which would have been the third polymorph in the chronological order [94].

The initial experiments carried out by Zerr were directly targeted on the synthesis of a high pressure phase of silicon nitride. They had been spurred by the theoretical considerations of Peter Kroll and Sefan Reschke. Their underlying train of thought might be formulated as follows: α - Si_3N_4 and β - Si_3N_4 have been proposed as the first structure models for the crystalline form of C_3N_4 , the hypothetical nitride of the lightest group 14 element. Further structure models for graphite-like C_3N_4 followed. TETER and HEMLEY postulated a cubic polymorph for C_3N_4 with a tetrahedral N environment around the C-atoms, based on *Willemite II*, the high pressure phase of ZnSiO_4 [95]. This carbon nitride was originally denoted as “*c*- C_3N_4 ” but shall rather be named w_{II} - C_3N_4 in the following in order to avoid further confusion with *c*- Si_3N_4 etc. The atomic packing of w_{II} - C_3N_4 would be more dense than the α - C_3N_4 and β - C_3N_4 polymorphs and the Willemite II structure therefore appeared Kroll and Reschke to be also a potential structure type for a high pressure form of Si_3N_4 . Considering further possible structures for Si_3N_4 , Kroll was able to predict from subsequent density functional calculations, that the octahedral coordination of Si was the important structural motif of the most stable and therefore most likely high pressure phase of Si_3N_4 .

The second series of experiments actually were targeting on the synthesis of β - C_3N_4 . They have been prepared by the author and were conducted by George Serghiou at the Max-Planck-Institut in Mainz. They will be described in the following section as a part of this dissertation.

The underlying idea was initiated by reported efforts to synthesise β - C_3N_4 by gas phase processes, using β - Si_3N_4 as a substrate for heteroepitactical growth [96] and the occurrence of intermediate $\text{C}_{3-x}\text{Si}_x\text{N}_4$ -layers, where Si substrates have been used for similar experiments [97]. Consequently, a carbon nitride precursor, C_3N_{12} , was mixed with β - Si_3N_4 seed crystals. Upon the HP/HT treatment in a diamond anvil cell, a part of these crystals transformed into the the new high density Si_3N_4 polymorph. Later, larger amounts of γ - Si_3N_4 were synthesized by the MA-technique, which allowed a more thorough characterisation, including structure refinement with the Rietveld method and will be described in Section 3.3 on page 84 and following sections.

Finally, a method that could enable industrial production of γ - Si_3N_4 was sought in several shock wave experiments. Table 3.1 on the next page provides an overview of the high pressure experiments conducted on Si_3N_4 within this work.

Table 3.1: Overview of HP/HT-experiments in the system Si-N-(O)

Exp. No.	starting materials	sample environment	capsule size $\emptyset \times h$ [mm]	pressure assembly	p_{max} [GPa]	T_{max} [°C]	t_{raise}^T [s]	t_{hold}^T [s]	result
SN0A	β -Si ₃ N ₄ / C ₃ N ₁₂	Ar	--	DAC	29.2	2300	—	1200	β - and γ -Si ₃ N ₄
SN0B	β -Si ₃ N ₄ / C ₃ N ₁₂	Ar	--	DAC	38.5	2500	—	1200	in CN _x -matrix
SN01	<i>a</i> -Si ₃ N ₄	Re/MgO	1.6 × 2.9	14 M	15	^[a] 2300	<i>n.n.</i>	175	γ -Si ₃ N ₄ , Re ^[b]
SN02	<i>a</i> -Si ₂ N ₃ H	Re/MgO	1.6 × 2.6	14 M	15	1800	<i>n.n.</i>	60	γ -Si ₃ N ₄
SN03	<i>a</i> -Si ₃ N ₄	Pt/MgO	1.6 × 2.6	14 M	15	1800	960	60	γ -Si ₃ N ₄
SN04	<i>a</i> -Si ₂ N ₃ H	Pt/MgO	2.0 × 3.7	14 M	10	1800	840	540	β -Si ₃ N ₄
SN05	<i>a</i> -Si ₂ N ₃ H	Pt/MgO	1.6 × 2.7	14 M	15	1800	1200	120	γ -Si ₃ N ₄
SN06	<i>a</i> -Si ₂ N ₃ H	Re/MgO	2.0 × 3.4	14 M	15	1800	<i>n.n.</i>	900	γ -Si ₃ N ₄
SN07	<i>a</i> -Si ₂ N ₃ H	Pt/Mo/MgO	2.0 × 3.5	14 M	15	1800	<i>n.n.</i>	90	γ -Si ₃ N ₄
SN08	<i>a</i> -Si ₂ N ₃ H	Pt/Mo/BN	2.0 × 3.5	14 M	15	1800	900	90	γ -Si ₃ N ₄
SN09	<i>a</i> -Si ₃ N ₄	Pt/Mo/BN	2.0 × 3.5	14 M	15	1800	<i>n.n.</i>	90	γ -Si ₃ N ₄
SN10	<i>a</i> -Si ₂ N ₃ H	Pt/Mo/BN	2.0 × 3.5	14 M	12.5	1600	<i>n.n.</i>	300	γ -Si ₃ N ₄
SN11	β -Si ₃ N ₄ / <i>a</i> -Si ₂ N ₃ H	Pt/Mo/BN	1.7 × 3.1	14 M	13	^[c] 1500	1033	5100	β -Si ₃ N ₄
SN12	<i>a</i> -Si ₂ N ₃ H / γ -Si ₃ N ₄ ^[d]	Pt/BN	1.9 × 3.1	14 M	13	1600	930	14400	β -Si ₃ N ₄ , <i>r</i> -SiO ₂
SN13	cutting tool	Pt/MgO	1.6 × 3.3	14 M	15	1800	19	164	dense γ -Si ₃ N ₄

^[a]last value before strong temperature fluctuations occurred ^[b] sample partially molten^[c]thermocouple failure, value estimated from applied electrical power (590 W). ^[d]from SN07

3.1.1 Synthesis of $\gamma\text{-Si}_3\text{N}_4$ in a Diamond Anvil Cell

Experimental Procedure

Starting Materials

- C_3N_{12} (1,3,5-triazido-2,4,6-triazine): The compound was synthesized according to the procedure described by Ott and Ohse [98]. It should be noted that this material exhibits the properties of a *brisant priming explosive, i.e. it may explode upon mechanical shock, friction or spark*. Moreover, its detonative strength is higher than that of TNT. However, it was found that it can be handled safely in the form of a fine powder in amounts below 500 mg. The as-synthesized compound melted below 90 °C and was reported not to explode below 150 °C.
- $\beta\text{-Si}_3\text{N}_4$ was purchased as light grey powder from the Bayer Company, Germany. Prior to the experiment, it was vacuum-dried in a quartz glass tube at about 150 °C and then stored in argon drybox.
 - Powder-XRD: ~ 100 vol% $\beta\text{-Si}_3\text{N}_4$
 - Combustion elemental analysis: 0.3% O

Sample Preparation A small amount of C_3N_{12} was molten on a thin PTFE-sheet placed on a hotplate. Two mixtures with different $\beta\text{-Si}_3\text{N}_4$ contents were created by dropping silicon nitride powder into an excess of C_3N_{12} melt, which was then left to freeze.

- SN0A: More $\beta\text{-Si}_3\text{N}_4$
- SN0B: Less $\beta\text{-Si}_3\text{N}_4$

Diamond Anvil HP/HT Experiment A small piece ($\sim 70\text{ }\mu\text{m}$) was cut from each mixture, using a scalpel. The samples were loaded into a DAC, which was thereafter filled with compressed Ar as a pressure medium. After pressurisation to 29.2 GPa (SN0a) and 38.5 GPa (SN0b), the samples were heated with a CO_2 laser to 2300 K and 2500 K respectively. Quenching was accomplished after approximately 20 minutes by switching off the laser power.

Sample Recovery The quenched samples were unloaded, taken out of the DAC's, crushed between two diamond anvils without a gasket, and directly transferred to a copper grid for TEM.

3.1.2 TEM Sample Characterisation

The samples were investigated with TEM, including SAED and EDX-chemical analysis. It was found that the C₃N₁₂ precursor had transformed into an amorphous CN_x matrix as evidenced by a low, homogeneous contrast in the bright field image and a diffuse spot in the diffraction-mode for all particles investigated. A high intensity of the N-*K* peak at ~ 400 eV in the EDX spectrum indicated a high nitrogen content. The signal was so strong that the C-*K* peak was entirely covered under its rising edge, thereby prohibiting any closer quantification. Similar results had been obtained in previous high pressure runs on pure C₃N₁₂. Further investigation showed that part of the β -Si₃N₄ had remained unchanged. Also no ternary Si-C-N phases were found. SAED-patterns of other particles however, indicated a cubic lattice symmetry, with their EDX-spectra yielding the same Si:N ratio as β -Si₃N₄. Fig. 3.1 (A) shows a brightfield image of two crystals, the left being β -Si₃N₄ and the right one the new cubic silicon nitride polymorph (γ -Si₃N₄).

From SAED-patterns a cubic face centered cell with a lattice constant of $a_0 = 7.80 \pm 0.08$ Å was derived. In Fig. 3.1 (B), the diffraction pattern of the [001] zone is shown. The zero order Laue zone (LZ) in the center is surrounded by a circular pattern of further reflections that originate from the 1st order LZ. The distance between these $hk1$ reflections is one half that of the $hk0$ reflections. This means that there are extra extinctions in the first order LZ. Only reflexions which obey the condition $h + k = 4n$ are present. This indicates a *d*-glide plane in the crystal lattice of γ -Si₃N₄ which therefore must belong to one of the three following space groups: *Fd* $\bar{3}$, *Fd* $\bar{3}m$ or *Fd* $\bar{3}c$. The latter, *Fd* $\bar{3}c$, can be excluded because all sites with multiplicities < 96 lead to the extra condition that for all possible reflexions, $(h,k)l$ must be even, which contradicts the observation of the first order LZ ($hk1$). Multiplicities ≥ 96 , for a composition Si₃N₄, would require a number of formula units per unit cell $Z \geq 24$, leading to unrealistically high densities of $\varrho_0 \geq 11.8$ g/cm³.

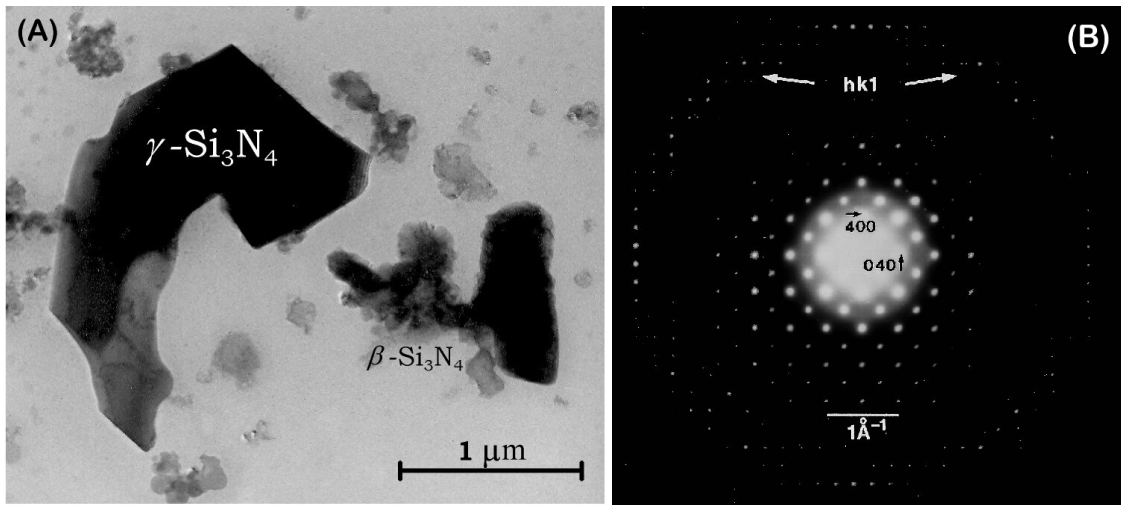


Figure 3.1: (A) TEM-brightfield image of a crystal of the new $\gamma\text{-Si}_3\text{N}_4$ -phase (left) and an agglomerate of $\beta\text{-Si}_3\text{N}_4$ (right), as identified by selected area electron diffraction (SAED). (B) SAED-pattern of zone $[001]$ of the spinel silicon nitride showing extinctions due to the d-glide plane.

3.1.3 $\gamma\text{-Si}_3\text{N}_4$ and the Spinel Structure

A realistic structure for $\gamma\text{-Si}_3\text{N}_4$ with $Z = 8$, corresponding to $\varrho_0 \approx 4 \text{ g/cm}^3$, can be derived from both, $Fd\bar{3}m$ (Nr. 227) and its subgroup $Fd\bar{3}$ (Nr. 203), in two different ways. (Tab. 3.2)

Setting I	Setting II	Equi- point*	site symmetry	fractional coordinates of lattice sites		
Si^{tet}		$8a$	$\bar{4}3m$	$1/8$	$1/8$	$1/8$
	Si^{tet}	$8b$	$\bar{4}3m$	$3/8$	$3/8$	$3/8$
	Si^{oct}	$16c$	$. \bar{3}m$	0	0	0
	Si^{oct}	$16d$	$. \bar{3}m$	$1/2$	$1/2$	$1/2$
N		$32e$	$. 3m$	\mathbf{u}	\mathbf{u}	\mathbf{u}
	N	$32e$	$. 3m$	u'	u'	u'

$$u_{ideal} = 0.25 \quad u' = u + \frac{1}{8}$$

Table 3.2: Two equivalent settings for the structure of $\gamma\text{-Si}_3\text{N}_4$

*Wyckoff notation

The settings are equivalent descriptons of the ***spinel structure***, named after the naturally occurring gemstone spinel $\gamma\text{-MgAl}_2\text{O}_4$ (which is also used as a ceramic material). The general formulation of spinel compounds is AB_2X_4 . The structure is usually described as a face-centered-cubic (*fcc*) array of anions X. One eighth of the tetrahedral intersticies and one half of the octahedral ones are occupied by cations A and B, respectively. In this particular case, Si atoms occupy both A and B sites. They will hereafter be labeled Si^{tet} and Si^{oct} , respectively. Hence, a more precise formulation for $\gamma\text{-Si}_3\text{N}_4$ is $\text{Si}^{\text{tet}}[\text{Si}^{\text{oct}}]_2\text{N}_4$.

Throughout the entire document, structural information will solely be given and discussed with respect to **I** and the origin of the unit cell set to the center of symmetry in 16c (“*origin choice 2*”, International Tables [99]). The unit cell of the spinel structure, visualized with respect to this setting, is shown in Figure 3.2 on the facing page.

Cation Coordination The ***sixfold coordination of silicon*** by nitrogen in $\gamma\text{-Si}_3\text{N}_4$, which previously was known only for some complex silicate anions [100] and one oxide nitride compound [101]. In the nitride $\gamma\text{-Si}_3\text{N}_4$, one third of the Si atoms remain in tetrahedral coordination, as in the low pressure polymorphs α - and $\beta\text{-Si}_3\text{N}_4$, but the coordination number of the nitrogen atoms is increased: While being in a trigonal planar configuration within the low pressure phases, the γ -phase has ***fourfold coordinated nitrogens*** in tetrahedral configuration, similar to the conditions in the ammonium-ion, NH_4^+ . The average coordination number of the first coordination sphere can thus be calculated as follows:

$$\bar{N}_c(\gamma\text{-Si}_3\text{N}_4) = \frac{N_{\text{Si}^{\text{tet}}} + 2 \cdot N_{\text{Si}^{\text{oct}}} + 4 \cdot N_{\text{N}}}{\text{atoms/formula unit}} = \frac{2 \cdot 6 + 1 \cdot 4 + 4 \cdot 4}{7} \approx 4.57 \quad (3.1)$$

The similarly calculated $\bar{N}_c(\alpha\text{-}/\beta\text{-Si}_3\text{N}_4) \approx 3.43$. Thus, the average coordination is increased by $\sim 33\%$, whereas the increase in mass density is $\sim 26\%$.

Charge balance considerations Compared with conventional oxide spinels, $\gamma\text{-Si}_3\text{N}_4$ and the other group 14 nitride spinels are unique in many regards. While the binary oxide spinels based on transition metals, such as Fe_3O_4 or Fe_3S_4 , still contain differently charged cation species ($\text{Fe}_3\text{X}_4 = \text{Fe}_2^{3+}\text{O}_3 \cdot \text{Fe}^{2+}\text{O}$, “2-3 spinels”)

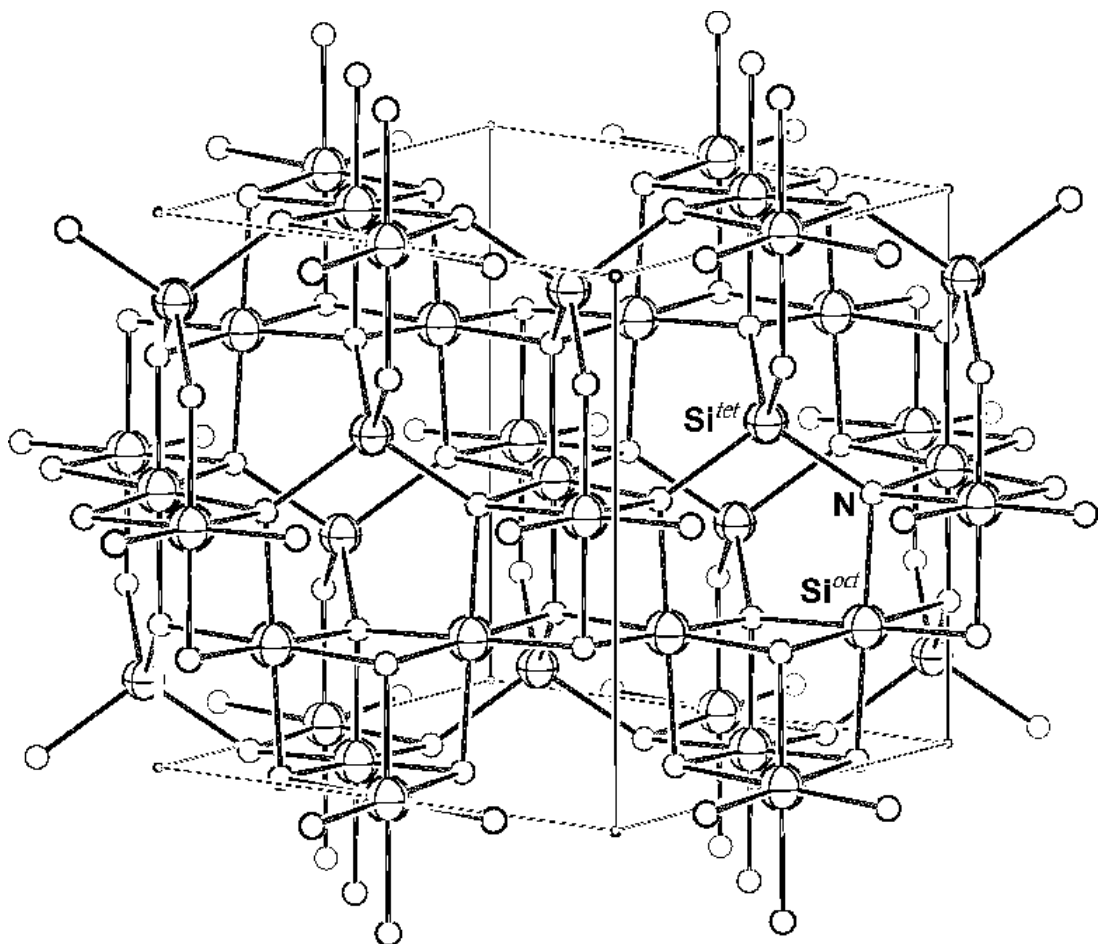


Figure 3.2: The spinel-structure (unit cell with origin at $16c$ (point symmetry $\bar{3}m$)). $\gamma\text{-Si}_3\text{N}_4$ consists of edge connected SiN_6 octahedral units which run parallel and perpendicular to each other and are connected by SiN_4 tetrahedra which are corner connected with the SiN_6 octahedral units of the criss-crossing chains.

the electronic structure of the light main group elements does not allow different oxidation states, so that all sites will be occupied by ‘cations’ with a formal charge of +4 (‘4-4 spinels’). As a consequence, there is an ***absence of local electroneutrality***: The tetrahedrally coordinated nitrogen ‘anion’ shares its formal charge of -3 with four surrounding silicon atoms of charge +4. This results in finite charges q that are centered at the locations of Si^{tet} and Si^{oct} .

Their formal magnitude can be calculated according to the simple electrostatic Pauling rule as follows:

$$q(\text{Si}^{tet}) = q(\text{Si}) + N_{\text{Si}^{tet}} \cdot \frac{q(\text{N})}{N_{\text{N}}} = 4 + 4 \cdot \frac{-3}{4} = +1e \quad (3.2)$$

$$q(\text{Si}^{oct}) = q(\text{Si}) + N_{\text{Si}^{oct}} \cdot \frac{q(\text{N})}{N_{\text{N}}} = 4 + 6 \cdot \frac{-3}{4} = -0.5e \quad (3.3)$$

In reality, these charges will be somewhat lower due to redistribution of the electron density but they will nevertheless remain of finite magnitude. An indication for a high electron density around the Si^{oct} site was found via ²⁹Si MAS NMR by SEKINE et al. [102]. The NMR-signal exhibits an unusually large negative chemical shift of -225.0 ± 0.2 ppm which is less than that of the SiO₆ unit (-200 ppm) and corresponds to a strong shielding of the Si^{oct} nucleus. The signal corresponding to Si^{tet} in γ -Si₃N₄ was found to be only marginally different to that of β -Si₃N₄ (-50.0 ± 0.2 ppm versus -49.1 ± 0.2 ppm).

We can expect an *intrinsic polarity* to be a *common feature among all spinel nitrides* of Si, Ge and Sn and—if they exist—also those of Ti, Zr, and Hf, as well as all their possible ternary and multinary solid solutions. The resulting ionic interactions will have important implications on the electronic structure of these compounds and their physical properties such as thermal expansion behavior or thermal conductivity (see e.g. Section 3.8.7 on page 173).

Anion position In the spinel structure, the anion position is not entirely fixed by symmetry, but can deviate along the $\langle 111 \rangle$ direction, which gives rise to one free parameter, sometimes called “*spinel parameter*”[103] and denoted with \mathbf{u} . Only for $\mathbf{u} = \frac{1}{4}$, the anions are ideally cubic close-packed. In most cases however, there is a finite dilation, given by $\mathbf{u} = \frac{1}{4} + \delta$.* This has several important crystallographic implications, including changes in bond lengths, bond angles, interstice volumes and the symmetry of coordination polyhedra. The actual value of δ for γ -Si₃N₄ could not be determined from the SAED-pattern but was later derived by refinement of the structure based on powder-XRD (see below). Nevertheless, at that state of the investigations, it was clear from the *pressure-distance*

*often another value of $\mathbf{u} = \frac{3}{8} + \delta$ is given, i.e. with respect to the origin at $8a$ with symmetry $\bar{4}3m$ (“*origin choice 1*”, International Tables [99])

paradox introduced in Section 1.4.2, that δ had to be smaller than $\frac{1}{80}$, because at this value, the Si–N distances of Si^{oct} and Si^{tet} would be equal.

The structural flexibility provided by the free anion parameter \mathbf{u} suffices to accommodate a large range of cations and cation charge combinations. Already more than a hundred spinel-compounds, many of them important minerals or commercially important magnetic oxides, were known [21, 104] before 4-4* nitride spinels were discovered in 1999. Table 3.3 on the following page gives some examples.

The structural details of the new nitride spinels will be discussed in Section 3.5.1 on the basis of the precise structure determination of $\gamma\text{-Si}_3\text{N}_4$ by Rietveld refinement.

Cation Disorder in Spinels It is evident from Table 3.3, that the vast majority of spinel compounds contains two different cation species, even in the case of binary spinels like Fe_3O_4 , where Fe^{3+} and Fe^{2+} ions are present. The possibility to distribute these different cations on A and B sites results in the existence of what is called *normal*, *inverse* and *intermediary* spinels, the general formulation of which may be given by



where i is called the “*inversion parameter*”. Normal spinels correspond to $i = 0$ and Equation (3.4) reduces to $\text{A}^{\text{tet}}[\text{B}_2]^{\text{oct}}\text{X}_4$. For full inversion i equals 1, thus giving $\text{B}^{\text{tet}}[\text{AB}]^{\text{oct}}\text{X}_4$. A totally random cation distribution is given by $i = 2/3$. It is to be noted that the space group symmetry is retained for intermediary and inverse spinels, as long as A and B cations are randomly distributed among the octahedral sites. Preferential occupation of *specific* octahedral sites within the unit cell leads to superstructures and the lowering of symmetry. The concept of normal and inverse spinels was introduced by VERWEY and HEILMANN (see [104] and references therein). Originally, the separation between normal and inverse was made according the ionicity of the constituent cations: Spinels containing the lower valent cation in sixfold coordination were denoted as inverse. In the

*the numbers refer to the (formal) cation charges, e.g. $[\text{Si}^{4+}]_2\text{Si}^{4+}\text{N}_4 \cong 4\text{-}4$, $\text{Mg}^{2+}[\text{Al}^{3+}]_2\text{O}_4 \cong 2\text{-}3$, and so on

Table 3.3: Some spinel compounds with different anions and cation charge combinations

	Compound	Characteristics	Ref.
Oxide Spinels			
2-3	Mg[Al] ₂ O ₄	<i>the</i> spinel	
3-3	Al _{2.6} □ _{0.3} O ₄	γ-Al ₂ O ₃	
	Fe _{2.6} □ _{0.3} O ₄	γ-Fe ₂ O ₃ , magnetic data recording	[105]
3-2-3	Fe[Fe] ₂ O ₄	Magnetite, the ancient sailor's loadstone	[106]
	Fe[MgFe]O ₄	Magnesioferrite	
	RV ₂ O ₄	R = La-Lu, Y; ferrimagnetic RE-spinels	[107]
2-2-4	Mg ₂ SiO ₄	high-press. polymorph of forsterite	
	Fe ₂ TiO ₄	Ulvöspinel, giant magnetoresistance	
1-3-4	LiTi ₂ O ₄	superconducting	[108]
1-1-6	Ag ₂ WO ₄		
Sulfide Spinels*			
	Fe[Fe] ₂ S ₄	Greigite	[21]
	CuCo ₂ S ₄	Carollite, a natural metallic spinel	[21]
	Al _{0.75} [Mo] ₂ S ₄		[109]
	Ga _{0.5} [V] ₂ S ₄		[109]
Oxide Nitride Spinels			
2-3-5	Mn[MnTa ₃]N _{6-δ} O _{2-δ}		[110]
3-3	Al ₂₃ O ₂₇ N ₅		[111]
4-3	γ-Si _{3-x} Al _x O _x N _{4-x}		[112, 113]
Nitride Spinels			
4-4	Si[Si] ₂ N ₄		[85]
	Ge[Ge] ₂ N ₄		[114, 89]
	(Si _x Ge _{1-x}) ₃ N ₄		[115]
	Sn[Sn] ₂ N ₄		[90]

*also denoted as "thiospinels"

case of the novel 4-4 spinels, where *tetrahedral as well as octahedral sites* are occupied by cations with a formal charge +4, the term “inverse spinel” has been used by some authors to discriminate between different configurations of ternary spinels, such as $[\text{Si}]^{\text{tet}}[\text{SiGe}]^{\text{oct}}\text{N}_4$ and $[\text{Ge}]^{\text{tet}}[\text{Si}_2]^{\text{oct}}\text{N}_4$ [116, 117, 118, 115].

Consequences of the Spinel Structure of $\gamma\text{-Si}_3\text{N}_4$ In spinels the number of positional parameters is $N_f = 1$. This means that materials with spinel structure *in general* do not fulfill all requirements for *ultrahardness*. However, there may well exist compositions with ideal atom sizes for which δ becomes sufficiently small so that the anion sites approach inversion symmetry and yielding due to internal displacements is diminished (recall Section 1.4.2 on page 6), and [6], page 17. What is more, the structural flexibility that is provided by δ will promote accommodation of a large number of dopant species and may therefore be exactly the quality that determines a “*useful*” material with tunable properties. Moreover, as other figures of merit like the average coordination number \bar{N}_c have actually improved, there was no striking reason to assume its hardness to be significantly below that of stishovite. With a microhardness of $H = 33$ GPa, $r\text{-SiO}_2$ had been called “*the hardest known oxide*”. It has also one parameter for the anion position [119].* A recent study of $\gamma\text{-Si}_3\text{N}_4$ suggests that the hardness expectations based on comparison with stishovite may be exceeded: Tanaka et al. found a maximum hardness value of 43 GPa at a load of 9.8 mN [120]. These results will be discussed in more detail in Section 3.8.1 on page 134.

*i.e. $N_f = 1$ as in the spinel structure

3.2 The High-Pressure Nitrides of Group 4, 13 and 14 Elements

As mentioned previously, the spinel nitrides of the three **group 14 elements** Si, Ge and Sn were all discovered within the years 1998/1999 (Section 3.1 on page 69) and have since spurred a notable number of experimental and theoretical investigations. The occurrence of γ -Si₃N₄ was titled as “*the most intriguing recent development in the field of silicon nitride ceramics*” [121] and the contributors to the spinel nitride literature originate from related but nevertheless different fields like materials science and engineering [122], solid state science [123, 124] and solid state chemistry [90, 91, 92], theoretical and applied physics [86, 116, 125].

Shortly after the spinel nitrides of the group 14 elements had been established, speculations on the possible existence of isostructural nitride spinels of the **group 4** transition metals, i.e. ‘ γ -Ti₃N₄’, ‘ γ -Zr₃N₄’ and ‘ γ -Hf₃N₄’ were raised by CHING and colleagues [126]. In the following, these researchers investigated the ‘would-be’ properties of these binary spinels as well as all kinds of combinations AB₂N₄, A,B = Ti, Zr, Hf, C, Si, Ge and Sn by ab-initio methods based on density functional theory [116, 127]. However, in 2002/2003 an experimental work by ZERR and MIEHE showed that *spinel is not the preferred structure type* for the nitrogen-rich group 4 compounds [84]: Heating Hf metal at 18 GPa and 2800 K in a DAC with nitrogen pressure medium yielded a novel hafnium (IV) nitride, Hf₃N₄ with thorium phosphide (Th₃P₄) structure. It exhibits a eightfold coordination of the metal atoms by nitrogen and is therefore significantly more dense than the spinel structure. Analogous syntheses of Zr₃N₄ were successful, and a subsequent theoretical investigation of the three Th₃P₄-type nitrides of Ti, Zr and Hf by KROLL [128] predict interesting properties such as potential superconductivity.

Apart from these very recent developments, it is remarkable that the corresponding high-pressure nitrides of the **group 13 elements** AlN, GaN, and InN that crystallize in the **rocksalt (rs-)** structure, arouse much less attention. The rock-

salt phase of AlN was first synthesized by VOLLSTÄDT et al. in 1990 [129]—8 years before γ -Si₃N₄— and was published in the *Proceedings of the Japanese Academy*, a journal with comparatively low impact factor. It initiated further research on *rs*-AlN and its heavier homologues, that however remained almost entirely within the physics and solid state community, as it was published in Journals like *Physical Review B* [130, 131, 132], *J. Phys.: Condens. Matter* [133, 134] and *J. Appl. Phys.* [135, 136]. The publications include theoretical studies of the structural, electronic and elastic properties of the rocksalt group 13 nitrides. The wurtzite \rightarrow rocksalt transformation was studied theoretically [133, 132, 137] and experimentally in static [131, 135] and dynamic [138] high pressure studies. To the best of my knowledge, no report on the synthesis of phase pure *rs*-AlN and consequently no experimental determination of its properties has been published so far. One reason could be the low stability of the group 13 rocksalt nitrides: Of the three compounds *rs*-AlN, *rs*-GaN and *rs*-InN, only the aluminum nitride was found to be metastable [135], while the other two phases show a reversible phase transformation to the wurtzite structure upon pressure release [132]. The phase transformations of all three nitrides can be driven at room temperature, which means that their activation barrier must in general be small in both directions: *wz* \leftrightarrow *rs*. Shock recovery experiments of *rs*-AlN failed*—most likely due to a low thermal stability of the material.

Both, the spinel nitrides and the corresponding group 13 rocksalt compounds resemble different packing arrangements of nitrogen ‘anions’ that differ by the ‘cation’ species occupying the interstices. Comparison between these phases will therefore provide instructive insights how structure and properties of this nitrogen-arrangement may be tailored via insertion of different cations. These comparisons will be drawn in the respective sections on the structure and properties of γ -Si₃N₄, where the corresponding data on the group 13 nitrides is available.

*T. Sekine, personal communication

3.3 Multianvil Press Synthesis of γ -Si₃N₄

The importance of γ -Si₃N₄ as the third polymorph of silicon nitride and its potential to provide properties superior to the quite successful conventional Si₃N₄-ceramics was immediately clear after it had been identified in the reaction products of the DAC experiments described above. Accordingly, a high pressure method capable to synthesize larger amounts of γ -Si₃N₄ that would enable characterization by other means than just TEM was sought. Our results from DAC experiments showed, that γ -Si₃N₄ formed at 15 GPa or higher, while a pressure of 5 GPa yielded only β -Si₃N₄ [85]. This led to the additional requirement to produce pressures of at least 10 GPa, in order to be on the safe side, thus ruling out techniques like piston cylinder and belt apparatus with capabilities of about 6 GPa [139]. As mentioned in section 2.1.2, the **multianvil** (MA-) technique is the method which comes closest to the *p-T*-range of DACs. Our investigations led us to the Bayerisches Forschungsinstitut für Experimentelle Geochemie und Geophysik (“**Bayerisches Geoinstitut**”, BGI) in Bayreuth, Germany. The BGI is a European Large Scale Facility in high pressure research and has four presses in the range between 500 and 5000 t force, suitable for MA-experiments up to 25 GPa and 3000 K on sample material in the order of several mg. All high pressure experiments described in the following sections have been carried out at the BGI.

3.3.1 Choice of starting materials

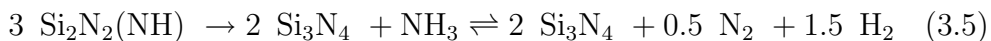
From publications prior to [85] it was known that α -Si₃N₄ sustains a pressure of 48 GPa at room temperature [140]. Also melting α -Si₃N₄ at pressures up to 37 GPa in a laser-heated DAC yielded no indications for γ -Si₃N₄ [141]. In the case of β -Si₃N₄, Zerr observed soft mode behavior of the three lowest frequency Raman modes upon compression. This is a sign of destabilization of the crystal lattice, however no phase transformation occurred up to 28 GPa at room temperature [142]. These results give prove to a considerable kinetic barrier for the phase transformation due to the rigid crystal lattice of the low pressure modifications. The successful DAC syntheses of γ -Si₃N₄ described in [142] had been carried out with either elemental silicon, which was molten inside the DAC and reacted in

3.3 Multianvil Press Synthesis of γ - Si_3N_4

situ with the nitrogen pressure medium, or, where modifications of Si_3N_4 had been employed as starting materials, at temperatures exceeding 2000 °C. For the MA-experiments, however, it was desirable to find starting materials that would readily transform at more moderate temperatures and be less difficult to prepare than silicon in an environment of compressed nitrogen. Additionally, as sample volume is limited, a high initial density would be clearly preferable in order to maximize the yield, that is that all educts should be in solid state. These considerations led to the choice of two amorphous Si-N compounds as starting materials for the experiments SN01–SN10.

- **amorphous silicon nitride imide**, $a\text{-Si}_2\text{N}_2(\text{NH}) \equiv a\text{-Si}_2\text{N}_3\text{H}$, an intermediate product in the synthesis of high purity silicon nitride powder via the diimide-route [143].^{*}
 - Elemental analysis:[†]
Si: 42.3 wt.%, N: 56.6 wt.%, H: 0.9 ± 0.1 wt.% O: 0.5 wt.%
 - Trace analysis:[‡]
Cl: 0.56 wt.%; Fe: 3 ppm; Al: 1 ppm; Ca: 3 ppm.

$\text{Si}_2\text{N}_3\text{H}$ also occurs in a crystalline form which is isotypic to silicon oxide nitride, $\text{Si}_2\text{N}_2\text{O}$. Upon heating, it releases ammonia and/or nitrogen and hydrogen:



These gases may promote diffusion in nitride materials in the same manner as water does in the case of the oxides and thereby provide an effective pathway to overcome the kinetic barrier of the phase transformation.

- **amorphous silicon nitride**, $a\text{-Si}_3\text{N}_4$, obtained by calcination of $a\text{-Si}_2\text{N}_3\text{H}$ at 1200 °C in flowing N_2 (grade 5.1) for 20 min.
 - Elemental analysis: Si: n.d., N: n.d., H: 1,07 wt.%, O: 3.2 wt.%.

^{*}We gratefully acknowledge the donation of considerable amounts of $a\text{-Si}_2\text{N}_3\text{H}$ by the Bayer AG, Krefeld

[†]Mikroanalytisches Labor Pascher, Remagen-Bandorf, Germany

[‡]according to Bayer

- SN11 was carried out after SN01–SN10 had been analyzed and were found to be too porous for hardness measurements: In order to achieve a high initial density, an **admixture of 20% *a*-Si₂N₃H and 80% *β*-Si₃N₄** was prepared. The *β*-Si₃N₄ was the same material that had been used for SN0A and SN0B (see Section 3.1.1 on page 73). The amorphous precursor was added in order to promote nucleation and grain-growth of the *γ*-phase.
- In Exp. SN12, a small amount ($\sim 1\%$) of *γ*-Si₃N₄ from SN07 to act as crystal-seeds, was mixed into the *a*-Si₂N₃H-precursor. The aim was to grow large *γ*-Si₃N₄ crystals.

3.3.2 Sample preparation and HP/HT- experiments

For Experiments SN01– SN10, a nitrogen filled glovebag was used in order to limit hydrolysis and contamination of the powders with oxygen. The sample capsules, prepared from Pt or Re foil according to the procedure described in Section 2.1.2 on page 28, were introduced into a metal die, subsequently filled with the powders and hammered close. Initially, these capsules were inserted into the standard MgO-tubes, but in experiments SN07–SN12 the samples were further encapsulated with molybdenum foil surrounded by a boron nitride container instead of MgO to minimize oxidation during the experiment.

For SN11 and SN12, the capsules were made from a seamless Pt tube* and had an arc-welded bottom. Prior to filling the capsules, the precursor mixtures were homogenized by hand, using an agate mortar and pestle. The samples were prepared in a glovebox, including the introduction into the octahedral pressure cell. SN12 however had been taken out from the glovebox for some time to be welded close. Traces of powder at the capsule walls initially prevented the formation of a proper weld seal. A major contamination with oxygen which was detected in the course of the sample characterisation after the HP/HT-treatment may have occurred during this preparation step.

*special thanks to Mrs. Kordula Koehler and the Heraeus Company, Precious Metals Division, Hanau, Germany, for generous support with platinum tubing

The samples were pressurized, heated and quenched according to the standard procedure described in Section 2.1.2 on page 31. The experimental parameters are listed in Table 3.1 at the beginning of this chapter.

3.3.3 Sample recovery

After 12 h of decompression, the samples were recovered from the pressure assembly. The MgO octahedron was broken to reveal the noble-metal foil capsules. In the first experiment, the rhenium partially melted upon too intense heating. In other cases the metal foils could be easily separated from the product. Figure 3.3 on the next page shows an SEM-image of a 15 GPa-sample, unleashed by removing the top part of the metal capsule. Successive images of the microstructure of the material were taken from the fractured area indicated by the arrow. The samples were pure white, opaque and had a glossy appearance.

From SN11 a thin cylindrical platelet for successive X-ray diffraction was cut with a diamond wire saw. The remaining cylinder was embedded and polished for hardness testing.

In contrary to the other samples, the grains of the Pt metal encapsulation of SN12 had grown very coarse, due to the prolonged heating time. The capsule behaved brittle and was obtained broken in half. It revealed infiltration of Pt into the porous product which was inhomogeneous in coloration, ranging from milky-white to colourless with a high brilliance. Figure 3.4 on the following page shows an SEM-image of the larger cylinder after embedding and polishing. This specimen surface was later removed with a diamond-grinder in order to obtain powder for the XRD phase analysis.

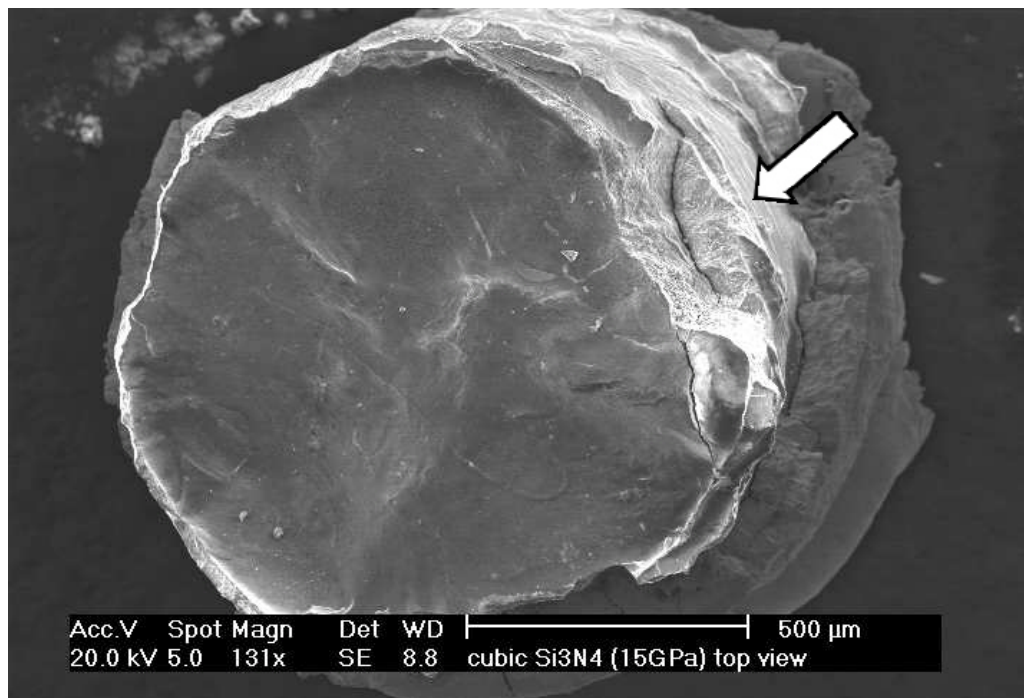


Figure 3.3: Top view of an unwrapped γ -Si₃N₄-sample cylinder (SN02) after recovery

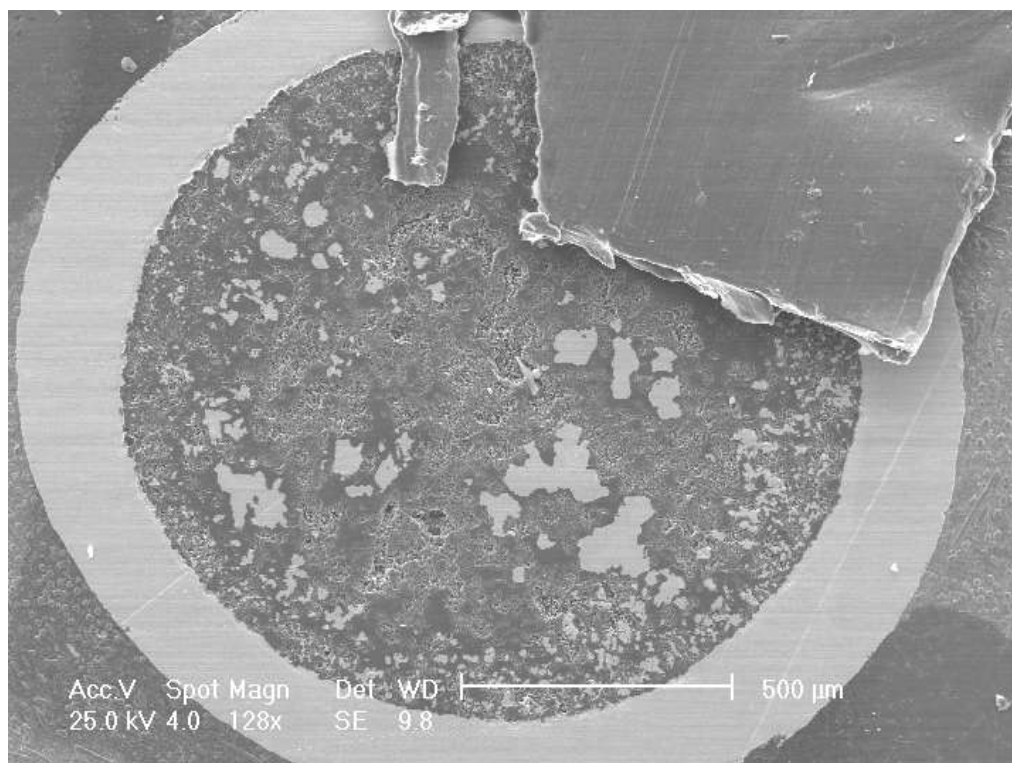


Figure 3.4: Top view onto the SN12 specimen after embedding and polishing showing pale grey zones of infiltrated Pt between porous product

3.3.4 Further Syntheses of γ -Si₃N₄ reported in Literature

The multianvil technique was also chosen by other groups as a means for the HP/HT conversion to γ -Si₃N₄. However, instead of amorphous precursors, the crystalline phases α - and β -Si₃N₄ were used as starting materials. JIANG et al. also profitted from the EU “TMR–Large Scale Facilities” program at Bayreuth and synthesized monolithic γ -Si₃N₄-samples, starting from a mixture of α - and β -Si₃N₄ powders [125]. TANAKA et al. employed high-purity β -Si₃N₄ powder with 0.5 wt% oxygen, in order to produce pure samples suitable for hardness measurements [120]. SOIGNARD et al. performed another DAC-synthesis experiment, starting from α -Si₃N₄ in a N₂ pressure medium. The aim was to determine the bulk modulus of the synthesized γ -Si₃N₄ [124]. The presented EDXD-patterns however reveal a poor crystallinity of the product. Peaks due to unreacted α -Si₃N₄ starting material and an unidentified phase were observed. The latter is possibly associated with the admixture of amorphous boron (*a*-B) powder to act as an absorbent for the laser heating. The pattern presented for the fully released DAC (0 GPa) is questionable to be that of γ -Si₃N₄ at all [82]. A first shock-wave synthesis series of γ -Si₃N₄ was reported in the early year 2000 by a Japanese group around SEKINE [87], who also holds the patent on the method [144] and, at the time of writing, published at least four further articles, mostly concerned with the dynamic phase transition and the properties of γ -Si₃N₄ [122, 102, 145, 146]. An overview on these HP/HT syntheses is provided in Table 3.4 on the next page

Table 3.4: Overview of γ -Si₃N₄ syntheses reported in literature

Ref.	starting materials	sample environment	sample size [mm]	pressure generation	p_{max} [GPa]	T_{max} [°C]	t_{hold}^T [s]	result
[85]	Si, α -, β -, a -Si ₃ N ₄	N ₂	—	DAC	15	1800	60–600	γ -Si ₃ N ₄
[124]	α -Si ₃ N ₄ / a -B	N ₂	—	DAC	20	15–20 W*	n. n.	nano- γ -Si ₃ N ₄ and α -Si ₃ N ₄
[125]	α -Si ₃ N ₄ / β -Si ₃ N ₄	Pt	2.0 × 3.5	MAP 18 M?	17 ± 0.5	1800	3600	γ -Si ₃ N ₄ and unid. phase
[120]	β -Si ₃ N ₄	Pt	1.0 × 1.8	MAP	18	1800	1200	γ -Si ₃ N ₄
[87]	β -Si ₃ N ₄	Pt, Cu	n. n.	Flyer Plate	12–115	1–3 · 10 ³	10 ^{–7} –10 ^{–6}	β -Si ₃ N ₄ and nano- γ -Si ₃ N ₄
[122]	β -Si ₃ N ₄ (sintered bodies)	—	10 × 12 × 3	Flyer Plate	28–150	187	10 ^{–7} –10 ^{–6}	β - and γ -Si ₃ N ₄ (not recovered)

* Nd:YAG laser

3.4 Sample Characterisation

The phase content of the MAP-derived samples was checked by micro-Raman spectroscopy and micro-XRD (Diffractometer A). $\gamma\text{-Si}_3\text{N}_4$ was found to be the major constituent phase of those samples from SN01–SN10, which had been subjected to a pressure of ≥ 13 GPa. Traces of the encapsulation metal was the only additional crystalline phase, except for SN01, where an additional single reflection of unknown origin was found at 2.77 Å. SN11 contained solely $\beta\text{-Si}_3\text{N}_4$ while SN12 showed the presence of $\beta\text{-Si}_3\text{N}_4$, Pt, and stishovite, which must have formed due to a major oxygen contamination.

The samples were further characterized with (HR-)SEM and TEM, powder-XRD (Diffractometers B and C) at room temperature and elevated temperature, micro-Raman and IR-spectroscopy. Microhardness testing was possible in the case of the dense $\beta\text{-Si}_3\text{N}_4$ (SN11) whereas the precursor-derived $\gamma\text{-Si}_3\text{N}_4$ specimen were too porous (see e.g. Fig. 3.5 on page 93). Thus the hardness of $\gamma\text{-Si}_3\text{N}_4$ was first studied via nanoindentation on SN03 and SN08, reported in [82], along with a DAC compression study to obtain the bulk modulus B_0 . These investigations will be treated in Section 3.8 on page 134.

Electron beam methods: SEM, TEM and EPMA

Grain size and morphology Closer investigation of the samples with SEM revealed a striking difference between the grain morphology of the β - and $\gamma\text{-Si}_3\text{N}_4$: Figure 3.6 depicts a SEM image of the as-received surface of sample SN04. The typical columnar morphology of the $\beta\text{-Si}_3\text{N}_4$ grains is apparent. The grains are $5\text{--}6$ µm in length and have aspect ratios between 7 and 14. In contrast, the crystallites shown in Fig. 3.5 are of an octahedral shape typical for spinel compounds with their surfaces consisting of $\{111\}$ planes. The image shows a nest of extraordinarily large (up to 18 µm) crystals which was found in the center of sample SN08. Smaller grains with sizes between 1 and 2 µm were found in other locations of the sample, especially close to the surface. Very small grains with sizes starting from 100 nm were ubiquitous, but appeared to be more common closer to the former Pt/Si₃N₄ interface. Figure 3.5 also reveals that there are voids between individual grains and no intergranular matrix phase is apparent. The cohesion between the grains is weak, which leads to a predominant if

not exclusive *intergranular* fracture mode and the macroscopic brittleness of the samples: As shown in Fig. 3.3 on page 88, small pieces could be easily broken off. This is the reason, why micro-hardness measurements were not attempted except for SN11, which showed a much better structural integrity but consisted solely of the β -phase.

In contrast to the strictly octahedral $\gamma\text{-Si}_3\text{N}_4$ crystallites observed e. g. in SN08, the samples which had been synthesized without double encapsulation were found to exhibit additional grain morphologies. As shown in Figure 3.7 on page 94, especially platelets with hexagon base planes are apparent at the former $\gamma\text{-Si}_3\text{N}_4/\text{Pt}$ interface. This indicates changes in the growth rates of individual crystal planes and may be attributed to impurities like oxygen.

Oxygen impurities Whilst EDX analysis showed no other elements than to Si and N in the central region of SN08, oxygen was present in detectable amounts in the single encapsulated samples. In addition to the above mentioned difference between the grain morphologies of SN08 and SN02, the presence of a second phase may be also attributed to oxygen: In Figure 3.6 it can be clearly seen that the $\beta\text{-Si}_3\text{N}_4$ grains are embedded within a porous material that appears to be partially transparent to the 20 kV electron beam. Similar but less obvious features can be seen in Figure 3.7, e. g. above the right part of the databar. Because the material was detected by neither XRD nor Raman spectroscopy, it can be considered as an amorphous SiO_2 or SiN_xO_y phase. The material might be identical to the amorphous layers surrounding every $\gamma\text{-Si}_3\text{N}_4$ grain found by HR-TEM (Fig. 3.8).

The occurrence of an oxidic glassy phase is well known from liquid-phase sintered $\beta\text{-Si}_3\text{N}_4$ ceramics, where it provides the necessary cohesion between the grains. This suggested a possible way of obtaining dense ceramic bodies of $\gamma\text{-Si}_3\text{N}_4$ and was indeed realized in experiment SN13, where a starting material containing sintering additives was employed (Sect. 3.7 on page 119). The total oxygen content of the untreated product of experiment SN06 was found to be as high as 12 wt.%, using combustion elemental analysis. After the sample had been etched with hydrofluoric acid until the obtained solution was free of silicon, a value of 4 wt.% oxygen was determined.* This suggests that the oxygen occurs

*Mikroanalytisches Labor Pascher, Remagen-Bandorf, Germany

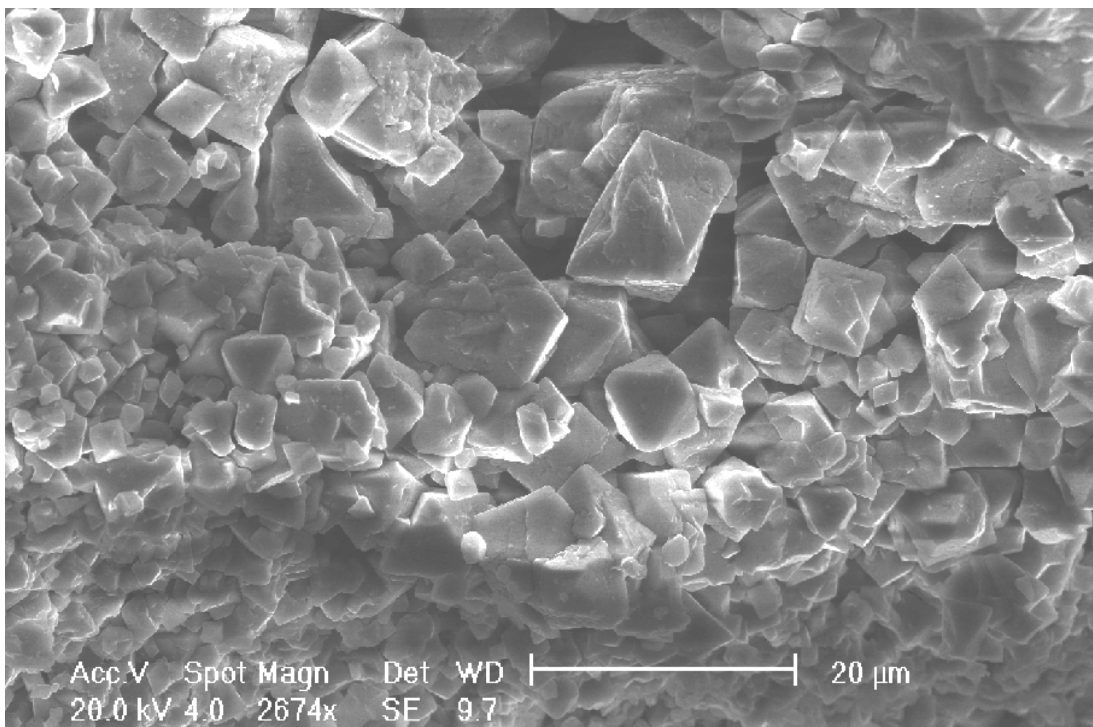


Figure 3.5: Microstructure of a fractured surface of SN02 ($p_{\text{maxi}} = 15 \text{ GPa}$), showing $\gamma\text{-Si}_3\text{N}_4$ crystallites with octahedral morphology, typical for spinel compounds.

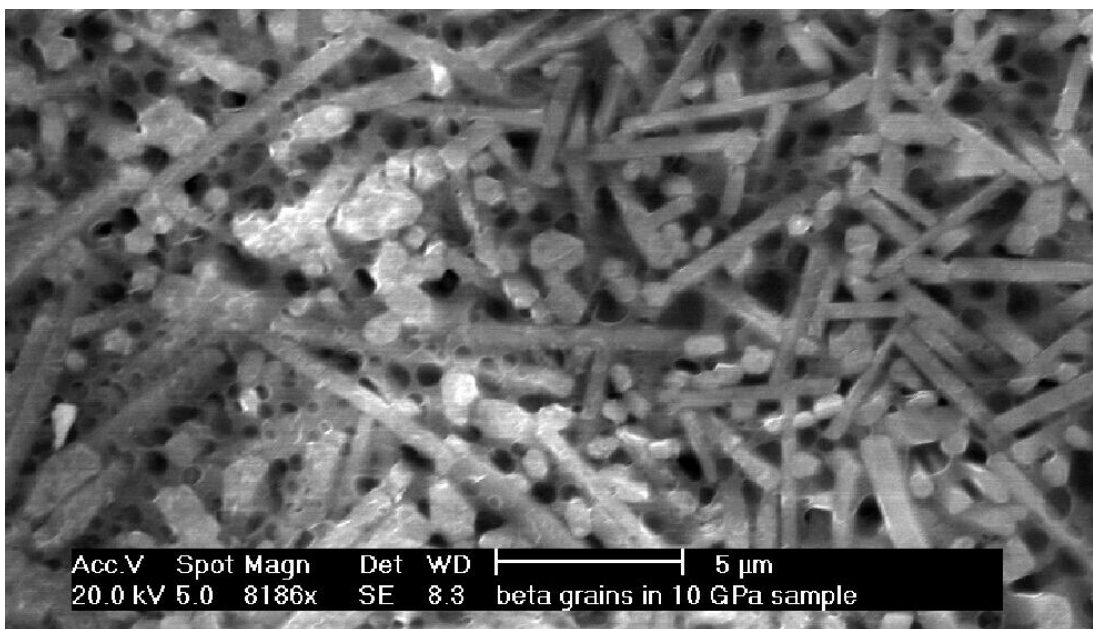


Figure 3.6: SEM image of the surface of SN04 ($p_{\text{maxi}} = 10 \text{ GPa}$) as obtained by removing the Pt-foil: $\beta\text{-Si}_3\text{N}_4$ crystallites with the typical columnar shape, embedded in a porous matrix.

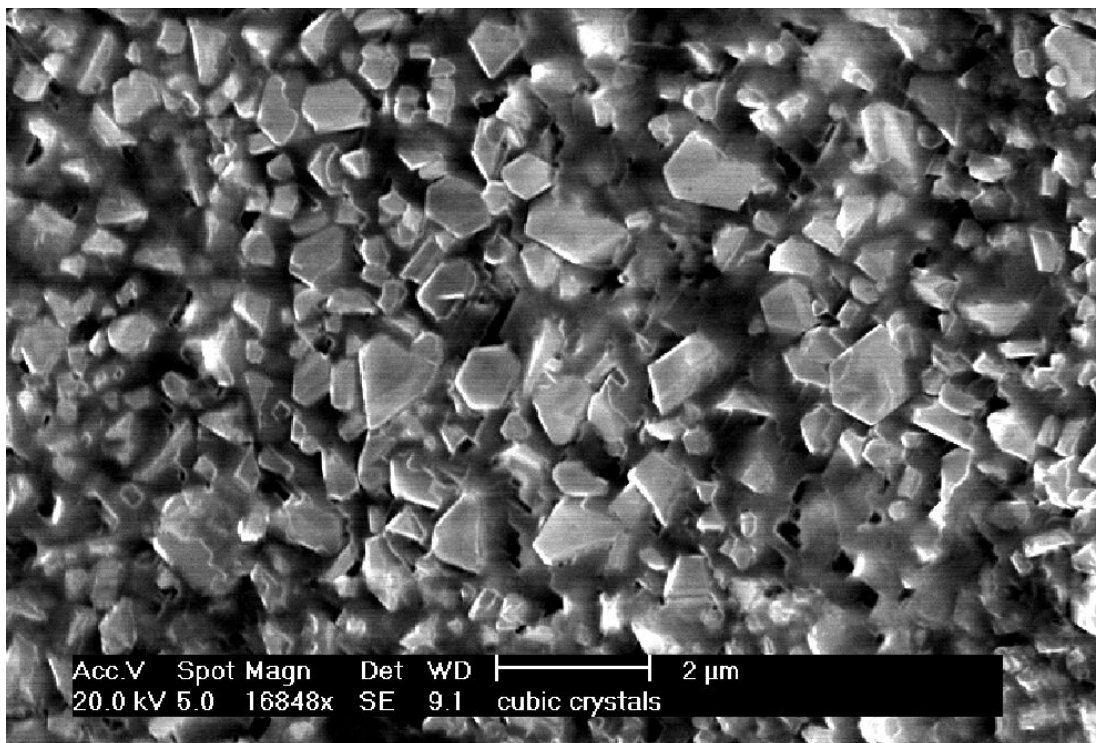


Figure 3.7: SEM image of the surface directly below the Pt-foil of $\gamma\text{-Si}_3\text{N}_4$ -sample SN02, showing crystallites with either (distorted) octahedral shape or platelets with hexagon base planes.

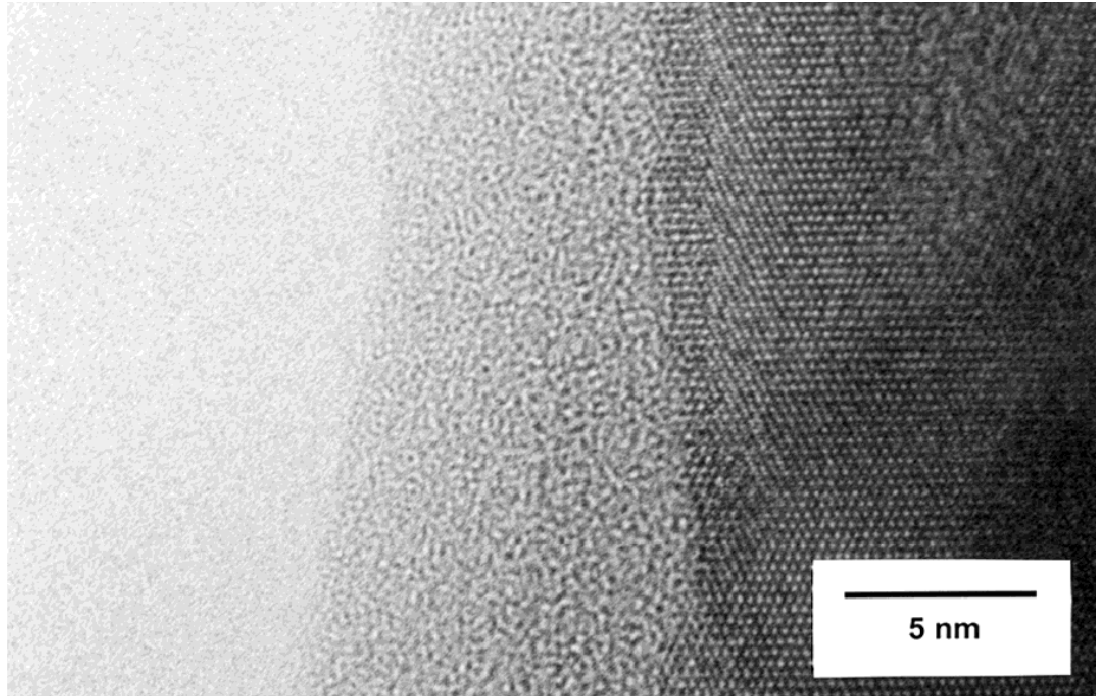


Figure 3.8: HR-TEM bright-field image (zone [114]) of sample SN06, showing an amorphous oxide layer of about 10 nm thickness on a $\gamma\text{-Si}_3\text{N}_4$ crystal surface.

Sample	Crystalline phase	Analytical method	Element percentage [wt.%]			
			Si	N	O	H
—	Si_3N_4	calcd.	60.06	39.94	—	—
—	$\text{Si}_2\text{N}_3\text{H}$	calcd.	56.62	42.36	—	1.02
—	$\text{Si}_2\text{N}_3\text{H}$	combust.	56.6	42.3	—	0.9 ± 0.1
—	$a\text{-Si}_3\text{N}_4$	combust.	<i>n.d.</i>	<i>n.d.</i>	3.2	~ 1.07
SN06	$\gamma\text{-Si}_3\text{N}_4$	EPMA ^[a]	50	30	13.9	<i>n.d.</i>
SN08	$\gamma\text{-Si}_3\text{N}_4$	EPMA ^[b]	56.5	43.9	3.6	<i>n.d.</i>
SN11	$\beta\text{-Si}_3\text{N}_4$	EDX	60.3	39.7	$\sim 0^{[c]}$	<i>n.d.</i>

^[a] average of 20 and ^[b] of 15 quantitative point measurements ^[c] below detection limit

Table 3.5: Elemental composition of Si_3N_4 starting materials and reaction products

primarily within the amorphous phase and at the surface of the crystals. The elemental compositions were also determined by EPMA. The results for samples SN06 and SN08 are shown in Table 3.5, along with the calculated composition for Si_3N_4 and the analytical results for $a\text{-Si}_2\text{N}_3\text{H}$ from the Bayer company and $a\text{-Si}_3\text{N}_4$ — the two starting materials. An average oxygen content of 14 wt.% was detected for a polished surface of SN06, which is in good agreement with the combustion elemental analysis. Sample SN08, which was produced using molybdenum and boron nitride outer capsules, contained less than 4 wt.% oxygen. The element mappings of both samples are shown in Figures 3.9 and 3.10 on the following page, respectively. While nitrogen and silicon are homogeneously distributed in both samples, SN06 shows spatial variations of the oxygen content, whereas in SN08, only small amounts of O are present directly at the interface between the $\gamma\text{-Si}_3\text{N}_4$ and the innermost (Pt) capsule. Accordingly, the high oxygen content in samples SN02–SN06 can be explained by a diffusion of oxygen from the surrounding oxide materials through the platinum into the precursor during heating. Therefore, experiments SN07, SN09, and SN10 were also carried out with multilayer encapsulation.

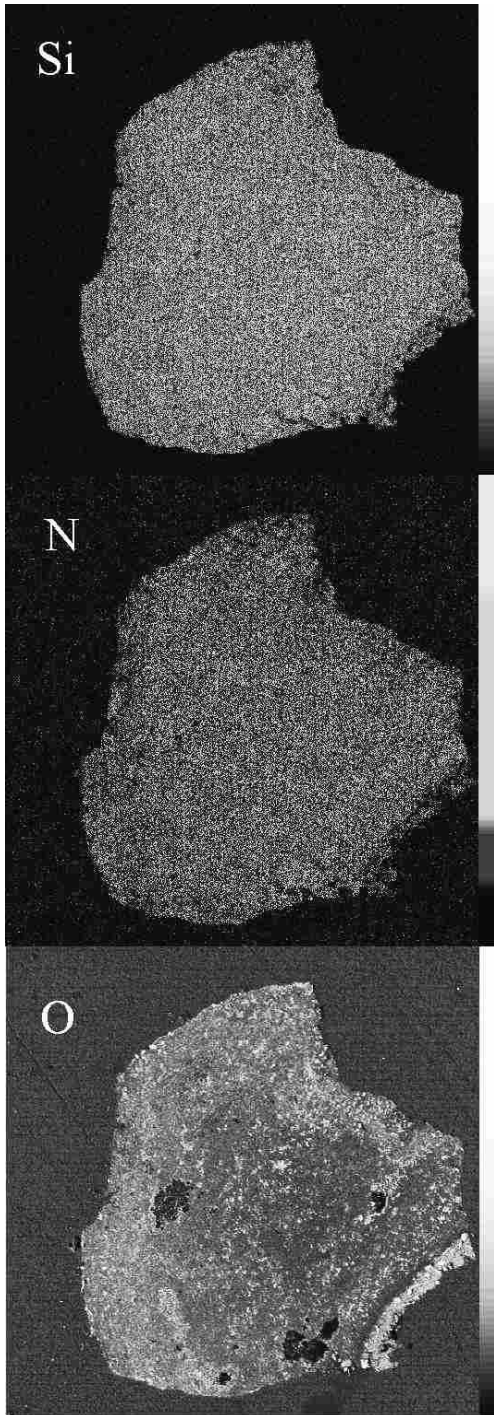


Figure 3.9: EPMA mappings of the polished sample surface of SN06: Si and N are equally distributed, while the oxygen concentration is high and shows considerable variations.

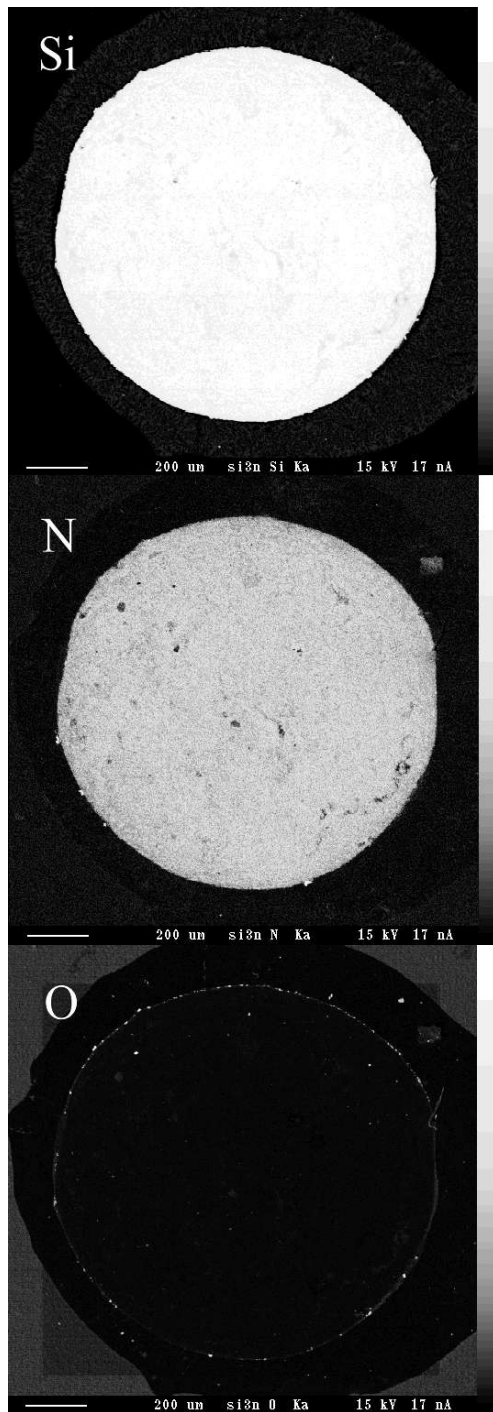
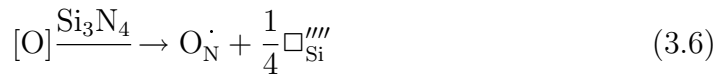


Figure 3.10: EPMA mappings of the polished sample surface of SN08: Traces of oxygen appear only at the interface between $\gamma\text{-Si}_3\text{N}_4$ and Pt-capsule, suggesting an inward diffusion of O during the heating of the experiment. The dark spots in the N-mapping are mainly caused by variations in surface topology

Since $\gamma\text{-Si}_3\text{N}_4$ was synthesized by direct nitridation of semiconductor-grade silicon in a pure nitrogen medium [85], it can be certainly considered to exist without any oxygen contamination at all. The experimental results presented above however indicate that $\gamma\text{-Si}_3\text{N}_4$ is able to incorporate variable amounts of oxygen into its crystal lattice. A similar behavior has been found for $\alpha\text{-Si}_3\text{N}_4$ the stability of which and its relationship to oxygen content has been discussed controversially in the past [147]. In order to conserve charge neutrality, the incorporation of oxygen can be counterbalanced by Si vacancies resulting in a defectuous spinel structure. Using the KRÖGER-VINK notation, this can be expressed as follows:



Here, O_N denotes an oxygen atom on a nitrogen site, \square_{Si} a silicon vacancy. A positive and a negative elementary charge with respect to the undisturbed lattice is indicated by \cdot and $',$ respectively. Oxygen in $\gamma\text{-Si}_3\text{N}_4$ appears to be complementary to the case of the Al–O–N system, where insertion of *nitrogen* into $\gamma\text{-Al}_2\text{O}_3$ gives rise to a spineloid oxynitride phase (“ $\gamma\text{-alon}$ ”), containing between 11 and 18 at.% N [148]. The issue of oxygen content in the crystal lattice of $\gamma\text{-Si}_3\text{N}_4$ will be further considered in the section on its Rietveld structure analysis, 3.5 on page 102.

A theoretical study of possible high pressure phases in the system Si–O–N was provided by KROLL [149, 150, 151]. He found that in the spinel structure, vacant Si^{tet} sites are energetically favoured over the respective octahedral vacancies and would attract clusters of oxygen atoms in their vicinity. A simplified explanation for this might be found in terms of the intrinsic charge imbalance of the 4-4 nitride spinels explained on page 78: If treated purely ionic, upon removal of Si, the absolute charge at the Si^{tet} site changes sign from $+1e$ to $-3e$. The Si^{oct} site is already negatively charged by $-1/2e$ and removal of the Si atom leads to a still higher negative charge accumulation of $-4.5e$. Clustering of oxygen atoms around the Si vacancies reduces the local charge imbalances and is to be expected in both cases, but $\square_{\text{Si}}^{tet}\text{-O}_\text{N}$ configurations are closer to electrostatic neutrality. Krolls calculations furthermore suggest that a spineloid Si-O-N phase with up to 20 wt.% may exist at 15 GPa and 2000 °C but would decompose into $\gamma\text{-Si}_3\text{N}_4$ and stishovite at higher pressures. Indications for a miscibility gap were also

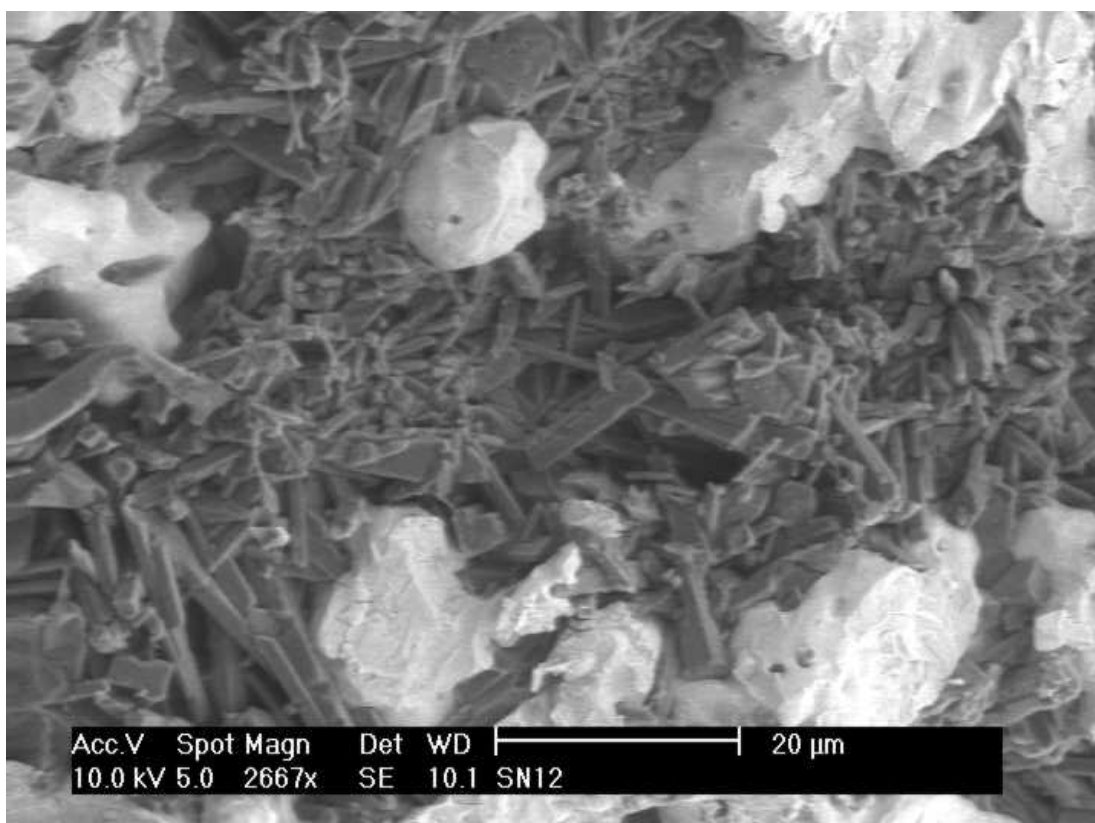


Figure 3.11: SEM image of SN12, showing elongated stishovite crystallites and lumps of infiltrated platinum

found for pressures *below* 10 GPa. In analogy to γ -Al₂O₃ and α -Al₂O₃, KROLL proposed spinel and corundum as possible high-pressure structures for silicon oxynitride, Si₂N₂O. However, he found that cation disorder—i.e. entropy—will exert a significant influence on the stability of these phases. This limits their predictability on the basis of theoretical calculations and leaves lots of interesting questions to be answered by future experiments. As already mentioned, SN12 was the sample to contain the most oxygen. In fact, SEM investigation of the smaller top part of the two pieces into which the sample was broken, revealed large columnar crystals of up to 15 μm length that contained only Si and O in an atomic ratio of 1:2 (Figure 3.11). Successive powder-XRD proved the SiO₂ phase to be stishovite. Other reflexions in the diffractogram were assigned to Pt and β -Si₃N₄, showing that some nitrogen-rich material remained in the depth of the larger sample part. These results will be further discussed in Section 3.6.1 on page 116.

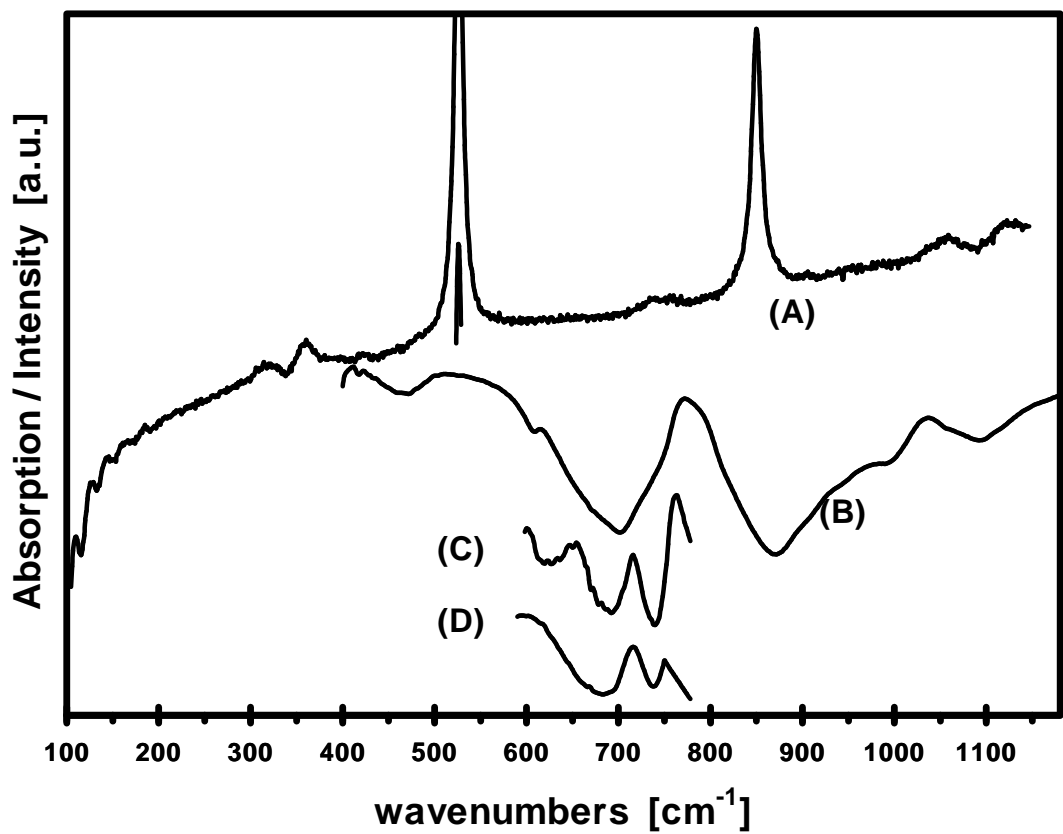


Figure 3.12: Raman spectrum (A) and near-IR transmission spectrum (B) of γ -Si₃N₄ sample SN06. (C), (D): Splitting of the IR absorption band, observed in more recent spectrum of SN06 and the shock-synthesized FP-SN1 sample, respectively.

Raman and Infrared Spectroscopy

In Figure 3.12, both Raman and infrared (IR) spectra of γ -Si₃N₄ are shown. They were obtained at ambient conditions from sample SN06 using the **Raman A** spectrometer and the ‘simple’ KBr method (recall Sect. 2.3 on page 63). Two strong and sharp Raman signals at 526 and 850 cm⁻¹ in trace (A) are characteristic for γ -Si₃N₄. They are in agreement to spectra from previous DAC syntheses [85] and have been used to identify the spinel phase in several multianvil experiments. The Raman spectrum presented in [85] appears to be blue-shifted about ~ 26 cm⁻¹ with respect to the present data, because it was recorded at 5.2 GPa in the DAC. The line positions of the weaker Raman signals are 317(w), 360(m), 736(vw), 1055(m) and 1120(m), as obtained by least square profile fitting.

Also the infrared spectrum of γ -Si₃N₄ (trace (B), sample SN06) is dominated by two strong bands with absorption maxima at 702 and 872 cm⁻¹. The spectrum differs significantly to those of the α - and β -Si₃N₄ polymorphs but is not unlike the IR-spectrum of MgAl₂O₄ spinel with similar broad bands around 660 and 775 cm⁻¹ [152]. The positions of observed absorptions of trace (B) are given as follows: 465(w), 610(m), 702(s), 872(vs) and 1094(m), a shoulder at 990 cm⁻¹ probably indicates Si–O units. A second spectrum of SN06, obtained after \sim 2 years storage in air, and also the shock-synthesized FP-SN1 sample (cf. Sect. 3.9 on page 189) showed a splitting of the 702 cm⁻¹ band into two absorption maxima at \sim 680 and 735 cm⁻¹. The corresponding portions of these spectra are shown in trace (C) and (D), respectively.

According to the factor group analysis of FANG et al. [153], only the 610 and 702 IR absorption band can be assigned to calculated optical modes, so that both Raman and IR spectra contain more signals than expected (4 IR-active and 5 Raman active modes). The assignment of individual vibrational modes will be discussed on the basis of all data available for the spinel nitrides γ -Si₃N₄, γ -Ge₃N₄ and γ -Sn₃N₄ in Section 3.8.9 on page 182.

3.5 Rietveld Structure Analysis of γ -Si₃N₄

A detailed structural characterization of γ -Si₃N₄ was carried out by Dr. G. Miehe at the Fachgebiet Strukturforschung at our Materials Science Department in Darmstadt and appeared in a joint publication in 2000 [154]:* An X-ray powder diffractogram (Fig. 3.13) was taken from sample SN08 in transmission geometry on **Diffractometer C**. The calibration was performed externally with an NIST-NBS640B Si standard. The FWHM of the γ -Si₃N₄ lines is even smaller than that of the Si standard. Crystallographical data of γ -Si₃N₄ and further details and results of the data acquisition and structure refinement are shown in Table 3.6 on page 102, along with the data published by JIANG et al. ([125], recall 3.3.4 on page 89) for comparison .

The Rietveld refinement was carried out with the program LHPM-7 [155] and the presented results are based on scattering curves of neutral atoms. Since the

*My grateful acknowledgement for the very fruitful and long lasting cooperation that existed prior to and went far beyond the structure elucidation of γ -Si₃N₄

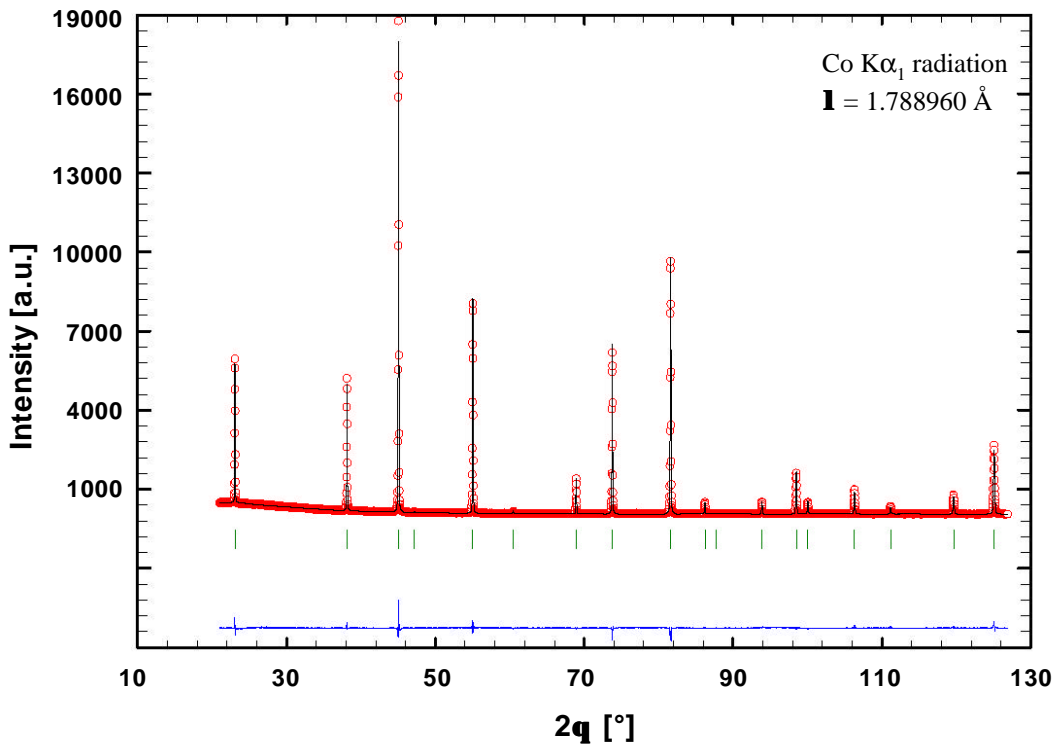


Figure 3.13: XRD powder pattern and difference plot of γ -Si₃N₄ (sample SN08)

scattering curves for other valence states influence mainly the low- 2θ reflections, the use of Si⁴⁺ and N³⁻ scattering curves leads to nearly the same result. With the three sites of the spinel structure (Si^{tet}, Si^{oct}, and N) fully occupied and \mathbf{u} , the thermal parameters, the profile parameters, and the global parameters given free for refinement, a Bragg R-value of 5.42% ($\chi^2 = 1.4$) is obtained. Atom coordinates and selected bond lengths and angles are given in Tables 3.7 and 3.8 on page 103, respectively.

Lattice Parameter The values for the lattice parameter a_0 from the present refinement and that of Jiang et al. show a difference of only 0.004 Å. Given the fact that they were obtained from two differently synthesized γ -Si₃N₄ samples (recall 3.3.4 on page 89) using different X-ray sources and diffraction systems, this gives a realistic value for the magnitude of the actual experimental error of the structure determination. This error will be higher than the estimated standard deviation given in parentheses behind the value which was derived from

Quantity	Symbol	Unit	SN08	Ref. [125]
Space group	-		<i>Fd</i> $\bar{3}m$ (No. 227)	
Lattice param.	a_0	[\AA]	7.7381(2)	7.7339(1)
Anion param.	\mathbf{u}		0.25968(1)	0.2583(1)
Volume	V_0	[\AA^3]	463.34	462.59
No. of atoms	Z		8	8
Molecular weight	M	[g mol ⁻¹]	140.28	140.28
Density	$\varrho_{calc.}$	[g cm ⁻³]	4.02	3.75
Radiation	λ	[\AA]	1.78896 ($\text{Co}_{K\alpha_1}$)	1.52161(1) (synchrotr.)
Profile range	$2\theta_{min}; 2\theta_{max}$	[$^\circ$]	21 ; 127	8.6 ; 100
	$d_{max}; d_{min}$	[\AA]	4.9 ; 1.0	10.1 ; 1.0
Step size	$\Delta(2\theta)$	[$^\circ$]	0.020	0.005
Varied parameters				
Profile function			pseudo-Voigt	Voigt
R values	R	[%]	3.70	4.12
	R_w	[%]	4.96	6.43
	R_{Bragg}	[%]	5.42	0.84
	χ^2	[-]	1.42	n.n.

Table 3.6: Crystallographic data for γ -Si₃N₄ (Rietveld refinement) from this work and Ref. [125]

statistics of the recorded diffraction pattern. By releasing the site occupancy factors (sof's) for the silicon positions (the sof of N was left fixed to define the intensity scale) JIANG et al. obtained a high concentration of silicon vacancies $\square_{Si}^{tet} \approx 15\%$ and $\square_{Si}^{oct} \approx 9\%$ in the course of their structure refinement. In order to conserve charge neutrality within such a cation deficient spinel, nitrogen can be substituted by oxygen according to Equation 3.6 on page 97. The corre-

3.5 Rietveld Structure Analysis of γ -Si₃N₄

Atom	Position	Site symmetry	fractional coordinates			$100 \times U_{iso}$ [Å ²]
			<i>x</i>	<i>y</i>	<i>z</i>	
Si ^{tet}	8a	$\bar{4}3m$	1/8	1/8	1/8	1.27
Si ^{oct}	16d	. $\bar{3}m$	1/2	1/2	1/2	1.00
N	32e	.3m	0.25968(1)	0.25968(1)	0.25968(1)	2.08

Table 3.7: Atomic coordinates of γ -Si₃N₄, as determined by Rietveld refinement of powder-XRD data from SN08

Dist./angle	Multiplicity	SN08	JIANG et al. [88]	difference [%]
a_0	-	7.7381(2) Å	7.7339(1) Å	-0.05
\mathbf{u}	-	0.25968(1)	0.2583(1)	-0.5
$d(\text{Si}^{tet}\text{-N})$	4	1.8051(2) Å	1.7849(16) Å	-1.13
$d(\text{Si}^{oct}\text{-N})$	6	1.8626(1) Å	1.8718(9) Å	+0.5
$d(\text{Si}^{oct}\text{-Si}^{oct})$	$(= a_0/\sqrt{8})$	2.7358(1) Å	2.7343(1) Å	-0.05
$\angle (\text{Si}^{oct}\text{-N-Si}^{oct})$		94.51°	92.85°	-1.8
$\angle (\text{Si}^{tet}\text{-N-Si}^{oct})$		122.00°	123.27°	+1.0

Table 3.8: Selected bond lengths and bond angles of γ -Si₃N₄, calculated from \mathbf{u} of the SN08 sample in Table 3.6

sponding oxygen content would be 15.8 wt.% O. Interestingly, this corresponds exactly to the stoichiometry Si₂N₂O. Releasing the sofs in the refinement based on *our* data leads to an even higher apparent cation deficiency of $\square_{Si}^{tet} \approx 24\%$ and $\square_{Si}^{oct} \approx 28\%$, corresponding to 25.8 wt.% O. At the same time R is decreased to 2.04% ($\chi^2 = 1.12$) and \mathbf{u} acquires a value of 0.2586. Such a high oxygen content can be definitely excluded, because according to combustion chemical analysis, SN08 contained only 3.6 wt.% O (cf. Section 3.4 on page 92). In the publication of JIANG et al., the oxygen content of the sample is said to be below 1 at.%, as ‘determined’ by secondary ion mass spectrometry (SIMS). Quantitative analysis with this method is to be calibrated against standards, because the ion current of the analyzed element depends on matrix effects of the sample. No standard

was mentioned in the respective publication. It would have first to be established for a novel material like γ -Si₃N₄. Nevertheless, as the lattice parameters a_0 and \mathbf{u} coincide quite well, the oxygen contents may well lie in the same range. Normalizing the silicon occupancies to a weak scatterer like N can easily lead to artefacts. High vacancy or oxygen concentrations resulting from this can therefore be not considered to display physical reality.

The lattice constant of γ -Si₃N₄ is small compared to the ‘classical’ spinel compound MgAl₂O₄ (8.0831 Å) and the silicon-containing high-pressure mineral ring-woodite, γ -Mg₂SiO₄ (a_0 = 8.113 Å).^{*} Somewhat closer are the spinelloid γ -Al₂O₃ and an aluminum oxynitride compound with a claimed stoichiometry Al₃O₃N, with lattice parameters of 7.924 and 7.91 Å respectively. This suggests a possible miscibility between γ -Si₃N₄ and these phases which was finally demonstrated by the successful HP/HT-synthesis of *spinel*-Si_{3-x}Al_xO_xN_{4-x}, discussed in Chapter 4 of this work.

Anion parameter and Bond Lengths Both values for the anion parameters \mathbf{u} are in fairly good agreement with one another and indicate a significant deviation $\delta = 0.008\text{--}0.01$ from the ideal *fcc* arrangement of the anion sublattice. Especially the slightly higher value of our refinement corresponds well with the theoretical result $\mathbf{u} = 0.2594$ that was calculated by MO et al. [86]. In terms of bond lengths, this means that the Si^{oct}–N distance is \sim 1.86 Å which, on the one hand, is to be compared to the Si^{tet}–N distances 1.73 and 1.70 Å found in β -Si₃N₄ and on the other hand to $d(\text{Si}^{\text{oct}}\text{--O})$ as found e.g. in stishovite (1.807 Å). The bond lengths obtained from ab initio total energy calculations by MO and coworkers were $d_{\text{calc}}(\text{Si}^{\text{tet}}\text{--N}) = 1.831$ Å and $d_{\text{calc}}(\text{Si}^{\text{oct}}\text{--N}) = 1.885$ Å [86, 156], respectively. As already noted in Section 1.4.2 on page 10, an increase in coordination number is always accompanied by an increase of atomic distance, and the smaller Si^{oct}–O distance can be attributed to the smaller ionic radius of O²⁻ compared to N³⁻. The SiN₆ unit has been known from molecular compounds, where Si–N bond lengths range between 1.70–1.84 Å (see e.g. References in [101]). KÖLLISCH and SCHNICK found a significantly larger Si^{oct}–N distance of 2.1 Å in Ce₁₅Si₁₆O₆N₃₂, for which they claim to be the first inorganic solid to contain the SiN₆ unit [101].

^{*}<http://webmineral.com/data/Ringwoodite.shtml>

Because the coordination of nitrogen has also changed from a trigonal planar NSi₃ to a tetrahedral NSi₄ arrangement, $d(\text{Si}^{tet}-\text{N})$ is as well significantly increased with respect to the low pressure phases. The NSi₄ unit, like SiN₆, is found very rarely among solid state structures. In fact, the nitridosilicates BaYbSi₄N₇ and SrYbSi₄N₇, discovered in 1996 by HUPPERTZ and SCHNICK [157], are so far the only other structures possessing this feature. Here, $d(\text{Si}^{tet}-\text{N}^{tet})$ is significantly longer and ranges from 1.87 to 1.96 Å. As these compounds were synthesized at ambient pressure and are less condensed, they can be said to resemble a kind of ‘relaxed’ NSi₄ environment. The difference to the respective bond length in γ -Si₃N₄ sheds light on the high volumetric constriction in this nitride spinel.

3.5.1 Structural Comparison I:^{*}

Anion Parameter in Nitride and Oxide Spinel

Figure 3.14 visualizes the variation of the anionic position parameter \mathbf{u} within the homologous series of the group 14 spinel nitrides, γ -C₃N₄, γ -Si₃N₄, γ -Ge₃N₄ and γ -Sn₃N₄, along with those of selected oxide spinels for comparison. Abscissa and ordinate are fully correlated by a geometrical function, which corresponds to the dotted curve [104]:

$$\mathbf{u}^{3m} = \frac{\frac{1}{4}R^2 - \frac{2}{3} + \sqrt{\frac{11}{48}R^2 - \frac{1}{18}}}{2R^2 - 2} \quad \text{where} \quad R = \frac{d^{oct}}{d^{tet}} \quad (3.7)$$

The spinels provided for comparison were either chosen, because they are *also binary* compounds (Fe₃O₄, Fe₃S₄), or — as γ -Si₃N₄ — are spinels comprised of cations from the *third-row* of the periodic table, i.e. Mg and Al. Furthermore, the magnesium silicate spinels contain SiO₄ and SiO₆ units to be compared with the corresponding nitride polyhedra in γ -Si₃N₄. It is apparent, that the anion positions for all nitride spinels are situated comparatively close, indicating a similar packing of the nitrogen atoms. The data points **a**, **b** and **c** of γ -Si₃N₄ correspond to the results of the Rietveld refinements by SCHWARZ et al. [154] and Jiang et al. [125] treated in the previous section, and that of the γ -Si₃N₄-‘ceramic’ (SN13) from Section 3.7.3, respectively. Their variation indicates either

^{*}for a re-worked version of the following two sections see [158]

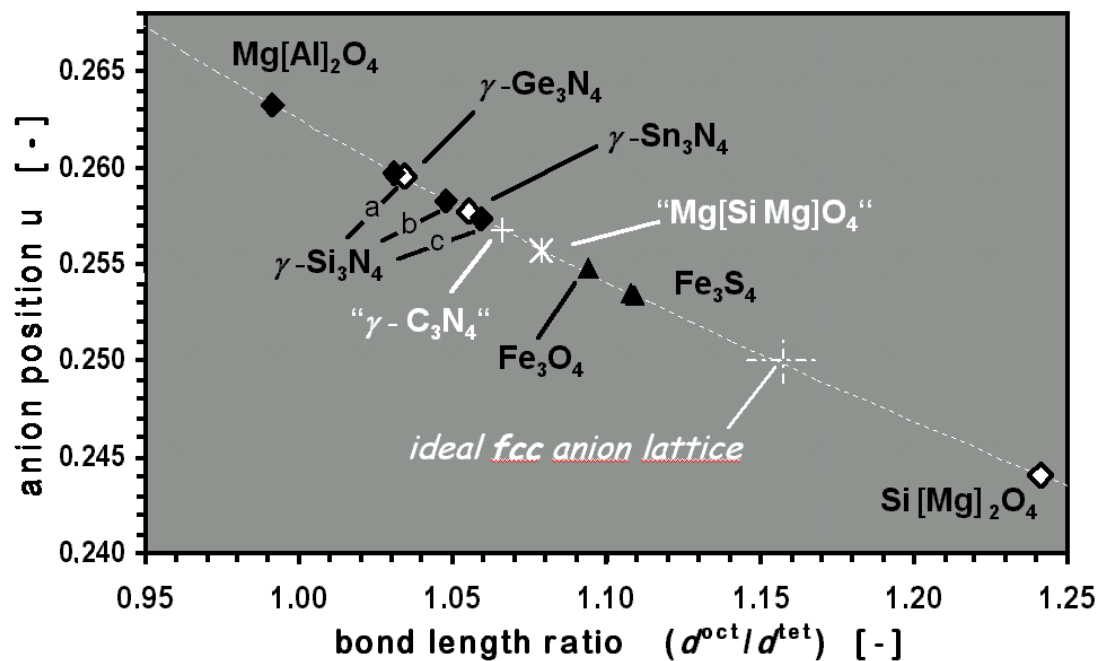


Figure 3.14: Structural comparison between group 14 element spinel nitrides and other prominent spinels: Anion positional parameter u versus the ratio of the octahedral and tetrahedral bond lengths.*

the data scatter due to experimental uncertainties — or, what is more likely and has been discussed in the respective sections — is at least biased by an increasing oxygen content in the direction of $\mathbf{a} < \mathbf{b} < \mathbf{c}$. If we assume \mathbf{a} to be the closest estimate to pure $\gamma\text{-Si}_3\text{N}_4$ and take the hypothetical $\gamma\text{-C}_3\text{N}_4^\dagger$ out of the consideration, u appears to decrease with increasing atomic number and the gap between $\gamma\text{-Si}_3\text{N}_4$ and $\gamma\text{-Ge}_3\text{N}_4$ on the one side and $\gamma\text{-Sn}_3\text{N}_4$ on the other, would resemble the jump between the semiconducting/metallic borderline that runs between Ge and Sn in the periodic table. Also the pressure of formation for the respective spinels shows a pronounced jump from Ge to Sn: While $\gamma\text{-Ge}_3\text{N}_4$ requires a pressure similar to that of $\gamma\text{-Si}_3\text{N}_4$ [89], $\gamma\text{-Sn}_3\text{N}_4$ forms already at ambient [90]. All spinel nitrides possess smaller bond length ratios than would be required for an ideal *fcc* anion arrangement. This is a consequence of the occupation of both types of sites by the *same element*, where the relative size increase from fourfold

*Data sources: MgAl_2O_4 , Fe_3O_4 [21]; $\gamma\text{-Si}_3\text{N}_4$: **a** sample SN08 Sect. 3.5, **b** [125], **c** $\gamma\text{-Si}_3\text{N}_4$ -‘ceramic’ SN13 Sect. 3.7.3; $\gamma\text{-Ge}_3\text{N}_4$ [89]; $\gamma\text{-Sn}_3\text{N}_4$ [159]; $\gamma\text{-C}_3\text{N}_4$ [86]; Fe_3S_4 [160] Mg_2SiO_4 [161]

[†]spinel-type C_3N_4 , see next section

to sixfold coordination is not very large. The spinels based on iron show the same trend. However, while Fe_3O_4 and Fe_3S_4 do still contain the two *different cation species* Fe^{2+} and Fe^{3+} that allow for a larger size difference, the group 14 elements are further restricted to the *same formal charge* +4. Spinel, $MgAl_2O_4$, and the magnesium silicate ringwoodite $Si[Mg]_2O_4$ were added to exemplify extreme cases. They obey either the rule of local charge neutralization of Verwey and Heilmann or Pauling's first rule which postulates a preference of high-valence cations like Si^{+4} towards small interstices and small coordination numbers (see [104] and references therein). Hence, in spite of the slightly larger ionic radius of Mg^{2+} , it preferentially occupies tetrahedral sites within spinel, resulting in local charge neutrality and a bond length ratio that is slightly below unity. In the normal ringwoodite, the cation size differences are so large that the conditions are reverted. The smaller, but higher charged Si occupies tetrahedral sites and the large Mg appears to suit best to octahedral interstices. In both compounds, cation disorder is observed, however not to the extend of fully inverse spinels, i.e. the u given for inverse ringwoodite $Mg[Si,Mg]_2O_4$ is a result of a theoretical calculation [161].

3.5.2 Structural Comparison II:

Group 14 Spinel Nitrides and Group 13 Rocksalt Nitrides

As already introduced in Section 3.2 at the beginning of this chapter, comparison between the high and low pressure polymorphs of the homologous series of the group 13 and 14 element nitrides will provide insights into the general features of a close packed ionic-covalent bond arrangement of nitrogen atoms and its variation upon insertion of different cation species. While the anion parameter u and lattice constant a_0 provide useful measures for a structural comparison between *individual spinel-type structures*, other characteristic features must be used, where comparisons between *substances with different structure types* are to be drawn. In Figure 3.15 on page 110, the average atomic volume $\langle \Omega \rangle$, plotted against the bond lengths is used to present structural data of the group 13 and 14 nitrides, along with that of the two most important oxides within this system, Al_2O_3 and SiO_2 ^{*}. $\langle \Omega \rangle$ provides a direct measure for the absolute packing density

^{*}low-quartz modification

and is simply derived by division of the unit cell volume via the number of contained atoms. The axis direction of the $\langle \Omega \rangle$ -values is chosen so that the ordering of the Element-Nitrogen compounds corresponds with that of the periodic table. The stepped lines represent hypothetical ‘*ionic bond lengths*’ calculated from the Shannon effective ionic radii [162] of **E** and **N** within the respective coordination. The *y*-coordinate of the steps was chosen arbitrarily. The vertical black lines corresponds to $1.5r(N^{3-})^{tet}$ the ion radius of four-coordinate nitrogen and was drawn to discuss phase stability from atomic packing considerations. The radius of octahedrally coordinated nitrogen N^{oct} , corresponding to the conditions within the rocksalt nitrides, was not available from [162].

The Group 14 Element Nitrides

For the diagram of the spinel nitrides, the same data as shown in the previous Figure 3.14 on page 106 was chosen. The additional values for γ -Sn₃N₄ were calculated by applying the only available anion parameter which was provided by SHEMKUNAS et al. [159] and is based on neutron diffraction data, to the X-ray-derived lattice constant from the original work of SCOTTI and coworkers [90]. Each two horizontally aligned data points correspond to the tetrahedral and octahedral bond lengths $d^{tet} = d(E^{tet}-N)$ and $d^{oct} = d(E^{oct}-N)$, respectively.

The Metastable Spinel Nitrides For the three metastable spinel nitrides γ -Si₃N₄, γ -Ge₃N₄ and γ -Sn₃N₄ the gap between d^{tet} and d^{oct} appears to be constant: Their structural data can be fitted by two parallel lines, showing the systematic increase in cation size with atomic number within the same coordination environment. The calculated ionic bond lengths (the white lines) are larger than those found experimentally. In the case of γ -Si₃N₄ and γ -Ge₃N₄, the actually observed d^{tet} happens to coincide with the calculated *octahedral* length, whereas for γ -Sn₃N₄, the dotted line runs between d^{tet} and d^{oct} . This coincides with a partial covalent bonding for all three solids with a higher polarity in the case of the heavier element tin.

The low pressure modifications β -Si₃N₄ and β -Ge₃N₄ (phenacite structure) also have two non-equivalent bonds. However, because of the all-tetrahedral cation coordination, the difference between the respective bond lengths is much smaller

and these solids hence appear as a narrow pair of black triangles.

The volume change of the $\beta \rightarrow \gamma$ transition for Si and Ge appears to be similar, while that between the silicon oxide phases quartz and stishovite is much larger. Stishovite is also more dense than γ - Si_3N_4 which is a result of sole presence of Si^{oct} -O bonds and the shorter bond length. The heavier element 14 oxides, from GeO_2 to PbO_2 are also known to crystallize in the rutile structure [162], but were omitted here.

The Instable Spinel Nitrides The calculated bond lengths and atomic volume of the hypothetical “ γ - C_3N_4 ” deviate significantly from the two trend lines that connect the heavier group 14 nitride spinels. They are also markedly shorter than the ionic radii sums, represented by the white lines. This is indicative for a stronger covalent interaction. The existence of “ γ - C_3N_4 ” is however sheer speculation. Not enough that no crystal structure determination of *any* carbon nitride, neither a graphitic (= low pressure) nor a phenacite-type (e.g. β - C_3N_4), has ever been presented [14], the spinel γ - C_3N_4 would also contain carbon atoms in an energetically extremely unfavorable sixfold coordination. This problem has been recently addressed in a further theoretical study by KROLL [163]: While the energy difference between the spinel and the willemite II modifications of Si_3N_4 and Ge_3N_4 are -0.39 and -0.31 eV per formula unit (f.u.), respectively, the transformation γ - $\text{C}_3\text{N}_4 \rightarrow w_{II}$ - C_3N_4 would release as much as 7.19 eV/f.u. of energy. The C^{oct} -environment may possibly exist at very extreme pressures, but it can be doubted to pertain if the substance is quenched to ambient. The theoretical calculations of MO et al. predict that the zero-pressure density of γ - C_3N_4 would be the same as diamond but its bulk modulus would be notably lower ($B_0 = 369$ versus 442 GPa) [86]. This manifests the paradox of this compound: Compressibility scales with atomic volume and diamond is known to have one of the smallest.

On the low density side of the $\langle \Omega \rangle$ -scale of the homologous series, there would be a ‘ γ - Pb_3N_4 ’. Attempts to prepare this compound so far failed* and in addition to the fact that there is already no other stable tin nitride known but γ - Sn_3N_4 and no binary Pb–N compound but lead(II)azide $\text{Pb}(\text{N}_3)_2$ has been reported [48],

*A. Zerr, private communication

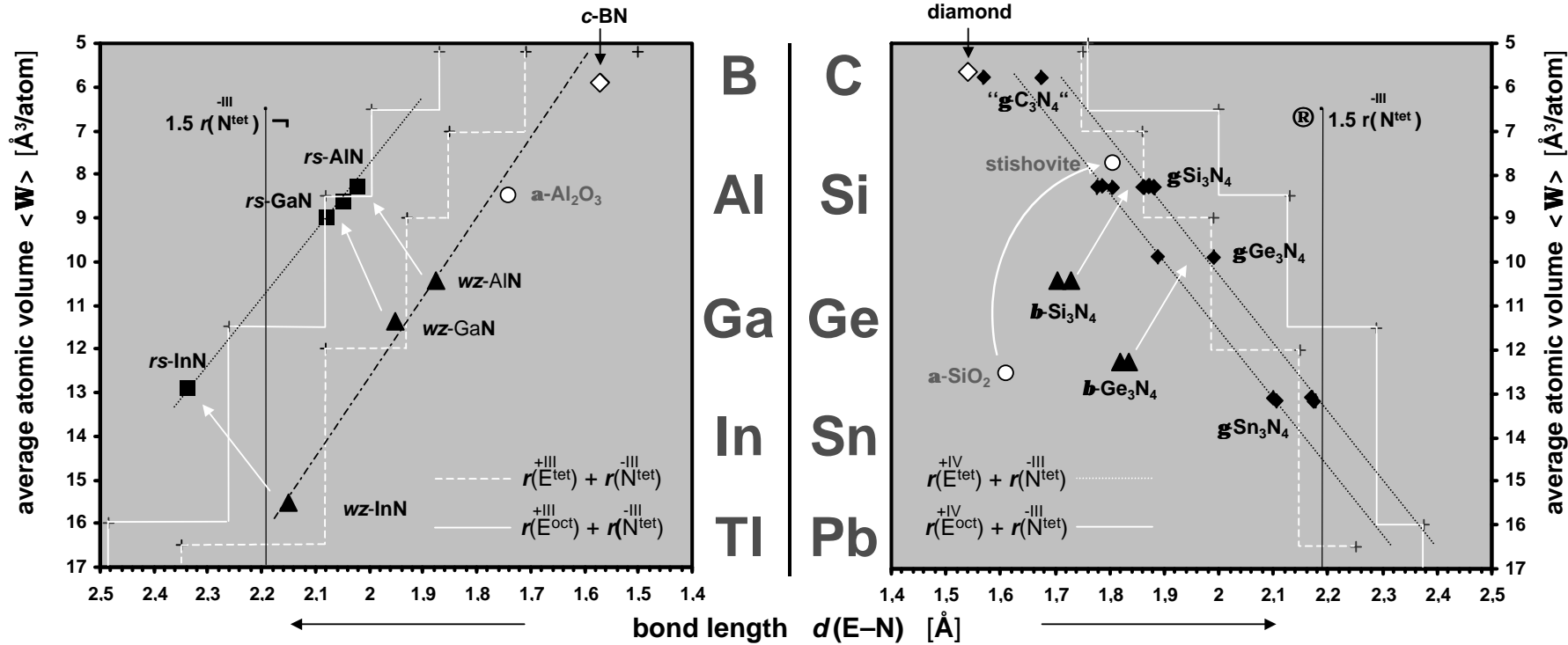


Figure 3.15: Structural comparison between the nitrides and some important oxides of group 13 and 14 elements. Values given for ambient conditions. Source data: See Fig. 3.14; PDF cards No. 65-675 (diamond), 35-1365 (c-BN); 33-1162 (quartz), 33-160 (β - Si_3N_4), 45-1374 (stishovite); β - Ge_3N_4 : [164]; rocksalt nitrides: [129, 138, 165]

some features from the diagram indicate that $\gamma\text{-Pb}_3\text{N}_4$ will possibly never exist: Soon below Sn, the trend lines for both d^{tet} and d^{oct} of the nitride spinels cross the vertical black line that is defined by $1.5r(\text{N}^{3-})$. According to geometrical considerations of a simple hard-sphere model, occupation of octahedral interstices will be favoured above $d(\text{E-X}) \geq 1.414r(\text{X})$, where X denotes the larger anion.* In other words, the size of the Pb(IV) cation would be too large to fit the tetrahedral site within of a nitride spinel — or formulated complementary: The nitrogen ions are too small to inhabit the lead ions. This latter statement corresponds to the feature in the low right corner of the graph. Here, the extrapolated trend lines exceed the effective radii sums for Pb(IV) in both coordinations. These were calculated from the Shannon effective radii. For comparison, the smallest Pb–N distance in $\alpha\text{-Pb}(\text{N}_3)_2$, where Pb exists in a distorted tetrahedral environment, is 2.58 Å, followed by distances at 2.61, 2.64 and 2.67 Å [166].

Mixed Spinel Nitrides in the System Si–Ge–N Preparation of solid solutions between $\gamma\text{-Si}_3\text{N}_4$ and $\gamma\text{-Ge}_3\text{N}_4$ was attempted by SOIGNARD et al. [118]. However, HP/HT treatment of mixtures of $\beta\text{-Si}_3\text{N}_4$ and $\beta\text{-Ge}_3\text{N}_4$ in a diamond anvil cell revealed evidence for spinels with discrete composition $(\text{Si}_x\text{Ge}_{1-x})_3\text{N}_4$ with $x \approx 0.6$, rather than a continuous miscibility range. Additionally, a preference of the Ge atom for the ‘smaller’ *tetrahedral* site was found. Subsequent theoretical investigations by the same group showed that $\gamma\text{-Si}_3\text{N}_4$ and $\gamma\text{-Ge}_3\text{N}_4$ are indeed separated by two miscibility gaps and the *normal* spinel $\text{Ge}^{\text{tet}}[\text{Si}]^{\text{oct}}_2\text{N}_4$ is the only stable intermediate phase [115]. The authors argue that an octahedral coordination of Ge would afford $\text{Si}^{\text{tet}}\text{-N-Ge}^{\text{oct}}$ units with a noticeable asymmetric bonding around the N atoms: $d(\text{Ge}^{\text{oct}}\text{-N}) = 1.98$ Å and $d(\text{Si}^{\text{tet}}\text{-N}) = 1.76$ Å versus $d(\text{Ge}^{\text{tet}}\text{-N}) = 1.85$ Å and $d(\text{Si}^{\text{oct}}\text{-N}) = 1.88$ Å. These large discrepancies in bond length are not compatible with the high degree of covalent bonding. Hence, the inverse spinel $\text{Si}^{\text{tet}}[\text{Ge},\text{Si}]^{\text{oct}}\text{N}_4$ as well as the composition SiGe_2N_4 are predicted to be unstable, which is in contrast to theoretical results of CHING et al. published in 2001 [117].

*see e.g. [21] pp. 126–128

3.6 Phase Relationships of γ -Si₃N₄

From the HP/HT experiments in the system Si–N–(O), previously described in Section 3.3 and summarized in the Tables 3.1 on page 72 and 3.4 on page 90, a first p – T diagram of Si₃N₄ can be constructed. Accompanied by theoretical calculations, the experimental results elucidate the phase relationships of the different silicon nitride phases. They also allow deductions on *different* types of phase transformations from an initial phase into γ -Si₃N₄ and their kinetics.

3.6.1 A First p–T Diagram of Si₃N₄

For the construction of a first ‘phase diagram’ of silicon nitride at high pressures (Fig. 3.16), the experiments SN01–SN10 turned out to be of particular importance. While solely β -Si₃N₄ was found in experiment SN04, which had been subjected to a pressure of 10 GPa, the other samples from SN02 to SN10 solely contained γ -Si₃N₄, in spite of comparatively short heating times ($t_{raise}^T + t_{hold}^T \approx 20$ to 30 min). Thus, the observed crystalline phases must have formed *directly* from the amorphous state. It appears reasonable that the precursors keep their amorphous nature at high pressures until they rapidly transform into the equilibrium Si₃N₄ phase of the given pressure upon heating.

By synthesizing β -Si₃N₄ directly from silicon and N₂ in a laser-heated DAC,[85] Zerr showed it to be the thermodynamically stable phase at 5 GPa. According to Exp. SN01–SN10, the stability field of β -Si₃N₄ reaches certainly up to 10 GPa and the experimental borderline to the stability field of γ -Si₃N₄ lies at or below 13 GPa (Exp. SN10). This is also the equilibrium pressure $p_{eq}(\beta\text{-Si}_3\text{N}_4 \rightleftharpoons \gamma\text{-Si}_3\text{N}_4)$ which was obtained by a common tangent construction of the energy-versus-volume (E – V) curves of first principles calculations at 0 K ([85], see Fig. 3.17 on page 115). These results seem to leave no space for the second hexagonal polymorph α -Si₃N₄ at high pressures. Its density and bulk modulus are both smaller than those of β -Si₃N₄* and KRUGER et al. concluded it to be metastable to at least 48 GPa [140]. As previously mentioned, an indication for the lattice instability of both, α - and β -Si₃N₄, evidenced by a soft-mode behavior of their low-frequency Raman modes upon compression to 40

*assorted theoretical and experimental values from various sources are presented e.g. in [156] and [82]

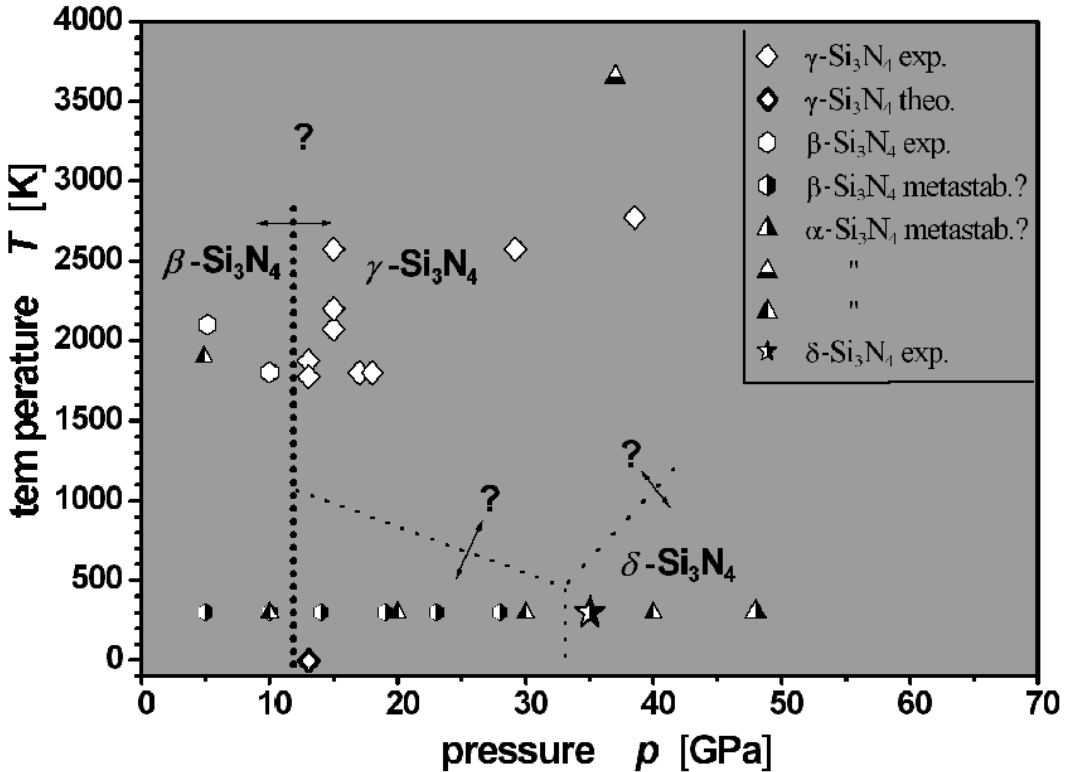


Figure 3.16: Various results of HP/HT-experiments and theoretical calculations, assembled into a preliminary p-T-diagram of Si_3N_4 . The dotted lines indicate possible phase boundaries. References are given in the text.

and 28 GPa, respectively, was found by ZERR and SERGIOU [142]. Nevertheless SUEMATSU et al. found that $\alpha\text{-Si}_3\text{N}_4$ survives a HP/HT treatment at 4.9 GPa and 1600 °C and that the longly known $\alpha \rightarrow \beta$ transformation requires not only heat but also the presence of a liquid phase to occur [167]. New indications for a positive, but small difference in the enthalpy of formation with respect to $\beta\text{-Si}_3\text{N}_4$ were published by LIANG et al. in 1999 [168].

Despite the resilience of $\alpha\text{-Si}_3\text{N}_4$, experiments SN04 and SN10 definitely prove $\beta\text{-Si}_3\text{N}_4$ and $c\text{-Si}_3\text{N}_4$ to be the thermodynamically stable phases at high pressures and the coincidence in the 13 GPa-value between experiment and theory could suggest their common phase boundary to be almost straight over a temperature range from 0–2200 K. This is indicated by the vertical dotted line in Fig. 3.16. However, a series of DAC-experiments by ZERR and SERGIOU at room tem-

perature [142] demonstrates that the case is not so simple: As also shown in Fig. 3.16, no other phase than β -Si₃N₄ could be identified up to a pressure of at least 31.7 GPa. At 35 GPa, instead of transforming into γ -Si₃N₄, a *fourth* polymorph of Si₃N₄ occurred, which was named δ -Si₃N₄ [169]. The corresponding phase transformation was evidenced by a significant reduction of the number of raman modes with respect to β -Si₃N₄ (at 38.2 GPa only 10 bands remain) and the appearance of new lines in the diffraction pattern. The crystal structure of δ -Si₃N₄ could not be unambiguously determined from the EDXD patterns, but of the three possible solutions presented, a distorted *w_{II}*-Si₃N₄-structure with a tetragonal symmetry appears to be the best candidate. The two remaining structure candidates are tetragonal and orthorhombic.

Interestingly, a theoretical [164] as well as a subsequent experimental [170] compression study of β -Ge₃N₄ suggests the formation of a metastable “ δ -Ge₃N₄” with fourfold Ge coordination and *trigonal* symmetry: The calculations predict that compressing β -Ge₃N₄ to 38 GPa leads to reduction of symmetry according to the sequence $P6_3/m \rightarrow P\bar{6} \rightarrow P3$. The experiment confirmed a collapse of the β -Ge₃N₄ structure between 22 and 25 GPa [170]. Upon further pressurization above 45 GPa at ambient temperature, β -Ge₃N₄ as well as α -Ge₃N₄, and any trace assignable to δ -Ge₃N₄ was found to become amorphous. In future, it will be extremely interesting to see if α - and β -Si₃N₄ can also be amorphized at extreme pressures.

According to the experimentally determined ‘transition pressures’ to the metastable δ -forms (35 GPa for β -Si₃N₄ and 22–25 GPa for β -Ge₃N₄), the nitride of silicon seems to be more stable against compression than that of its heavier Ge homologue—in agreement to the “*Druck–Homologenregel*” (e.g. described by KLEBER and WILKE [19]). In contrary, the wurtzite \rightarrow rocksalt transformation of the group 13 nitrides AlN and GaN follows an abnormal trend: While *wz*-AlN \rightarrow *rs*-AlN is reported to occur between 15 [129] and 20 GPa [138], both theoretical and experimental results give values between 31 and 50 GPa for GaN [137]. CORKILL, RUBIO and COHEN pointed out that this discrepancy would be most likely caused by the repulsive potential of the *d* core electrons of gallium [134].

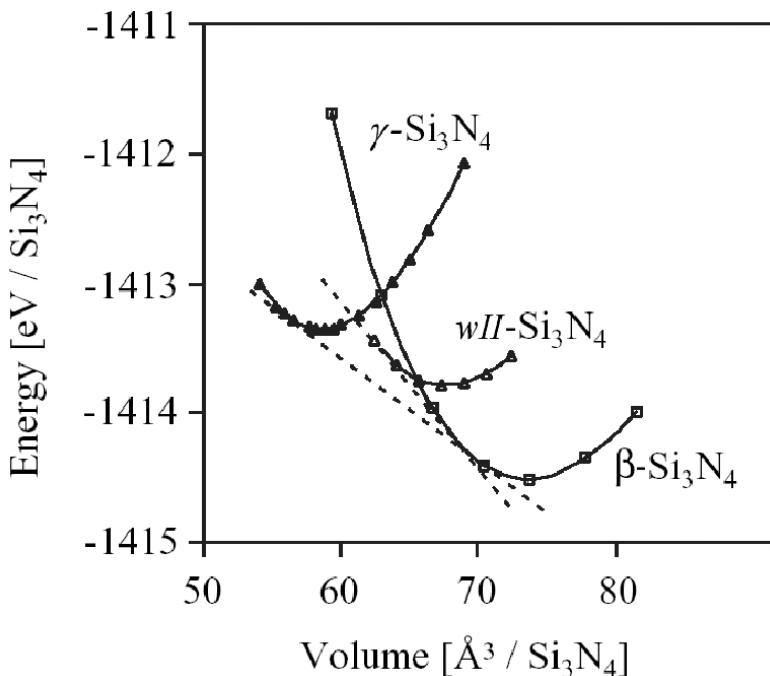


Figure 3.17: Calculated energy-versus-volume data for three Si_3N_4 structures (at zero temperature) from [85]. The solid lines are fits of the Murnaghan equation of state. The dashed lines are common tangents the slope of which gives the equilibrium pressure p_{eq} between the respective phases.

The willemite II polymorph of Si_3N_4 , $w_{II}\text{-Si}_3\text{N}_4$, has already been introduced in Section 3.1 on page 69. The question why it did not occur instead of $\gamma\text{-Si}_3\text{N}_4$ in the first place could also be answered from the above mentioned E – V -curves shown in Fig. 3.17. It can be seen that the specific volume of $\gamma\text{-Si}_3\text{N}_4$ is smaller than that of $w_{II}\text{-Si}_3\text{N}_4$. This was to be expected from the higher \bar{N}_c of the γ phase. According to LE CHATELIER's principle, $\gamma\text{-Si}_3\text{N}_4$ will be the stable phase at high pressures. The calculated equilibrium pressures $p_{eq}(\beta\text{-Si}_3\text{N}_4 \rightleftharpoons \gamma\text{-Si}_3\text{N}_4)$ and $p_{eq}(\beta\text{-Si}_3\text{N}_4 \rightleftharpoons w_{II}\text{-Si}_3\text{N}_4)$, which are identical to the slopes of common tangents between the E – V curves [171], are 13 GPa and 20 GPa, respectively. Thus, on compression, $\beta\text{-Si}_3\text{N}_4$ will directly transform to $\gamma\text{-Si}_3\text{N}_4$ and not to the hypothetical $w_{II}\text{-Si}_3\text{N}_4$ with lower density. However, as will be discussed later, there are several indications that the $\beta \rightarrow \gamma$ transformation requires cleavage and re-formation of Si–N bonds and will therefore be hampered at low temperatures. Upon pressurization, the low-pressure polymorph persists until a phase transformation with a low kinetic barrier occurs, usually forming a metastable intermediate phase. This is what has been observed in the formation of $\delta\text{-Si}_3\text{N}_4$. For the oxide SiO_2 , a whole wealth of these transformations, including pressure induced amorphisation, are known. Interestingly, at about the same time $\delta\text{-Si}_3\text{N}_4$

was found, HAINES et al. were able to show that pressurization of α -quartz to 45 GPa under close-to-hydrostatic conditions at room temperature yielded a novel crystalline form of silica with monoclinic symmetry and octahedral coordination of silicon [20]. Indications for a structural relationship between the δ -phase and willemite II are again given by the E – V curves in Figure 3.17. The slope of the β -Si₃N₄-curve, where it intersects with that of w_{II} -Si₃N₄ is \sim 40 GPa. This is only slightly above the observed phase transition to δ -Si₃N₄. Moreover, the structure which could be described by a doubled unit cell of w_{II} -Si₃N₄ and, with $Z = 8$, would have a volume of 57.5 Å³. At this volume, the extrapolated E – V curve of w_{II} -Si₃N₄ happens also to have a slope equivalent to 40 GPa. Being a ‘derivative’ of w_{II} -Si₃N₄, this tetragonal polymorph would have a density smaller than that of γ -Si₃N₄ ($0.9 \times \varrho(\gamma\text{-Si}_3\text{N}_4)$ at 42.6 GPa). Therefore, it may be seen as an intermediate between β -Si₃N₄ and γ -Si₃N₄. Zerr proposed two further structure models for δ -Si₃N₄. Both would possess *higher* densities than γ -Si₃N₄ and therefore be treated as “*post-spinel*” phases [169]. The effort to elucidate the structure of δ -Si₃N₄ is complicated by the fact that it was found to be unstable at ambient pressure.*

It also remains unclear, why β -Si₃N₄ and not γ -Si₃N₄ was found in sample SN12, although it had been pressed at 13 GPa. From the presence of stishovite as an oxidic impurity phase, one would deduce that high oxygen contents shift the β to γ -phase boundary towards higher pressures. This contradicts the finding that the oxygen concentration in β -Si₃N₄ — albeit at ambient pressure — was never observed to exceed 0.6 wt.% [172], while according to the aforementioned analysis results, an oxygen concentration of 4 wt.% cannot be excluded to exist within the *bulk* of γ -Si₃N₄. According to the aforementioned calculations of Kroll [149, 150], the possible oxygen saturation in the γ -phase may be even higher.

*A. Zerr, personal communication

3.6.2 Theoretical Predictions of post-spinel Si₃N₄-phases

The discovery of γ -Si₃N₄ can be said to have happened in the drag of theoretical predictions and first principles calculations on novel materials with outstanding properties, in particular those concerning the elusive “*harder-than-diamond*” C₃N₄ phases (recall Sect. 3.1). As shown above, ab initio calculations also helped to understand the higher stability of γ -Si₃N₄ with respect to competing structure models of other possible high-pressure polymorphs. As already outlined in Sect. 3.2 on page 82, a large number of theoretical papers dealing with the properties of γ -Si₃N₄, γ -Ge₃N₄ and possible single- and mixed cation spinel-nitrides of group 4 and 14 elements, has been published since experiments unveiled spinel to be the structure type of the high-density phases of the nitrides of Si, Ge and Sn. Knowledge of the spinel structure also provides a clue for the theoreticians to predict further Si₃N₄-phases at still higher pressures: They can choose among the “*post-spinel*” structures of oxidic systems that have been documented by geologists and mineralogists as well as other solid state structures with general compositions A₃X₄ or A₂BX₄ and a larger \bar{N}_c than that of γ -Si₃N₄ ($\bar{N}_c \approx 4.57$, recall Equation 3.1 on page 76, *cation coordination* $\bar{N}_c^{cat} = 16/3 = 5.33$). Possible post spinel phases from the view of an inorganic chemist were already proposed by W. SCHNICK in 1999, in the first highlight article on the new group 14 nitride spinels [92]. His candidates were Zr₃N₄ with a distorted Eu₃O₄-type structure, Mg₃NF₃ (\simeq defect NaCl) and a so far not well characterized W₃N₄. The theoreticians P. KROLL and J. VON APPEN [173] performed a more systematic approach: By screening about 30 binary and ternary structure types that complied with above mentioned guidelines, they determined three closer candidates. K. TATSUMI et al. performed calculations on 6 possible phases, shortlisting 4 of them. The candidate structures from both publications are summarized in Table 3.9 below.

Both groups mostly chose their candidates among three-dimensional networks of MO₆ octahedra, linked by sharing their corners or edges. They agree in their preference for the CaTi₂O₄ structure type as the most likely post-spinel phase for which their calculations yielded comparable results. The energy difference ΔE between β -Si₃N₄ and γ -Si₃N₄ can be considered as a reference for the other theoretical results. The values correspond to -107 and -134 kJ/mol for Kroll and

KROLL et al. [173]				TATSUMI et al. [174]			
Structure type	space group	V_0^{calc} / V_{spinel}	ΔE [eV/at.]	Structure type	space group	V_0^{calc} / V_{spinel}	ΔE [eV/at.]
β -Si ₃ N ₄	<i>P</i> 6 ₃ / <i>m</i>	1.256	-0.16	β -Si ₃ N ₄	<i>P</i> 6 ₃ / <i>m</i>	1.26	-0.2
Ni ₃ Se ₄	<i>C</i> 2/ <i>m</i>	0.986	0.27	K ₂ NiF ₄	<i>I</i> 4/ <i>mmm</i>	1.12	1.5
CaFe ₂ O ₄	<i>Pnma</i>	0.976	0.54	SrPb ₂ O ₄	<i>Pba</i>	1.06	0.2
				(MgFe) ₂ SiO ₄	<i>Pbnm</i>	1.03	0.1
CaTi ₂ O ₄ *	<i>Cmcm</i>	0.928	0.51	CaTi ₂ O ₄ *	<i>Cmcm</i>	0.93	0.5
$p_{eq}(\gamma\text{-Si}_3\text{N}_4 \rightleftharpoons *)$ 160 GPa				210 GPa			

Table 3.9: Two sets of possible structure types for post-spinel phases of Si₃N₄ reported in literature. Values given relative to γ -Si₃N₄ at 0 GPa and 0 K.

Tatsumi respectively, i.e. the same order of magnitude. An experimental enthalpy difference of -29.2 ± 3.5 kJ/mol between γ -Si₃N₄ and β -Si₃N₄ was determined at ~ 1700 K by SEKINE and MITSUHASHI (see Section 3.8.6 on page 171). Determination of the entropy term $-TS$ of γ -Si₃N₄ will have to show, if these theoretical ΔE values represent good estimates for ΔH .

In the case of other possible structure types, Kroll seems to have taken a luckier choice: The phases that were also taken into closer consideration by Tatsumi et al. are *less* dense than γ -Si₃N₄ at zero pressure. This was at least to be expected for olivine, (Mg,Fe)₂SiO₄, because minerals of this group are actually known to be *pre-* and *not* post-spinel phases ([21], pp. 398–399). Initially, Tatsumi et al. also took CaFe₂O₄ into consideration, but then found it to be too high in energy compared to CaTi₂O₄ above 60 GPa. In both publications the CaTi₂O₄ type silicon nitride is the most dense phase and was calculated to possibly have the lowest transformation pressure. These ‘lowest’ predicted values of 160 and 200 GPa, respectively, will however pose a considerable challenge for the experimentalists. The fact that these pressures are so far from the observed p_t of the β -Si₃N₄ \rightarrow δ -Si₃N₄ transition, provides another hint that δ -Si₃N₄ is not a post-

spinel phase. From the perspective of *useful* materials, a synthesis attempt of post-spinel silicon nitride may not be worth the effort all: If the predictions of Tatsumi et al. are trustable, the energy of the CaTi_2O_4 type polymorph is almost four times as high as that of γ - Si_3N_4 , which leaves an almost negligible chance for it to be metastable. Not enough, even if quenched to ambient conditions, its properties would be paradoxically *inferior* to those of γ - Si_3N_4 : The predicted bulk modulus, B_0 , is 307 GPa which is *just as high* as that of γ - Si_3N_4 itself! The shear modulus G_0 and hence the hardness would also be low, as the electronic band gap is predicted to be only $E_{gap} = 1.3$ eV (γ - Si_3N_4 3.2–3.7 eV). This means that the bond character would be more metallic and less covalent, which, according to our considerations in Section 1.4.2, can only lead to a higher compliance in shear. The bulk moduli of *all* other candidate structures were predicted to be *even lower* than those of γ - Si_3N_4 .

3.7 The first dense γ - Si_3N_4 -based ceramic

As previously stated in Section 3.4 on page 91, the precursor-derived γ - Si_3N_4 samples from the multianvil experiments were found to be too porous and brittle for microhardness testing, thus preventing the assessment of one of the most important properties in terms of the aim of this thesis (cf. Section 1). Consequently, a method to produce dense polycrystalline samples was sought. It was found in the successful conversion of a sintered commercial silicon nitride ceramic, containing $\sim 10\%$ additives into a dense ceramic body at 15 GPa and 1800 °C, again using the multianvil technique. SEM and XRD studies showed, that the material consists of spinel crystallites that are bound with an amorphous intergranular matrix in the same manner as conventional Si_3N_4 ceramics. The sample could be characterised by Vickers, Knoop and depth-sensing hardness testing with up to 2 kg load. The hardness almost doubled with respect to the β - Si_3N_4 -based starting material: Typical hardness values of $HV_2 = 29$ GPa and $HK_2 = 22$ GPa versus 14.5 GPa and 14.6 GPa, respectively, were obtained. Further investigations using SEM/EDX, TEM/EELS and electron probe micro-analysis (EPMA) provide evidence that part of the former sintering additives Al, Mg, O (and possibly Y) were actually *incorporated* into the spinel crystal lattice.

3.7.1 Experimental Procedure

Starting material The choice for a commercial liquid phase sintered Si₃N₄ ceramic as starting material was guided by two simple considerations:

- Applying pressure and heat to an already dense sintered material, it appears almost impossible to end up with something porous.
- Sintering additives may have a similar beneficial effect on densification and strength as in conventional Si₃N₄-ceramics.

A cutting tool insert from CeramTec* was used. According to the manufacturer, the material of type SL 200 contains sintering additives and impurities in the following proportions:

- Additives: Y₂O₃ 3.1 wt.%; Al₂O₃ 2.8 wt.%
- Impurities: MgO < 0.05 wt.%; CaO < 0.2 wt.%; Fe₂O₃ < 0.1 wt.%

Figure 3.18 shows the polished and plasma-etched surface of the SL 200 ceramic. Although the SEM image was recorded in the SE and not the BSE mode, the (element) contrast between the darker β -Si₃N₄ grains and the Y-rich glass phase is very high. Quantitative phase analysis of this and a second image at $\sim 7900\times$ magnification using the program Lince[†] gave an approximate glass phase content of 16 vol.%. In contrast, if the additives were assumed to remain crystalline, their volume content would be 4.3 vol.% $((V(\text{Al}_2\text{O}_3) + V(\text{Y}_2\text{O}_3))/V_{total})$. The discrepancy may be explained by dissolved Si₃N₄ and a significantly smaller density of the glass phase as compared to the crystalline state.

Sample preparation and HP/HT-experiment As indicated in Figure 3.19 on page 122, a small cylinder ($\varnothing = 1.5$ mm, $h = 1.9$ mm) was removed from the aforementioned cutting tool insert, using a diamond core drill.[‡] The sample was wrapped in 25 μm thick Pt-foil and inserted in a standard 14M octahedral

*CeramTec AG, Innovative Ceramic Engineering, Geschäftsbereich Werkzeuge, D-73061 Ebersbach (Fils)

[†]Lince v2.31 , Sergio Luis dos Santos e Lucato, TU Darmstadt, FB Materials Science, Ceramics Group; http://www.tu-darmstadt.de/fb/ms/fg/naw/soft/l_soft.html

[‡]special thanks to Emil Aulbach from the Nonmetallic Inorganic Materials group at our Institute for performing this operation

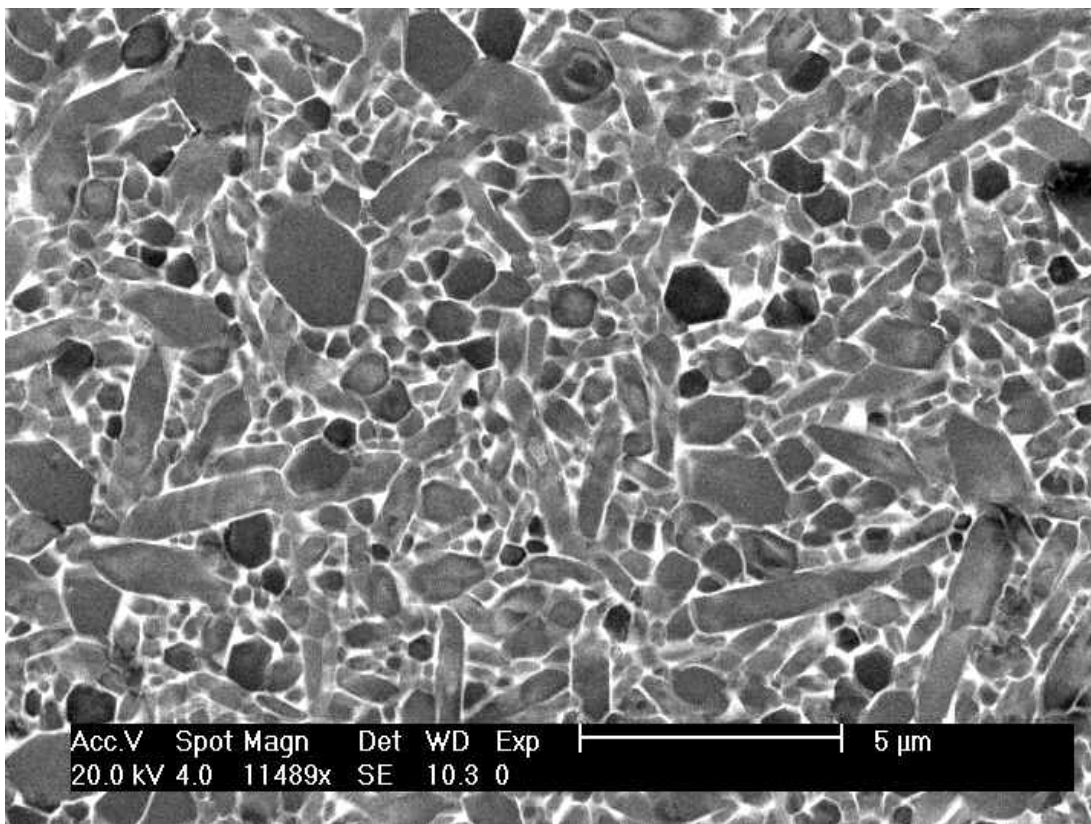


Figure 3.18: SEM SE image of the microstructure of the SL 200 silicon nitride ceramic starting material, showing typical elongated prismatic β - Si_3N_4 grains. The intergranular phase has a high contrast due to presence of the heavy element Y.

pressure cell (cf. Figure 2.3 on page 27). Applied pressure- and temperature conditions can be seen in Table 3.1 on page 72.

3.7.2 Sample recovery and preparation

The recovered pressure cell was broken and the noble metal capsule cut open with a razor blade. The sample had a darker coloration than the starting material and a granular surface (Figure 3.20). It was sonicated in methanol in order to remove part of the loose surface layer. The thus obtained suspension was left to evaporate and X-rayed on **Diffractometer B** in transmission geometry to obtain **Diffractogram 1**.

The sample was then mounted on an adhesive carbon pad and investigated by optical and scanning electron microscopy in combination with EDX for chemical

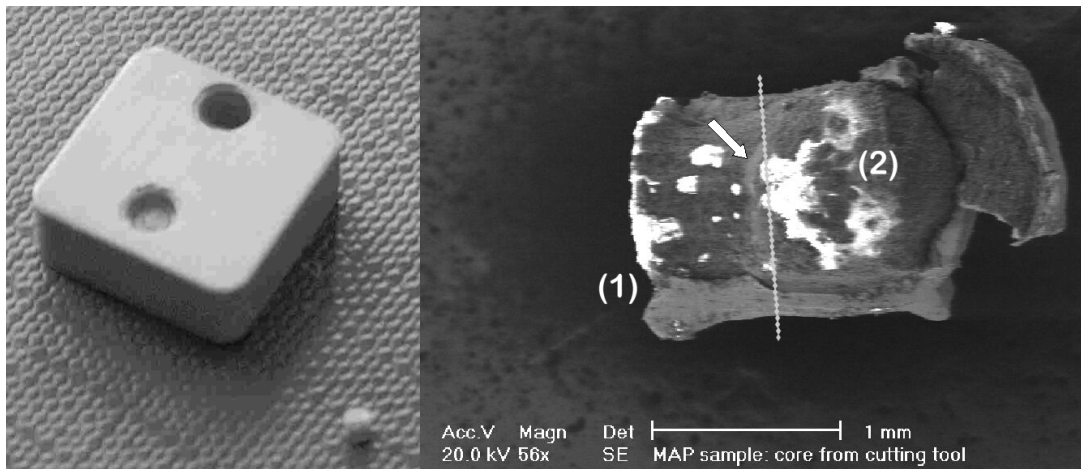


Figure 3.19: Cutting tool insert (CeramTec SL 200) and cylindrical sample cored out from the platelet

Figure 3.20: SEM image of sample SN13 with partially removed Pt-foil after HP/HT treatment. Dotted line indicates cutting plane for diamond wire saw.

characterisation . The next preparation step consisted in the entire removal of the platinum and cutting into two specimen **(1)** and **(2)**, as indicated in Figure 3.20, by means of a diamond wire saw (recall Sec. 2.1.2 on page 32). The interior of the sample was opaque with a light fawn coloration and looked much more homogeneous than the surface. Part of the freshly cut surface of specimen **(1)** was removed with a diamond-tipped portable grinder in order to obtain a small amount of powder to be further characterized by XRD and TEM. .From the thus obtained powder, an X-ray diffractogram, suitable for Rietveld structure refinement was recorded using Diffractometer B in transmission geometry (**Diffractogram 2**). Specimen **(2)** was hot-embedded into a phenolic resin with mineral filler (Struers, DuroFast) and polished for optical microscopy, hardness testing and element mapping as well as quantitative chemical analysis, using an electron microprobe . Because of the large differences in hardness between sample and embedding medium, sufficient planarity and edge retention could only be obtained after **(2)** was inserted into the bore within the cutting tool from which the starting material had once been taken from. This was also of advantage because the commercial Si₃N₄ ceramic would provide a standard for the hardness testing within the same specimen. It was found that wet-grinding with comparatively rough 1200-mesh SiC paper led to the best surface finish of **(2)**, while scratches remained upon using finer SiC paper or diamond suspensions. Vickers

and Knoop hardness indents were made into the polished surface and measured both, optically and by using the SEM. The sample was then submitted to the *Institut für Chemie anorganischer Materialien* at the Munich Technical University for instrumented hardness testing. After the hardness measurements, specimen (2) was plasma etched (recall “Experimental Techniques” on page 63) to uncover any (oxidic) secondary phases (in particular grain boundaries) and once again investigated by SEM. For all electron beam methods, the specimen was coated with a thin carbon layer to avoid charging.

3.7.3 Characterization: Results and Discussion

XRD and Rietveld structure refinement

Diffractogram 1 The loose material that had been removed by sonication of the sample in methanol exhibited a very complex powder pattern (Fig. 3.21 on the following page), indicating a reaction at the interface between Pt capsule and sample. None of the observed peaks could be attributed to either β - Si_3N_4 , c - Si_3N_4 or metallic platinum. No further attempt to identify possible reaction products such as platinum silicides or Y-containing phases was made.

Diffractogram 2 The material which had been sampled from the center of specimen (2) proved to be almost pure spinel (Fig. 3.22). The structure was refined from 15 theoretical reflections within the range shown. A total of 18 parameters were included in the final refinement. The parameters for the spinel structure included a scale factor, lattice parameter a_0 , the half-width parameter U and W, 1 isotropic temperature factor and anion position \mathbf{u} . The remaining 12 parameters were the zero-point, 9 background points, the η mixing coefficient for the chosen pseudo-Voigt profile function and its angular dependency. Only scattering factors for Si and N were used, assuming full occupation of both the anion and cation sublattice. The corresponding R values are $R_p = 4.82$, $R_{wp} = 6.39$, $R_{Bragg} = 4.96$, $R_F = 3.73$, and $\chi^2 = 0.89$. The structural parameters a_0 and \mathbf{u} and selected bond lengths are given in Table 3.10, together with those that have been previously determined from the precursor-derived material SN08.

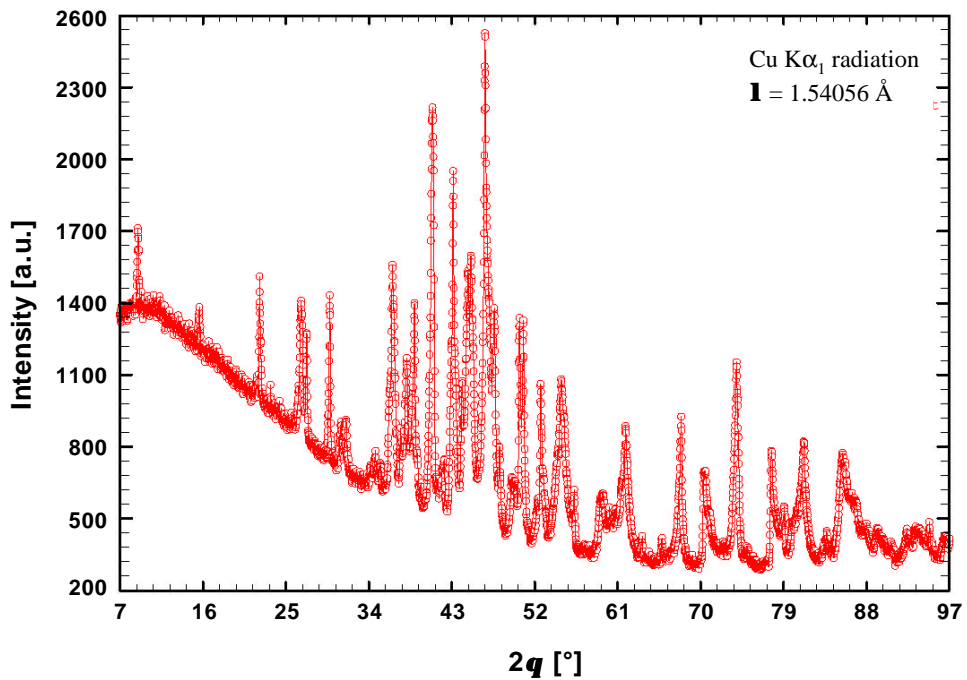


Figure 3.21: Diffractogram 1: XRD powder pattern from the former Pt/sample interface

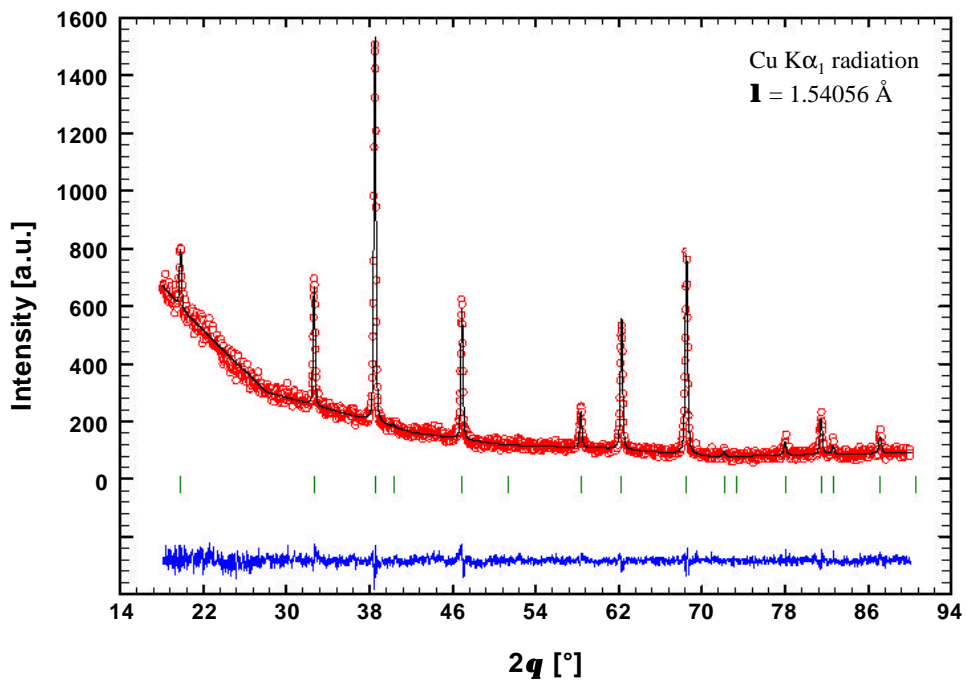


Figure 3.22: Diffractogram 2: XRD powder pattern and Rietveld difference plot of the ' γ - Si_3N_4 ceramic' SN13

Param./dist.	Multiplicity	SN08	SN13	difference [%]
a_0	-	7.7381(2) Å	7.7425(3) Å	+0.06
\mathbf{u}	-	0.25968(1)	0.2574(6)	-0.88
$d(\text{Si}^{tet}-\text{N})$	4	1.8051(2) Å	1.7754(1) Å	-1.65
$d(\text{Si}^{oct}-\text{N})$	6	1.8626(1) Å	1.8801(1) Å	+0.94
$d(\text{Si}^{oct}-\text{Si}^{oct})$	$(= a_0/\sqrt{8})$	2.7358(1) Å	2.7374(1) Å	-0.06

Table 3.10: Structure parameters and selected bond lengths obtained from powder diffraction data of the Si_3N_4 -precursor derived sample SN08 and the dense sintered γ - Si_3N_4 -based ‘ceramic’ SN13. The relative differences are given with respect to the values of the ‘pure’ γ - Si_3N_4 sample SN08 (Sect. 3.5 on page 100)

The relative differences of the primary structural parameters a_0 and \mathbf{u} of the two γ - Si_3N_4 samples are very small (below 1%). This is remarkable, given the fact that the starting material for SN08 was as pure as possible, while that for SN13 contained $\sim 10\%$ sintering additives. Accordingly, a higher difference in a_0 and \mathbf{u} would have been expected in the case of an excessive insertion of these ‘impurities’ into the spinel crystal lattice. Because of the long heating time ($t_{hold}^T = 164$ min) we can well assume that all phases were in thermodynamic equilibrium. This means either that γ - Si_3N_4 shows a low solubility for these impurity elements or that their substitutional effects on the lattice parameter are small or cancel out one another. It appears to be reasonable to give preference to the first hypothesis, because it complies with the observations in the SL 200 starting material and liquid phase sintered β - Si_3N_4 -based ceramics in general: After sintering, the elements added as additives are found within a well separated intergranular glass phase, while the β - Si_3N_4 grains remain almost free of impurities.

Microstructure

Sample Surface The SEM image depicted in Figure 3.23 shows the former Pt/sample interface, taken at the location indicated by the white arrow in Fig. 3.20 (SEM session 1). It shows a comparatively smooth and dense surface layer with cracks that has partially fallen off due to the ultrasonic treatment. Presence of the elements Si, O, C and Pt as determined by EDX-analysis, indicated a re-

action between sample and capsule material during prolonged heating. It can be clearly seen that the reaction layer is thin and suspended on a much more porous, granular material showing irregular grain morphologies. Approximate element ratios of Si:N = 53:48 and Mg:Al:O = 24:18:58 were determined (as an average of a larger area). Initially, Mg existed only as trace element in the starting material (cf. 3.7.1 on page 120). It must therefore originate from the sample encapsulation and has penetrated the Pt-foil. This hypothesis was later confirmed by elemental mapping treated in Section 3.7.3 below. Y was not detected by EDX, because the applied acceleration voltages between 15 and 25 kV were not sufficient for the excitation of its *L* line at approximately 27 kV. At other locations, the porous material consisted of well faceted crystals with octahedral habit (Fig. 3.24). Spinel frequently acquire this habit. The presence of Al, Mg and O-lines in the EDX spectrum provided a first indication for the existence of mixed (Mg)–Si–Al–O–N oxide nitride spinels. However, these results could not be seen as a proof, because the excitation volume of the electron beam is \sim 10–20 μm in diameter and reaches up to several ten μm deep into the material. It is therefore larger as the direct secondary electron image and the corresponding EDX spectrum may contain contributions from several phases with different compositions.

Sample Cross Section A reaction between the Si₃N₄ sample and Pt capsule that has already been suggested from the surface investigations in the previous paragraph, was confirmed via optical and electron microscopy of the cross sectioned specimen (2): Dark zones at the circumference of the sample cylinder were visible in the optical microscope (Fig. 3.25 on page 128). In the electron microscope, inclusions with high element contrast were seen. Simultaneously, the Pt *L* and *M*-lines occurred in the EDX spectra. The inset shows the interface between these Pt-rich inclusions and undisturbed core of the sample. A further SEM image of the core region of specimen (1). The grains do not show any well-developed facets as is to be expected within a dense bulk material where grain growth is limited by neighbor crystallites. Typical grain sizes range between 0.2 and 1 μm . The arrow on the image points on small circular spots of darker contrast indicating a secondary phase. The presence of an intergranular phase is clearly evident

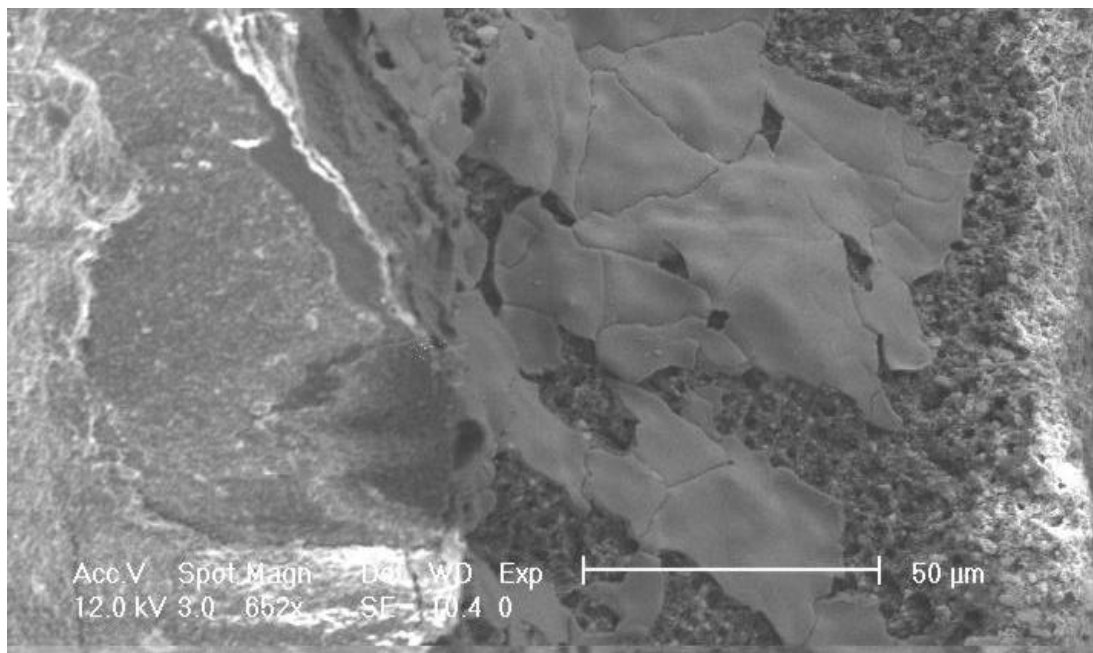


Figure 3.23: Dense layer at the former Pt/sample interface of SN13 and porous subsurface regions.

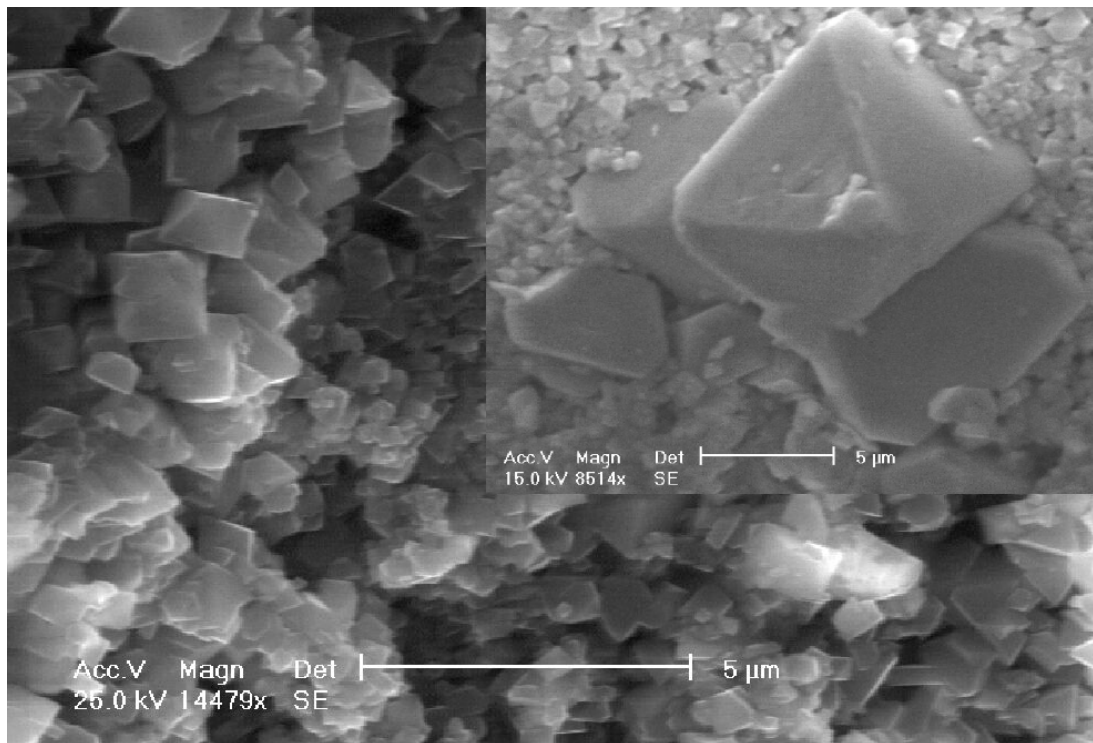


Figure 3.24: Closeup view of a selected subsurface region showing well faceted, octahedral crystallites.

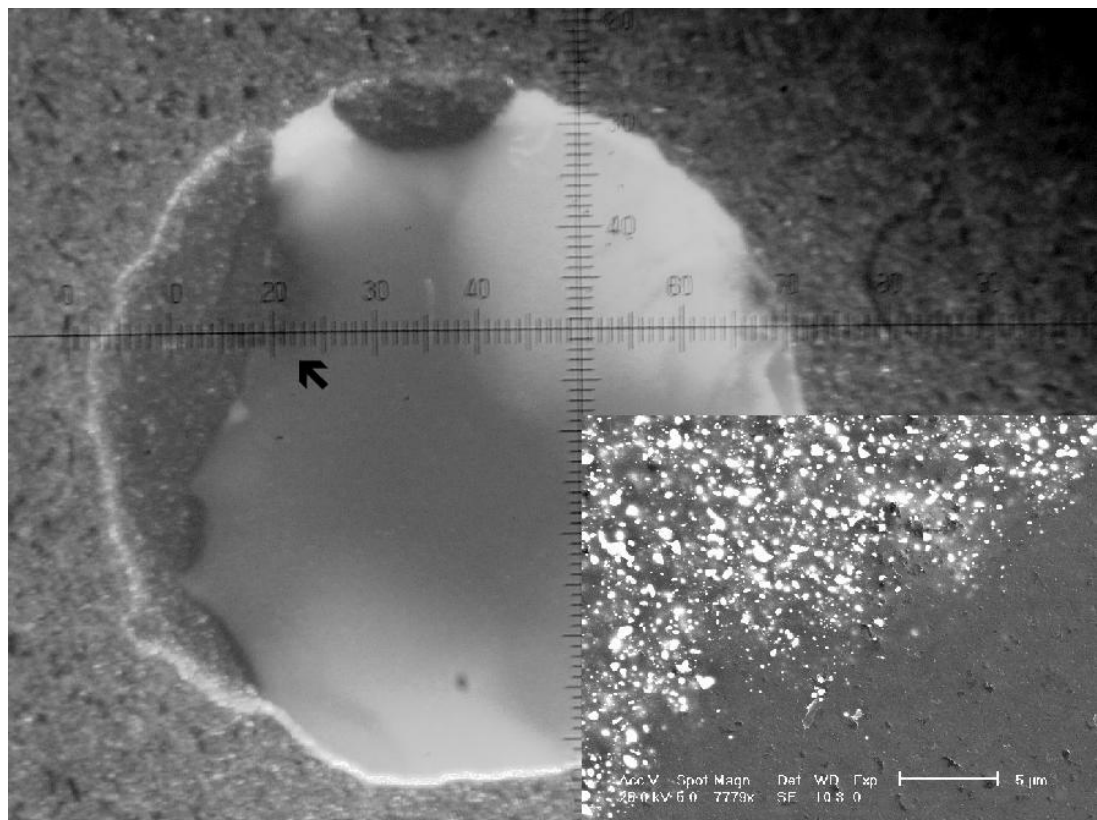


Figure 3.25: Optical image of the embedded and polished SN13 specimen (2) with darker reaction zones at the left. Inset: SEM image of Pt or platinum silicide inclusions (bright spots), approximate location of the image is indicated with an arrow.

from Figure 3.27. This image proves that γ -Si₃N₄ can be selectively plasma etched in a very similar manner to the low pressure polymorph β -Si₃N₄. From the absence of diffraction lines other than that of spinel it can be deduced that the intergranular phase must be predominantly amorphous and oxidic, just as in the case of the conventional Si₃N₄ ceramics. Its thickness was measured \sim 30 nm.

Figure 3.27 also shows bigger accumulations —‘glass pockets’— at triple junctions and also inclusions within the grains. The diameters of the spherical inclusions range between 60 and 90 nm which is in good agreement with the dark spots in Figure 3.26. Larger round shaped features that appear to lie on top of the surface are possibly soot particles deposited together with the antistatic carbon coating. A quantitative graphical phase analysis based on the linear intercept method was carried out on this and a further SEM-image at

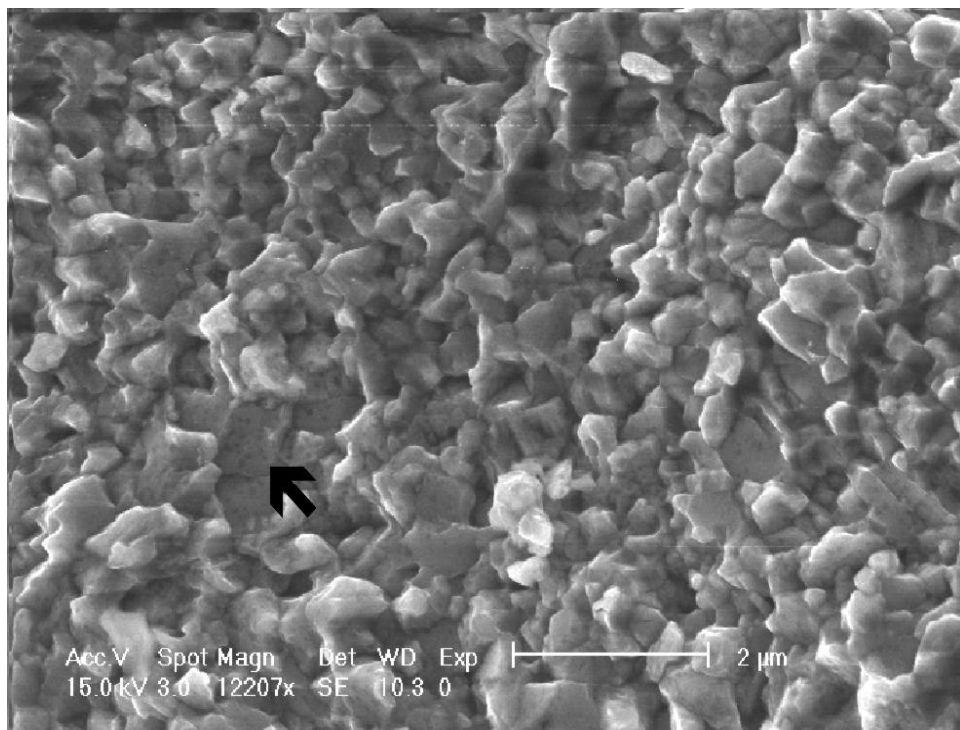


Figure 3.26: Microstructure of a fractured surface from the core region of SN13

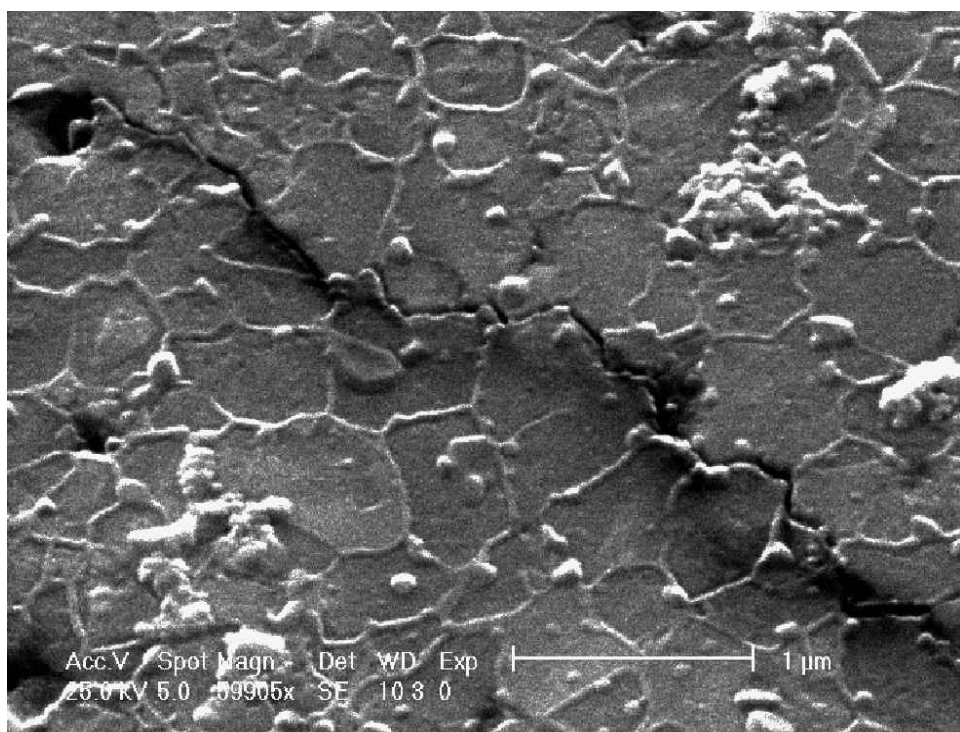


Figure 3.27: Plasma-etched surface with trace of a radial indentation crack. The presence of an intergranular phase is clearly evident.

lower magnification ($\sim 31,000\times$) using the computer program Lince*. In both cases, the fraction of glass phase was found to be ~ 19 vol.%. This value corresponds well with the initial 16 vol.%, if the density increase of the silicon nitride $\varrho(\beta\text{-Si}_3\text{N}_4) = 3.22 \text{ g/cm}^3 \rightarrow \varrho(\gamma\text{-Si}_3\text{N}_4) = 4.01 \text{ g/cm}^3$ is considered. Thus, volume and density of the glass phase must have stayed approximately constant. In coincidence with the XRD-results, this provides another indication that the impurity level within the spinel crystallites cannot not be very high.

The crack diagonally spanning Figure 3.27 is the surface trace of a Vickers radial. Fracture is predominantly intergranular and the glass phase sticks to either one or the other side of the crack. This indicates that the glass/spinel interface is the inferior part of the $\gamma\text{-Si}_3\text{N}_4$ ceramic. However, this fracture behavior is beneficial because it forces the crack on a zig-zag path which leads to crack bridging and toughening of the material.

Further details on the micromechanical characterisation of this sample using SEM to determine hardness and toughness will be treated in Section 3.8 on page 134.

Electron Microprobe: Elemental Mapping and Quantitative Analysis

Mappings of the elements Al, Mg, N, O and Y were obtained from the embedded and polished specimen (2) after coating with a ~ 20 nm thick layer of amorphous carbon. They are shown on page 132. Nitrogen, oxygen and yttrium are distributed evenly over the entire cross section of the sample cylinder. Because of the finite size of the excitation volume under the incident beam, the method is however not capable to resolve compositional differences between the $\gamma\text{-Si}_3\text{N}_4$ grains and the intergranular phase shown in Fig. 3.27. The most apparent feature is a radial gradient of the Mg distribution with high Mg concentrations at the circumference of the cylindrical sample. This indicates an inward diffusion of Mg originating from the furnace part F4 (recall Section 2.1.2 on page 28). Apparently the Pt-foil does not provide an effective barrier at the applied HP/HT conditions. The core of the sample can be considered to be almost free of magnesium, as the

*see page 120

starting material did only contain traces of this element. Furthermore, the Al mapping indicates a slight depletion of this element within the Pt reaction zone considered in the previous paragraph which is most likely an artifact due to the different surface roughness with respect to the unreacted material.

Transmission Electron Microscopy

The material that had been removed from the center of specimen (1) was investigated with TEM in combination with EDX. The carbon coated sample holder was scanned for small agglomerates or single crystallites and their spinel structure verified by measuring the distances and angles between individual reflections of their electron diffraction patterns. Only in one case a material of different structure was found. Two crystallites unambiguously identified as spinel were analyzed with EDX. The results are given in Table 3.11.

Specimen	element/cation percentage [at.-%]					
	Si	N	Al	Y	Mg	O
Calculated:						
SL 200 (total)	41.03	54.71	1.12	0.56	0.03	2.55
SL 200 (cations)	96.01	—	2.62	1.31	0.06	—
TEM / EDX:						
Agglomerate	69	24	3	0.6	—	3
Crystallite 1	94	—	4.8	0.8	0.44	—
Crystallite 2	39	65	1.7	0.2	0.08	2.3
Crystallite 2	95	—	4.3	0.4	0.19	—

Table 3.11: EDX analysis results for different spinel crystallites and agglomerates from the center of sample SN13, investigated by TEM. Quantification of the anions was partially omitted to determine the cation ratios more precisely.

These results indicate that γ - Si_3N_4 may indeed contain impurity elements. The insertion of oxygen has already been discussed in previous sections. Simultaneous insertion of O and Al into the γ - Si_3N_4 lattice was unambiguously verified by the synthesis of the γ - $\text{Si}_{3-x}\text{Al}_x\text{O}_x\text{N}_{4-x}$ solid solution series, treated in Chapter 4. Also the insertion of Mg appears to be very probable, as Mg together with Al

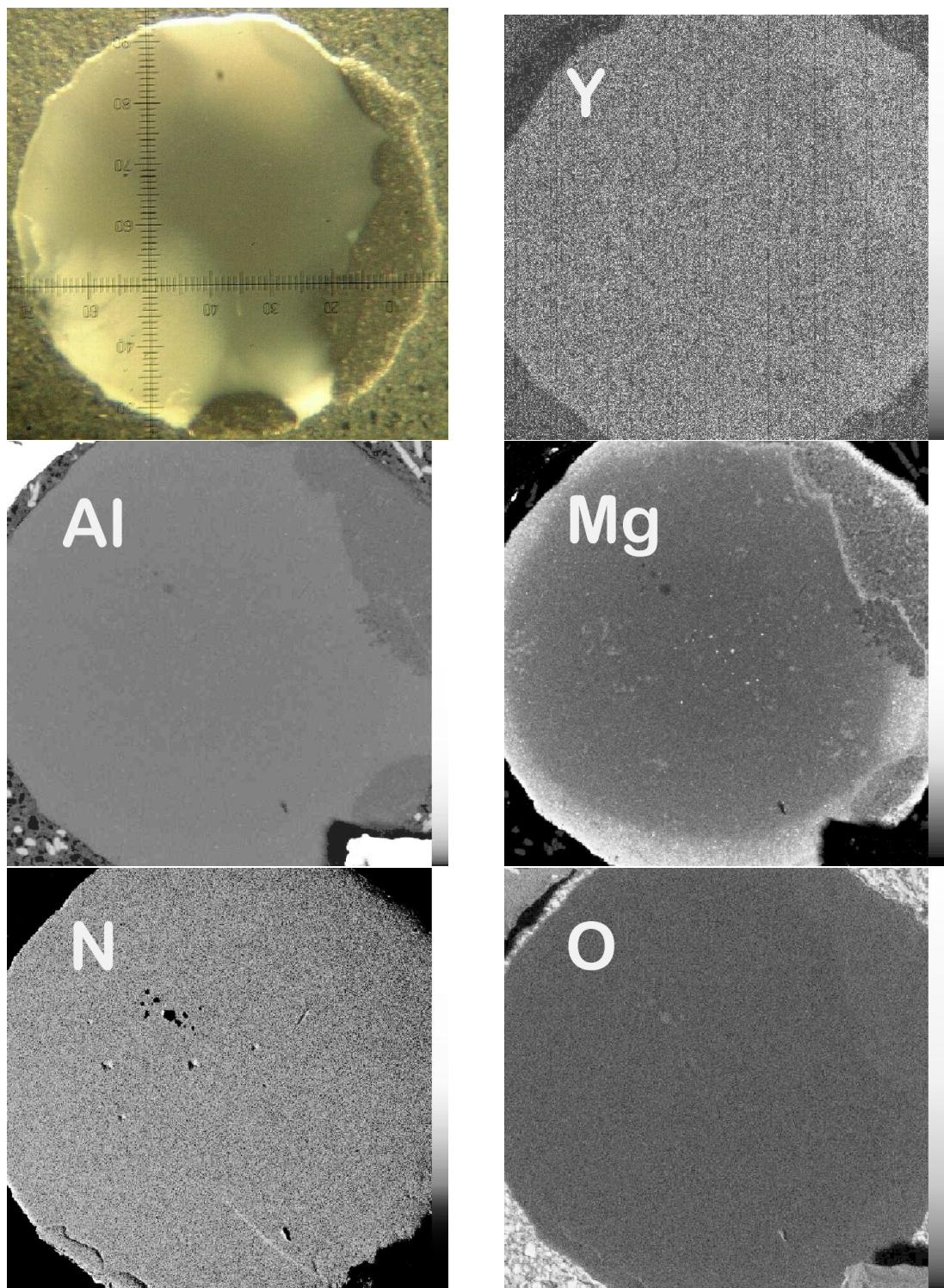


Figure 3.28: Optical image and element mappings of a cross section through (specimen (2)) from the ' γ - Si_3N_4 ceramic' SN13. Image contrast only qualitative.

forms **the** spinel prototype compound MgAl_2O_4 and a variety of other spinels that also contain silicon (Mg_2SiO_4) or even nitrogen, as established by WEISS, GREIL and GAUCKLER [175]. Moreover, the existence of Mg–Si–Al–O–N solid solutions that possess the β - Si_3N_4 structure was proved by WILD et al. in 1981 [176]. It should be noted, however, that the EDX method is not suitable to prove the presence or absence of elements within the investigated object with certainty, as the excited volume from which the specific X-ray radiation originates is often larger than the projected image itself. Amorphous glass phase in close vicinity of the investigated crystallites may therefore be responsible for some of the observed signal intensity. This could explain the presence of Y within the spectrum, the insertion of which into the spinel lattice is not very likely: The radius of the Y^{3+} ion in octahedral coordination with 104 pm [162] is more than double the size of Si^{oct} and should hence cause severe distortions. The large size of the Y ion is also evidenced by the long Y–N/O distances in the two Y–Si–O–N compounds $\text{Y}_2\text{Si}_3\text{N}_4\text{O}_3$ (“*N-Melilite*”) and $\text{Y}_4\text{Si}_2\text{O}_7\text{N}_2$ (“*J-Phase*”), the structures of which were refined by MACKENZIE et al. in 1996 [177]. Here the smallest Y–N/O distance is 2.30 and 2.28 Å, respectively, which is significantly larger than the bond lengths in γ - Si_3N_4 (~1.80 and 1.86 Å, respectively). Y seems also to prefer higher coordination numbers than those occurring in spinel: In these ambient pressure compounds $N_c(\text{Y})$ is already 6, 7 and 8, respectively. Also, no oxide spinel containing Y is known. Within the all-nitride pseudo-binary system Si_3N_4 –YN, only one compound has been confirmed (see [178] and references therein) and it is commonly agreed that the β - Si_3N_4 structure does not show any solubility for Y. The α - Si_3N_4 structure can accommodate the large ion at cage-like interstitial sites which gives rise to the α -sialon solid solutions [179], cf. 4.1.1. The largest interstitial in spinel is the vacant 16c site. The N–N distance across this site is $\frac{1}{2}a_0 = 3.87$ Å — from nucleus to nucleus. Thus, in order to estimate the available space, one may subtract two times the standard ionic radius of nitrogen $2 \cdot r(\text{N}^{3-})$ [162]: The result is 1.23 Å, which is only 60% of the Y^{3+} diameter.

3.8 Properties of γ -Si₃N₄

In the previous sections, phase relationships and the internal structure of γ -Si₃N₄ have been analysed and documented in detail and will provide a firm basis for the understanding of its properties. A preparation method to obtain dense polycrystalline samples has been found and will enable to pre-evaluate the performance that can be expected from of a γ -Si₃N₄-based cutting material. In the following, the contemporary knowledge on the properties of γ -Si₃N₄ is summarized in the order of importance *to a hard material*. Special attention is paid to difficulties in their determination and how these may be overcome in future. Values obtained by experiment and theory, from own investigations and from sources in literature are considered and will be compared where possible.

The properties of γ -Si₃N₄ compared to established materials — but also the effort required to synthesize γ -Si₃N₄ — will determine whether it will become a commercially available hard material or remain a scientific curiosity.

3.8.1 Hardness

Nanoindentation Studies on Precursor-derived γ -Si₃N₄

In the case of the ‘pure’ but porous, precursor-derived γ -Si₃N₄-samples (SN01–SN10), sufficiently smooth surfaces, suitable for nanoindentation studies could be obtained by careful mechanical grinding and polishing with diamond abrasive paper.* These measurements were carried out by A. ZERR, M. KEMPF and M. GÖKEN at the facilities of the Universität des Saarlandes, Fachbereich Werkstoffwissenschaften, Saarbrücken, Germany, and published in a joint article [82]. Samples SN08 and SN06, containing 4 and 14 wt.% oxygen on average, as previously determined by EPMA, were used for the investigations. The indentations, ranging from 130–200 nm in depth, were made with a cube-corner diamond tip mounted on an atomic force microscope with an add-on-force transducer [82]. Load–displacement curves were recorded up to a maximum force of F_{max} of 3 and 5 mN for the two γ -Si₃N₄ samples as well as sapphire and single crystal *c*-BN for comparison. The ‘*nanohardness*’ was obtained in analogy to the plastic hardness HU_{pl} according to Equation (2.15) on page 56, using the appropriate

*A. Zerr, personal communication

area function $A_c(h)$. The average hardness values are shown in Table 3.12, with the maximum variation of the measured values given in parentheses. Determination of the reduced modulus E_r from the same nanoindentation data will be discussed in the following section on the elastic moduli of γ - Si_3N_4 . For further experimental details, data acquisition and data processing please see Ref. [82].

<i>c</i> -BN	γ - Si_3N_4 , SN08	Al_2O_3	γ - Si_3N_4 , SN06
single cryst.	(~4 wt.% O)	single cryst.	(~14 wt.% O)
97(3) GPa	36(8) GPa	32(2) GPa	30(9) GPa

Table 3.12: ‘Nanohardness’ from nanoindentation study of MAP-synthesized γ - Si_3N_4 [82].

It is to be stressed that the *c*-BN and Al_2O_3 specimen were surfaces of single crystals and their hardness values compared to literature data was attributed to the indentation size effect. In contrary, the γ - Si_3N_4 samples were polycrystalline, with grain sizes around 1 μm . A comparability of the hardness readings under these circumstances could be justified on the basis of the indentation dimensions, which are in the same length scale as the average grain size: A high likeliness for hitting a single crystallite by each indentation was assumed.

A subsequent SEM examination of SN08 by myself however does not support this primary hypothesis: Although none of the indentations could be found, comparison of their would-be dimensions* with the microstructure, shows that simultaneous indentation of a few nested grains is the most likely process (Figure 3.29). Figure 3.30 is an SEM image of the same sample surface at lower magnification. It can be seen that islands of clustered γ - Si_3N_4 grains are alternating with relatively large pores. The would-be dimensions of the impressions are also plotted as white triangles and highlighted with a white circle. The inhomogeneous surface topology of the γ - Si_3N_4 samples is also mirrored by the large scatter of the measured hardness values (± 9 GPa). On the other hand, the *average* hardness of the porous SN08 was found to be higher than that of the dense sapphire.

*Assuming an ideal cube-corner geometry, the indentation depth $h = 130\text{--}200$ nm corresponds to indentation edge lengths between 300 and 460 nm

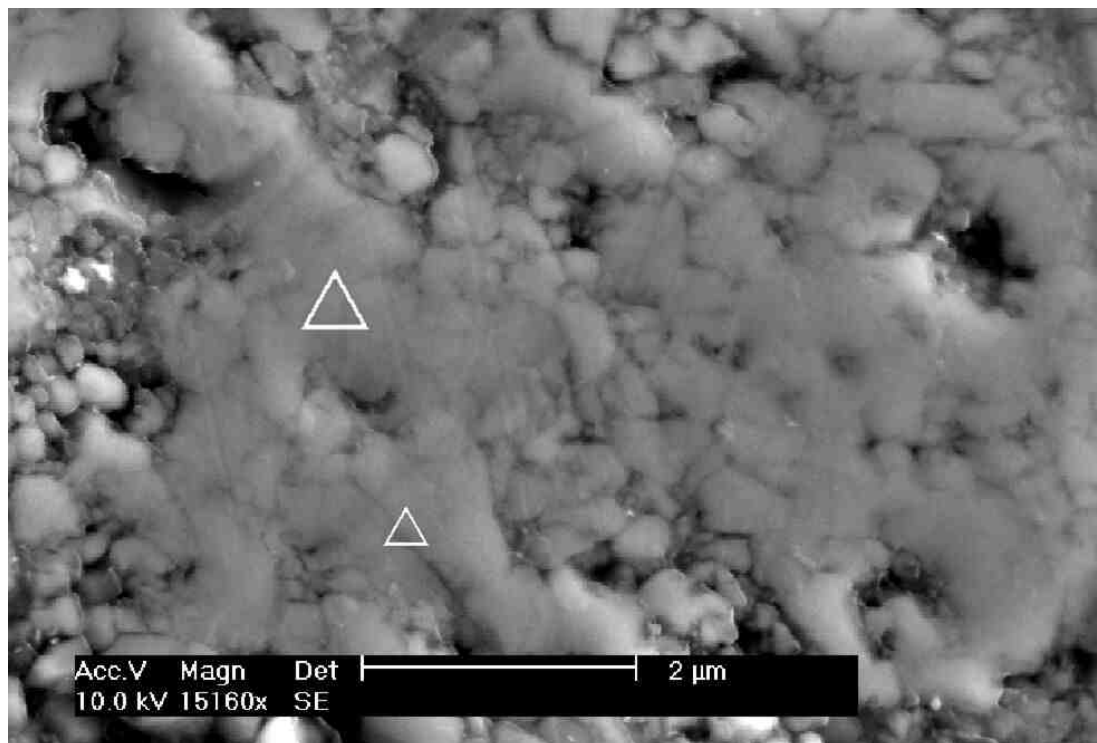


Figure 3.29: Ground surface of SN08. The would-be dimensions of cube-corner nanoindentations at 3 and 5 mN load are indicated by triangles.

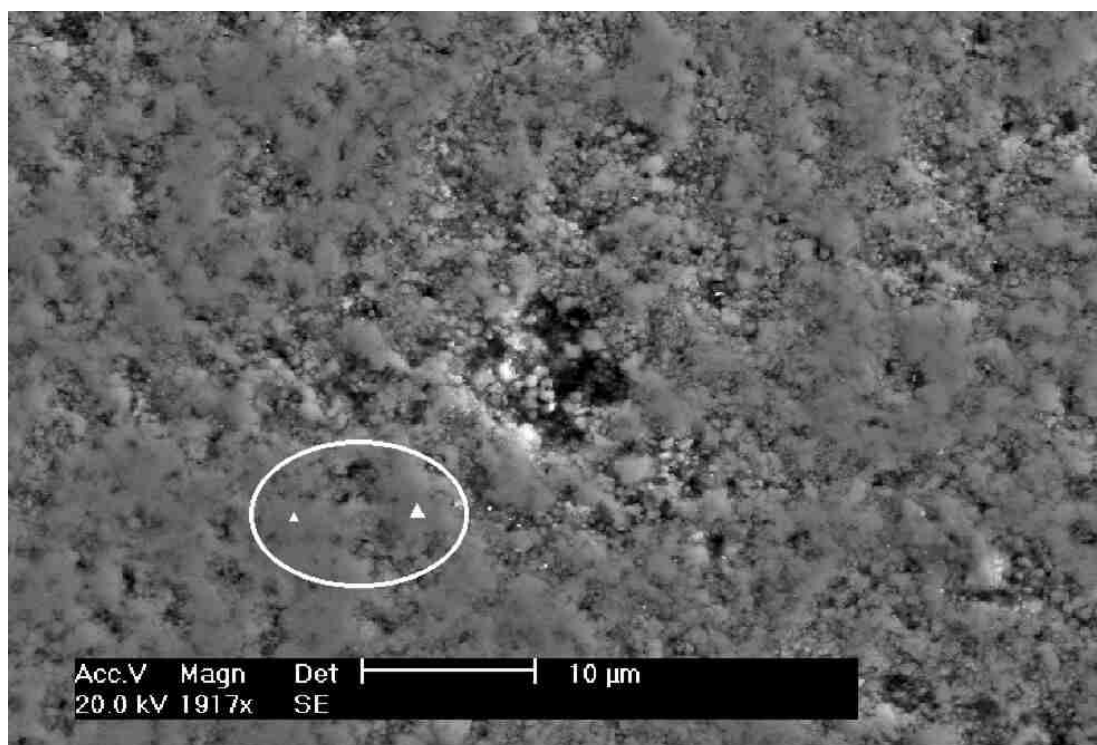


Figure 3.30: The ground surface of SN08 at lower magnification, showing islands of almost dense γ -Si₃N₄ that alternate with porous areas.

This provides evidence that the indented γ -Si₃N₄ islands were sufficiently strong to support the load of the indenter and the material deformed plastically instead of breaking apart. As previously mentioned, small loads 3 and 5 mN were used. For an evaluation of γ -Si₃N₄ as potential hard material, the data based on the microhardness scale (i.e. 100 mN–10 N) would be of higher relevance, because it is traditionally used for the characterisation of materials in both, science and industry. ZERR et al. therefore tried to estimate $HV_{0.5}$ (microhardness at 500 g load) by extrapolating their hardness data under the assumption of similar load size effects in γ -Si₃N₄ and (macroscopically available) sapphire α -Al₂O₃. According to these calculations, $HV_{0.5}$ of a dense γ -Si₃N₄ sample, corresponding to SN08 with 4 wt.% O, would be 25 GPa. Assuming the oxygen content to be present as a weak impurity phase*, $HV_{0.5}$ of *phase pure* and *oxygen-free* γ -Si₃N₄ could range between 30 and 43 GPa [82].

Hardness Studies Reported in Literature

JIANG et al. were able to perform direct microhardness measurements on their dense sintered sample, which had been synthesized in a MAP (recall Sect. 3.3.4 on page 89). Obviously, crystalline Si₃N₄ starting materials result in samples more suitable for hardness testing. The authors report an average hardness of 35.31 GPa, obtained from 40 indentations [88]. However, they omitted to mention the applied load(s) which would have been essential for an unambiguous comparison with other values.

The third hardness study of γ -Si₃N₄ reported in literature so far was carried out by Tanaka and colleagues [120], who also used the multianvil technique and employed high purity single phase β -Si₃N₄ as starting material (Sect. 3.3.4). The sample may be comparable to that of JIANG et al., with a small average grain size D 20–200 nm. For the *lowest* load of 9.8 mN, a hardness of 43 GPa — the upper estimate of ZERR et al. for pure γ -Si₃N₄ — was found. However, the measured hardness readings show a very pronounced indentation size effect (Table 3.13), which was attributed to weak grain boundaries.

*4 wt.% O correspond e.g. to 14 vol.% of amorphous SiO₂ with a density of \sim 2.0 g/cm³

	This work				ZERR et al. ^[a]		TANAKA et al. ^[b]		JIANG et al. ^[c]	
Sample	$\gamma\text{-Si}_3\text{N}_4$				$\gamma\text{-Si}_3\text{N}_4$		$\gamma\text{-Si}_3\text{N}_4$		$\gamma\text{-Si}_3\text{N}_4$	
Specifications	SN13, dense, D \approx 0.5 μm 18–20 vol% glass phase				SN08, porous, D = 0.2–1.3 μm ~ 4 % oxygen	SN06, porous D = 0.2–1.3 μm ~ 14 % oxygen	dense sintered, D = 20–200 nm ~ 0.5 % oxygen		dense sintered, D \approx 140 nm < 0.8 % oxygen	
Indenter type	Vickers	Knoop			cube corner	cube corner	Vickers		Vickers	
Load / Hardness	0.1 N	34(3) GPa			3 mN	37(8) GPa	9.8 mN	43 GPa	? N	35(2) GPa
	1.0 N	31(2) GPa			5 mN	36(5) GPa	32 mN	31 GPa		
		2.9 N	25 GPa				98 mN	24 GPa		
	4.9 N	28.5 GPa	4.9 N	23 GPa			320 mN	19 GPa		
	19.6 N	27.8 GPa	19.6 N	22 GPa			981 mN	13 GPa		
Reference material 1	$\beta\text{-Si}_3\text{N}_4$				$\beta\text{-Si}_3\text{N}_4$					
Specifications	SN11, dense sintered D = 0.2–3 μm , \leq 1 % oxygen				high purity, hip, D \approx 1 μm					
Load / Hardness	19.6 N	13.6 GPa	–	–	981 mN					
Reference material 2	$\beta\text{-Si}_3\text{N}_4$				$\alpha\text{-Al}_2\text{O}_3$					
Specifications	CeramTec SL 200 cutting tool				sapphire single crystal					
Load / Hardness	4.9 N	16 GPa	4.9 N	15 GPa	1 mN					
	19.6 N	15 GPa	19.6 N	14 GPa	32(2) GPa					
Reference material 3	$c\text{-BN}$				$c\text{-BN}$					
Specifications	DB A 80 cutting tool, 80% c-BN				single crystal (111) face					
Load / Hardness	4.9 N	38 GPa	4.9 N	30(2) GPa	5 mN					
	19.6 N	32(1) GPa	19.6 N	26(1) GPa	97(3) GPa					

Table 3.13: Summary of currently available hardness data on $\gamma\text{-Si}_3\text{N}_4$ and reference materials from ^[a] [82], ^[b] [120] and ^[c] [88]. The hardness value marked with ^[d] refers to the identical reference material that has been measured with a different tester [120]

The dominance of a grain boundary-mediated deformation mechanism is discussed as one possible reason for the so called “*inverse Hall–Petch effect*” [26] in nanocrystalline materials. This effect denotes the breakdown of the grain size hardening mechanism below a critical diameter D_c , where the crystallites become too small to sustain dislocation pile-ups, as previously discussed in Section 1.4.3 on page 10. The equilibrium distance between two edge dislocations was assumed as an estimate for D_c [25]. It mainly depends on the burgers vector and the shear elastic constants of the solid [24]. The grain sizes observed by Tanaka and coworkers are large (see above) compared with the typical values for D_c given in literature (10–25 nm). This suggests that γ -Si₃N₄ has either an unusually large D_c or the grain boundaries are indeed very weak. As even the strongest solid, diamond, shows dislocation arrays with spacings of 30 nm or less (see e.g. [180]), the latter must be the case. This once again shows that control over the grain boundaries and intergranular cohesion will be a key step towards the realization of γ -Si₃N₄-based materials.

Micromechanical Characterization of Sample SN13

With SN13, a polycrystalline γ -Si₃N₄-based ceramic material, suitable for determination of mechanical properties like hardness, indentation toughness and elastic modulus was realized. The crystallites were found to be surrounded by a \sim 30 nm thin layer of a presumably oxidic intergranular phase, providing adequate cohesion. The observed grain sizes are in the sub-micron range so that testing results would not be obscured by any reverse Hall–Petch effect and hence may be directly compared to other conventional ceramics.

Reference Materials and Sample Preparation Testing the HP/HT treated SN13 against the SL 200 β -Si₃N₄ starting material is almost self-explanatory. As a second reference material, a *c*-BN-based cutting tool insert (*Amborite* DBA 80, 90% *c*-BN content, DE BEERS INDUSTRIAL DIAMONDS Pty. Ltd., now ElementSix) was chosen. As previously mentioned on page 122, the SN13 specimen had to be inserted into the bore within the cutting tool, where it once had been taken from. However, because of the large hardness difference, no satisfying results could be obtained for both Si₃N₄ surfaces using the same grinding treat-

ment. Hence, an identical β -Si₃N₄ cutting tool insert was prepared separately. It was wet ground down to 4000 grit SiC paper. The *c*-BN cutting tool was only rough ground with SiC paper and then polished with diamond abrasive down to 6 μm grit size. Because of the extreme hardness of the material, the surface roughness remained considerably higher than that of the two Si₃N₄ materials.

Hardness Tests Two series of experiments were performed:

- Conventional Vickers and Knoop microhardness testing
- Instrumented (= load-depth sensing) hardness testing at small loads

Vickers and Knoop Microhardness Testing: Results & Discussion An optical image of SN13 specimen (2) after the first sets of indentations had been made is shown in Figure 3.33 on page 142. The results for the Knoop and Vickers indentations in SN13 and the β -Si₃N₄-based SL 200 cutting tool inset, that were made with **Tester A** and **B** are summarized in the graph depicted in Fig. 3.31. It can be seen that the Vickers hardness of the transformed silicon nitride has effectively doubled upon the HP/HT treatment: Whereas SL 200 shows a hardness around 15 GPa, the high load hardness of SN13 scatters around 30 GPa. Knoop and Vickers hardness of SL 200 are approximately the same, while for SN13 *HK* is around 23 GPa. A larger discrepancy can be seen for the *c*-BN cutting tool, the data of which is provided in the Figure 3.32 below, where $HK \approx 25$ GPa and $HV \approx 35$ GPa. This sample could only be measured at high loads, because of the small indent size and the comparatively high surface roughness already mentioned. Also for the smoothly polished SN13 sample, it became increasingly difficult to obtain meaningful hardness readings towards smaller loads by using the available equipment: As an example, a $HV_{0.025}$ impression on the surface of the β -Si₃N₄ material is shown in Fig. 3.34 on page 142. The SEM image indicates that the tip radius of the employed Vickers indenter is in the range of 1–2 μm so that almost arbitrary dimensions may be taken from the blunted indent. The increasing span of the error bars on the graphs display this variance in the hardness readings of an individual indentation. It is also evident from Fig. 3.31 that the resolution limit for the optical measurement (full symbols + Δ) is reached

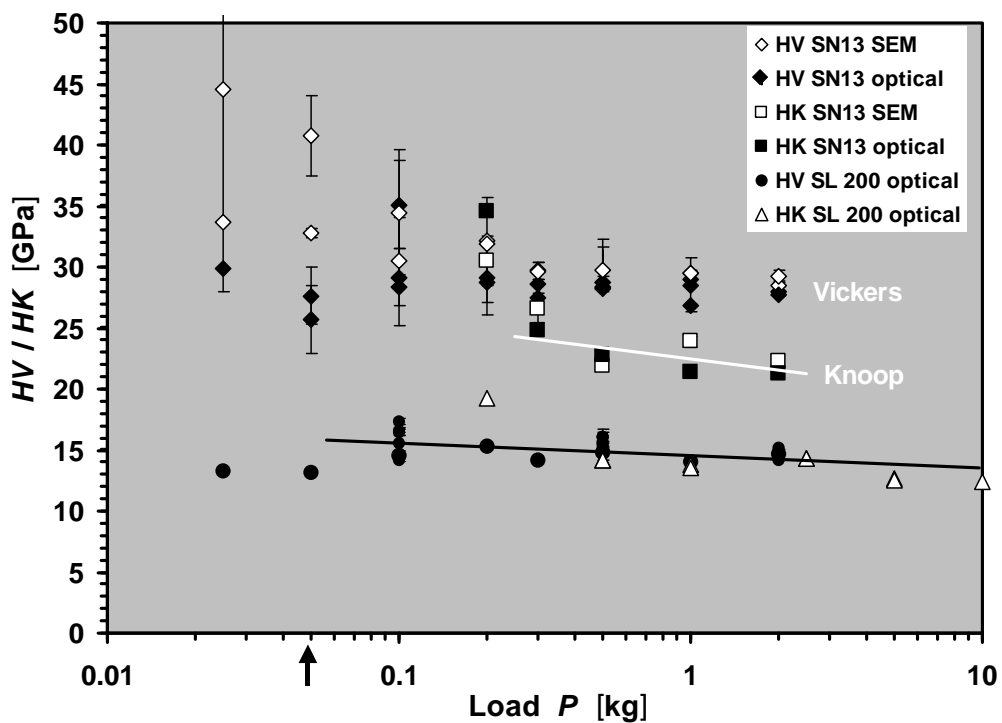


Figure 3.31: Vickers and Knoop microhardness data for SN13 and the $\beta\text{-Si}_3\text{N}_4$ starting material (SL 200)

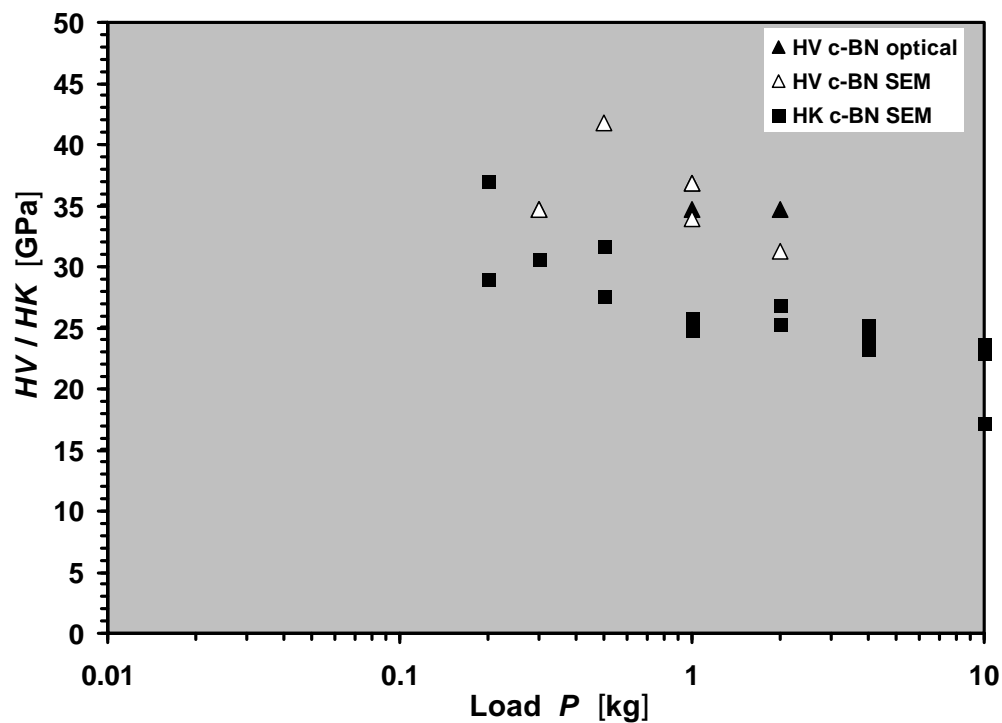


Figure 3.32: Vickers and Knoop microhardness data for the c-BN-based cutting tool (Amorphite DBA 80)

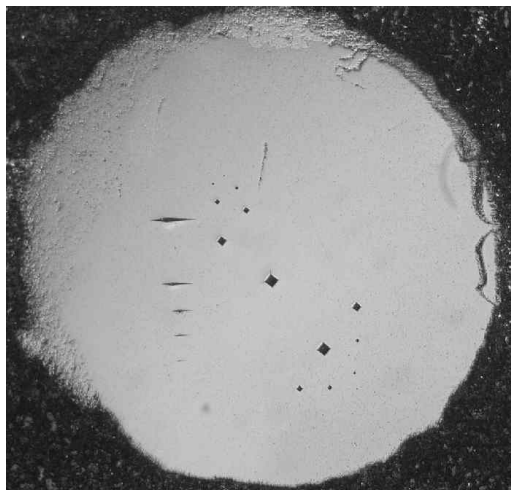


Figure 3.33: Optical image of SN13 specimen (2) with Knoop and Vickers indents

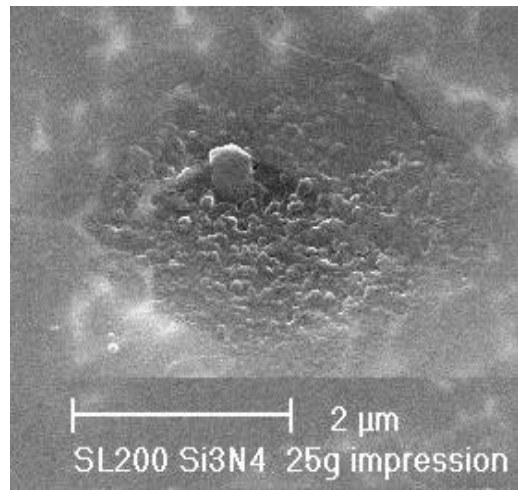


Figure 3.34: Blunted Vickers impression at 25 g (245 mN) load in the β -Si₃N₄ material: The indenter tip of Tester A is too blunt for smaller loads.

for indentations below 0.1 kg, as it fails to continue the trend of the ISE from the higher load hardness readings. The apparent hardness remains constant or even drops off. Most of the SEM measures yield somewhat higher hardness readings which may be attributed to the lack of a precise calibration scale.

The above mentioned uncertainties are also a result of the quadratic dependence between hardness and the indentation dimensions: Small differences in the measurement of low load impressions lead to large discrepancies in the corresponding hardness readings and hence data scatter. This can be partially solved by using the directly measured indentation diagonals for data analysis, as explained in Section 2.2.1 on page 38. Figure 3.35 shows the corresponding plot for the Vickers data. The normalized hardness and the magnitude of the indentation size effect can be estimated from the slope and the intersect of a regression line, respectively. Equivalent analysis was performed for the Knoop data. The results are summarized in Table 3.14.

In the case of the normalized Vickers hardness (HV_n) of *c*-BN, both optical and SEM measures were taken in order to have sufficient data for the regression. The respective HV_n values for the Si₃N₄ materials reproduce the trend of higher

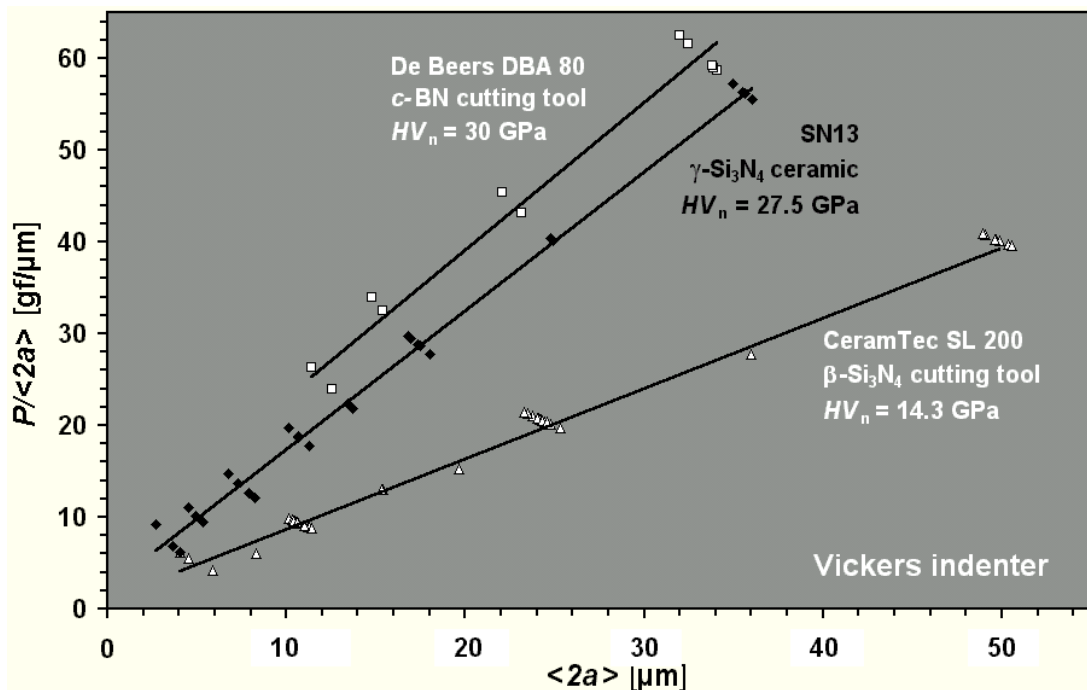


Figure 3.35: Linearized plots of the Vickers data of all three materials. The normalized hardness values HV_n were determined from the slope of the regression lines.

	Sample	DBA 80	SN13	SL 200
	Method	$c\text{-BN}$	$\gamma\text{-Si}_3\text{N}_4$	$\beta\text{-Si}_3\text{N}_4$
HV_n [GPa]	optical	30.0	27.4	14.3
	SEM		27.6	14.5
ISE [$\mu\text{m/g}$]	($= 1/c_1$)	0.2	0.4–1	0.4–0.8
HK_n [GPa]	optical	22.0	17.5	11.8
	SEM		19.6	13.7
ISE [$\mu\text{m/g}$]	($= 1/c_1$)	0.4	0.4	0.6–0.7

Table 3.14: Normalized (“load independent”) Vickers and Knoop hardness values and ‘indentation size coefficients’ (ISE), as obtained by linear regression of hardness/load data.

apparent hardness readings obtained by SEM-measurement but do not differ significantly. In the case of HK_n , the discrepancies are larger, especially for SN13 where only a few Knoop indents could be made owing to limited sample surface. Both, the HV_n and HK_n data draw a congruent image: The γ -Si₃N₄-based ceramic is considerably harder than the β -Si₃N₄ starting material. Its plastic deformation behavior is closer to that of the *c*-BN composite, but it cannot really compete. However, keeping in mind that SN13 was the result from a single experiment, while the DBA 80 cutting tool is a commercial product which has certainly been optimized in many repetitive steps, the properties of the γ -Si₃N₄ ceramic are nevertheless impressive. The *c*-BN material and also SN13 show a trend towards smaller ISE coefficients, which means that their hardness is less dependent on load. However, the available data stock is too small to draw any final conclusions concerning the ISE. What can be said with certainty is that SN13, provided with a hardness $HV_1 \approx 28$ GPa, shows a much less pronounced ISE than the nanocrystalline material synthesized by Tanaka et al.: According to the hardness–load data published, the hardness measured at 1000 mN ($\simeq HV_{0.1}$) [120] was significantly *below* 20 GPa (recall Table 3.13 on page 138).

Instrumented Hardness Testing

In the preceding section it has been shown that conventional Vickers and Knoop hardness testing yields only trustable results at an intermediate load range, between ~ 0.1 and 2 kg ($\simeq 1$ –20 N), using the equipment available at our institute. In order to obtain a larger overlap between the current data and e.g. that of Tanaka et al., the micromechanical characterization of sample SN13 was extended by load–depth sensing indentation study at the Institut für Chemie anorganischer Materialien at the Munich Technical University. Details on the collaboration and the employed **Tester C** are given at page 47.

Four series of hardness measurements in the range between 100–1000 mN with 3 points at each load were carried out, the results are visualized in Figs. 3.36 and 3.37. For all measurement series, load–indentation curves were recorded. Determination of the corresponding indentation modulus E_{IT} from this data will be discussed in the section on the elastic properties of γ -Si₃N₄, on page 152.

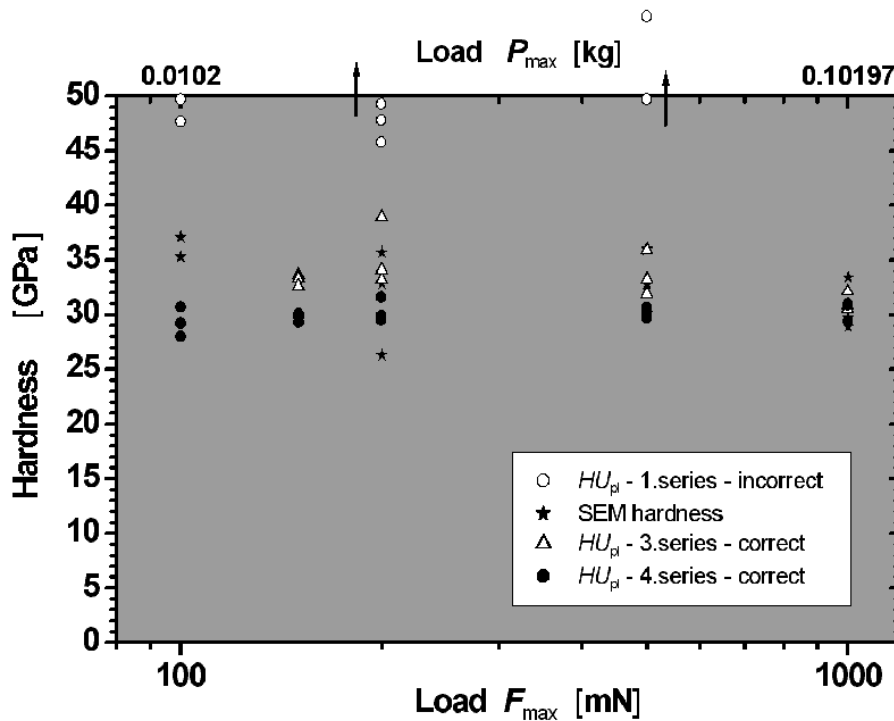


Figure 3.36: Dependence of the plastic hardness HU_{pl} on the load for three series of the instrumented hardness measurements.

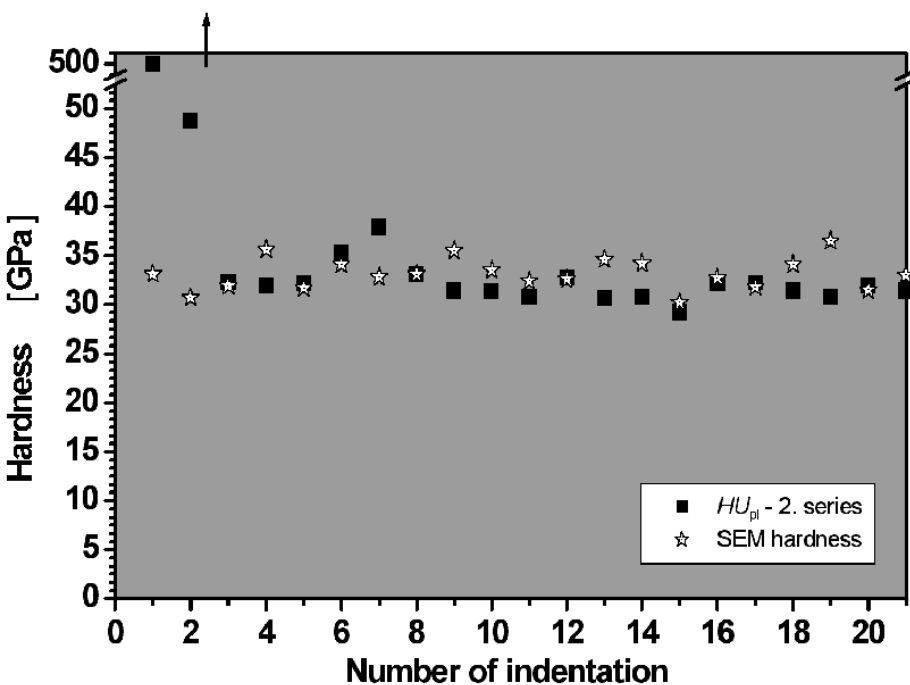


Figure 3.37: Instrumented and SEM hardness readings for the second indentation series, performed at a load of 500 mN.

The first series of hardness measurement, marked with \circ in Figure 3.36 gave incorrect and too high HU_{pl} values. The measured hardness decreased during the measurement from absurd values of 500 GPa to values around 50 GPa. All indentation curves showed negative creep. The effect can be explained by anelastic or another time delayed deformation response of the polymeric embedding matrix as shown in Figure 2.15 on page 61: In order to fix the position of the sample, the Fischerscope 100 hardness tester first presses a thick ring made of strong steel to the surface of the sample with a load of 50 N and only afterwards the indenter in the center of that ring begins to approach and contact the surface. The high load on the ring causes a slight ‘lift-up’ deformation of the sample within and around the ring which consists of an instantaneous elastic and a small, time delayed anelastic or viscoplastic deformation. The deformation appeared to be permanent, because the HU_{pl} values of all following measurement series (except of the first series and starting points in second series) showed much better agreement to the previous results discussed in Section 3.8.1. No negative creep was observed on the loading-unloading curves. Measurement of the indentation diagonals via SEM, confirmed that the instrumented hardness readings from the first series \circ were incorrect. The corresponding hardness values obtained by SEM, are marked with \star (Fig. 3.36). The average of these values is approximately 34 GPa. The second series of indentations was also checked via SEM and a much better coincidence between the instrumented HU_{pl} hardness values and the SEM hardness readings was found (Fig. 3.37). Comparison with Figure 3.31 on page 141 reveals furthermore, that the data scatter of these measurements is notably smaller than that of the preceding conventional hardness study at the same load ($500 \text{ mN} \simeq 0.05 \text{ kg}$, indicated with an arrow at the abscissa of Figure 3.31 on page 141). The *median* value of the conventional measurements in turn coincides well with the 34 GPa SEM-derived average hardness of series 1 and 2. The same average value was determined from the instrumented measurement (HU_{pl}) of the following third and fourth series (\triangle and \bullet in Fig. 3.36).

3.8.2 Elastic Moduli

Theoretical Predictions reported in Literature

As mentioned in Sections 3.1 and 3.6.2 on page 117, the emergence of γ -Si₃N₄ was accompanied by theoretical calculations based on electronic structure theory [85, 181]. These calculations proved to be valuable in the fast prediction of properties of new and unknown phases [8]. A first estimation for the bulk modulus $B_0(\gamma\text{-Si}_3\text{N}_4) = 300$ GPa and a c_{44} shear elastic constant of 340 GPa was derived by KROLL and presented already in our first joint publication [85]. The former value is similar to those found for stishovite ($B_0(\text{r-SiO}_2) = 281\text{--}313$ GPa) [182] and represents the lower bound for highly incompressible solids, such as diamond, WC, c -BN, RuO₂ [6], Os [13] and crottunite-type TiO₂ [38].

Soon after the discovery of γ -Si₃N₄ had been announced, MO et al. came up with an own calculation result, 280 GPa for B_0 and 3.48 for its first pressure derivative B'_0 [86], which also appears in subsequent publications [126, 156, 116, 117, 183, 127]. KROLL refined his calculations and published new values in 2000: $B_0 = 313$ GPa and $G_0 = 261$ GPa [181]. The latter refers to a polycrystalline body and was derived from the crystal elastic constants as an average of the Hashin and Shtrikman formulations. SOIGNARD et al., who applied the same procedure to the results of their LDA calculations, yielded a very similar value of 258 GPa for γ -Si₃N₄ [124]. For γ -Ge₃N₄, they obtained 176 GPa. The authors also present theoretically and experimentally derived elastic constants of the oxide spinels γ -MgAl₂O₄ and γ -Mg₂SiO₄. The nitride spinels were predicted to be significantly stiffer than these and to exhibit a substantial Cauchy violation ($c_{44}/c_{12} > 1$) of 1.8 (γ -Si₃N₄) and 1.4 (γ -Ge₃N₄), indicating strong covalent bonding. An even higher value of 1.95 was derived by KOCER et al. employing both, local density - (LDA) and generalized gradient approximation (CGA) to calculate the elastic constants of γ -Si₃N₄ [184]. In contrast to Kroll and Soignard, these authors define the shear modulus as the average of c_{44} and $(c_{11} - c_{12})/2$ and obtained a high value of 349 GPa. Calculation of the stress-strain curves in tension and shear indicated a failure of the γ -Si₃N₄ crystal lattice for maximum strains $\varepsilon_{11} = 0.16$ and $\varepsilon_{23} = 0.15$, the corresponding “ideal” tensile and shear strengths were found to be $\sigma_{max} = 45$ and $\tau_{max} = 47$ GPa, respectively. A lower value of $\sigma_{max} \approx 28$ GPa was found by TROMANS and MEECH [185]

using an analytical method based on the Morse potential and the experimental Young's modulus of γ -Si₃N₄ as determined by ZERR et al. ($E_Y = 379$ GPa, see Section “Published Data” on page 152 and following). First measurements of the yield strength under non-hydrostatic compression suggest values between 9 and 22 GPa, depending on the pressure (see Section 3.8.2 on page 151).

Determination of the Bulk Modulus B_0 reported in Literature

Dynamic Compression Experiments H. HE, T. SEKINE and coworkers were the first to report an experimental value for the bulk modulus of γ -Si₃N₄ in November 2000 [122]. In their shock-compression study of dense sintered Si₃N₄ bodies they measured the Hugoniot curve of β -Si₃N₄ up to 150 GPa and observed an incomplete $\beta \rightarrow \gamma$ phase transformation, with an onset at 36 GPa. From certain assumptions about the β -Si₃N₄/ γ -Si₃N₄ mixture created within the shock wave and the Hugoniot data, the isentrope of γ -Si₃N₄ (i. e. the p - V pathway by which the shocked material decompresses) was constructed by fitting a third order Birch–Murnaghan equation of state (EoS). B_0 and B'_0 are parameters within this equation and the fitting procedure yielded 300 ± 10 GPa and 3.0 ± 0.1 respectively. In order to perform these calculations, three preassumptions were made:

1. $\alpha_V(\gamma\text{-Si}_3\text{N}_4) \approx \alpha_V(\beta\text{-Si}_3\text{N}_4) = 1.08 \cdot 10^{-5} \text{ K}^{-1}$ * [$1.95 \cdot 10^{-5}$ (1000 K)]
2. $C_V(\gamma\text{-Si}_3\text{N}_4) \approx C_V(\beta\text{-Si}_3\text{N}_4) = 98.2 \text{ J/mol K}$ [92.4 J/mol K (300 K)]
3. $\Delta E(\beta\text{-Si}_3\text{N}_4 \rightarrow \gamma\text{-Si}_3\text{N}_4) \approx \Delta E(\alpha\text{-quartz} \rightarrow \text{stishovite}) = +821 \text{ J/g}$

$[\Delta H = +208.2 \text{ J/g (1670 K)}] \quad [+799 \text{ J/g (1700 K)}]$

The values in square brackets show the corresponding experimental and theoretical results for the assumed properties that have been derived later by Sekine himself [186] (Sect. 3.8.6) and Fang et al. [153] (Sect. 3.8.8), respectively. Within the present work, however, Sekine found the influence of C_V and ΔE to be small: Doubling both changed their result of B_0 by less than 3%. In fact, the experimental value for the enthalpy difference $\Delta H \approx \Delta E$ is found to be 4 times the assumed value, while the assumption of C_V appears to be quite good, so that the result for B_0 still coincides well with those of the static measurements.

* α_V = volume coeff. of thermal expansion

Static Compression Experiments Also in September 2000, the publication of E. SOIGNARD et al. on a static compression study of γ - Si_3N_4 using a DAC up to a pressure of 35 GPa was approved. It is accompanied by the theoretical calculations of elastic constants mentioned in the previous paragraph and was published in 2001 [124]. The synthesis and questionable purity of the investigated material have been already treated in Section 3.3.4 on page 89 and were critically revised in Ref. [82]. The authors obtained $B_0 = 308 \pm 5$ GPa and $B'_0 = 4 \pm 0.2$ by fitting their p - V data to a third order Birch–Murnaghan EoS.

ZERR et al. used well defined material from our MAP-experiment SN08 in a similar compression study, carried out at the DESY synchroton source in Hamburg, Germany. The results were published together with those of the nanoin-dentation experiments (recall Section 3.8.1) [82]. Diffraction patterns were taken by EDXD up to a pressure of 53 GPa, almost 20 GPa more than in the experiments of Soignard et al. Moreover, the ruby fluorescence scale as well as the known pressure dependency of argon diffraction lines were used as pressure standard. The data was fitted to the third order Birch–Murnaghan EoS. Leaving both parameters B_0 and B'_0 unconstrained, values of 290 ± 5 GPa and 4.9 ± 0.6 respectively were obtained, whereas fixing B'_0 to 4.0 led to a higher bulk modulus of 302 ± 6 GPa. Both fits agreed, within the experimental uncertainties, to the recorded p - V data. The determined B'_0 of 4.9 GPa is the highest value so far proposed for γ - Si_3N_4 . High values of the pressure derivative have also been reported for stishovite ($B'_0 = 5.3$) [187] and for ferrous ringwoodite, γ -(Mg,Fe)₂SiO₄ [188] ($B'_0 = 5.0$ –5.6), the high pressure modification of olivine. They give evidence of a high anharmonic proportion of the interatomic potential around the octahedral silicon Si^{oct}. Also the larger thermal expansion coefficient of γ - Si_3N_4 (as compared to β - Si_3N_4) is a consequence of this anharmonicity. Measurements of the thermal expansion of γ - Si_3N_4 will be discussed in Section 3.8.7 on page 173.

JIANG et al. conducted an elaborate characterization of γ - Si_3N_4 , including a third compression study in a DAC up to 42 GPa and determination of the thermal expansion behavior by powder-XRD at variable temperature [189]. These researchers report one of the highest experimental values for B_0 (317 ± 11 GPa) and an unusually low pressure derivative $B'_0 = 2.3 \pm 2.1$, both values accompa-

nied with relatively high uncertainties (the lower bound $B'_0 = 2.3 - 2.1 = 0.2$ is almost absurd). Constraining B'_0 to 4.0 gave $B_0 = 309 \pm 3$ GPa. In contrary to the previous studies of Soignard and Zerr, Jiang et al. used the Birch EoS. Possibly the most interesting part of Jiang's investigations is the Rietveld refinement of the diffraction data at high pressure, which provides a more detailed insight into the structural changes of the spinel under compression. As these structural refinements also revealed deviatoric strain above 20 GPa, induced by increasing shear gradients within solid argon pressure medium, Jiang et al. decided to include only data that had been measured below this pressure. (If shear indeed has a significant influence on the compressibility of γ -Si₃N₄, the investigations of Soignard and Zerr may have to be revised.) The structural refinements of Jiang et al. indicate that the SiN₄ tetrahedron is more compressible than the SiN₆ octahedron within γ -Si₃N₄. This corresponds to a decrease of the anion parameter with increasing pressure ($\partial \mathbf{u} / \partial p < 0$) which was also predicted by CHING et al. [117]. This behavior can be easily understood, as it means that upon pressurization, the nitrogen sublattice starts approaching the ideal cubic packing arrangement at $\mathbf{u} = 0.25$ (recall Fig. 3.14 on page 106) Also the own theoretical calculations of Jiang et al. confirmed the trend: The so called “*polyhedral bulk moduli*” $B_0^{oct} = B_0(\text{SiN}_6)$ and $B_0^{tet} = B_0(\text{SiN}_4)$ were found to be 361 GPa and 298 GPa, respectively. The bulk modulus of the spinel structure as a whole was calculated 328 GPa. This confirms that the simple average of the polyhedral moduli provides a good prediction for compressibility of the bulk — a fact that had been established previously for oxide spinels by FINGER and colleagues [190] and RECIO et al. [191].

At this point it is interesting to note that the bulk modulus of the high pressure modification of *aluminum* nitride *rs*-AlN was found to be also around 300 GPa [138, 192]: In this material, all cations are in octahedral coordination, so that $B_0^{oct} \equiv B_0$, the nominal charge (Al³⁺) is *less* than in γ -Si₃N₄ with Si⁴⁺, and the Al–N bond distance of ~ 2.02 Å [129] is *larger* than the 1.80 and 1.86 Å observed for γ -Si₃N₄. According to the “*Principles of Hardness*” set out on page 6 in Chapter 1, this should result in a lower stiffness and compressibility. However, this weakening effect appears to be exactly cancelled out by the increased coordination numbers $\bar{N}_c = N_c(\text{Al}) = N_c(\text{N}) = 6$. As shown in Fig. 3.15 on page 110, γ -Si₃N₄ and *rs*-AlN have also comparable specific volumes $\langle \Omega \rangle$ of 8.28 and 8.27 Å³ per atom, respectively.

An extremely high initial bulk modulus of 685 ± 45 GPa associated with a kind of ‘compressibility hysteresis’ is reported WANG et al. [193]. According to the authors, it was observed at the first compression of shock-synthesized nanocrystalline γ - Si_3N_4 from ambient up to ~ 40 GPa, using a diamond anvil cell. Above this “critical pressure” a constant B_0 of 415 ± 10 GPa was obtained by fitting X-ray synchrotron data recorded up to 120 GPa. Upon decompression, when the pressure dropped below 40 GPa again, the γ - Si_3N_4 nanocrystals exhibited only the lower modulus of 415 GPa. This value is still 38% higher than the ~ 300 GPa, obtained for microcrystalline material as discussed above. Calculating the lattice constant (a) from individual reflections hkl , the authors moreover observed a systematic increase of a for high index reflections (small d_{hkl}). The reason for all this is seen in the small crystallite size around ~ 30 nm and the associated high surface energy of the material. The article leaves however a number of questions unanswered. For example, the authors left B'_0 fixed to 4 at all times and did not disclose the result of their fit when B'_0 was left free. Secondly, a possible influence of shear strain on the results is not discussed, although the sample has been loaded into the DAC without any pressure medium.

An important further DAC study on identical shock-synthesized material by KIEFER et al. so far is only available as conference abstract*. It indeed showed that omission of a pressure medium will result in considerable deviations from hydrostaticity. These conditions were intended in order to study the yield strength of γ - Si_3N_4 as a function of pressure in a similar manner as has been done for stishovite [194]. Based on first principles calculations of the elastic tensor of γ - Si_3N_4 at pressure, the maximum shear strains, as determined from synchrotron data, correspond to a yield strength of 9.1 GPa at an isostatic stress component p_{iso} of 20 GPa. It rapidly increases to 18.7 GPa at $p_{iso} = 40$ GPa and then more slowly approaches a value of 22 GPa at $p_{iso} = 70$ GPa. According to these values, γ - Si_3N_4 shows one of the highest yield strengths observed to date.

Resumé After a large number of theoretical and at least four experimental investigations, the uncertainty about the bulk modulus B_0 of γ - Si_3N_4 has become sufficiently small: There is a high confidence that the true value may be found within 300 ± 10 GPa, which qualifies it for the upper mid range of incompressible

*<http://www.compres.stonybrook.edu/Meetings/2003-06-18/Abstracts/Kiefer.html>

materials. The range between $B_0 = 300\text{--}500$ GPa is — in absolute numbers — dominated by about 20 transition metals and their nitrides, carbides, and a few oxides (see e.g. [93], Figure 2).

Indentation Moduli E_r , E_{IT} and Shear Modulus G_0

By the determination of the bulk modulus of $\gamma\text{-Si}_3\text{N}_4$, one of the two independent constants necessary to describe the elastic behavior of a polycrystalline body of this material was known. Determination of any additional elastic constant would enable the derivation of all other entities that are regularly used in the field of materials engineering (E_Y , ν , G_0 etc.). Moreover, knowledge of G_0 would in turn allow to predict the *maximum achievable hardness* of $\gamma\text{-Si}_3\text{N}_4$ by using the empirical scale established by Teter [8]. Together with other data, this upper bound for the hardness is helpful to evaluate the potential of $\gamma\text{-Si}_3\text{N}_4$ in comparison to other abrasive or structural materials.

Published Data A first estimation of the engineering elastic constants of $\gamma\text{-Si}_3\text{N}_4$ became possible by the combined nanoindentation and compression study of samples SN08 (< 4 wt.% O) and SN06 (14 wt.% O), published in [82].* Comparison of the load-displacement curves of the $\gamma\text{-Si}_3\text{N}_4$ samples to those of the reference materials, single crystal *c*-BN and sapphire, revealed identical trends in both, their hardness and stiffness: $c\text{-BN} > \gamma\text{-Si}_3\text{N}_4$ (4 wt.% O) $> \alpha\text{-Al}_2\text{O}_3 > \gamma\text{-Si}_3\text{N}_4$ (14 wt.% O). The corresponding values for the reduced moduli E_r and other elastic constants are listed in Table 3.16 on page 162, along with those of the ‘ $\gamma\text{-Si}_3\text{N}_4$ ceramic’ SN13, and reference materials.

In [82], E_r was obtained in two ways. One is according to the standard procedure of OLIVER and PHARR, outlined on page 57 of this thesis. As indicated previously, this method was found to be inappropriate for materials with extreme hardness and a discrepancy of $\sim 20\%$ was found for the experimental E_r value for the *c*-BN (111) surface (415 GPa) with respect to that calculated from elastic constants ($E_r^{calc} = 518$ GPa). For the ‘softer’ sapphire crystal, the corresponding discrepancy was less (6%). Accordingly, a second method that is based on the

*see also Sect. 3.8.1 on page 134

Hertzian contact model was employed: By fitting the load-displacement data of the *first part* of the *first loading cycle* in the *c*-BN crystal to the equation $F = \frac{4}{3} \cdot E_r^{calc} \sqrt{R} h^3$,* the tip radius $R = 102$ nm of the diamond indenter was obtained. The result for R was then in turn used to determine a second value for E_r of γ -Si₃N₄ by fitting the load-displacement curves to the same Hertzian equation. The resulting values were similar to those obtained from the Oliver/Pharr method: The average E_r of sample SN08 is within the range 285–300 GPa, with an experimental error of about ± 17 GPa.

The SEM investigations of sample SN08, represented Figure 3.29 and 3.30 on page 136 have shown that simultaneous indentation of a few nested grains is the most likely event of the underlying nanoindentation study. This does not change the point of our previous argumentation in [82], where we assumed that each measurement would affect only a *single* but randomly oriented crystallite. In both cases, an averaged E_{IT} , obtained from several indentations should provide a good estimate for the Young's modulus E_Y of the polycrystalline material — *provided that the classical interpretation of E is valid for this material*.† Based on this argumentation and using the previously determined bulk modulus B_0 of 290–300 GPa and equation (2.18), (2.20) and (2.21) on page 59, respectively, an estimate for the shear modulus of γ -Si₃N₄ $G_0 = 148 \pm 16$ GPa was obtained. This is more than 100 GPa lower than the theoretical predictions of KROLL et al. (261 GPa, [181]) and SOIGNARD et al. (258 GPa, [124]) and will be discussed in Section 3.8.3 on page 158, after the results of the equivalent indentation study of the dense SN13 sample have been treated.

Indentation Elastic Properties of SN13 As mentioned in Section 3.8.1 on page 144, the first indentation series in SN13 gave erroneous load-displacement data, from which neither meaningful hardness nor correct intention moduli could be obtained. The remainder three series of indentations however, yielded correct hardness readings around $HU_{pl} = HV = 34$ GPa. The corresponding load-displacement data was evaluated to determine the reduced modulus E_r as a function of applied maximum load F_{max} . In this case, the E_r -values were obtained

* F = indentation force, h = indentation depth

†See ages 57 and 62

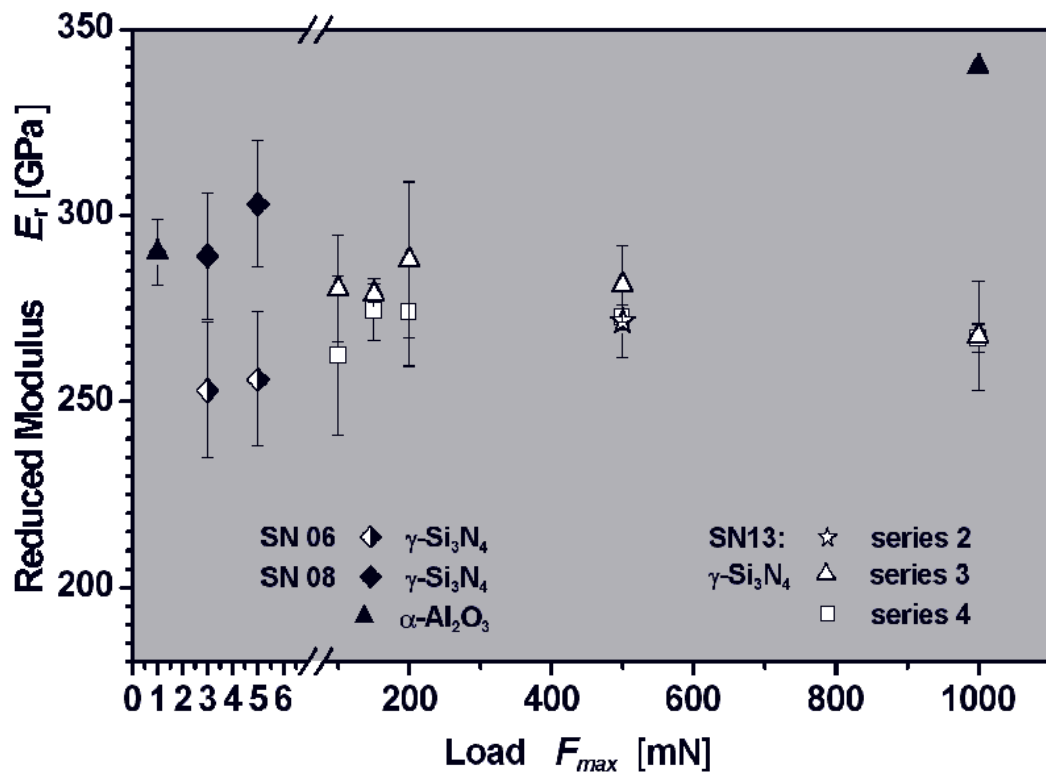


Figure 3.38: Reduced elastic moduli of SN13 (SN08 and SN06 from [82]) as a function of the maximum indentation load.

by linear extrapolation of first unloading part of the load-displacement curves.* The results are plotted in Figure 3.38, along with those of our previous nanoindentation study on SN06 and SN08, respectively. At first glance, the reduced moduli of the dense SN13 sample appear to be intermediate between the two γ -Si₃N₄ samples with the different oxygen contents and show a slight decrease with increasing F_{max} . The averages of E_r range from about 260 to 290 GPa and the experimental uncertainties appear to be in the same order of magnitude for both investigations, in spite of the fact that SN13 has been measured at significantly higher loads.

In order to calculate the elastic properties of SN13 on the basis of the conventional interpretation of E_r and E_{IT} ,† the average of the E_r -values of the 500 mN

*see pages 58 and 46, respectively

†see Sect. 2.2.6 on page 57

measurements, $\langle E_r \rangle = 275 \pm 10 \text{ GPa}$, was chosen. This intermediate load is believed to be best-suited, because on the one hand, the corresponding indentations are approximately $5.2 \mu\text{m}$ in diameter and therefore should cover a sufficiently large area to randomize anisotropy from the crystallites ($D \approx 0.5 \mu\text{m}$) and inhomogeneities. On the other hand, the extent of irreversible deformation due to microcracking may be still small in comparison to higher loads. The lower E_r -values observed at 1000 mN load could be a consequence of such microcracking. Finally, the average over the *entire* load range was found to be almost the same: 274 GPa. Assuming a Poisson ratio of $\nu = 0.27$, the values listed in Table 3.15 were derived.

The SEM investigations of SN13 in Section 3.7.3 on page 125 revealed, that this material consists of $\gamma\text{-Si}_3\text{N}_4$ with 18–20 vol.% of an amorphous matrix. Hence, its elastic recovery and consequently the experimentally determined reduced modulus E_r will not be identical to that of *pure* $\gamma\text{-Si}_3\text{N}_4$. According to analysis given further below, the assumption of $\nu = 0.27$ corresponds to a shear modulus $G_0(\gamma\text{-Si}_3\text{N}_4) = 166 \text{ GPa}$ at a glass phase content of 19 vol.%.

$\langle E_r \rangle$ [GPa]	$E_{\text{IT}} \approx E_Y$ [GPa]	B_0 [GPa]	G_0 [GPa]	ν [–]
275(10)	335(16)	243(12)	132(6)	0.27

Table 3.15: Reduced modulus and derived elastic constants of SN13

If the elastic properties of the glass phase were known, the elastic behavior of SN13 could be modeled as that of a two-component composite material and informations on the shear modulus of $\gamma\text{-Si}_3\text{N}_4$ may be extracted. In the following, such a modeling is outlined, using the Reuss and Voigt rules of mixture for the effective moduli. *The possible effect of pressure-enhancement of the indentation elastic properties at load is **not** addressed.*

For a composite material, the reduced modulus and Poisson's ratio in Equation (2.18) is to be substituted by the effective Moduli. Moreover, the formula

is re-written to directly include the effective shear modulus G_{eff} :

$$\frac{1}{E_{r,\text{eff}}} = \frac{1 - \nu_{\text{eff}}^2}{E_{\text{eff}}} + \frac{1 - \nu_i^2}{E_i} \equiv \frac{1 - \nu_{\text{eff}}}{2 \cdot G_{\text{eff}}} + \frac{1}{E_i^*} \quad (3.8)$$

Again, E_i and ν_i denote the elastic properties of the indenter (usually diamond). The effective moduli of the composite are now approximated by the rules of mixture:

$$\text{upper limit} \quad M_{\text{Reuss}} \equiv M_R = f \cdot M_{\text{glass}} + (1 - f) \cdot M_{\text{Si}_3\text{N}_4} \quad (3.9)$$

$$\text{lower limit} \quad \frac{1}{M_{\text{Voigt}}} \equiv \frac{1}{M_V} = \frac{f}{M_{\text{glass}}} + \frac{(1 - f)}{M_{\text{Si}_3\text{N}_4}} \quad (3.10)$$

$$\text{effective average} \quad M_{\text{eff}} \equiv M_{RV} = \frac{1}{2}(M_R + M_V) \quad (3.11)$$

Where f denotes the volume fraction of the glass phase and M represents the bulk- or shear modulus of the glass and γ -Si₃N₄, respectively. Poisson's ratio of the composite can be explicitly expressed by:

$$\nu_{\text{eff}} = \frac{1}{2} \left(\frac{3B_{RV} - 2G_{RV}}{3B_{RV} + G_{RV}} \right) = \frac{3B_{RV} - G_R - G_V}{6B_{RV} + G_R + G_V} \quad (3.12)$$

The intergranular phase is most likely a Y–Si–Al–O–N glass. Assuming that the high pressure derived material is not too different from the yttrium-rich glasses in regular Si₃N₄-ceramics, typical literature values may be employed: $E_Y = 140$ GPa and $G_0 = 55$ GPa $\Rightarrow B_0 \approx 103$ GPa [195]. The density of the material is not relevant, as f has been determined directly from SEM-images (recall Sect. 3.7.3 on page 130) The bulk modulus B_0 of γ -Si₃N₄ was determined in the aforementioned compression studies. For the following analysis, two values, $B_0(\gamma\text{-Si}_3\text{N}_4) = 290$ and 300 GPa are used. Of all elastic constants necessary to describe E_{eff} , only the shear modulus G_0 of γ -Si₃N₄ (hereafter named $G_{\text{Si}_3\text{N}_4}$) or its Poisson ratio ν , remains unknown. Upper and lower limits for $G_{\text{Si}_3\text{N}_4}$ were determined in two ways:

(1) A certain value for $G_{\text{Si}_3\text{N}_4}$ is assumed and used to calculate the effective reduced modulus $E_r(f)$ as a function of the glass volume fraction. The result

may then be compared to the experimental values for E_r and the measured glass volume fraction f_{exp} :

$$E_r(f) = \left[\frac{1 - \nu_{\text{eff}}(f)}{2G_{\text{eff}}(f)} + \frac{1}{E_i^*} \right]^{-1} \quad \begin{aligned} B_{\text{Si}_3\text{N}_4}, G_{\text{Si}_3\text{N}_4} &= \text{const.} \\ B_{\text{glass}}, G_{\text{glass}} &= \text{const.} \end{aligned} \quad (3.13)$$

(2) G_{eff} (and hence $G_{\text{Si}_3\text{N}_4}$) in Equation (3.14) below are adjusted to a fixed (experimentally derived) value of E_r , while f is varied. In other words: Any weakening of the calculated elastic properties of the composite that would result from an increase of f must be exactly cancelled out by simultaneously assuming a higher $G_{\text{Si}_3\text{N}_4}$.

$$E_r = \text{const.} = \left[\frac{1 - \nu_{\text{eff}}(G_{\text{Si}_3\text{N}_4}, f)}{2G_{\text{eff}}(G_{\text{Si}_3\text{N}_4}, f)} + \frac{1}{E_i^*} \right]^{-1} \quad \begin{aligned} B_{\text{Si}_3\text{N}_4} &= \text{const.} \\ B_{\text{glass}}, G_{\text{glass}} &= \text{const.} \end{aligned} \quad (3.14)$$

The values for the shear modulus $G_{\text{Si}_3\text{N}_4}$ and/or Poisson ratio of γ -Si₃N₄ required to satisfy this condition can then be plotted against f .

The results for these two types of calculations are shown in Figure 3.39 and 3.40, respectively. Fig. 3.39 shows the calculated effective reduced modulus $E_r(f)$ and shear modulus G_{eff} as a function of the volume fraction of γ -Si₃N₄ in the composite. Equation (3.13) was fitted so that the $E_r(f)$ -lines touch the upper and lower error bar of the highest and the lowest measured value (white squares), respectively. The black lines correspond to calculations with an assumed bulk modulus $B_{\text{Si}_3\text{N}_4} = 300$ GPa and the corresponding shear moduli for pure (= 100 vol.%) γ -Si₃N₄ would be 195 and 125 GPa. If γ -Si₃N₄ is assumed to be somewhat more compressible ($B_{\text{Si}_3\text{N}_4} = 290$ GPa), the high estimate for its shear modulus is slightly increased to 205 GPa. In Figure 3.40, the shear modulus of *pure* γ -Si₃N₄, $G_{\text{Si}_3\text{N}_4}$, was treated as a variable and fitted so that $E_r = 281$ GPa (the highest experimental value) is obtained for *every* volume fraction f of the glass phase. The calculations show that the experimental data allows for a shear modulus of 161 GPa, if the true glass phase content is 15 vol.%, 176 if it is around 18 vol.% and 192 GPa, if the amount of the Y–Si–Al–O–N glass within SN13 should be 25 vol.%. In the same range of f -values, the calculated Poisson ratio for γ -Si₃N₄ drops from 0.266 to ~ 0.23 . For comparison, a load-depth

sensing indentation study on β -Si₃N₄ whiskers [196], gave values of $\nu = 0.25$ and 0.35 parallel and perpendicular to the *c*-axis, respectively. Using the value corresponding to 18 vol.% glass phase ($G_{\text{Si}_3\text{N}_4} = 176$ GPa), the Young's modulus E_Y of γ -Si₃N₄ would be ~ 440 GPa, which is significantly higher than both, the upper (329 GPa) and the lower (310 GPa) bound of a dense, polycrystalline β -Si₃N₄ with random grain orientation [196]. This value would be also higher than that of α -Al₂O₃ with $E_Y = 410$ GPa.

It remains to be noted that the value of the effective shear modulus of the *composit*, G_{eff} , that is listed in Table 3.15 is somewhat too low to comply with Teter's empirical G_0 -versus-hardness ranking [8]: According to Teter's data, no solid with a Vickers hardness around 27 GPa and a shear modulus *lower than* 160 GPa has been observed yet. On the basis of the aforementioned analysis, a G_{eff} of this magnitude can only be achieved, if the highest estimate for the shear modulus of γ -Si₃N₄, $G_{\text{Si}_3\text{N}_4} = 205$ GPa, is assumed. In this case, the effective Young's modulus of SN13 would be as high as ~ 380 GPa.

3.8.3 G_0 of γ -Si₃N₄: Current Status of Knowledge

If evaluated according to the standard interpretation of indentation elastic properties, the study of the dense ' γ -Si₃N₄ ceramic' SN13 suggests that the shear modulus of γ -Si₃N₄ is higher than originally assumed in our first work ([82], $G_0 = 148 \pm 16$ GPa). The highest value that complies with the current experimental data is ~ 205 GPa and a value of at least ~ 166 GPa can be assumed with high confidence — from both, the experimental data and the empirical correlation between hardness and G_0 , established by TETER [8]: Because it was coincidentally measured to be harder, γ -Si₃N₄ should have a shear modulus that is *at least* equivalent to that of α -Al₂O₃ (162 GPa, [8]). A violation of this rule would be very unusual, especially for such a highly symmetric crystal structure like spinel with many accessible glide systems for dislocation movement.

In the following, two possible reasons for the likely underestimation of G_0 in our first survey are considered:

- (1) Porosity
- (2) Presence of a weak oxide phase

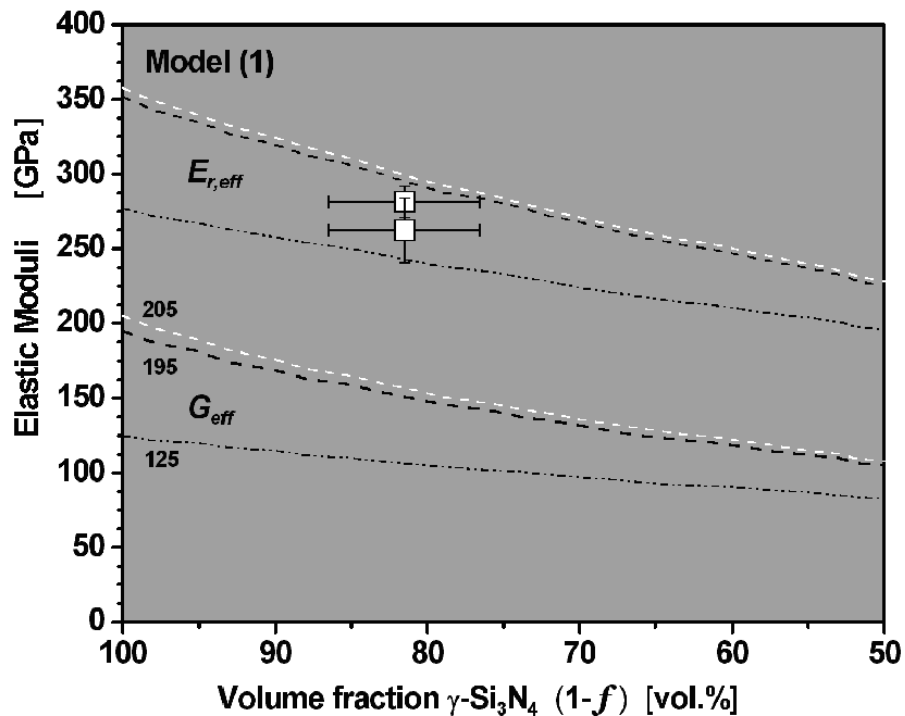


Figure 3.39: Calculated effective elastic moduli of a γ -Si₃N₄/Y-Si-Al-O-N glass composite, fitted to indentation elastic data of SN13 (Equation 3.13)

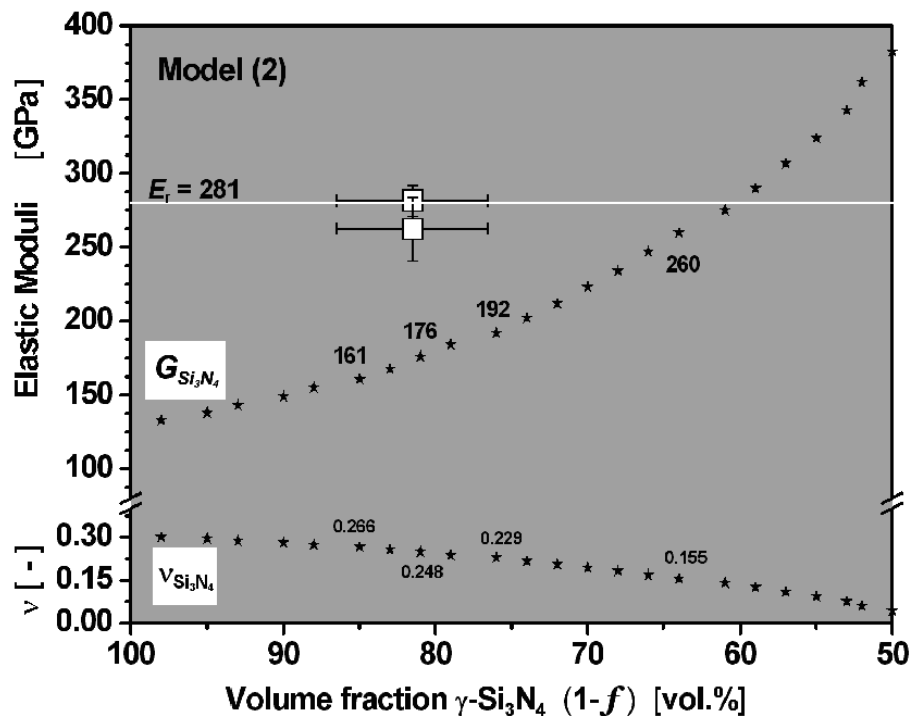


Figure 3.40: Possible shear modulus and Poisson ratio of pure γ -Si₃N₄, fitted to indentation elastic data of SN13 (Equation 3.14)

Ad 1.: SEM investigations have shown that the microstructure of SN08 consists of agglomerates of γ -Si₃N₄ grains that are surrounded by less dense areas with pores and voids (Fig. 3.30 on page 136) that will increase the compliance of the sample surface. Even if one assumes that the indentation is made into the center of a dense and hard agglomerate, the lack of support underneath it would allow the entire agglomerate to be pushed ‘into the sample surface’ and ‘dive up’ again during an indentation cycle. Because the agglomerate itself would behave rigid, the *size of the indentation* and hence the measured *plastic hardness* would *remain unaffected*.

Ad 2.: In [82] the possible presence of a soft glassy phase in the samples was considered for the prediction of the micro- or macrohardness from the obtained nanoindentation data. For the determination of the *elasticity* however, these considerations were omitted. If the 4 wt.% O in SN08 are assumed as silica glass with a density around 2 g/cm³, the volume fraction f of this glass phase would be as high as 11 vol.%.

Figure 3.41 on the next page shows the results of an analysis equivalent to those previously performed for SN13. For the second phase, the elastic constants of fused silica were assumed: $E_Y = 73$ GPa, $G_0 = 31$ GPa and $\nu = 0.17$.

The black dotted lines describe the effective moduli of the γ -Si₃N₄/SiO₂-composite as a function of volume fraction or oxygen content. Starting from a initial value $G_{\text{eff}}(0\%) = G_{\text{Si}_3\text{N}_4} = 260$ GPa, the effective shear modulus and the corresponding $E_r(f)$ drop steeply. At 4% oxygen, $E_r(f)$ is in the range of the experimentally observed value. At this percentage, the composite effective shear modulus G_{eff} represented by the lower black line acquires a value of 178 GPa. This is *larger* than the 148 GPa from [82] which were derived *under the assumption of pure* γ -Si₃N₄ with a bulk modulus of 290 GPa. However, the calculated *effective* bulk modulus of the γ -Si₃N₄/SiO₂-composite with this oxygen concentration is only 209 GPa.

The two rows of white stars again represent the hypothetical shear modulus and Possion’s ratio of γ -Si₃N₄, necessary to keep a constant E_r of 303 GPa (the hori-

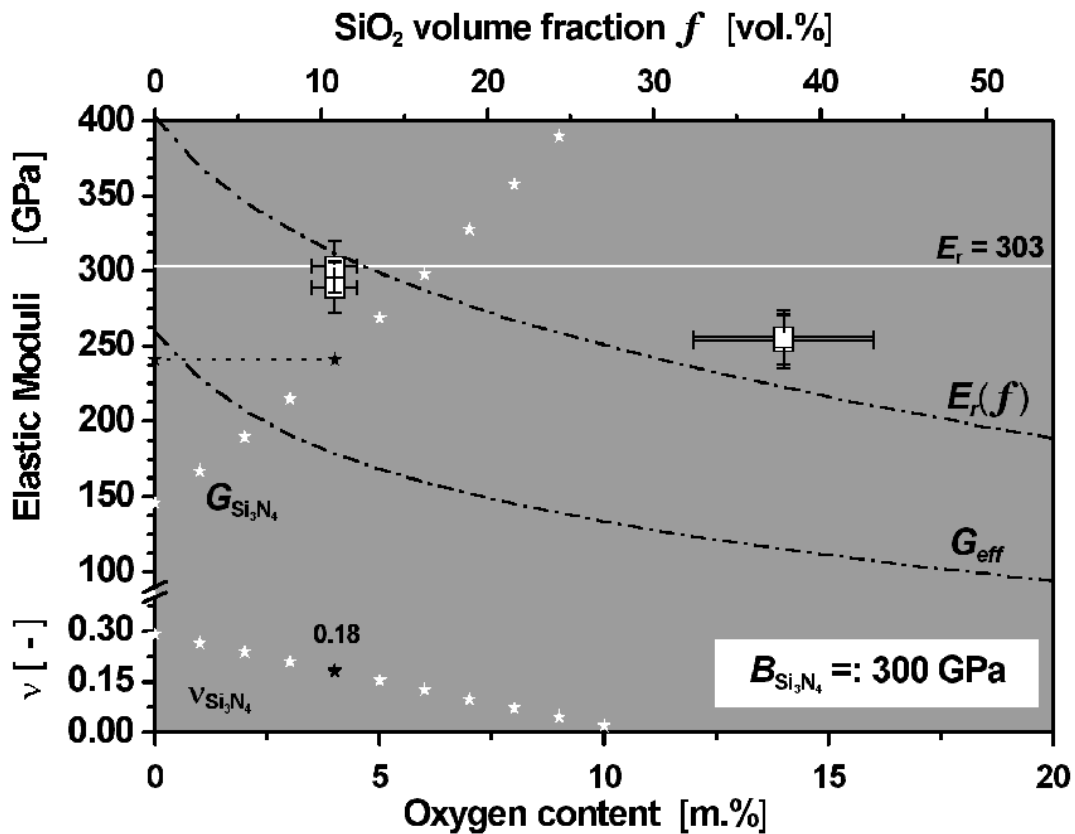


Figure 3.41: Revision of possible shear modulus of pure γ - Si_3N_4 under the assumption that specimens SN08 and SN06 were γ - Si_3N_4 /SiO₂-composites.

zontal white line) for all oxygen concentrations. The values corresponding to 4% oxygen are marked with a black star: $G_{\text{Si}_3\text{N}_4} = 241$ GPa and $\nu = 0.18$.

At still higher oxygen concentration, the upper black $E_r(f)$ -line actually misses the experimental data (SN06 with 14%). This indicates that the assumption of a γ - Si_3N_4 /SiO₂ -mixture is certainly too simple to describe the real mechanical behavior of these materials. A pronounced decrease in both, G_0 and B_0 has also been predicted for the case, where oxygen is actually *incorporated* within the spinel lattice by KROLL [150].

Table 3.16: Assorted elasticity data on γ -Si₃N₄ and related materials

Modulus	γ -Si ₃ N ₄		γ -Ge ₃ N ₄		γ -Sn ₃ N ₄		γ -Al ₂₃ O ₂₇ N ₅	γ -Mg ₂ SiO ₄ ^[124]		MgAl ₂ O ₄ ^[124]	
	theor.	exp.	theor.	exp.	theor.	exp.	exp. ^[111]	theor.	exp.	theor.	exp.
B_0 [GPa]	300 ^[85]	300(10) ^[122]	242 ^[124]	286 ^[197]	204 ^[127]		206–214	185	184	187.4	197.9
	305 ^[124]	308(5) ^[124]	269 ^[117]		186 ^[198]						
	312 ^[181]	290(5) ^[82]	266 ^[199]								
G_0 [GPa]	261 ^[181]	148(16) ^[82]	176 ^[124]	141 ^[197]		64 ^[198]	123–128	127	119	103.0	108.5
	258 ^[124]	205–260*		146 ^[198]							
C_{44} [GPa]	340 ^[85]		235 ^[124]							140	112
	341 ^[124]									148.6	155.4
C_{12} [GPa]	191 ^[124]		165 ^[124]						111	126	148.0
ν [-]		0.20–0.28*		0.29 ^[197] ,		0.34 ^[198]	0.25		0.23		0.27
				0.26 ^[198]							
E_r [GPa]		303(17) ^[82]		295(21) ^[198]		167(36) ^[198]					
		275(10)*									
E_Y [GPa]		379 ^[82]		370 ^[198]		172 ^[198]	307–320				
		335(16)*									
C_{11} [GPa]	533 ^[124]		395 ^[124]					334	327	266.2	282.9

* this work, see Sections 3.8.2 and 3.8.3

In summary, these considerations show that the predicted high values for the shear modulus of γ - Si_3N_4 *cannot be proved wrong* on the basis of currently available experimental data. The question about the *true* shear modulus of γ - Si_3N_4 and the discrepancies between the highest estimates for G_0 that comply with experimental data (205 GPa from SN13, 260 GPa from SN08) is likely to remain until single crystals of γ - Si_3N_4 large enough to measure this important property with more rigorous methods are available.

3.8.4 Indentation Toughness

Crack Bridging in SN13 The surface traces of the Palmqvist cracks extending radially from the Vickers indents were investigated for microstructural toughening mechanisms. The SEM image in Figure 3.42 on the following page shows that the cracks indeed exhibit a prominent zig-zag pattern indicating microfrictional and possibly elastic crack bridging. Figure 3.43 is a magnification from the area above the scale bar in Fig. 3.42. Here, the crack trace went around two single grains which appear to be rotated with respect to their initial orientation. Further separation of the crack surfaces would require further rotation of the grains, which is restrained by their residual contacts to the surrounding material. Via these contacts, the grains are loaded in compression and shear and hence act as “rotational” elastic crack bridges. Figure 3.44 on page 165 finally shows an image of a crack path after plasma etching. It is obvious that the crack propagates preferentially via debonding of the γ - Si_3N_4 /glass interface.

Determination of Indentation Fracture Toughness The conventional Vickers hardness and indentation fracture data of SN13 was evaluated in a similar manner as demonstrated for the NIST reference material SRM 2100 in Section 2.2.5 on page 48. In Figure 3.45 crack radius $\langle c \rangle$ (and indentation radius $\langle a \rangle$) are plotted against the indentation load. It can be seen that also SN13 exhibits a typical c - P dependency described in Section 2.2.2 on page 41. Again, discrepancies between the $\langle c \rangle$ values measured optically and those obtained by the SEM are revealed. In this case however, the $\langle c \rangle$ -values obtained from optical measurement are *smaller* than the SEM-derived ones (compare to Fig. 2.11 on page 51). As the main reason for this, the smaller crack opening of the Palmqvist cracks in

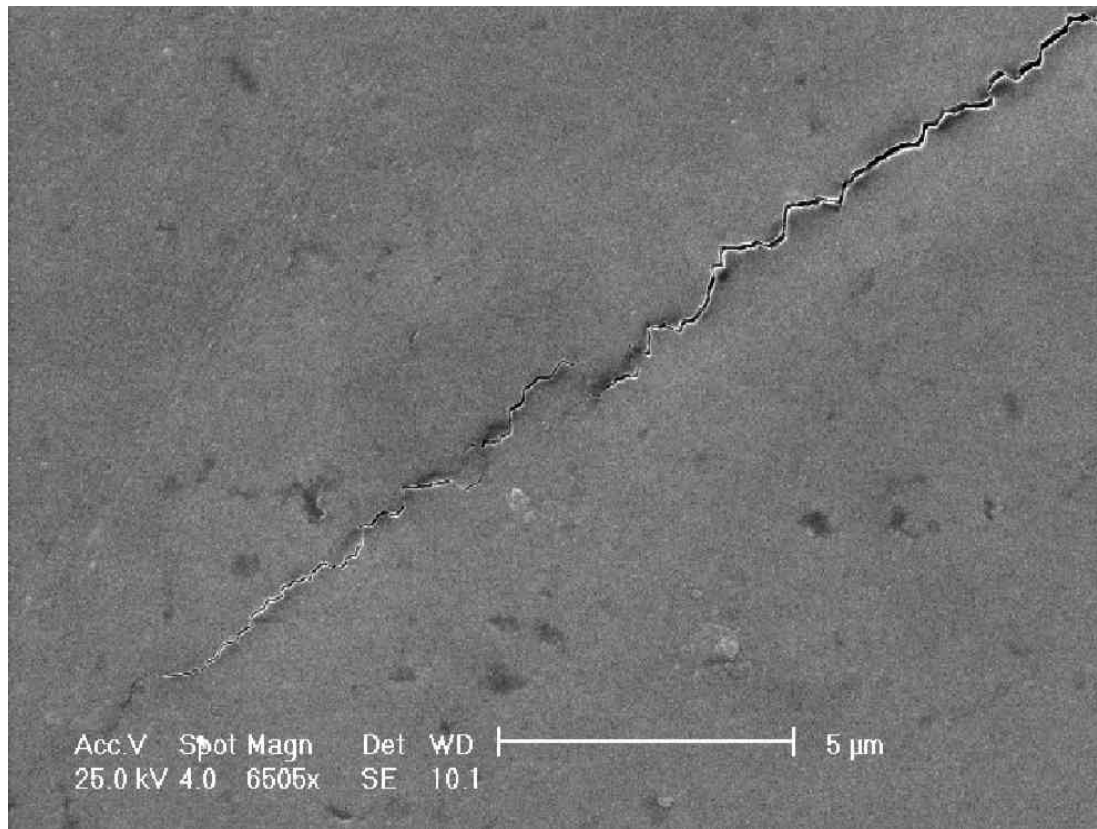


Figure 3.42: Surface trace of a Palmqvist crack in SN13

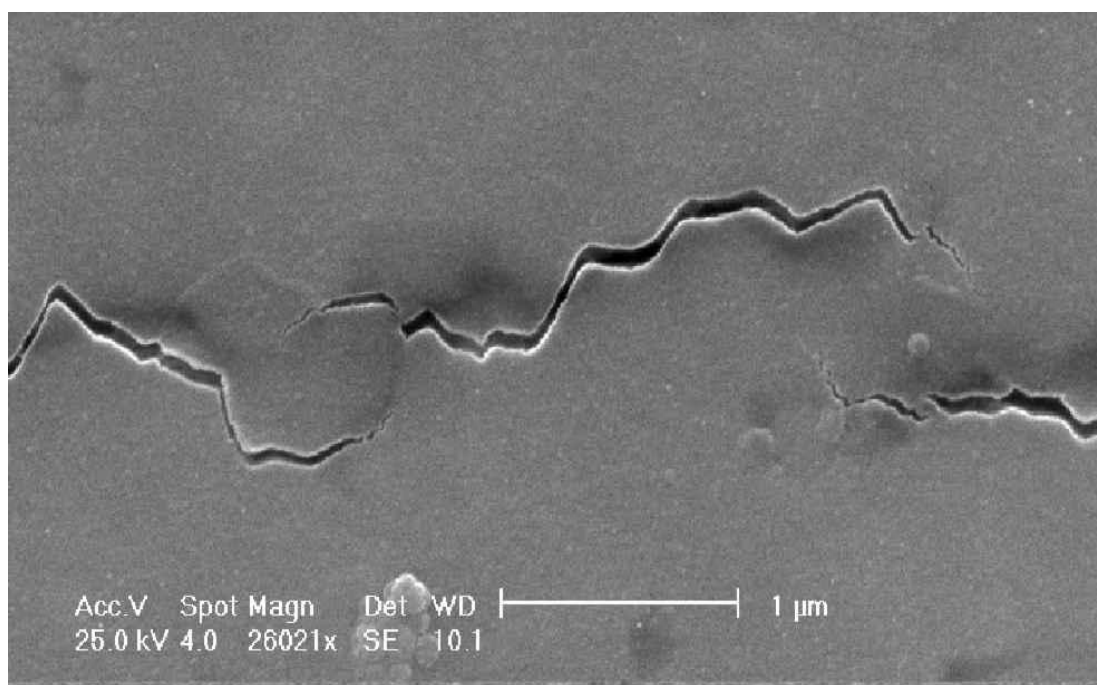


Figure 3.43: Closeup view on individual crack bridges in SN13

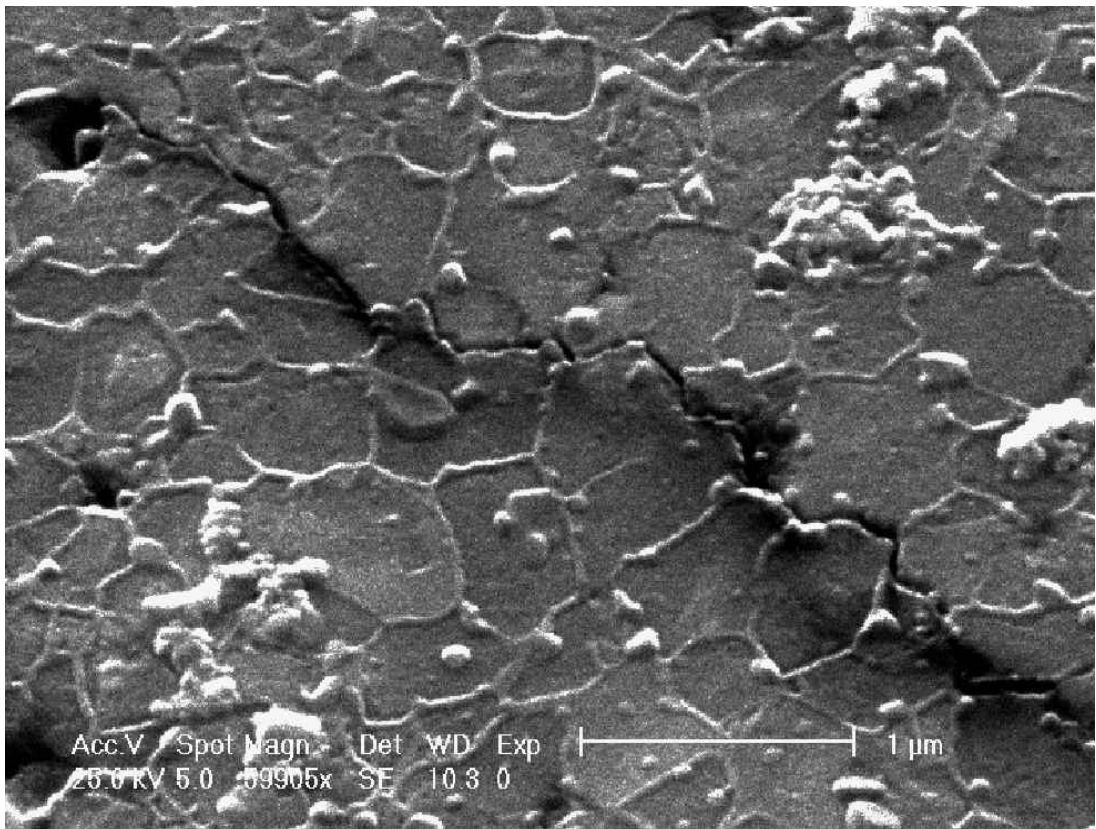


Figure 3.44: Plasma-etched surface of SN13 revealing transgranular crack propagation and grain/matrix debonding

SN13 is assumed: SN13 has different elastic properties than SRM 2100 and was moreover indented at a smaller load range. The very narrow surface traces of the cracks are difficult to resolve under the optical microscope. The true location of the crack tip is missed and $\langle c \rangle^{opt}$ hence measured too short. In the case of the indentations, there are no such contrast problems so that the SEM and optical measures for the indentation radii $\langle a \rangle$ coincide well with one another. Both sets of crack length data were fitted to Equation (2.10), and further treated according to the ‘Anstis-procedure’. The H/E ratios necessary to calculate the fracture toughness were obtained from the Knoop indentations according to the method of Marshall, Noma and Evans, described in Section 2.2.1 on page 38, and calculated from the indentation elastic modulus E_{IT} and normalized Vickers hardness HV_n of SN13, respectively. The results are listed in Table 3.17.

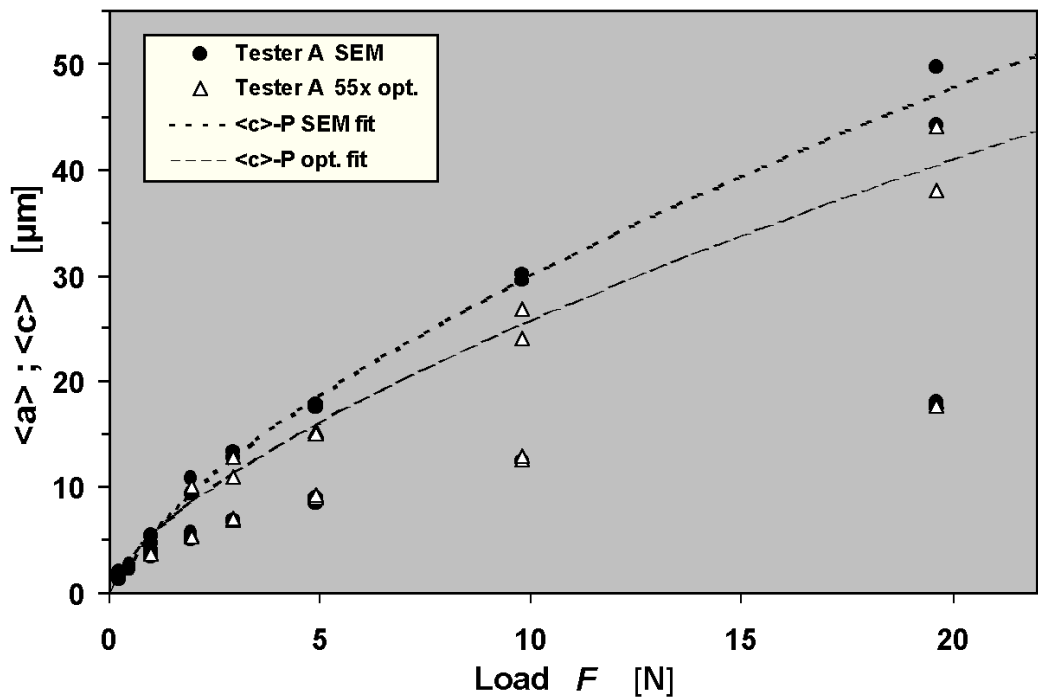


Figure 3.45: SN13: Crack radius plotted versus indentation load

H/E	Source	Value	Scaling factor	Scaled	'Type'
$(H/E)_{MNE}$	55× opt.	0.087(3)	$2/(1.8544 \cdot 1.4229)$	0.066(2)	(1)
$HV_n^{[a]}$ / $E_{IT}^{[b]}$		0.082	$2/1.8544$	0.088	(2)

^[a] HV_n (optical) = 27.4 GPa (page 143) ^[b] E_{IT} = 355 GPa (Table 3.15 on page 155)

Table 3.17: Hardness-to-modulus ratios of SN13

It can be seen that in this case the agreement between the *unscaled* ratios is better than after applying the ‘correction factor’ for the Knoop geometry (1.4229). As discussed further below, knowledge of the ‘appropriate’ H/E ratio appears to be a critical point for this method, especially for unknown and not well characterized materials. HV_n , as well as E_{IT} and $(H/E)_{MNE}$ are subject to experimental errors, moreover other factors than just the indenter geometry may contribute to the correlation between the two differently determined hardness-to-modulus ratios. This latter problem is beyond the scope of this thesis and

will not be considered any further. Using both types of H/E values and the fit results for χ , the indentation fracture toughness was calculated (Table 3.18).

Data	P_0	χ	$K_{\text{IC-IF}}^{(1)}$	$K_{\text{IC-IF}}^{(2)}$
Source	[N]	[$\mu\text{mN}^{-2/3}$]	[$\text{MPa m}^{1/2}$]	[$\text{MPa m}^{1/2}$]
optical	–	5.59	4.7	4.1
	0.06	5.57	4.7	4.1
SEM	–	6.41	3.8	3.3
	0.21	6.52	3.7	3.2

(1),(2) see Table 3.17 on the preceding page

Table 3.18: Indentation fracture toughness values of SN13 according to the ‘Anstis-procedure’

The values obtained by this method are to be compared to those produced with the Shetty formula (2.13). The corresponding $K_{\text{IC-IF}}$ -values, plotted as a function of crack length, are shown in Figure 3.46, along with those of the SRM 2100 β - Si_3N_4 reference material. The increasing toughness at higher crack radii indicate the onset of an R-curve behavior also in the case of SN13. The load range applicable to this small sample was however too limited in order to proof this with certainty. Clearly evident is the higher indentation fracture toughness of SN13: The calculated values vary between 5 and 7 $\text{MPa m}^{1/2}$, while the plateau value for the reference material is given by 4.57 $\text{MPa m}^{1/2}$. In contrary to the measurements on SRM 2100, the $K_{\text{IC-IF}}$ results from the Shetty method differ considerably from those determined by the Anstis procedure. In his comparative study on different indentation toughness formulae, DUSZA found that the Anstis formula indeed underestimates the toughness of β - Si_3N_4 ceramics, as compared to both, SENB measurements and the Shetty formula [72]. The magnitude of the discrepancy was however less: $K_{\text{IC-IF}}^{\text{Anstis}} : K_{\text{IC-IF}}^{\text{Shetty}} : K_{\text{IC}}^{\text{SENB}} \approx 80:93:100$.

Again given the fact that SN13 is the product of a single experiment without optimization, its toughness between 5 and 7 $\text{MPa m}^{1/2}$ is quite remarkable. Toughness values slightly above 6 $\text{MPa m}^{1/2}$ are reported for commercial cutting tools with high c -BN content, such as the DBA 80 material that was used as a hardness

reference. For binder-free, polycrystalline ("translucent") *c*-BN TANIGUCHI and coworkers measured an indentation toughness of $5 \pm 0.5 \text{ MPa m}^{1/2}$ based on the Anstis-method [36]. This value was later corrected to $6.8 \text{ MPa m}^{1/2}$, according to a more precise determination of the Young's modulus of the *c*-BN material [200]. Binder-free, polycrystalline *c*-BN exhibits also superior hardness: A constant Vickers hardness of 49 GPa was observed at high loads exceeding 50 N.

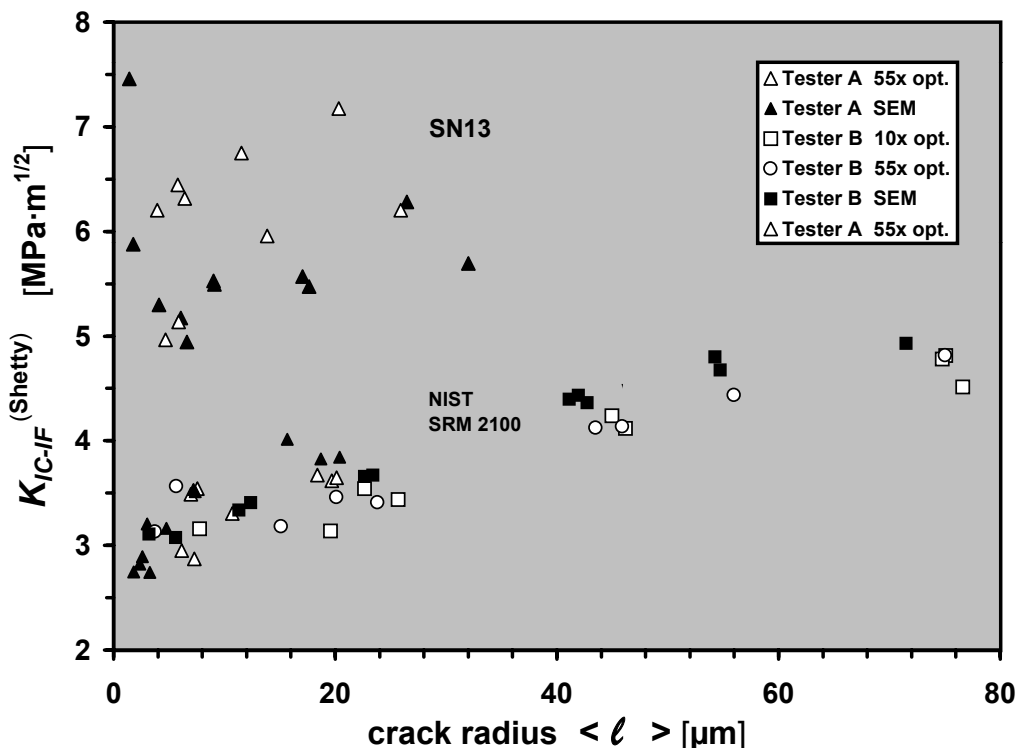


Figure 3.46: Indentation fracture toughness of SN13 and SRM 2100 calculated for each indentation according to the Shetty formula (Eqn. (2.13) on page 45).

Recently, the transgranular and intergranular fracture toughness and energy release rate of covalent crystals, among them γ -Si₃N₄ and *c*-BN, were investigated theoretically by TROMANS and MEECH. On the basis of a semiempirical approach, including experimentally determined elastic constants to calculate the energy for bond separation, they obtained values of 0.94, 1.14 and $2.74 \text{ MPa m}^{1/2}$ for the transgranular fracture of β -Si₃N₄, γ -Si₃N₄ and *c*-BN, respectively [185]. The values obtained for intergranular fracture (i.e. including crack paths along

grain boundaries) were even lower. Both results are to be seen as estimates for the intrinsic or crack-tip-toughness K_{I0} of these materials (valid for crack length $c \rightarrow 0$). In the first place, they thus give trends for the friability of single grains or small agglomerates, which is important with respect to their use as particulate grinding media and the energy input necessary to obtain fine powders that are more easy to sinter. In contrast, the experimental values given above were obtained from finite crack lengths of several tens of microns, and—as evidenced by electron microscopy—include additional contributions from the microstructure (such as crack bridging, recall electron micrographs on page 164). Comparison between the translucent c -BN noted above and tough β - Si_3N_4 -based ceramics with $K_{Ic} > 6 \text{ MPa m}^{1/2}$ shows that microstructural effects easily nivelize the influence of the intrinsic toughness K_{I0} and can clearly dominate the performance of a monolithic ceramic material. Moreover, surface re-organization, emission of sound, electrons and the occurrence of surface charges provide further contributions to K_{I0} which could not be recognized by the simple bond-breaking model of Tromans and Meech. According to one of the latest investigations published by KOUNGA et al., the experimental value for K_{I0} of β - Si_3N_4 is found to be $1.7 \text{ MPa m}^{1/2}$ [201].

3.8.5 A Note on the (Micro-)Mechanical Properties of $\gamma\text{-Ge}_3\text{N}_4$ and $\gamma\text{-Sn}_3\text{N}_4$

A study on the hardness, elasticity and fracture toughness of the two remaining homologous spinel nitrides $\gamma\text{-Ge}_3\text{N}_4$ and $\gamma\text{-Sn}_3\text{N}_4$ was published by SHEMKUNAS et al. in May 2004 [198]. Dense sintered specimen were obtained by multianvil compression and subjected to a set of testing procedures very similar to those applied for $\gamma\text{-Si}_3\text{N}_4$ throughout this thesis: Via combination of nanoindentation, Vickers hardness testing and by employing the available (experimental and theoretical) data on the bulk moduli of $\gamma\text{-Ge}_3\text{N}_4$ and $\gamma\text{-Sn}_3\text{N}_4$, the corresponding shear moduli G_0 and Poisson's ratios ν were derived. Hardness and toughness are given in Table 3.19, while the elasticity data has been included in Table 3.16 on page 162. Both, elasticity and hardness data of the element group 14 spinel nitrides gives a consistent image that was to be expected in terms of previous knowledge such as the atomic volumes and bond lengths (recall Fig. 3.15 on page 110, the melting points of the pure elements and finally the comparatively low difference between the hardness of $\beta\text{-Si}_3\text{N}_4$ and $\beta\text{-Ge}_3\text{N}_4$: The values of all properties drop somewhat from $\gamma\text{-Si}_3\text{N}_4$ to $\gamma\text{-Ge}_3\text{N}_4$ and then decrease steeply for $\gamma\text{-Sn}_3\text{N}_4$: With a microhardness of $HV_{0.1} = 28$ GPa, $\gamma\text{-Ge}_3\text{N}_4$ is for example still well above many conventional nitride bulk ceramics, such as $\beta\text{-Si}_3\text{N}_4$ or β -sialons, while $\gamma\text{-Sn}_3\text{N}_4$ with $HV_{0.1} = 11$ GPa is barely harder than pure silicon. The low indentation fracture toughness and the high effort required to obtain dense-sintered $\gamma\text{-Sn}_3\text{N}_4$ (multianvil compression of separately synthesized powder at 23 GPa, [198]) may be due to the fact that tin oxides are mostly crystalline, while Si and Ge are capable of forming glassy oxides that can act as a cohesive film between adjacent nitride grains.

Material	Grain size D [μm]	H_c^* [GPa]	Load [mN]	$HV_{0.1}$ [GPa]	$K_{\text{IC-IF}}^\dagger$ [MPa $\text{m}^{1/2}$]	Load [kg]
$\gamma\text{-Ge}_3\text{N}_4$	n.n.	31(6)	5	28(5)	2.3	1
$\gamma\text{-Sn}_3\text{N}_4$	0.1–1	13(5)	3	11(2)	1.4	0.1

* "Nanohardness", cube corner indenter [†] Authors also used Eqn. (2.9), see page 43

Table 3.19: Hardness and indentation fracture toughness data of $\gamma\text{-Ge}_3\text{N}_4$ and $\gamma\text{-Sn}_3\text{N}_4$, cited from [198]. Values in parenthesis give the maximum observed deviation from average.

3.8.6 Thermal and Oxidation Stability of γ -Si₃N₄

Own experiments In the first announcement of γ -Si₃N₄, we already were able to prove that it is metastable to at least 700 K [85]. A second attempt using MAP-derived material in an in situ X-ray measurement showed that the material also survives heating to 760 °C. In situ studies were limited to this temperature due to the capabilities of the employed furnace. Using other facilities, the maximum achievable temperature would have been constrained by the softening temperature of the silica capillaries (~1200 °C) that would have to be used to carry the powdered sample material. The underlying experiment was nevertheless used to study the thermal expansion of γ -Si₃N₄ up to 760 °C, which will be reported within the next section in more detail.

Measurements reported in Literature Since these above mentioned attempts, a high thermal stability of γ -Si₃N₄ was documented by two other groups. An elaborate high temperature study was presented in 2001 by SEKINE and MITSUHASHI [186]. The researchers used shock-synthesized γ -Si₃N₄ powder, that had been subsequently purified and separated from remanent low pressure Si₃N₄ phases and coexisting amorphous (oxygen-rich [145]) material via a treatment with hot hydrofluoric acid. The samples were investigated by DTA/TG up to $T_{max} = 1480$ and 1520 °C at heating rates between 5 and 20 K/min in Ar atmosphere. In agreement with earlier* studies,[125, 146] it was found that β -Si₃N₄ is the major (final) transformation product and that ~5% of the initial γ -Si₃N₄ survived heating to 1790 K at 5 K/min, indicating slow kinetics of the back-transformation. The onset of the back-transformation of the oxygen-free material at ~1400 °C was shifted to higher temperatures compared to previous DTG runs with impure material [146, 186] and a strong exothermic peak was observed between 1350 and 1500 °C. Calibrating the peak area for the pure material to the melting of nickel, Sekine et al. determined the enthalpy difference between γ -Si₃N₄ and β -Si₃N₄ to be -29.2 ± 3.5 kJ/mol. This value is valid for temperatures where the transformation had been observed and hence cannot be directly compared to the theoretical zero-Kelvin energy differences of -0.16 and -0.2 eV

*although [146] was submitted one month *before* [186] it was published about half a year later

per atom (i.e. -107 and -134 kJ/mol) calculated by Kroll and Tatsumi*. Sekine et al. suggest these values to be too high, even taking into account the effect of temperature. Direct comparison of the measured energy differences between the high and low pressure forms of SiO_2 and Si_3N_4 is however well possible and by doing so, Sekine et al. find that the SiN_6 arrangement in $\gamma\text{-Si}_3\text{N}_4$ is energetically more favourable than the SiO_6 octahedron in stishovite. This is simply another way to look on the large difference in the thermal stability of these phases: 600 versus 1400 °C.

The measurements of Sekine and Mitsuhashi demonstrate that the thermal stability of $\gamma\text{-Si}_3\text{N}_4$ is in the range of the $c\text{-BN} \rightleftharpoons h\text{-BN}$ equilibrium (~ 1400 °C) [40, 35] and the graphitization onset of diamond (~ 1500 °C) [39]. It thus fulfils an important prerequisite for a *useful* high-pressure derived hard material, that was already explained in Section 1.5.2 on page 14. An earlier study on bulk- $\gamma\text{-Si}_3\text{N}_4$ shows that a kinetic stabilisation of the γ -phase up to higher temperature may be possible: JIANG et al. [125] annealed part of their MAP-synthesized sample (recall Section 3.3.4 on page 89) at 1150 °C, 1250 °C, 1400 °C and 1600 °C **in air**, for 30 min each time. Upon heating, the initially dense sintered, transparent sample turned black and developed cracks. Taking XRD-patterns after each annealing step, α - and $\beta\text{-Si}_3\text{N}_4$ were found only after the highest temperature had been applied. Some of the $\gamma\text{-Si}_3\text{N}_4$ remained even after this treatment, while in the case of loose powders of Sekine, almost all $\gamma\text{-Si}_3\text{N}_4$ had transformed upon heating to 1500 °C **in argon**. This shows that dense $\gamma\text{-Si}_3\text{N}_4$ ceramics may have also a well acceptable resistance to oxidation.

It remains to be clarified, by which reaction pathway the desintegration of $\gamma\text{-Si}_3\text{N}_4$ occurs. Jiang et al. suggest it to proceed along a *subsequent* reaction $\gamma \rightarrow \alpha \rightarrow \beta$. This interpretation of their data is based on the statement, that the $\alpha \rightarrow \beta$ transformation generally occurs above 1400 °C, cited from [202]. Jiang omitted to mention that $\alpha\text{-Si}_3\text{N}_4$ can persist to even 2150 °C, unless a liquid phase is present [167]. However, *this* high value was measured for comparatively large single crystals and may not apply for crystallite sizes of only several ten nanometers, which was the range for both, the shock-synthesized and the multianvil-derived $\gamma\text{-Si}_3\text{N}_4$.

*see Sec. 3.6.2 on page 117

A dissolution–precipitation mechanism, similar to the liquid phase sintering of conventional Si₃N₄ ceramics, where the unstable α -phase dissolves while β -Si₃N₄ precipitates, may have mediated the decay of γ -Si₃N₄ in the case of Jiang’s multi-anvil sample and the early studies of Sekine: Here, powder-XRD revealed cristobalite to be present in the oxidized samples and from the weight gain after heating to 1500 °C, formation of ~7 wt.% SiO₂ was deduced. In the purified samples heated under argon however, the content in cristobalite *and also* α -Si₃N₄ was found to be negligible [186], so that the presence of β -Si₃N₄ can not be attributed to oxygen. Neither the data presented by Jiang et al, nor those provided by Sekine and coworkers do, *with certainty*, allow to rule out two competing solid-solid reactions, namely $\gamma \rightarrow \alpha$ and $\gamma \rightarrow \beta$. All we can say is, that in this case, the $\gamma \rightarrow \beta$ would be faster. Future experiments will be necessary to establish an exact understanding of the transformation mechanism(s), which will be another prerequisite to make full use of γ -Si₃N₄ and to fathom its principal limitations as an engineering material.

3.8.7 Coefficient of Thermal Expansion

To determine the thermal expansion of γ -Si₃N₄, the lattice parameter of a multi-anvil-derived sample was measured at nine steps between room temperature and 750 °C (1020 K) by Dr. Helmut Ehrenberg at HASYLAB, DESY synchrotron source, Hamburg, Germany. Thermal expansion data is also available from two other groups: (1) The combined compressibility and thermal expansion study on multi-anvil-synthesized γ -Si₃N₄ by JIANG et al. which had already been mentioned in Section 3.8.2 on page 148 [189]. The same γ -Si₃N₄ sample was later investigated by PASZKOWICZ et al. with respect to its low temperature expansion behavior [203]. (2) another study on shock-synthesized γ -Si₃N₄ powder in the temperature range between 300 and 1000 K was published by HINTZEN, FANG, SEKINE and colleagues [204]. The Eindhoven group around Hintzen and Fang also performed first-principles calculations of the thermal properties of γ -Si₃N₄ [153]. I wish to thank H.T. Hintzen and C.M. Fang for interesting discussions and for sharing their data prior to publication. This section also benefitted a lot from an e-mail correspondence with P. Kroll.

Experimental Procedure

Material from MAP-experiment SN08 was pulverized and mixed with NaCl serving as temperature standard and wavelength calibrant, and filled in a quartz glass capillary under air. The capillary was placed in a furnace for in situ XRD measurement (Stoe Company). The lattice parameters $a(T)$ and their standard deviation were obtained by a least-squares fit of 5 peak positions of each diffractogram recorded at temperature T . The quality of the diffractograms unfortunately was not sufficient to retrieve the anion parameter u as a function of temperature by Rietveld refinement.

Results and Discussion

Temperature Dependence of Lattice Parameter A comparison of all available data on γ -Si₃N₄ is shown in Figure 3.47 on the next page. With a small difference of only 0.001 Å, the lattice constants of the own measurements coincide well with those provided by Jiang et al. The researchers from Denmark also used multianvil-synthesized γ -Si₃N₄ [125] and performed their measurements at a synchrotron facility. The lattice constants measured by Hintzen et al. are about 0.035 Å larger, probably due to a high defect density in the shock synthesized material. The overall trend of the three measurements is similar up to a temperature of 800 K. Above this point, the expansion of the shock synthesized material appears to increase, while the own measurement indicates a slight degression. The expansion according to Jiang et al. appears to proceed unaltered. Figure 3.48 shows the results of the own measurements alone. The error bars correspond to the standard deviations as obtained from a Rietveld refinement using the software package GSAS [205]. The thermal expansion behavior of γ -Si₃N₄ is not linear and can be fitted to a third order polynomial function (dotted line) of the form:

$$a(T) = a_0^* + a_1 \cdot T + a_2 \cdot T^2 + a_3 \cdot T^3 \quad (3.15)$$

In order to comply with the boundary conditions $\alpha_{\text{th}} = 0$ and $\partial\alpha_{\text{th}}/\partial T = 0$ at 0 K, the linear coefficient a_1 was set to zero (Table 3.20). Including the $a_3 \cdot T^3$ term helps to model the tendency of thermal expansion towards a constant value at high temperature, as demanded by the Dulong and Petit-rule ($\alpha_{\text{th}} \propto C_p \propto 3R$).

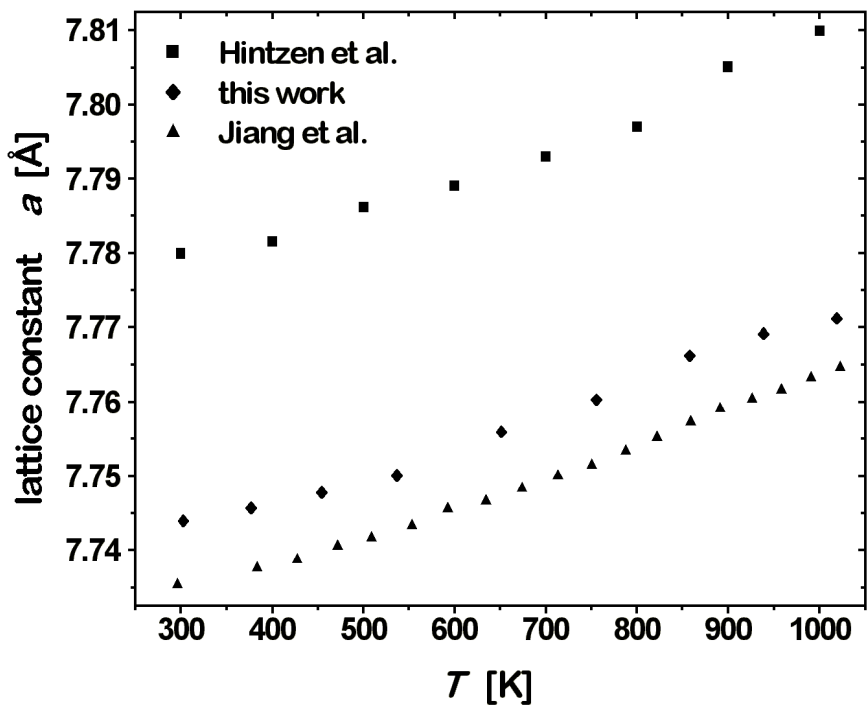


Figure 3.47: Comparison of currently available thermal expansion data on γ - Si_3N_4 .

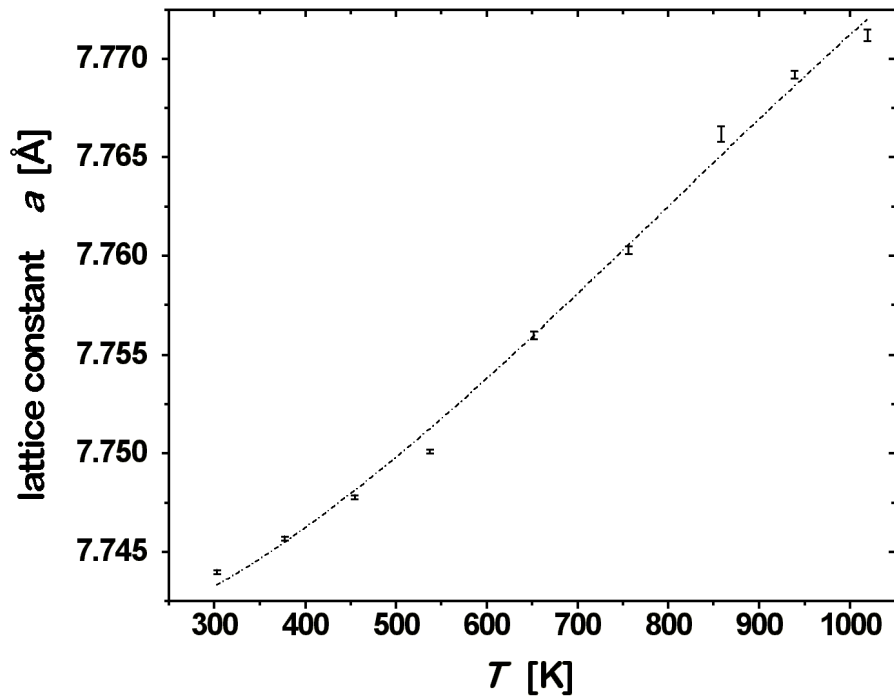


Figure 3.48: Detail plot of own expansion data.

The same function and conditions had also been chosen by Hintzen et al. [204]. The fit results for the individual data sets are given in Table 3.20.

Ref.	Temp. range [K]	a_0^* [Å]	$a_1 \cdot 10^5$ [Å/K]	$a_2 \cdot 10^8$ [Å/K ²]	$a_3 \cdot 10^{11}$ [Å/K ³]	Statistics	
						χ^2	$R^2[10^{-7}]$
γ -Si ₃ N ₄	300–1020	7.739(1)	$\equiv 0$	5.5(7)	−2.3(7)	0.9951	7.1
	300–800	7.7408(7)	$\equiv 0$	3.4(6)	0.097(7)	0.99813	1.9
NaCl	300–1020	5.611(1)	$\equiv 0$	38(1)	15(1)	0.99982	13.1
Hintzen [‡] [204]	300–1000	7.7334	$\equiv 0$	3.8654	−0.49271		
	300–1000	7.777(1)	$\equiv 0$	3.3(9)	(0.8)	0.99439	9.1
	300–800	7.775(1)	$\equiv 0$	5(1)	−2.0(1.0)	0.99441	4.6
Jiang [‡] [189]	296–1074	7.7274	2.0893	1.5537	$\equiv 0$		
	296–1074	7.7270(1)	2.0(2)	1.5(2)	$\equiv 0$	0.99874	1.4
	296–1074	7.7313(3)	$\equiv 0$	4.9(2)	−1.7(1)	0.99441	0.7

Table 3.20: Fit results for the three currently available thermal expansion data sets shown in Fig. 3.47. The corresponding fit results from literature are marked with [‡]

Coefficient of Thermal Expansion The linear expansion coefficient α_{th} can be derived from the temperature dependency of the lattice constant $a(T)$ according to:

$$\alpha_{\text{th}}(T) = \frac{1}{a(T)} \cdot \frac{\partial a(T)}{\partial T} \quad (3.16)$$

Care has to be taken with this procedure, if $a(T)$ is determined by fitting experimental data to an empirical function as in the present case. This is because the result is decoupled from the measured values and solely depends on the chosen function and its fit parameters such as a_0^* , a_2 and a_3 . This is vividly documented in Fig. 3.49 on the next page: In (A), the original literature data from Hintzen and Jiang and the theoretical prediction of $\alpha_{\text{th}}(T)$ provided by Fang is shown. In their publication [189], Jiang et al. used a second order polynomial of the form $a(T) = a_0^* + a_1 \cdot T + a_2 \cdot T^2$ that does not comply with the boundary conditions mentioned above. Re-evaluation of the data using Equation (3.15) yields a result

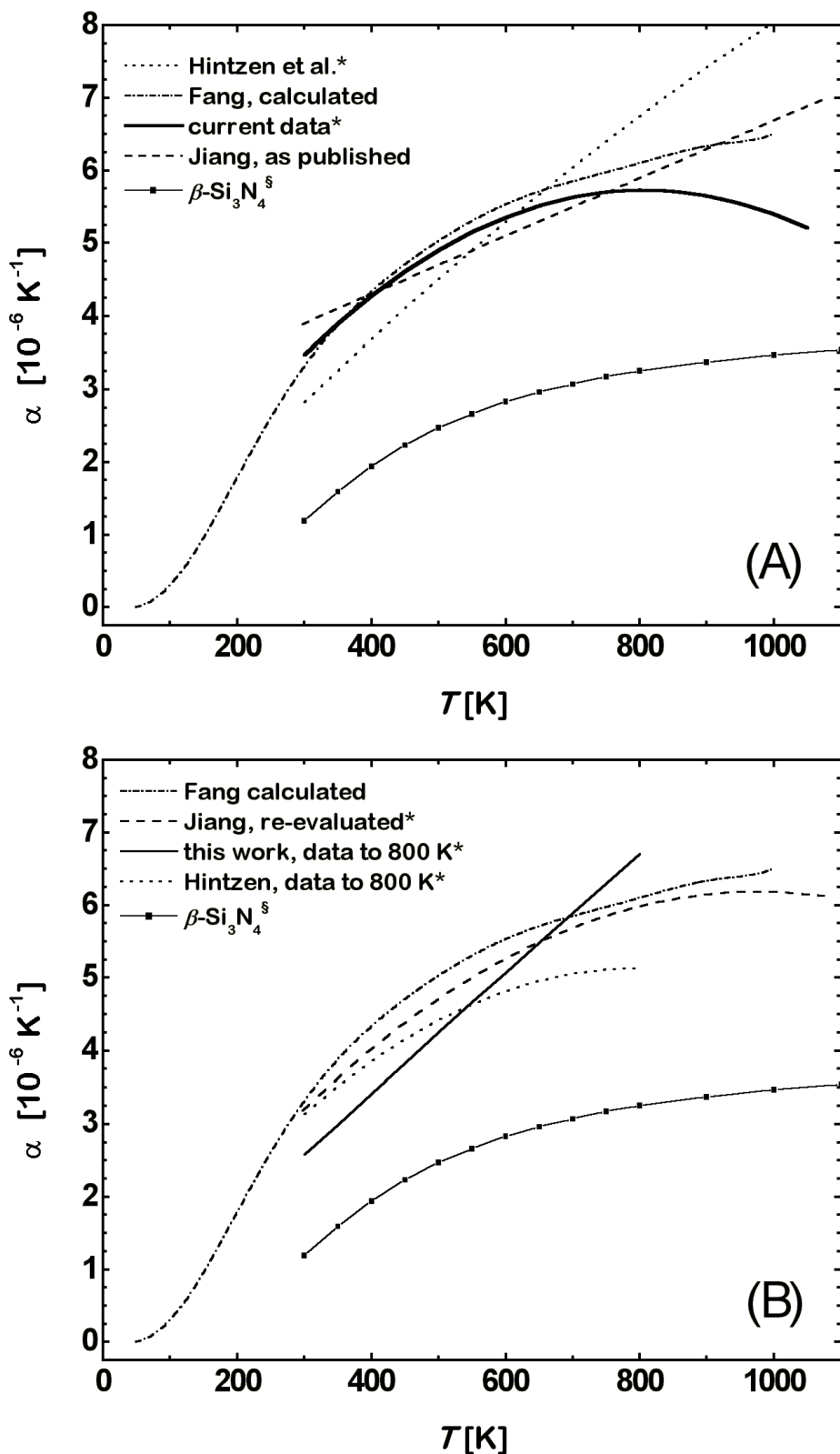


Figure 3.49: Linear expansion coefficient α_{th} (of $\gamma\text{-Si}_3\text{N}_4$) determined by different approaches. Lines marked with * obtained by fitting Equation (3.15). [§]Data for $\beta\text{-Si}_3\text{N}_4$ from [206]

that compares very well to Fang's prediction (Fig. 3.49 (B)). Still more complex polynomials containing $a_4 \cdot T^4$ and $a_{-1} \cdot T^{-1}$ terms were used in a more recent study by PASZKOWICZ et al. (see below).

The solid black line in (A) corresponds to the temperature dependence of α_{th} obtained by applying Equations (3.15) and (3.16) to *all* own data points shown in Fig. 3.48. Like Jiang's data, it gives a good resemblance of the theoretical prediction, especially between 300 and 700 K. Above this temperature, the calculated $\alpha_{\text{th}}(T)$ reaches a maximum at 800 K and then decreases again. It has been already mentioned that the last two data points in Fig. 3.48 seem to indicate a degression in the expansion behavior. However, assuming a real physical meaning behind this appears questionable, because a decrease of thermal expansion coefficients towards high temperatures is observed rarely and only for specific directions in less symmetric structures. The drop is probably a result of inaccuracies in the measurement combined with the small number of data points and the empirical nature of applied fitting function (3.15): The data set of Jiang et al. contains more data points and the agreement to the predicted curve in (B) is kept up to higher temperatures. At the high temperature end of the data range however, the curve also passes through a maximum at about 1000 K and the mathematical model fails to extrapolate according to physical reality. Fig. 3.49 (B) moreover shows that a better agreement between the data provided by Hintzen and the theoretical prediction may be reached, if one omits the last two data points above 800 K. Similar treatment of the own data however (fitting without the two last measurements that apparently indicate a decrease of α_{th} above 800 K) leads to a very different 'expansion behavior' (solid black line).

A low temperature thermal expansion measurement using the identical sample as in [189] was published in 2004 by PASZKOWICZ and colleagues [203], along with a revision of the high-temperature expansion data of [189] and theoretical calculations of the lattice parameter over the entire temperature range. The measurement down to a temperature of 14 K shows that the thermal expansion coefficient of $\gamma\text{-Si}_3\text{N}_4$ approaches zero for $T < 100$ K. The low- (LT) and high temperature (HT) experimental data was fitted to the following equations [203]:

$$a_{LT}(T) = 7.73248 - 2.809 \cdot 10^{-8} T^2 + 3.002 \cdot 10^{-10} T^3 - 3.679 \cdot 10^{-13} T^4 \text{ \AA} \quad (0-393 \text{ K})$$

$$a_{LT}(T) = 7.72026 - 3.204 \cdot 10^{-5} T + 9.911 \cdot 10^{-9} T^2 + 1.256 T^{-1} \text{ \AA} \quad (393-1673 \text{ K})$$

Comparison to β -Si₃N₄ Irrespective of the precise temperature dependency, it is obvious from Fig. 3.49 that the thermal expansion coefficient of γ -Si₃N₄ is notably larger than that of the low pressure polymorph β -Si₃N₄, the data of which was taken from a compilation of BRULS, HINTZEN and coworkers [206]. While $\alpha_{\text{th}}(\beta\text{-Si}_3\text{N}_4)$ increases from 1 to $3 \cdot 10^{-6} \text{ K}^{-1}$ within the shown temperature range, it is about 3 for γ -Si₃N₄, increasing to $\sim 6.5 \cdot 10^{-6} \text{ K}^{-1}$. This is consistent with the result obtained by PASZKOWICZ et al. ($3.16 \cdot 10^{-6} \text{ K}^{-1}$ at 300 K) [203] and the theoretical investigations published in [153]: $3.3 \cdot 10^{-6} \text{ K}^{-1}$ at 300 K and $6.5 \cdot 10^{-6} \text{ K}^{-1}$ at 1000 K.

Atomistic aspects of expansion behavior As α_{th} relates to anharmonicity, this indicates that the interatomic potential of the Si–N bond in cubic γ -Si₃N₄ is less symmetric than in the hexagonal β -Si₃N₄, which also means that it is *less covalent*! This fact is only surprising at first sight: First, it is to be noted that interatomic potential is mainly determined by the nearest neighbor interactions, which are given by the different coordination polyhedra, SiN₄, NSi₃, SiN₆ etc. The symmetry of the crystal structure is therefore of minor importance. Secondly, it was repeatedly mentioned, that the coordination numbers in γ -Si₃N₄ are increased. As explained in Section 1.4.2 on page 6, this leads generally to a more spherical distribution of the electrons and hence to a decrease of electron density along the Si–N bond axis. Thirdly it was discussed in Section 3.1.3 on page 76, that the two different silicon coordinations in γ -Si₃N₄ imply the absence of local electroneutrality and thus lead to stronger ionic interactions within γ -Si₃N₄ as compared to β -Si₃N₄. These electrostatic considerations were also used by Hintzen et al. [204] to interpret the different expansion behavior of the Si^{tet}–N and Si^{oct}–N bond found by Jiang et al. [189]: According to their structural refinement of the temperature dependent XRD data, the anion parameter \mathbf{u} varies with temperature so that the overall expansion is due to the increase of the octahedral bond length, whereas the SiN₄ tetrahedron remains almost constant in size. On the basis of bond sum calculations, Hintzen et al. argue that an in-

crease of $d(\text{Si}^{\text{oct}}\text{-N})$ helps to diminish the charge imbalance, while an increase of $d(\text{Si}^{\text{tet}}\text{-N})$ would increase it. The same phenomenon can also be seen under the aspect that the SiN₆ octahedron is actually the metastable component of $\gamma\text{-Si}_3\text{N}_4$. Accordingly, upon thermal activation this unit will be increasingly de-stabilized and finally collapse to result in an all-tetrahedral coordination of silicon again. Kroll suggests therefore an abnormal increase of α_{th} when T is approaching the metastability limit of $\gamma\text{-Si}_3\text{N}_4$.*

3.8.8 Specific Heat and Thermal Conductivity

Hintzen, Fang and coworkers combined their thermal expansion data and calculations on the basis of density functional theory to determine further important thermal and thermodynamic properties of $\gamma\text{-Si}_3\text{N}_4$ [204, 153]. As already mentioned, a theoretical value for the thermal expansion coefficient was derived from calculated phonon spectra that were further used to derive the specific heat and the Raman and IR-active vibrational modes. The latter will be treated in more detail within the next section. Part of the procedures used to calculate the thermal properties from the acquired data had been published in a preceding paper [206]. The results for $\gamma\text{-Si}_3\text{N}_4$ can be summarized as follows:

Possibly one of the most important outcomes of the presented data is the *smaller* thermal conductivity of $\gamma\text{-Si}_3\text{N}_4$ as compared to that of $\beta\text{-Si}_3\text{N}_4$, which is obviously another consequence of the ‘ionic’ character of the high pressure phase. The given value of 60–70 W/mK for $\gamma\text{-Si}_3\text{N}_4$ represents an estimate of the intrinsic ($=\text{ideal}$) conductivity, while the >100 W/mK represent recent developments of *real* ceramics that were achieved by careful densification of high-purity $\beta\text{-Si}_3\text{N}_4$ (see e.g. [208] and references therein) so that the corresponding *theoretical* value for $\beta\text{-Si}_3\text{N}_4$ should be even higher. The current value of λ_{th} for $\gamma\text{-Si}_3\text{N}_4$ is however — at least partially — a result of theoretical calculations and hence should be treated with some reservation. As discussed in Section 1.5.6 on page 18, a low thermal conductivity can be beneficial for high-speed cutting applications, because more heat is rejected to the chip rather than absorbed by the tool. The machined metal thus softens more, leading to lower thrust

*P. Kroll, private communication

Quantity	Symbol	Unit	300 K	1000 K
Specific heat (of β -Si ₃ N ₄)	C_V	[J/mol K]	92.39	162.99
	C_p	[J/mol K]	92.72	166.95
		[J/mol K]	90.68	163.67
Entropy	S	[J/mol K]	-106.40	216.72
Helmholtz free energy	F	[kJ/mol]	-5.13	92.39
Thermod. Grüneisenparam. (of β -Si ₃ N ₄)	γ_{th}	[$-$]	1.19	1.35
		[$-$]	0.40	0.63
Mode Grüneisenparam.*	γ_{i0}	[$-$]	1.27–1.61	
Thermal conductivity (of β -Si ₃ N ₄)	λ_{th}	[W/mK]	60–70	
		[W/mK]	>100	
Debye Temperature (of β -Si ₃ N ₄)	Θ_D	[K]	1050–1100	
		[K]	1140	

Table 3.21: Predicted thermal and thermodynamic properties of γ -Si₃N₄ compiled from [204] and [153]. Values for β -Si₃N₄ [206] and Grüneisen parameters determined from the pressure shift of some Raman modes* [207] are provided for comparison.

forces on the work piece. The thermal conductivity of spinel γ -Si₃N₄ may be further decreased by appropriate doping, rather than decreasing the fraction of this phase in the cutting material. The latter has been necessary in the case of the highly-conducting ultrahard solids diamond and *c*-BN with their small interatomic distances and very rigid lattice symmetry unsuitable to incorporate excessive amounts of heteroelements. Thus, part of their high hardness was so far sacrificed for an intended drop in thermal conductivity.

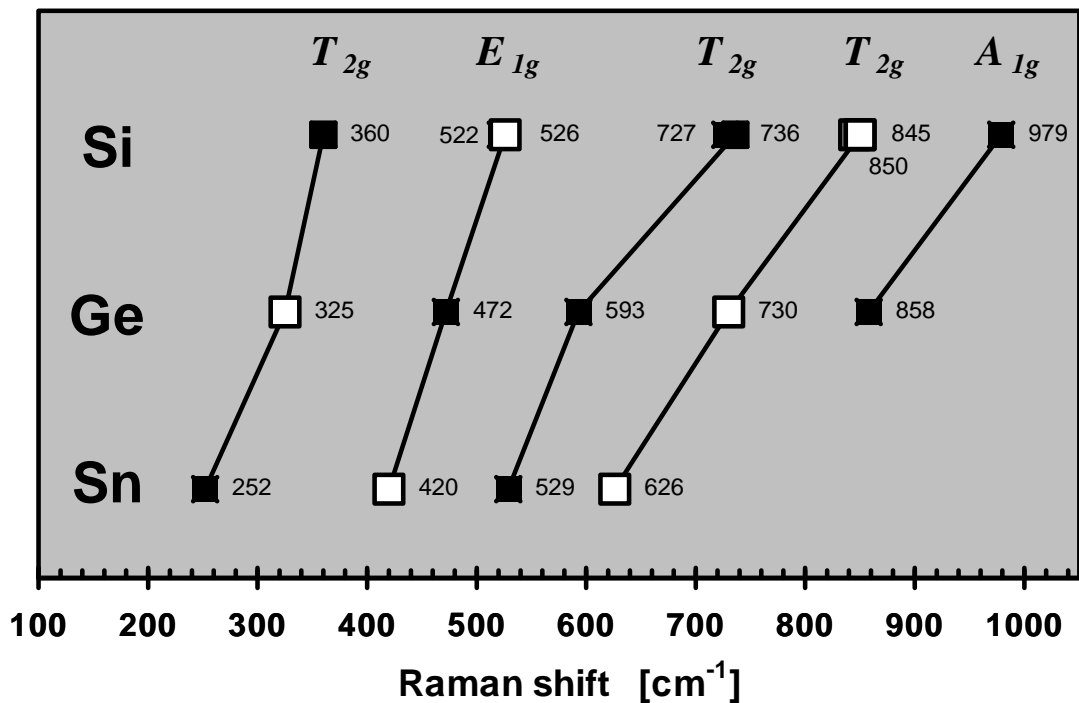


Figure 3.50: Overview of all assignable experimental Raman shifts of the group 14 spinel nitrides. Data from SN06 (see Page 99), Jiang [88], Deb [123] and Shemkunas [159] was used. Strong Raman bands indicated with empty squares

3.8.9 Vibrational Properties of $\gamma\text{-Si}_3\text{N}_4$, $\gamma\text{-Ge}_3\text{N}_4$ and $\gamma\text{-Sn}_3\text{N}_4$

The crystal symmetry of spinel implies 5 Raman and four IR-active modes. An assignment of the experimental data from SN06 (cf. Sect. 3.4 on page 99) is given in Table 3.22. It was carried out using the factor group analysis for $\gamma\text{-Si}_3\text{N}_4$ from FANG et al. [153] who cite further theoretical works on the phonon spectrum of $\gamma\text{-Si}_3\text{N}_4$. The table also contains the theoretical and experimental results for $\gamma\text{-Ge}_3\text{N}_4$ from Dong et al. and Deb et al. [164, 123] and for $\gamma\text{-Sn}_3\text{N}_4$ [159]. Fang and Deb give coincident assignments for the Raman active modes and their calculated frequencies show reasonable agreement with observed values for both $\gamma\text{-Si}_3\text{N}_4$ and $\gamma\text{-Ge}_3\text{N}_4$. Plotting the observed Raman line positions as done in Fig. 3.50, reveals an almost uniform decrease of the Raman shifts with increasing element number. Because of the strong bonding and low cation mass, $\gamma\text{-Si}_3\text{N}_4$ shows the largest dispersion, with a calculated upper bound of $\sim 1030\text{ cm}^{-1}$ for the longitudinal optical (LO) T_{1u} mode (Tab. 3.22, second column from left). Modes

of the LO branch should only appear for very thin films. According to Fang, the high energy range of the phonon spectrum is dominated by the N cations, and the low-energy vibrations $< 500 \text{ cm}^{-1}$ were predominantly influenced by the cations, with Si^{oct} especially contributing to the very low energy range between 200 and 400 cm^{-1} [153]. All Raman spectra of γ - Si_3N_4 show more lines than theoretically predicted, especially in the high frequency region above 1000 cm^{-1} . One additional line occurs at the low frequency end of the spectrum of SN06 at 317 cm^{-1} . It is tabulated in square brackets in Table 3.22. It is interesting to note that this frequency happens to coincide exactly with the ‘silent’ T_{2u} mode and that the same is observed in the case of γ - Sn_3N_4 . Also for the DAC-synthesized γ - Ge_3N_4 , additional lines were found at low and intermediate frequencies [123]. The authors point out that all five modes belonging to the spinel structure were nevertheless present and the additional lines vanished after optimizing the synthesis conditions of the β - $\text{Ge}_3\text{N}_4 \rightarrow \gamma$ - Ge_3N_4 conversion. The additional features were therefore assigned to structural defects or the presence of an intermediate phase. Fang et al. also assume structural defects to be the origin of additional lines in the γ - Si_3N_4 spectrum of Jiang et al. (Table 3.22 on the following page) and the same may apply to SN06, that had been synthesized without the double encapsulation technique (recall Sect. 2.1.2 on page 28 and Table 3.1 on page 72). A detailed study on the possible origin of these “extra” Raman modes was published in Sept. 2004 by SOIGNARD and McMILLAN [207]: γ - Ge_3N_4 and γ - Si_3N_4 were synthesized directly from the elements, using a laser-heated DAC. Samples that had been quenched from very high temperatures $> 2500 \text{ K}$ showed additional modes at ~ 770 and 820 cm^{-1} (doublet) for γ - Ge_3N_4 and between 550–600 and 900–1050 cm^{-1} for γ - Si_3N_4 , respectively. In the case of γ - Ge_3N_4 it was shown that these features disappear upon annealing at lower temperatures. The authors conclude that the Raman modes are caused by defects, namely N^{3-} vacancies in the anion sublattice, the concentration of which rises with temperature [207].

$\gamma\text{-Si}_3\text{N}_4$				$\gamma\text{-Ge}_3\text{N}_4$			$\gamma\text{-Sn}_3\text{N}_4$	
predicted modes		experimental results			predicted modes		experimental results	
	FANG et al. ^[a]	SN6	SN6	ZERR ^[b]	JIANG ^[c]	DEB et al. ^[d]	DONG ^[e]	SHEMKUNAS et al. ^[f]
T_{2u}	317		[317(w)]			T_{2u}	153	[160(w)]
T_{1u}	406(410)	IR				T_{1u}	224	IR
T_{2g}	415	R	360(m)			T_{2g}	245	R
E_u	455		[465(w)]			E_u	245	
T_{1g}	504					T_{1u}	406	IR
E_{1g}	522	R	526(vs)	522(vs)	522(vs)	T_{1g}	453	
T_{1u}	619(718)	IR	609(m)			A_{2u}	455	
T_{2u}	631					E_g	467	R
T_{2g}	726	R	736(vw)	754(w)	727(m)	T_{2g}	472(m)	420(vs)
T_{1u}	729(764)	IR	702(s)*			T_{1u}	475	IR
E_u	775					T_{2u}	535	
A_{2u}	782					T_{1u}	576	R
T_{1u}	819(1030)	IR	872(vs)			E_u	593(m)	529(m)
T_{2g}	840	R	850(vs)	864(m)	845(vs)	T_{1u}	656	IR
A_{2u}	946					E_u	667	547(vs)
A_{1g}	972	R		979(w)	979(m)	T_{2g}	710	R
not assigned			1055(m)	1034(w)	1055(m)	A_{2u}	730(vs)	626(vs)
		1094(m)	1120(m)			A_{1g}	830	R
							858(s)	

Table 3.22: Assignment of the vibrational modes for the spinel nitrides $\gamma\text{-Si}_3\text{N}_4$, $\gamma\text{-Ge}_3\text{N}_4$, and $\gamma\text{-Sn}_3\text{N}_4$ from ^[a][153], ^[b] [85], ^[c][125], ^[d][164], ^[e][123] and ^[f][159]. Values are given in $[\text{cm}^{-1}]$. The bracketed values in the second column denote the LO modes of the IR active species. Raman shifts from ^[b] corrected for pressure-induced blue shift (cf. Sect. 3.4 on page 99)

Assignment of IR-active modes appears to be less definitive. The discrepancies between the observed IR bands of γ -Si₃N₄ (SN06) and the calculated frequencies are notably larger than in the Raman case. Fang did not assign the strongest band at 872 cm⁻¹ to the high-energy Si–N stretching mode (T_{1u} symmetry) with a calculated frequency of 819 cm⁻¹ and points out that from the theoretical point of view, there should be no further absorptions in the high frequency range above 800 cm⁻¹. For the second strongest band at 702 cm⁻¹ (predicted: 729 cm⁻¹) that is marked with an *, a splitting into two separate bands with absorption maxima at \sim 685 and 735 cm⁻¹ was observed in other IR spectra of γ -Si₃N₄ (see Sect. 3.4 on page 99). Theory predicts a T_{1u} mode with $\tilde{\nu} = 406$ cm⁻¹ for *both*, γ -Si₃N₄ and γ -Ge₃N₄. Experimental verification of this will be difficult, as it is very close to the cutoff-frequency of the KBr window material. At the time of writing no IR-spectrum of γ -Ge₃N₄ was available. The weak band at 465 cm⁻¹ in the IR-spectrum of SN06 could not be directly assigned to any of the modes predicted by Fang, but the blue shift with respect to the prediction at 406 cm⁻¹ would be similar to that of the high-energy T_{1u} mode noted above. It should be noted that especially within this energy-region, discrepancies between the theoretical results of Fang and Deb exist, as indicated by the vertical gaps in Table 3.22. If the calculations of Deb should turn out to be more precise, so that the T_{1u} mode for γ -Ge₃N₄ is indeed found close to 406 cm⁻¹, the corresponding value for γ -Si₃N₄ could be blue shifted (as is observed for all Raman modes) and assignment of the absorption at 465 cm⁻¹ to the same T_{1u} symmetry appears to be reasonable. For γ -Sn₃N₄ Shemkunas et al. observed only one absorption band at 547 cm⁻¹ that was assigned to the Sn–N stretching vibration [159].

3.8.10 Electronic Properties

Theoretical Predictions The electronic structure of a solid represents the essence of any theoretical investigation from first-principles. Hence, it is almost trivial that electronic properties of γ -Si₃N₄ and related nitride spinels were among the first features that have been calculated for these materials. Particular interest arose due to a direct electronic band gap energy E_{gap} of about 3.4 eV for γ -Si₃N₄, first predicted by MO et al. in December 1999 [86]. This value is close to that of GaN ($E_{gap} = 3.2$ eV), the preferred material for blue light emitting diodes (LED), and it indicated that γ -Si₃N₄ could not only be suitable as a hard material, but also for optoelectronic applications. A somewhat higher value of $E_{gap} = 3.68$ eV based on local density functional potential and linear combination of atomic orbital formalism, was published in 2001 by BAGAYOKO et al. [209].

The possibility of “band-gap engineering” as is state of the art for the system Al,Ga,In–N was immediately recognized and a notable number of *theoretical* works addressing the electronic properties of various spinel nitrides have been published meanwhile: CHING, MO and colleagues studied the electronic properties of Ti₃N₄ and SiTi₂N₄ [126], Si₂GeN₄ and SiGe₂N₄, as well as various combinations AB₂N₄, A,B = Ti, Zr, Hf, C, Si, Ge and Sn [116, 127]. The binary nitrides γ -Ge₃N₄ and γ -Sn₃N₄ have predicted E_{gap} of 2.2 and 1.3 eV respectively. The recent findings of ZERR et al. on the thorium phosphide structure of Hf₃N₄, Zr₃N₄ (and possibly also Ti₃N₄) at high pressure (recall Sect. 3.2 on page 82) rendered the predictions on “ γ -Ti₃N₄”, “ γ -Zr₃N₄” and “ γ -Hf₃N₄” and their mixtures as almost worthless, but the results on the solid solutions within the homologous series of the group 14 nitrides and their effective doping with other elements remain important for possible future applications. The latter problem of identifying effective dopants and defect structures was addressed in first-principles calculations by OBA, TATSUMI, TANAKA and coworkers [210, 211, 212]. Al, O and P were suggested as *p*- and *n*-type dopants for γ -Si₃N₄, respectively, for γ -Ge₃N₄ the best candidates would be Sb and O (*n*-type) and also Al for *p*-type doping.

As β -Si₃N₄ and amorphous Si₃N₄ are also frequently used as a passivating or dielectric layer in microelectronics, it is interesting to know the dielectric func-

tions of the corresponding spinel nitrides. Again, CHING et al. performed the corresponding calculations and predict static dielectric constants $\varepsilon_1(0)$ of 4.7, 6.5, 6.2 and 5.9 for γ - Si_3N_4 , Si_2GeN_4 , SiGe_2N_4 and γ - Ge_3N_4 , respectively [117]. These values are higher than those of the (binary) low pressure modifications: β - Si_3N_4 ($\varepsilon_1(0) = 3.9$) [213]. The refractive index n of γ - Si_3N_4 is approximated by $\sqrt{\varepsilon_1(0)} = 2.16$ (diamond: 2.42, SiC: 2.6–2.7*). The spinel nitrides may hence also be suitable for certain optical applications – or even as fancy synthetic gemstones!

Experimental Efforts In our attempts to determine E_{gap} of γ - Si_3N_4 in cooperation with “Fachgebiet für Elektronische Materialeigenschaften”[†] in Darmstadt, we faced several problems, mostly arising from the small dimensions and the polycrystalline (and porous) nature of the MAP-derived samples. First it turned out that the available surface area of the cylindrical samples was too small for reflectance measurements: Filtering the excitation wavelength from the backscattered spectrum left almost no intensity. On the other hand, the material appeared to be too brittle for the preparation of thin sections for transmission measurements. Later, Zerr succeeded in preparing a tiny γ - Si_3N_4 -‘window’ by pressing a small amount of the multianvil-synthesized material into the gasket of a diamond anvil cell. The spectrum of the transmitted light did not show a sharp absorption edge. It was possibly blurred due to scattering effects of the micron and sub-micron sized crystallites and leaking of light from the primary beam. Fitting the absorption profile, a preliminary value for $E_{gap} \approx 3.2$ eV was obtained. Direct electronic excitation of γ - Si_3N_4 with an electron beam revealed a strong cathodoluminescence, probably due to recombination at radiation-induced defects. The results were presented by A. Zerr at the 104th Annual Meeting of the American Ceramic Society, St. Louis, MO, 2002 [214]. On the same conference, PETUSKEY briefly announced that the band gap of γ - Ge_3N_4 would be larger than 1.8 eV [215]. Obviously, other researchers have faced similar problems as to my knowledge, no publication on electronic band gap measurements of γ - Si_3N_4 , γ - Ge_3N_4 or γ - Sn_3N_4 via optical methods was reported until the end of 2003. Band gaps of

^{*}<http://mineral.galleries.com/minerals/elements/moissani/moissani.htm>

[†]special thanks to Dr. Roland Schmechel and Robert Kolb for performing the spectroscopic measurements

4.8 eV and 3.6 eV for β -Si₃N₄ and shock-synthesized γ -Si₃N₄ respectively, were deduced from high-resolution XPS* core and valence spectra of the two polymorphs [216]. According to the authors, the obtained value for γ -Si₃N₄ is in agreement to combined x-ray emission/absorption spectroscopy measurements ($E_{gap} = 3.7$ eV) which remained unpublished.

In addition to the difficulties with the precise determination of the band gap energies, experimental as well as theoretical investigations show that tailoring of E_{gap} via formation of mixed group 14 element spinels such as (Si_xGe_{1-x})₃N₄ faces intrinsic limitations, because γ -Si₃N₄ and γ -Ge₃N₄ may not have a continuous miscibility range (cf. Sect. 3.5.2 on page 111).

Nevertheless, the commercial exploitation of the *electronic* properties of the group 14 spinel nitrides for certain applications may be in closer reach than their use as abrasives or structural materials. This is because in this case *small volumes* of these difficult-to-prepare materials may suffice to *serve a useful and valuable function*, whereas for structural applications, large amounts of bulk material will be inevitable. Finding a method to grow single crystals from spinel nitrides will be a crucial step, especially, but not exclusively, for their further validation as electronic materials.

*X-ray photoelectron spectroscopy

3.9 High Pressure Shock Synthesis of γ -Si₃N₄

3.9.1 Motivation

Within this thesis so far, the discovery and the HP/HT synthesis of γ -Si₃N₄ in sufficient amounts and quality to determine key properties for potential applications has been reported. However, the high pressure of *at least* \sim 12 GPa required to synthesize this phase (cf. Sect. 3.6.1) is more than twice as high as the pressure range of commercial diamond and *c*-BN production [139, 217]. This poses the important question if synthesis of γ -Si₃N₄ could ever become feasible in an industrial scale. Part of this question was answered with the successful synthesis of γ -Si₃N₄ by SEKINE et al. (see Section 3.3.4 on page 89 for references) using a shock wave method. Given the fact that the amounts initially synthesized were in the order of some hundred milligrams, the title “*Mass synthesis of Cubic Silicon Nitride Succeeded*” of a press release in STA Today, a monthly magazine of the Science and Technology Agency of Japan, in June 2000 appears to be a little bit overstated.* However, two years later, in Sept. 2002, K. ITO from the NOF Corporation 61-6, Aichi, Japan, reported on the shock synthesis of γ -Si₃N₄ powders in a multigram scale at the “**FIRST INTERNATIONAL WORKSHOP ON SPINEL NITRIDES AND RELATED MATERIALS**” at Rüdesheim, Germany. By applying explosive shock to mixtures of copper and α -Si₃N₄ or β -Si₃N₄, Ito and coworkers were able to convert up to \sim 60% of the starting material. Pure γ -Si₃N₄ consisting of spherical agglomerates of nano-crystallites could be obtained by a two step acid treatment.[†] The abrasive performance of the product was tested in lapping experiments of commercial Si₃N₄ ceramics in comparison to diamond abrasive powders.

In the publications that were available at the date of writing, only incomplete shock conversion of α - and β -Si₃N₄ into γ -Si₃N₄ was reported [122, 102, 145, 146]. It was thus to be tested, if the utilization of *amorphous* starting material leads to higher yields.

*<http://www.mext.go.jp/english/news/2000/07/s000702.htm>

[†]Patent pending, JP 2002-179412A

3.9.2 Appropriate Shock Conditions for γ -Si₃N₄-Synthesis: Literature before 1999

It is interesting to note that several shock investigations on Si₃N₄-materials were carried out before the discovery of γ -Si₃N₄ in 1998/99. In these investigations, a pressure induced phase transformation α -Si₃N₄ \rightarrow β -Si₃N₄ was commonly observed, however none of the authors reports on the presence of an unknown phase which may, with hindsight, now assigned to the spinel high pressure polymorph. Small fractions of the material could possibly have been overseen. By comparison between these older experiments and the shock conditions successfully applied by Sekine, important additional information on the shock synthesis of γ -Si₃N₄ may be gained. The brief review given below does not raise any claims for completeness.

In 1980 MITOMO and SETAKA [218] shock compacted pre-compressed α -Si₃N₄ powders at $\hat{p}_{eq} \approx 40$ GPa*, using an explosively driven flyer plate. The shocked samples were more than 94% dense and had a high hardness $HV_{0.1}$ of 18.6 GPa. The post-shock phase content varied between 87 and 100% β -Si₃N₄, depending on the nature of starting powder.

Another study using a coaxial explosive arrangement was reported in 1985 by PETROVIC et al. [219]. In contrary to the aforementioned results, the authors received compacted bodies of almost pure α -Si₃N₄ after applying \hat{p} of 20 and 50 GPa, respectively, while specimen subjected to higher shocks of 80 and 100 GPa were vaporized and could not be recovered.

Flyer-plate shock compaction experiments were also carried out by HIRAI and KONDO [220] in 1992. Nanocrystalline α -Si₃N₄ powders ($\bar{D} \approx 70$ nm) were used as starting material. The shock conditions were $\hat{p}_{eq} = 18, 30, 40, 46, 50$, and 60 GPa and $T \approx 700, 1000, 1200, 1400, 1500$ and 1700 K, respectively. These estimated temperatures refer to the equilibrated heat in the bulk after passage of the shock wave but the authors point out that the surface temperatures of individual grains during shock deformation may have been much greater. The onset of the shock-induced $\alpha \rightarrow \beta$ transformation was found for 50 GPa/1400 K (40% conversion) and 46 GPa/1500 K (100% conversion), respectively. TEM

*recall Sect. 2.1.3 on page 36

and electron diffraction studies of the products indicated surface melting and precipitation of β - Si_3N_4 crystallites. These were identified by a hexagonal SAED pattern and a d -value of ~ 2 Å, corresponding to the 220 reflections of β - Si_3N_4 . Only the 400 reflections of γ - Si_3N_4 would also have a d -value close to 2 Å but would be arranged in a rectangular pattern (recall Figure 3.1 on page 75). In 1998 TURNER-ADOMATIS and THADHANI observed that upon post-shock annealing, α - Si_3N_4 powders previously subjected to $\hat{p} = 21$ GPa* converted much more readily to β - Si_3N_4 than the corresponding untreated powders [221]. The XRD patterns of the shock-treated powders presented in the publication show considerable line broadening due to the high defect density and also some stronger additional reflections at $2\theta \approx 25^\circ$ and 45° which disappear upon annealing again.[†] These peaks however do not correspond to any reflection of γ - Si_3N_4 . Other low intensity reflections at ~ 46 and 68° could indicate, however not prove a trace amount of the high pressure phase.

In one of their first works in 2000 SEKINE et al. found that the lowest pressure required to transform the low pressure phases to γ - Si_3N_4 was 20 GPa—but only in conjunction with high shock temperatures (e.g. 3000 K) [87]. No γ - Si_3N_4 could be found in samples subjected to the same shock pressure at 1270 K. This indicated that the phase transformation from the low pressure polymorphs is temperature-activated and reconstructive rather than martensitic. Moreover, it emphasizes the important role of the copper powder additive for the synthesis of γ - Si_3N_4 to achieve high shock temperatures and rapid quenching (cf. Sect. 2.1.3 on page 35). An additive had not been employed by any of the aforementioned authors, a fact that might be the reason why γ - Si_3N_4 never was observed in shock-recovery experiments before 1999.

*pressure estimated from Mie-Grüneisen approximation for the Hugoniot of porous Si_3N_4

[†]comparing the diffraction lines for α - and β - Si_3N_4 it can be deduced that $\text{Cu } K_\alpha$ radiation was used

3.9.3 Starting Materials and Sample Preparation

For the present flyer plate investigations, commercial Si₃N₄-powder mainly consisting of α -Si₃N₄ (experiment FP-SN0) and amorphous silicon nitride (FP-SN1 and FP-SN2), a -Si₃N₄, obtained via pyrolysis of Si₂N₃H (cf. Section 3.3.1 on page 84) were employed as starting materials. Direct usage of the hydrogen-containing nitride imide precursor was considered to be less suitable: Release of ammonia or other gaseous products (recall Equation 3.5) could cause the sample capsule to burst upon shock release. The copper powder to be mixed with the silicon nitride was comprised of spherical particles with diameters between 50 and 80 μm . It was de-oxygenated by heating to 450 °C for 6 h in a quartz glass tube in the presence of paraformaldehyde and under flowing Argon. The mixtures of a -Si₃N₄ and Cu were pressed into copper capsules described in Section 2.1.3 and sealed under argon atmosphere.

3.9.4 Experiment and Sample Recovery

The experimental setup was as described in Section 2.1.3 on page 34. Table 3.23 summarizes the experimental parameters of the three flyer plate experiments. For the successful experiment FP-SN1, the shock pulse duration was \sim 0.3 and 0.27 μs directly below the cover plate and in the sample center, respectively.

Exp. No.	Starting material	m_{sample} [g]	ϱ_0 [g/cm ³]	Cu fract. [wt.%] [†]	Cu fract. [vol.%] [‡]	\hat{p}_0 [GPa]
FP-SN0	α -Si ₃ N ₄	1.20	6.7	80	n.d.	62
FP-SN1	Si ₃ N ₄ amorph.	0.44	5.6	90	57	62
FP-SN2	Si ₃ N ₄ amorph.	0.41	5.3	90	53	72

Table 3.23: Experimental parameters of the three shockwave experiments on Si₃N₄

[†]= $m_{\text{Cu}}/(m_{\text{Cu}} + m_{\text{sample}})$

[‡]= $V_{\text{Cu}}/V_{\text{capsule}}$

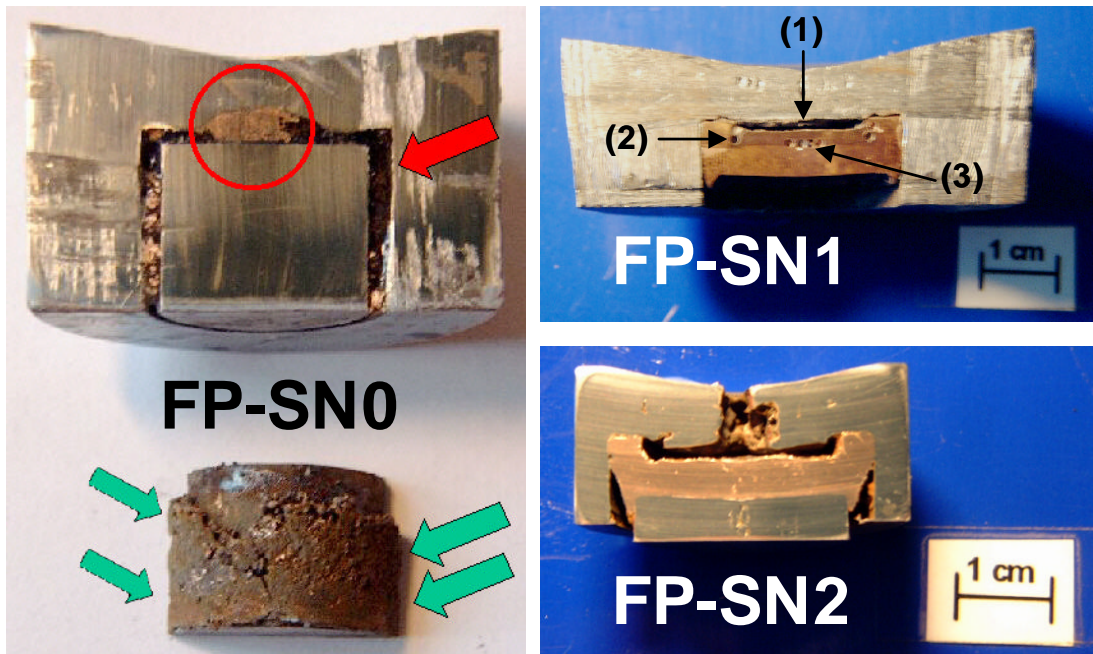


Figure 3.51: Cross sections of the recovered sample capsules.

The recovery containers were turned on a lathe or cut open with a metal saw, sectioning the sample capsule parallel to the cylinder axis. The sectioned specimen were then ground and polished to enhance the contrast between the sample material and the copper capsule. Optical photographs of the three polished specimen are shown in Figure 3.51.

FP-SN0 An exploratory experiment to check the experimental setup. The mixture of copper and crystalline β - Si_3N_4 was filled directly into the cylindrical sample volume. In the course of the shock treatment, most of the sample mixture was pushed down into the opening gap between the deformed sample container and the spacer rod and only a small portion remained between the rod and the cover plate (indicated by the arrows at the left side of Fig. 3.51, left side). Powder XRD-revealed that neither of these two sample portions had transformed into γ - Si_3N_4 . No further characterisation was carried out.

FP-SN2 This experiment was carried out to check the influence of \hat{p} on the $a\text{-Si}_3\text{N}_4 \rightarrow \gamma\text{-Si}_3\text{N}_4$ conversion. The density of the precursor/copper mixture was slightly lower than in FP-SN1. Opening of the recovered sample container revealed that the applied peak pressure of $\hat{p}_0 = 72$ GPa was too high (see Fig. 3.51): The sample cavity was found to be empty and a hole in the cover plate indicated the escape of nitrogen. A grayish layer at the inner surface of the sample capsule indicated the presence of silicon. The specimen was not further characterized.

FP-SN1 In Figure 3.51, a cross section of the recovered sample container is shown. Upon the shock treatment, the Cu/Si₃N₄ powder mixture was compacted into a solid composite (i.e. the darker zone in the middle of the sectioned copper capsule). The upper part of this material marked with (1) was detached from the rest of the bulk leaving a lateral circular crack. This probably happened upon passage of the rarefaction wave. The detached material adhered to the copper lid that had been used to seal the capsule. This foil in turn stucked to the cover plate of the recovery container. Both, polished and fractured surfaces of the compacted Cu/Si₃N₄ mixture were investigated with SEM. Samples were drilled out of the sectioned specimen at the three locations indicated in the figure. They were extracted from the copper via ultrasonication and sedimentation in alcohol. The obtained suspensions were dropped on copper grits for TEM investigations and dried to obtain powders for X-ray diffraction (Diffractometer B). Estimations for the relative phase contents were derived by quantitative phase analysis of the diffraction data.

3.9.5 FP-SN1: Characterization of Shock-Derived $\gamma\text{-Si}_3\text{N}_4$

Scanning Electron Microscopy, SEM

Figure 3.52 on the facing page shows the fractured surface of the recovered Cu/Si₃N₄ mixture at position (1). The microstructure is surprisingly porous. The initially spherical copper particles are completely deformed and may have even been molten. The Si₃N₄ powder forms coral-like agglomerates in the voids between the copper. A closeup image of such an agglomerate is provided in Figure 3.53. Particles with diameters between 50–70 nm can be resolved. TEM investigations (see below) revealed that this corresponds to the size of larger single crystallites.

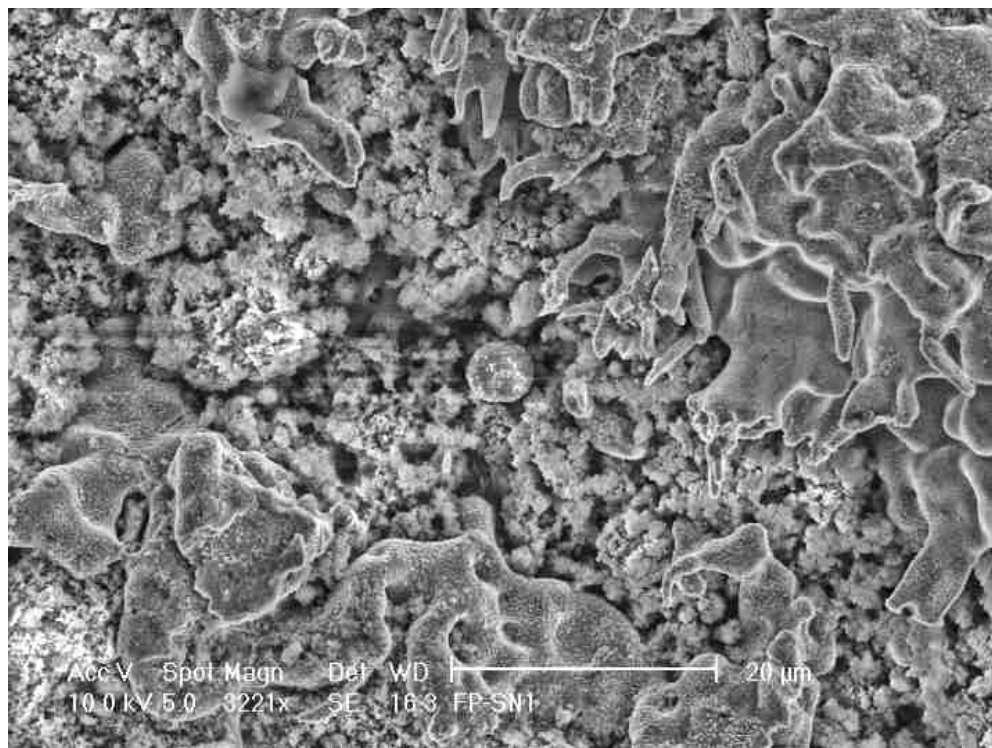


Figure 3.52: Microstructure of the shocked Cu/Si₃N₄ sample compact of experiment FP-SN1 at location (1).

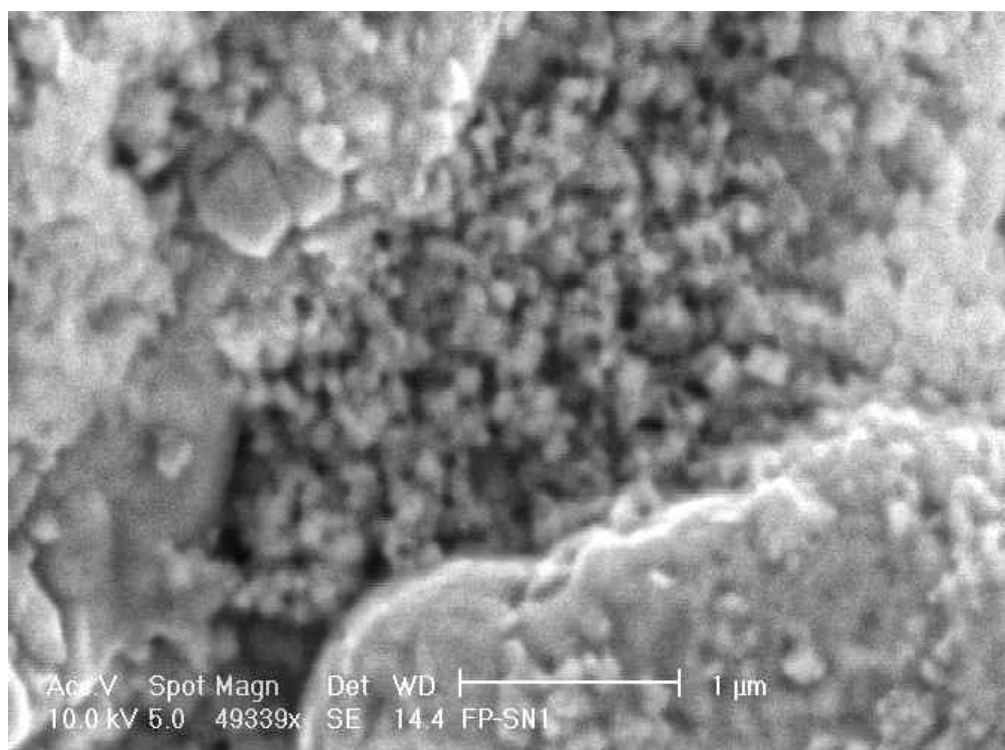


Figure 3.53: High-resolution SEM image of post-shock Si₃N₄ nanoparticles.

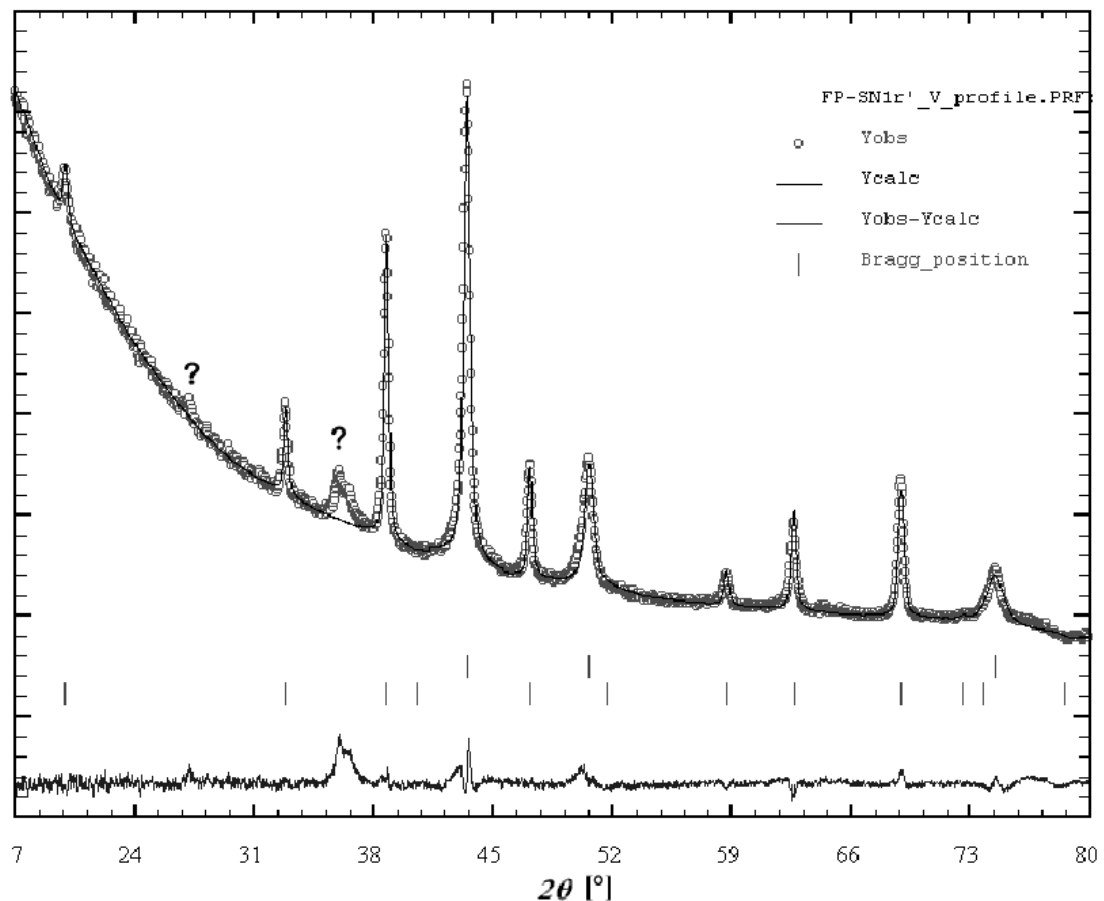


Figure 3.54: Powder pattern and difference plot (profile matching mode) of sample material from location (2), upper line indicators: Copper; lower line indicators: γ -Si₃N₄

X-ray Diffraction and Phase Analysis

The results of quantitative phase analysis are given as follows:

- (1) directly below the cover plate: γ -Si₃N₄: β -Si₃N₄ \approx 40:60 vol.%
- (2) at the bottom of the copper capsule: γ -Si₃N₄: β -Si₃N₄ \approx 80:20 vol.%
- (3) close to the rim of the copper capsule: γ -Si₃N₄, almost no β -Si₃N₄
 - In all three locations, an unidentified line occurred at $d \approx 2.5 \text{ \AA}^*$

* = $36.6^\circ 2\theta$, could not be assigned to α -Si₃N₄, β -Si₃N₄, w_{II} -Si₃N₄, Si₂N₂O, Si or Cu

These results show that \hat{p} and \hat{T} were sufficient to accomplish the transformation to γ -Si₃N₄ at any location in the sample. The most probable reason for the different β -Si₃N₄-contents is inhomogeneous quenching: During the passage of the compressive shock wave, heat is dissipated within the porous sample material. As mentioned before, the material at position (1) is detached from the remainder of the bulk upon pressure release. Hence, effective heat transfer could only take place towards the (iron) cover plate. At position (2), the heat could only be transferred towards the bottom of the copper capsule, whereas at position (3) it was absorbed by the bottom *and* the radial rim of the capsule. It thus can be deduced that the β -Si₃N₄ impurity presumably stems from the back-transformation of γ -Si₃N₄ due to the residual heat. If this is the case, the shock and post-shock temperatures therefore must have been beyond the thermal stability limit of γ -Si₃N₄, which has been estimated to about 1400 °C (Sec. 3.8.6 on page 171). Comparison of the diffraction patterns to those of the α - and β -Si₃N₄-derived samples presented by Sekine and coworkers [87, 102, 146] reveals a better crystallinity of the present sample. This is especially apparent from the 422 reflection at $\sim 59^\circ 2\theta$, that is clearly obvious in Figure 3.54 but can barely be recognized in the published diffractograms. Also the FWHM in the present patterns is $\sim 0.3^\circ$, which is half that of the materials synthesized by Sekine et al. (FWHM $\leq 0.62^\circ 2\theta$).*

*T. Sekine, personal communication

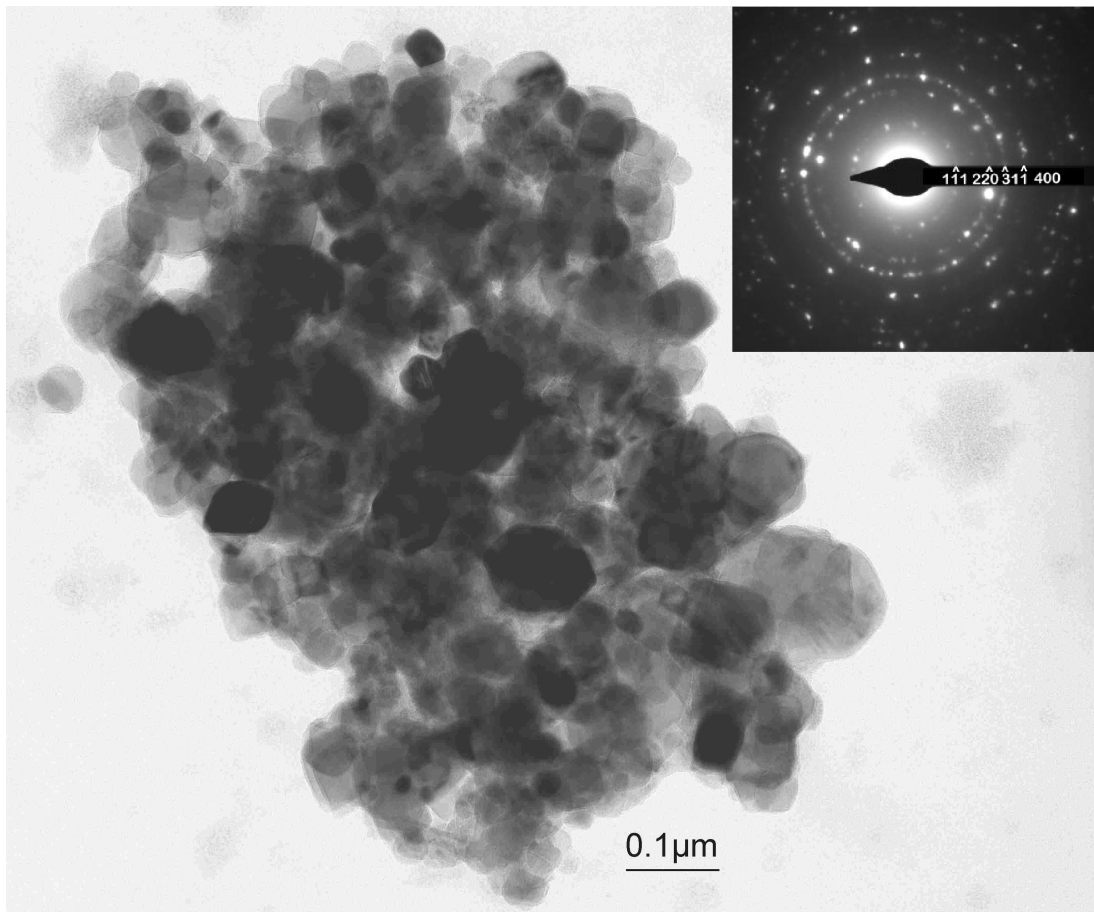


Figure 3.55: TEM Photograph of a typical agglomerate of γ -Si₃N₄ crystals from location (2) of Exp. FP-SN1

Transmission Electron Microscopy, TEM

The main intention of the TEM investigations was to determine whether the *a*-Si₃N₄ has been entirely converted into crystalline material or if some silicon nitride remained in the amorphous state. Material from location (2), where powder-XRD had revealed γ -Si₃N₄ as the predominant crystalline phase, was chosen. The material was investigated at several locations of the TEM sample holder and was found to consist of micron-sized agglomerates of γ -Si₃N₄ crystallites. None of the low pressure phases of Si₃N₄ were found. Figure 3.55 shows a representative bright field image along with the electron diffraction pattern.

The projections of the primary crystallites on the TEM photograph are noticeably rectangular, indicating a cube-like or octahedral habit. Some crystals

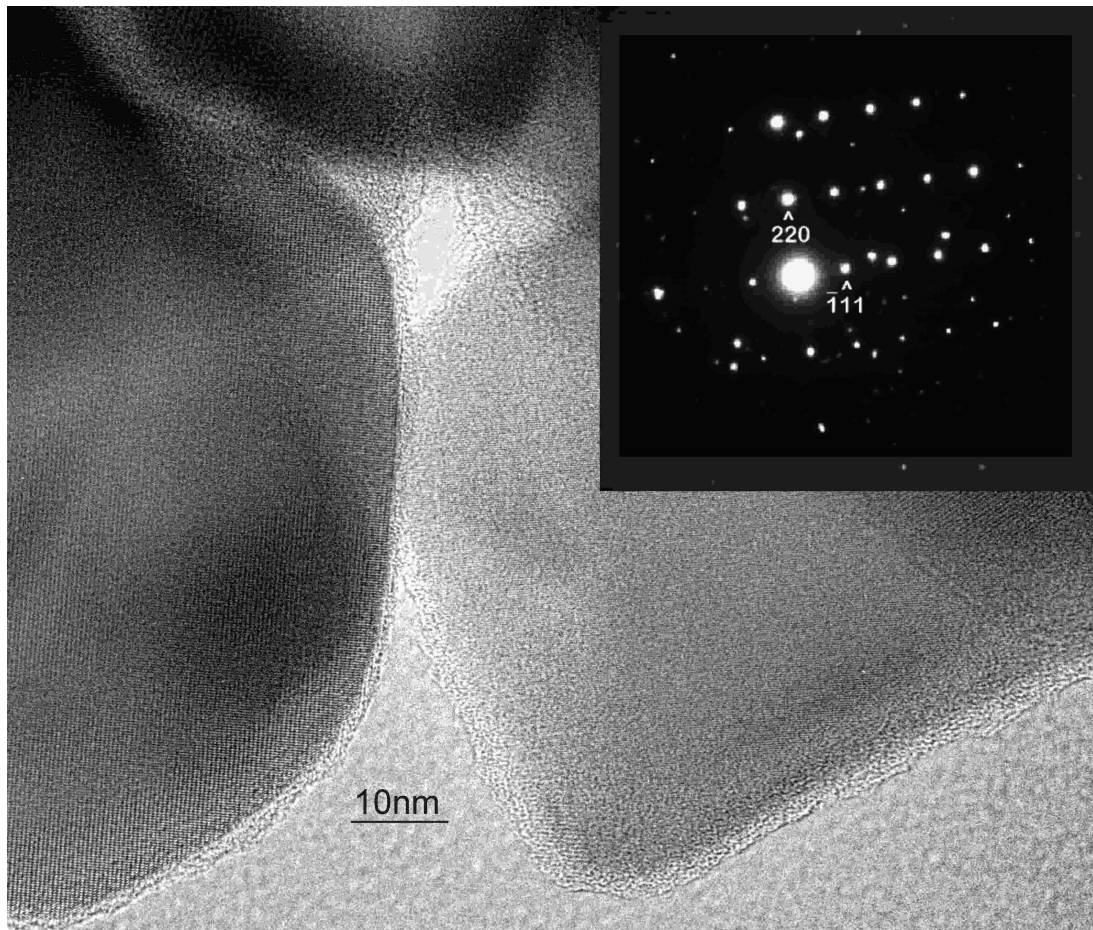


Figure 3.56: HR-TEM image of γ -Si₃N₄ crystallites. The corresponding SAED pattern shows reflexions from zone [112] of the left crystal.

approach 0.1 μ m in diameter, but their typical size ranges between 10 and 50 nm, which is exactly the same range as reported by Sekine and coworkers [87]. In the course of the investigations, no significant amounts of amorphous material could be found. Fig. 3.56 for example depicts two γ -Si₃N₄ crystallites at high resolution, the diffraction pattern of the same region is shown in the inset. The crystallites are covered by a 1–2 nm thin amorphous layer, thicker necks of amorphous material can be seen at the triple point in the upper part of the photograph. In the remaining gaps between crystallites no intergranular material is present. According to EDX in situ chemical analysis, oxygen was barely detectable and the strongest signals were those of N, Si and copper originating from both, the TEM sample holder and remaining pressure medium. Hence, not only the crystal-

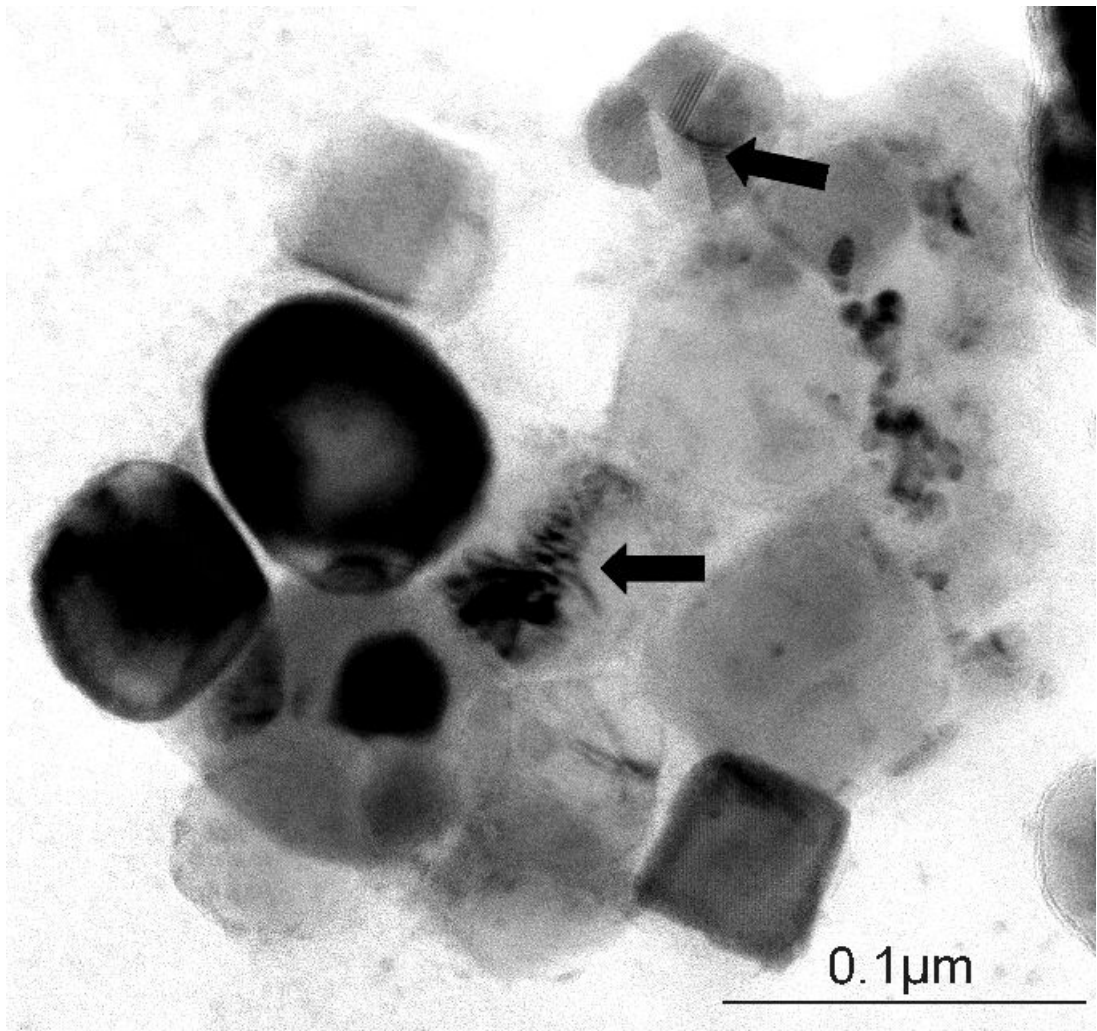


Figure 3.57: Localized defects in individual γ - Si_3N_4 grains: Upper arrow: Twinned crystal; lower arrow: Contrast variations indicate lattice distortions

lites, but also the amorphous material is comprised of silicon nitride resembling some residual starting material. The volume fraction of this amorphous phase is certainly less than the 20% of residual *crystalline* starting material reported by Sekine et al. [87]. In both crystallites, lattice fringes of the $(\bar{1}11)$ and (220) planes can be seen. Their lines are uninterrupted and evenly spaced, indicating an undisturbed lattice. In Figure 3.57 twinning and the presence of some lattice distortions are indicated by arrows. The remaining crystalline material appears to be surprisingly defect free, given the violent synthesis conditions.

3.9.6 Resumé: Shock Synthesis from Amorphous Precursors

The present flyer plate experiments demonstrate that *phase pure*, well crystallized γ -Si₃N₄ can be obtained directly via shock compression of amorphous silicon nitride precursors. The overall conversion of amorphous Si₃N₄ may approach 100%, if a rapid and homogeneous quenching can be accomplished throughout the entire recovery container. This would save a second purification step to dissolve the β -Si₃N₄ by-product of the shock treatment and help to reduce production costs. Application of peak shock pressures \hat{p} in excess of 62 GPa leads to decomposition. The lower bound for γ -Si₃N₄ formation remains to be determined.

It is interesting to note that the reported flyer plate experiments of Sekine et al. reveal inconsistencies concerning the conversion of α -Si₃N₄ and β -Si₃N₄: While in the early works [87] α -Si₃N₄ was suggested to have a higher energy barrier to transformation, it is later reported to give a higher γ -Si₃N₄-yield than the β -phase [146].

4 Spinel-Sialons: The First Derivatives of $\gamma\text{-Si}_3\text{N}_4$

4.1 Introduction

Soon after the new group 14 nitrides $\gamma\text{-Si}_3\text{N}_4$, $\gamma\text{-Ge}_3\text{N}_4$ and $\gamma\text{-Sn}_3\text{N}_4$ had been discovered, proposals on the corresponding spinel nitrides of the group 4 elements ($\gamma\text{-Ti}_3\text{N}_4$, $\gamma\text{-Zr}_3\text{N}_4$ and $\gamma\text{-Hf}_3\text{N}_4$) as well as ternary nitride spinels, containing two different cations out of these two series of homologous elements (recall Section 3.2), were made. Obviously, these predictions are based on the *chemical analogy* of the constituent *elements*. In Section 3.6.2 on page 117, where possible post-spinel modifications of $\gamma\text{-Si}_3\text{N}_4$ are considered, we have met another kind of prediction, based on *structural analogies*: In order to find structures that may form when $\gamma\text{-Si}_3\text{N}_4$ is further compressed, it appears to be reasonable to look for already known $\gamma \rightarrow$ *post-spinel* transitions. This principle may also apply into the opposite direction: If $\beta\text{-Si}_3\text{N}_4$ (and also $\alpha\text{-Si}_3\text{N}_4$) transform into a spinel-type structure, could there be related phases that might also undergo a $\beta \rightarrow \gamma$ transition? — To the best of my knowledge, a first suggestion of this kind was made by my Professor RALF RIEDEL and Prof. I-WEI CHEN [179] from the University of Pennsylvania. Their prediction, that some “**sialons**”, i.e. phases within the system (M)*–Si–Al–O–N, could undergo a transition into the spinel structure, was enhanced by the TEM investigations of sample SN13, where $\gamma\text{-Si}_3\text{N}_4$ was found to possibly incorporate Al, O and Mg. This finding suggested an extension of the investigations from the *pure* spinel *nitrides* towards **multinary oxide nitride** spinels. However, in order to gain *fundamental* insights, this extension was best to be made by using a system that contains *less* components than those found in SN13.

*M = RE or earth-alkaline metal

Among the large variety of known sialon phases and structures ([222], German translation: [223]), the first discovered, best characterized and technologically most important compounds do exhibit the same structures as α - and β - Si_3N_4 , respectively. Accordingly, they are denoted as α - and β -sialon and will be briefly introduced in the following. Research on sialons in general, their synthesis, properties and applications is a vast field and has been summarized in numerous reviews e.g. by EKSTRÖM and NYGREN [224], RILEY [147], IZHEVSKIY and coworkers [178], CHEN and SHUBA [179] and RAJU et al. [225], to name only some of them.

4.1.1 Prominent Sialon Phases

The right hand side of Figure 4.1 depicts the system $\text{Si}-\text{Al}-\text{O}-\text{N}$. The isothermal phase behavior diagram of the quasi-ternary subsystem $\text{Si}_3\text{N}_4-\text{SiO}_2-\text{AlN}-\text{Al}_2\text{O}_3$ treated as a reciprocal salt system [226] according to Jack [227] is shown on the left. Stable compositions are represented by black areas.

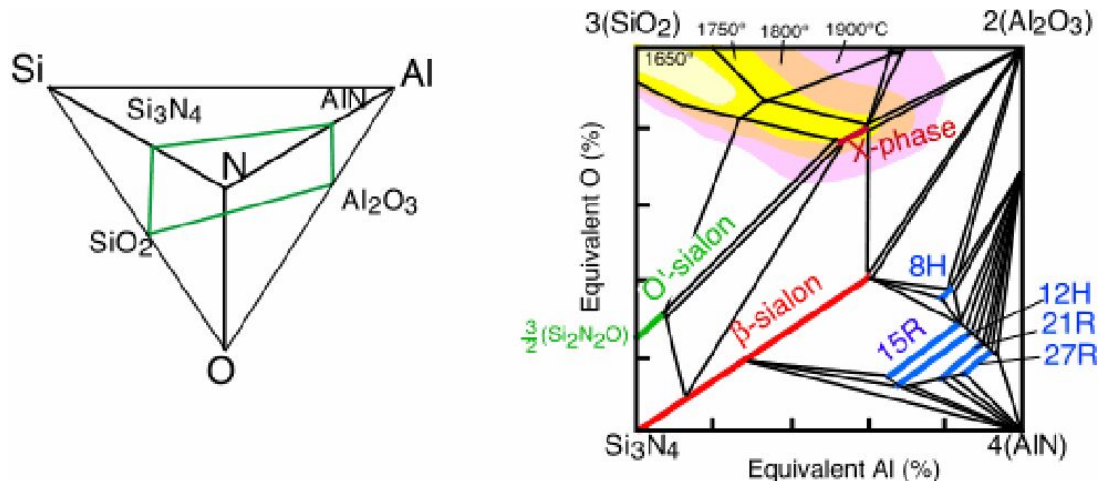


Figure 4.1: Left: $\text{Si}-\text{Al}-\text{O}-\text{N}$ system and the subsystem $\text{Si}_3\text{N}_4-\text{SiO}_2-\text{AlN}-\text{Al}_2\text{O}_3$. Right: behavior diagram of the subsystem $\text{Si}_3\text{N}_4-\text{SiO}_2-\text{AlN}-\text{Al}_2\text{O}_3$, illustrated as a reciprocal salt system at temperatures of 1700 $^{\circ}\text{C}$ to 1730 $^{\circ}\text{C}$. Both figures taken from [224]

β -sialon The so called β -sialons are formally derived by substitution of SiN versus AlO into the crystal lattice of β - Si_3N_4 . This gives rise to a solid solution series $\beta\text{-Si}_{3-x}\text{Al}_x\text{O}_x\text{N}_{4-x}$.* The net charge of the corresponding element pairs is the

*Often the formula $\text{Si}_{6-z}\text{Al}_z\text{O}_z\text{N}_{8-z}$ is used. Here I follow the recommendation of Ekström and Nygren [224] for a nomenclature that indicates the Si_3N_4 parent phase more clearly. More-

same: $[\text{Si}^{4+}\text{N}^{3-}]^{(1+)}$ and $[\text{Al}^{3+}\text{O}^{2-}]^{(1+)}$. Therefore, the overall charge neutrality of the crystal is conserved. However, *local* charge imbalances and a higher chemical affinity of Al towards O lead to clustering into Si–N and Al–O dominated layers [228]. An increase in x would thus correspond to thicker Al–O lamallae. The stability field of $\beta\text{-Si}_{3-x}\text{Al}_x\text{O}_x\text{N}_{4-x}$ is known to terminate at $x_{max} > 2.1$. This is possibly because a tetrahedral network solely consisting of these elements cannot be charge neutral and too thick Al–O layers become unstable. AlO insertion also causes the $\beta\text{-Si}_3\text{N}_4$ crystal lattice to expand. EKSTRÖM et al. established linear relationships between the substitution level and the hexagonal lattice constants [229]. For the formulation $\beta\text{-Si}_{3-x}\text{Al}_x\text{O}_x\text{N}_{4-x}$, these have the form

$$a_0 \text{ [\AA]} = 7.603(6) + 0.0148(2) \cdot x \quad (4.1)$$

$$c_0 \text{ [\AA]} = 2.907(8) + 0.0127(3) \cdot x \quad (4.2)$$

α -sialon While in β -sialon the Al:O-ratio is 1:1, α -sialon contains *more* Al than O and crystallizes in the $\alpha\text{-Si}_3\text{N}_4$ structure. The excess Al with a formal charge +3 occupies regular Si^{4+} lattice sites, with four nitrogen neighbors. Such a configuration lacks one positive charge and is therefore *negatively charged with respect to the lattice*. The Kröger-Vink symbol for such a substitutional defect is thus given by Al'_{Si} (recall equation 3.6 on page 97). Charge ballance is accomplished by additional cation species that are hosted at large interstitial sites within the cage-like topology of the $\alpha\text{-Si}_3\text{N}_4$ structure [179]. A general formula for α -sialon is given by $\text{M}_{m/\nu}\text{Si}_{12-m+n}\text{Al}_{m+n}\text{O}_n\text{N}_{61-n}$, where M is a metal with valence ν . Li, Ca, Mg, Y and lanthanides with $Z > 58$ have been observed for M [147]. α -sialons are thus at least quaternary compounds and hence do not appear in Figure 4.1.

γ -alon The composition $\text{Al}_3\text{O}_3\text{N}$ would correspond to full substitution ($x = 3$) in $\beta\text{-Si}_{3-x}\text{Al}_x\text{O}_x\text{N}_{4-x}$. It is said to have spinel structure, but in fact has not been documented up to the present day.* Given the existence of the spinel $\gamma\text{-Si}_3\text{N}_4$,

over, a better resemblance to the general formula for spinel compounds, AB_2X_4 is achieved. In the following, x or z are addressed as “*substitution level*” or “*insertion parameter*” and are connected by the relationship $2x \equiv z$.

*“ $\gamma\text{-Al}_3\text{O}_3\text{N}$ ” is found in the JCPDS database (PDF-No. 36-50). However, in the respective publication [230] no information on the composition of the investigated phases is given.

$\text{Al}_3\text{O}_3\text{N}$ would be the end member of a solid solution series



Stable spinels containing (cation-vacancy-type) defects are known to exist within the Al–O–N system at higher oxygen concentrations [111, 148]. These aluminum oxide nitrides are called γ -*alons*. For reasons that become clear further below, it is useful to describe the oxygen content in γ -alon with an *insertion parameter* x , similar to that in $\text{Si}_{3-x}\text{Al}_x\text{O}_x\text{N}_{4-x}$ and defined by



According to this scale, the stability field of γ -alon at ambient pressure is given by $4.2 \leq x \leq 4.7$, corresponding to $\text{Al}_2\text{O}_3 \cdot 0.3 \text{ AlN}$ and $\text{Al}_2\text{O}_3 \cdot 0.4 \text{ AlN}$, respectively [148]. Fang et al. recently investigated the hypothetical $\text{Al}_3\text{O}_3\text{N}$ -phase theoretically [231].

4.2 HP/HT-Studies of Sialons Reported in Literature

In spite of the large total number of papers on sialons, only three publications were concerned with their behavior at high temperatures with simultaneous application of *high pressures* in the GPa regime: Between 1992 and 1997 HAVIAR, HERBERTSSON and LENCES explored the compositional stability of β - and *yttrium- α* -sialons up to 6 GPa and 1800 °C respectively [232, 233, 234]. They observed a complicated decomposition behavior of α -sialon. Formation of β -sialon and other phases not further identified was observed. The authors also claim that the maximum substitution level x_{max} in $\beta\text{-Si}_{3-x}\text{Al}_x\text{O}_x\text{N}_{4-x}$ would decrease dramatically with pressure. This will be discussed in more detail in comparison with own results in Section 4.8 on page 255.

The successful shock-synthesis of $\gamma\text{-Si}_3\text{N}_4$ by T. SEKINE and coworkers has been noted previously (recall Sec. 3.3.4 on page 89). In May 2001—about half a year after the first multianvil synthesis of spinell-sialon at Bayreuth*—the

*Series I of the MAP experiments listed in Tab. 4.3 on page 217 were conducted in August/September 2000

same Japanese team demonstrated the possibility of shock induced conversion of β -sialon into the corresponding γ -sialon [112]. Sekine et al. applied the flyer-plate technique to sialons with compositions $x = 0.9$ and 1.4 that were mixed with an excess of Cu powder. At peak shock pressures $\hat{p}_{eq} \geq 50$ GPa no more starting material was found within the XRD-patterns of the recovered products. The recovered *spinel*-sialons showed poor crystallinity and were accompanied by large amounts (up to 70%) of amorphous sialon material, the formation of which was attributed to a sluggish phase transformation during shock treatment. These results are nevertheless of great importance because they provide a starting point for the development of a commercially viable synthesis of spinel sialons which may be then used e.g. as abrasive materials.

4.3 Multianvil Press Synthesis of γ -Sialons

4.3.1 Choice of Starting Materials

From the background-information given in Section 4.1.1, three reasons can be derived, why β -sialon and not α -sialon is the system of choice to study the possible formation spinel-type sialon:

- in the Si–N system, the β -phase, not the α -phase, has been shown to share a common phase boundary to $\gamma\text{-Si}_3\text{N}_4$ (recall Sect. 3.6.1)
- β -sialon contains no other cations than Si and Al. It is therefore less complex and more fundamental.
- β -sialon resembles a closer relationship to the Al–O–N system, where spinel type structures have been observed to occur at ambient pressure.

4.3.2 Synthesis of β -Sialon Starting Materials

Four different β -sialons with nominal compositions $x = 1.0, 1.1, 2.0$, and 2.1 were provided as hot-pressed platelets by Prof. I-Wei Chen (University of Pennsylvania, Dept. of Materials Sciene and Engineering) and I gratefully acknowledge their synthesis by M. Zenotchkine from Prof. Chen's group.

The synthesis-procedure was identical for all four stoichiometries. It is given exemplarily for Si_2AlON_3 ($x = 1.0$) as follows:

Considering the residual oxygen contents within the nitrides, a powder mixture of 66.61 wt.% Si_3N_4 (SN-E-10, Ube Industry, Japan, 1.32 wt.% O), 11.40 wt.% AlN (Type F, Tokuyama Soda Co., CA, 0.9 wt.% O), and 21.99 wt.% Al_2O_3 (AKP 50, Sumitomo Chemical America, NY) was prepared to give the nominal composition Si_2AlON_3 . The powder was attrition milled in isopropyl alcohol for 2 h with high purity Si_3N_4 milling media in a teflon-coated jar. The slurry was dried in a polyethylene beaker under a halogen lamp while being stirred. Finally, charges of the powders were hot pressed in a graphite furnace (1775 °C / 2 h / 30 MPa N_2).

4.3.3 Characterisation of β -Sialons

The phase content of the four β -sialons was verified by powder-XRD and the materials were further investigated by SEM in combination with EDX. The N and O content was furthermore determined by combustion elemental analysis (EA) for all four sialons and EPMA in the case of the sialons with formal compositions $x = 1.0$ and 2.1. The density of the hot-pressed bodies was measured using the Archimedes method.

X-Ray Diffraction

Thin slices suitable for XRD transmission measurements were cut from the hot-pressed sialon platelets and measured according to method *b*) described in Section 2.5.2 on page 66. Analysis of the background of the diffraction pattern revealed some trace impurities of other crystalline phases. In the case of the low substituted β -sialons, the majority of these lines could be assigned to $\alpha\text{-Si}_3\text{N}_4$ and $\beta\text{-Si}_3\text{N}_4$. In the higher substituted sialons other reflexions were found. The two strongest lines correspond to $d = 2.60$ and 2.79 Å with intensities of $\sim 1.5\%$ with respect to the (101) line of the β -sialon. Comparison with corundum, AlN, $\text{Si}_2\text{N}_2\text{O}$ and four different AlON-phases yielded no result. The lattice constants of the samples were obtained by profile-matching of the diffraction patterns. For all

measures derived from the lattice constants, the values given in parentheses correspond to the “*correlated residuals*” of a_0 and c_0 from the profile matching [235]. The knowledge of composition and lattice parameters also allows calculation of the theoretical density, which is shown in Table 4.2 on page 211.

Determination of Chemical Composition

The measured lattice constants were used to calculate the substitution parameter x according to Equations (4.1) and (4.2) on page 203. These x -values refer only to the β -sialon content within the starting materials so that the overall net composition may differ due to the impurity phases. The starting materials were thus further analyzed by EA, EDX and EPMA. All analytical results are given in Table 4.1. The table also contains EPMA data for two of the four HP/HT-treated spinel sialons (γ -sialons). The determination of their composition is prepended here, because it should be essentially identical to those of the β -sialon starting materials. Establishing a precise **compositional scale** is indispensable, if structure and properties of the novel γ -sialons are to be discussed *as a function of* substitution level x . The data of Table 4.1 is visualized in Figure 4.2. It can be seen that in the case of the low substituted sialons, the nominal compositions coincide fairly well with those measured by the various analytical methods. (The hatched line marks 100% correlation). For the high-substituted sialons, the scatter is larger. The x -values obtained from combustion elemental analysis (the black triangles) are notably off the line. These values were calculated from the measured nitrogen content by fitting the formula $\text{Si}_{3-x}\text{Al}_x\text{O}_x\text{N}_{4-x}$. The nitrogen content was lower than expected from the nominal composition in all cases, hence the corresponding x -values appear to be higher. A likely reason for this is that the automatic analyzer failed to detect all the N_2 released from the samples during their combustion. This is possibly due to an oversaturation of the detection cell as all four sialons are still very nitrogen-rich. Equivalent calculation of x using the EA-derived oxygen content gives lower values (empty triangles).

EPMA measurements have been carried out for the $x_{\text{nominal}} = 1.0$ β -sialon starting material and two of the transformed γ -sialons. The data for the spinel sialons is represented by the \star symbol in Fig. 4.2 on page 209. Especially the element percentages for the high substituted $\gamma\text{-Si}_{0.9}\text{Al}_{2.1}\text{O}_{2.1}\text{N}_{1.9}$ are in excellent

Elemental Composition of $\text{Si}_{3-x}\text{Al}_x\text{O}_x\text{N}_{4-x}$ starting materials and products

Analyt. method	Comment	Nominal composition x [–]			
		1.0	1.1	2.0	2.1
XRD	x calculated with a_0	0.98(1)	1.07(1)	1.83(0)	1.96(1)
	x calculated with c_0	0.99(1)	1.08(4)	1.97(0)	2.08(0)
	a_0 [Å] profile match.	7.6615(7)	7.6665(3)	7.7119(0)	7.7194(3)
	c_0 [Å] profile match.	2.9574(3)	2.962(1)	3.0074(0)	3.0129(1)
EA ^[a]	calcd. after N content*	1.25	1.205	2.150	2.270
	N [mass%] experiment	27.5	27.7	18.2	17.0
	N [mass%] theoretical	29.8	28.8	19.7	18.7
	cald. after O content	0.94	1.03	1.87	1.96
	O [mass%] experiment	10.70	11.70	21.00	22.50
	O [mass%] theoretical	11.33	12.47	22.54	23.64
EDX	x ^[b]	0.99	1.05	1.93	2.02
	EDX-counts	6239	6558	8140	9267
EPMA	Phase	β -sialon	β -sialon	γ -sialon	γ -sialon
	Acceleration Voltage	10 kV	20 kV	20 kV	20 kV
	No. of data points	3	3	8	60
	Nominal comp. x [–]	1.0	1.0	1.0	2.1
	Measured comp. x ^[b]	1.017[1]	0.984[1]	1.028[7]	2.09(1)
	Si [mass%]	36.8[1]	39.2[2]	36.9[4]	18.1(3)
	Al [mass%]	18.12[4]	18.39[4]	18.5[2]	39.9(1)
	O [mass%]	10.7[1]	10.3[1]	10.8[3]	23.4(7)
	N [mass%]	25[1]	23.3[7]	22.4[8]	18.6(7)
	Σ [mass%]	90[1]	91.2[7]	88.5[1]	100(1)

[a] combustion N/O analysis by hot-gas extraction method, LECO analyzer [b] according to Al:Si-ratio

Table 4.1: Elemental composition of β -sialon starting materials as determined by different analytical methods. Standard deviations are given in parentheses, while square brackets denote the maximum deviation from the average.

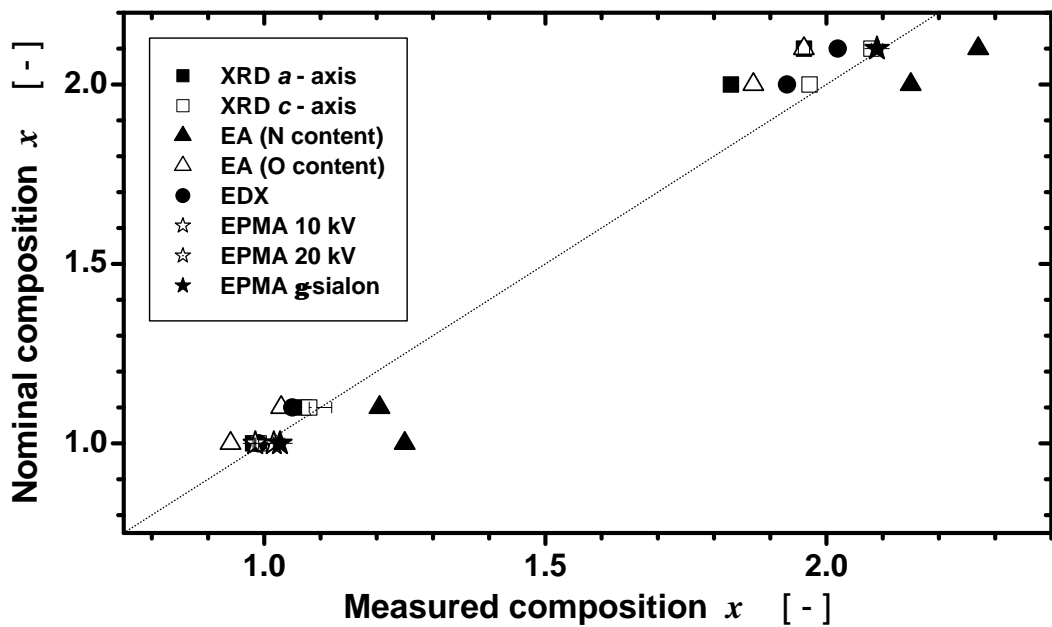


Figure 4.2: Visualization of the analytical results for the four β -sialon starting materials

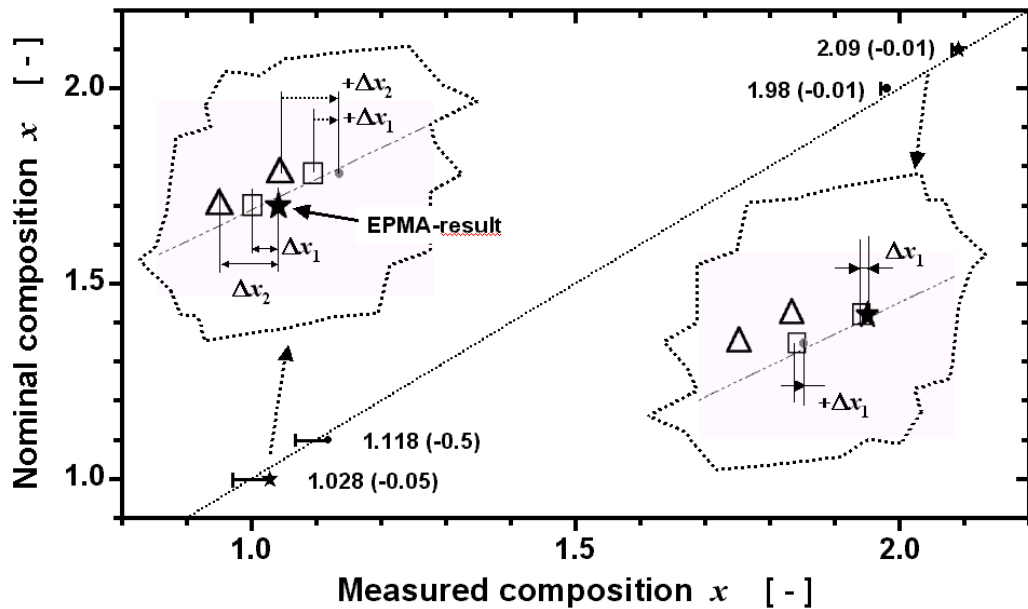


Figure 4.3: The compositional scale to be used throughout the following characterization of (β - and) spinel-sialons. Insets: Systematic differences $\Delta x_{1,2}$ between EPMA based data and the results of other methods is used to estimate the composition of the two γ -sialons with intermediate substitution.

agreement with the nominal values (cf. the last column in the lower right corner of Table 4.1). These results are based on 60 individual measurements which provides a good statistical basis. An experimental x value of 2.09 ± 0.01 was obtained and is to be compared with the nominal composition of 2.1. All x -values derived from the EPMA (and EDX) results were calculated from the ratio of the heavier elements Si and Al, while the measured percentages of the O and N yielded less accurate values. The difficulty to quantify these light elements using electron or X-ray excitation techniques is a well known problem. Si and Al are not volatile and hence the ratio of these elements should be the same before and after the HP/HT-treatment. The compositional differences that are apparent between the EPMA results for the $x_{nominal} = 1.0$ sample (Tab. 4.1, the three lowest columns in the middle) may be due to different surface roughnesses of the porous β -sialon starting material (see “Microstructure” further below) and the almost 100% dense spinel sialon.

Establishing a Compositional Scale for β - and γ -Sialons In Figure 4.3 on the preceding page the compositional scale that will be used throughout the entire following work to discuss the structure and properties of (β -) γ -sialon with respect to their substitution level x is shown. This scale was derived as follows:

- (1) EPMA of the transformed sialons is considered the most accurate method. This gives the composition of the highest and lowest substituted γ -sialon with $x = 1.028$ and 2.09 , respectively.
- (2) The compositions of the two other sialons that were not directly measured with EPMA are estimated using the systematic differences between the EPMA results and those obtained from the other methods, as illustrated in the insets of Fig. 4.2.
- (3) All experimental x -values except those obtained from the nitrogen content from the EA measurement are *smaller* than the EPMA results. The asymmetric error bars account for this observation: It is assumed that the true x is more likely smaller than the estimated values printed in Fig. 4.2.

Density Measurements using the Archimedes Method

One or two pieces (~ 0.25 g) of each composition were boiled in distilled water for several hours. Weighing in water was repeated four times. The weight of the dry samples was determined using the same balance after the specimen had been stored at 120 °C for several hours. The archimedean density values are tabulated together with the ‘theoretical’ densities determined from the lattice constants and the composition established in the previous section. Comparison between these values provides an estimate for the closed porosity, which becomes smaller at high substitution levels. This is in accordance to the better sinterability and densification behavior due to the more ionic character at increased AlO content.

x [-]	M [g/mol]	$\langle \Omega \rangle$ [Å ³ /atom]	ϱ_{XRD} [g/cm ³]	ϱ_{archi} [g/cm ³]	ϱ_{rel} [%]
1.03	141.20	10.738(2)	3.119	2.86(1)	91.8%
1.12	141.28	10.770(4)	3.112	3.01(1)	96.6%
1.98	142.04	11.064(1)	3.046	3.01(1)	98.9%
2.09	142.14	11.106(1)	3.036	3.00(2)	98.9%

Table 4.2: Densities of β -sialon starting materials as a function of substitution level

Microstructure of β -Sialons

Figures 4.4– 4.7 on page 213 show fractured surfaces of all four compositions of the starting materials as obtained by SEM in the SE mode. The low substituted sialons have well faceted, equiaxed grains with sizes between 0.4 – 1.6 μ m and 0.9 – 2.5 μ m, respectively. The grain size distribution of the high substituted samples is much broader. Large elongated (or plate-like) grains with sectional diameters between ~ 100 and 150 μ m and aspect ratios around 3 coexist with smaller crystallites with D ranging from 5 to several 10 microns.

Because all compositions were sintered for the same time, these differences in grain size reflect the enhanced diffusivity due to the more ionic bonding character at increased AlO contents.

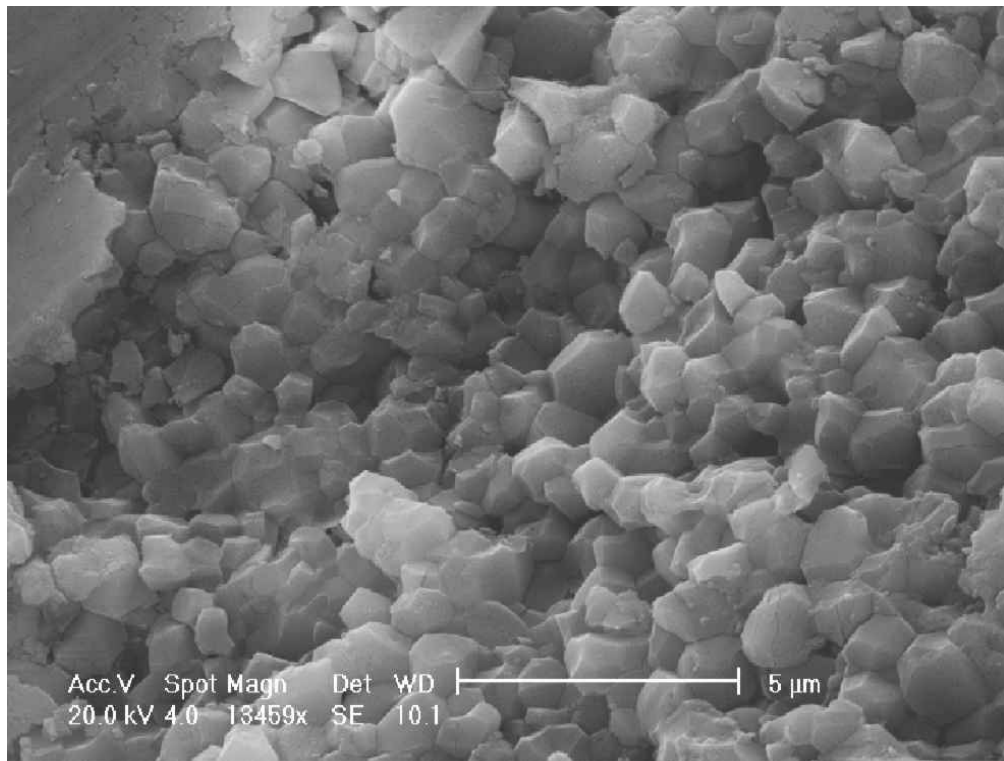


Figure 4.4: Fractured surface of β -sialon with nominal composition $x = 1.0$

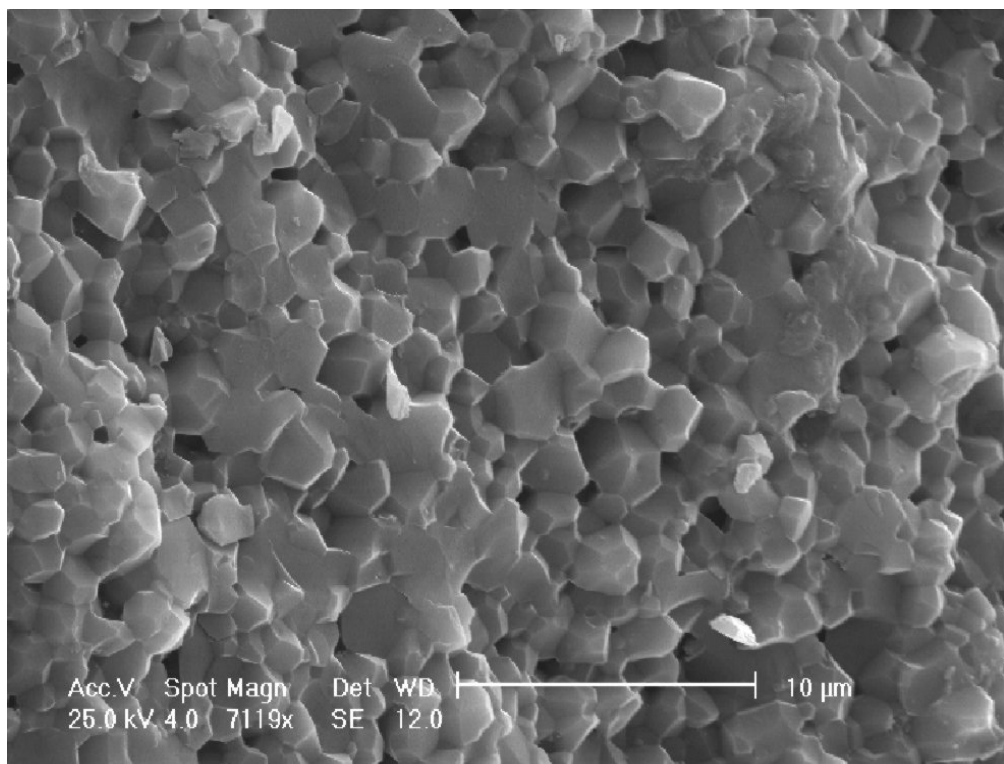


Figure 4.5: Fractured surface of β -sialon with nominal composition $x = 1.1$

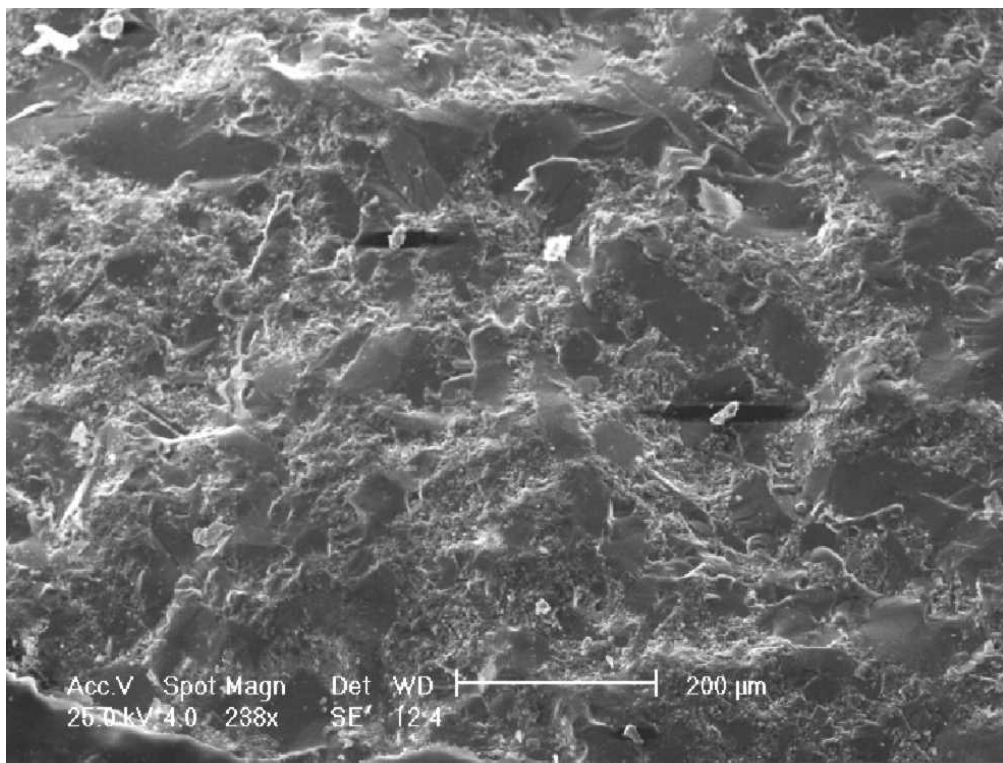


Figure 4.6: Fractured surface of β -sialon with nominal composition $x = 2.0$

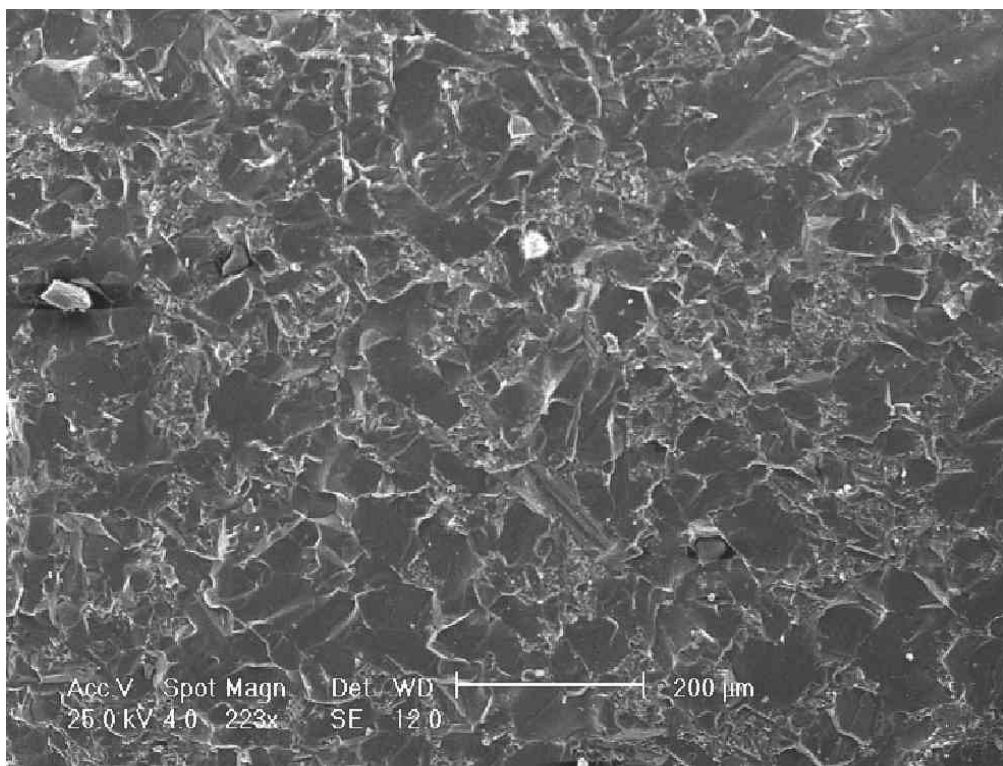


Figure 4.7: Fractured surface of β -sialon with nominal composition $x = 2.1$

Other specimen of the four β -sialons were hot embedded and wet-ground down to 4000 mesh SiC-paper. The low substituted samples showed considerable surface porosity that decreased towards higher AlO insertion. This trend is consistent with the grain sizes and the measured archimedian densities. However, as all pores were filled with water, the absolute values of the archimedian measurements do not include this open porosity. Subsequent SEM investigations after plasma etching did not reveal any indications for the presence of an oxidic intergranular phase. In conventional Si_3N_4 based ceramics, glass phase appears as a raised rim around each grain, because the etching rates of the oxide glass is lower than that of the nitride grains (recall Sect. 2.4 on page 63).

4.3.4 Sample Preparation and HP/HT- Experiments

As the β -sialon starting materials were already available as dense sintered compacts, the same approach as in the case of the $\beta\text{-Si}_3\text{N}_4$ -based ceramic of Experiment SN13, i.e. to prepare small cylindrical pieces to be inserted into the multianvil assembly, was chosen. In contrary to the tough $\beta\text{-Si}_3\text{N}_4$ ceramic, it was however not possible to obtain pieces of sufficient length using the diamanted core drill, because the material was too brittle for this operation. Instead, rectangular pieces of appropriate size were cut from the sintered platelets and subsequently wet-ground into cylinders by removing the edges. Representative specimen are shown in Figure 4.8. Table 4.3 on page 217 gives an overview on the corresponding sample dimensions, the employed sample encapsulation and the experimental parameters of the multianvil HP/HT-treatments.

Part of the sample preparation, multianvil experiments and characterization was conducted under my guidance by K. RAMA SUBRAHMANYAM in the course of a masters thesis at the Fachgebiet Disperse Feststoffe. I highly acknowledge his effort and achievements and thank also for fruitful discussions.

As can be seen in Table 4.3 on page 217, three series of MAP experiments, denoted as I, II, and III were conducted. In series I, both pressure and composition were varied because a decrease of the transformation pressure p_t with increasing x was suggested. Spinel-sialon was however only formed at the highest applied pressure (Experiment HP-Sial20-I, $p_{max} = 13$ GPa). This pressure was then applied in all subsequent experiments for all compositions.



Figure 4.8: Small cylinders of sintered β -sialon were used as starting material

In series II it was tried to maximize the amount of synthesized spinel sialon by omitting encapsulation with an MgO-tube (**F4**) or any equivalent part (recall Fig. 2.3 on page 27). Also, a shorter MgO-buffer piece (**F5**) was inserted to maximize the sample volume. The starting material was left in direct contact to the LaCrO₃ heater (**F4**). In case of Exp. HP-Sial42-II, MgO powder was used to fill up void space between the (not precisely cylindrical) sample and the LaCrO₃ tube. All three compositions were transformed into γ -sialons, but not without significant losses due a chemical reaction and melting at the sialon/LaCrO₃ interface. During the MAP-experiment, this reaction was recognized by strong fluctuations in heating power and displayed temperature. The T_{max} values given in Table 4.3 are the last temperature readings before the onset of the fluctuations. The heating was terminated shortly after the fluctuations occurred, but the actual temperatures at that time were likely higher.

For the third series, reaction between sample and heater was tried to be pre-

vented using BN-capsules of type 1 (Fig. 2.4 on page 29). MgO capsules were not used in order to avoid formation of complex Mg–Si–Al–O–N compounds. The BN-capsules were refluxed in methanol to remove any traces of boron oxide. Two samples were prepared for the nominal composition $x = 2$, in order to track differences between a powdered (HP-Sial20-IIIa) and a solid sintered (HP-Sial20-IIIb) starting material. The sialon powder of HP-Sial20-IIIa was packed in a Pt-capsule as described in Section 2.1.2 on page 28. Unfortunately, probably because of a reaction between the W/Re thermocouple and the purified BN, this latter experiment overheated and major parts of the octahedron interior melted (as revealed after sample recovery). To prevent this reaction, T_{max} was reduced in the subsequent experiments to 1650 °C while t_{hold}^T was extended to one h, intending to maintain a complete transformation. In these cases however, no γ -sialon but an assembly consisting of α -Al₂O₃ and unknown phases was obtained. Further results for all samples will be treated in subsequent sections.

4.3.5 Sample Recovery, Preparation and First Investigations

Series I The recovered pressure cells from series I were primarily broken and the noble metal partially removed. In subsequent preparation steps, also the diamond wire saw and other tools were used (recall Sec. 2.1.2 on page 32)

Series II The diamond wire saw was partially used right from the beginning. In particular, the whole octahedron of HP-Sial42-II was halved with the sample cylinder axis in the cutting plane. Both pieces were hot-embedded and polished.

Series III The two HP-Sial20-III samples were broken, while in the case of the higher substituted products HP-Sial40-III and HP-Sial42-III, the molybdenum plate (**O8**) and the MgO-buffer piece (**F5**) were removed by grinding (see Fig. 2.1.2 on page 32). Once the sialon material appeared at the surface of the pressure cell, two thin slices were obtained from each octahedron by diamond wire cutting perpendicular to the sample cylinder axis. The remaining larger octahedron pieces were hot-embedded, ground and polished for hardness testing.

Tables 4.4–4.6 on pages 218–220 provide an overview on the further characterization of the samples recovered from these three series.

Table 4.3: Overview of HP/HT-experiments in the system Si–Al–O–N

Exp. No.	composition x	sample en- vironment	capsule size $\oslash \times h$ [mm]	pressure assembly	p_{max} [GPa]	T_{max} [°C]	t_{raise}^T [min]	t_{hold}^T [min]	result
HP-Sial20-I	1.0	Pt/MgO	1.5 × 2.7	14 M	13	1800	19	–	γ -Si ₂ AlON ₃
HP-Sial22-I	1.1	Pt/MgO	1.5 × 2.8	14 M	11	\dagger 700	24	–	remains β -sialon
HP-Sial40-I	2.0	Pt/MgO	1.8 × 3.3	18 M	8	\ddagger 1700	15	5	decomposition:
HP-Sial42-I	2.1	Pt/MgO	1.7 × 3.5	18 M	10	1800	?	60	α -Al ₂ O ₃ (?) + X
HP-Sial22-II	1.1	LaCrO ₃	1.5 × 2.8	14 M	13	\S 1800	12	1	γ -Si _{1.9} Al _{1.1} O _{1.1} N _{2.9}
HP-Sial40-II	2.0	LaCrO ₃	1.8 × 3.3	14 M	13	\P 1800	12	10	γ -SiAl ₂ O ₂ N ₂
HP-Sial42-II	2.1	LaCrO ₃	1.7 × 3.5	14 M	13	$\ $ 1800	10	–	γ -Si _{0.9} Al _{2.1} O _{2.1} N _{1.9}
HP-Sial20-IIIa	1.0**	Pt/BN	1.5 × 2.7	14 M	13	1750	9	–	<i>molten</i>
HP-Sial20-IIIb	1.0	BN	1.5 × 2.7	14 M	13	1650	13	60	β -sialon + Y
HP-Sial22-III	1.1	BN	1.5 × 2.8	14 M	13	--	--	–	blowout, β -sialon
HP-Sial40-III	2.0	BN	1.8 × 3.3	14 M	13	1650	11	60	decomposition:
HP-Sial42-III	2.1	BN	1.7 × 3.5	14 M	13	1650	9	60	α -Al ₂ O ₃ (?) + Z

X, Y, Z: unidentified phases

Table 4.4: Overview on the investigations of HP/HT-derived sialon samples (series I)

Exp. No.	'Raw sample recovery'	First observations	Further Preparation	Characterized with ...
HP-Sial20-I	Two cylindrical pieces with surrounding encapsulation: (1),(2)	Fract. surface dark grey and opaque (starting mat.: white)	(1) broken and ground for XRD, (2) prepared for hardness test and EPMA, then broken for XRD	OM, SEM, XRD/Rietveld, EPMA, HV hardness testing, RAMAN
HP-Sial22-I	Single piece in intact (ductile) Pt-capsule	Pt/sample interface coarse and inhomogeneous	cut thin slice with wire-saw for XRD, material very soft	OM, SEM, XRD
HP-Sial40-I	Three cylindrical pieces (1),(2) and (3), Pt brittle and adhering to product	Pt partially molten at TC side, fract. surface inhomogeneous grey to black	small piece ground for XRD, dark (Pt-containing?) material separated by sedimentation	OM, SEM, XRD, TEM
HP-Sial42-I	Single piece in intact (ductile) Pt-capsule	Pt/sample interface coarse and inhomogeneous, white layer, grey body, black spots	Sample broken and small piece ground for XRD	OM, SEM, XRD, TEM

Table 4.5: Overview on the investigations of HP/HT-derived sialon samples (series II)

Exp. No.	'Raw sample recovery'	First observations	Further Preparation	Characterized with ...
HP-Sial22-II	Initially single piece seated in octahedron fragment	Several cracks \perp to cylinder axis, sample double cone shaped, fine grained, greenish opaque appearance	Sample embedded and sectioned with diamond saw. Prepn. of thin γ -sialon bar ($\sim 0.5 \times 0.5 \times 4$ mm) for synchrotron XRD.	OM, SEM, XRD (reflect. & transm. <i>Synchrotron</i>), Rietveld, <i>HV</i> and <i>HU</i> hardness testing
HP-Sial40-II	Single cylindrical piece, seated in octahedron fragment	Sample fine grained and almost translucent, cracks \perp to cylinder axis	Sample embedded and sectioned with diamond saw. Pieces for XRD and hardness testing	OM, SEM, XRD (reflect. & transm.), Rietveld, <i>HV</i> and <i>HU</i> hardness testing
HP-Sial42-II	Octahedron halved axially with diamond wire saw	Sectioned sample (formerly a cylinder) is hour-glass shaped due to reaction with heater.	Small sialon platelet cut for XRD, then both halves embedded and polished for Vickers and SEM	OM, SEM, XRD (reflect. & transm.), Rietveld, <i>HV</i> and <i>HU</i> hardness testing

Table 4.6: Overview on the investigations of HP/HT-derived sialon samples (series III)

Exp. No.	'Raw sample recovery'	First observations	Further Preparation	Characterized with ...
HP-Sial20-IIIa	Center of the octahedron partially diamond wire-cut and polished	Sample interior (including Pt and parts of BN-capsule and sample) was molten, former sialon difficult to identify	Thin section cut with wiresaw for XRD	OM, XRD
HP-Sial20-IIIb	Sample in one piece and smaller splinters	Sample has bluish-white, opaque appearance, fine grained.	Small sialon platelet cut for XRD, abnormally long cutting time	OM, SEM, XRD (transm.), Rietveld, Vickers
HP-Sial22-III	Unheated sample opened and measured			
HP-Sial40-III	Mo-plate (O8) and MgO-piece (F5) removed by grinding	Sample milky-white opaque	Two octahedr. slices cut \perp to cylinder axis, remaining piece embedded and polished ^[a]	OM, XRD (transm.), Rietveld, Vickers
HP-Sial42-III	Mo-plate (O8) and MgO-piece (F5) removed by grinding	Sample milky-white opaque	Two octahedr. slices cut (\perp to cyl. axis), remaining piece embedded and polished ^[a]	OM, XRD (transm.), Rietveld, Vickers

[a] encapsulation obviously converted to dense *c*-BN, sialon erodes much faster

4.4 X-Ray Diffraction Studies

4.4.1 Acquisition of Diffraction Data and Phase Identification

After the HP/HT-treated sialon samples had been recovered, prepared and investigated by optical microscopy, X-ray pattern were taken in order to check for the presence of any spinel and/or other phases. Except for HP-Sial20-I, which was the first γ -sialon synthesized and received special treatment (see below), either **Diffractometer A** or **Diffractometer B** was used.* According to these XRD results, the products of the HP/HT experiments can be divided into three groups, each represented by one of the graphs that are shown on the following pages (Figs. 4.9–4.11).

Group 1: Successfully synthesized spinel-sialons (γ -sialons):

- HP-Sial20-I
- HP-Sial22-II
- HP-Sial40-II
- HP-Sial40-II

Group 2: Essentially untransformed β -sialons:

- HP-Sial22-I
- HP-Sial20-II
- HP-Sial22-III[†]

Group 3: Decomposition into other (unknown) phases:

- HP-Sial40-I
- HP-Sial42-I
- HP-Sial40-III
- HP-Sial42-III

Comparing the synthesis conditions in Table 4.3 on page 217 with these results, it becomes clear that the γ -sialons (Group 1) were only obtained from experiments with the highest applied pressure and temperature of 13 GPa and 1800 °C.

*See page 65 in the techniques chapter

[†]The experiment could not be heated: A disruption of the pressure assembly occurred during compression (“blow out”)

Also the comparatively short heating times (t_{hold}^T) in these experiments may have played a role for the γ -sialon formation. Further evaluation of the experimental p - T - t data and identification of the decomposition products of the samples of Group 3 is attempted in Section 4.8 at the end of this chapter. It will provide some insights into the $\beta \rightarrow \gamma$ transformation and the stability of Si-Al-O-N materials at HP/HT-conditions in general. The major part of this work is dedicated to the novel γ -sialons. The fact that samples of *all four compositions* were successfully converted into the spinel phase confirms the existence of a γ - $\text{Si}_{3-x}\text{Al}_x\text{O}_x\text{N}_{4-x}$ solid solution series, as suggested in the introduction to this chapter. Sialon spinels are the first experimentally confirmed γ - Si_3N_4 -derivatives and the first spinels to contain quadrivalent and trivalent cations simultaneously (4-3 spinels). In the following section, quantitative determination of the relationship between substitution level x and the lattice parameter a_0 is presented. This leads to considerations on related phases such as the hypothetical end member γ - $\text{Al}_3\text{O}_3\text{N}$ ($x = 3.0$) and the γ -alons that are oxygen-rich spinels in the system Al_2O_3 -AlN. Determination of the second structural parameter, the anion position \mathbf{u} via Rietveld analysis was carried out in the case of sample HP-Sial20-I and published in [113]. It will be also presented here, and, together with the aforementioned lattice parameter a_0 , opens for the discussion of the bonding structure and cation disorder within the spinel sialons. Experimental as well as theoretical results from other researchers will be included here.

Acquisition of Diffraction Data Chronologically, sample HP-Sial20-I with an approximate stoichiometry Si_2AlON_3 was the first sialon successfully transformed into the spinel modification. For powder XRD, initially a piece of the recovered sample was ground in an unused agate mortar. This caused considerable wear, evidenced by a rapid roughening of the polished agate surface. The resulting XRD pattern (data set I) showed the presence of α -quartz that could be traced to debris from the mortar. A volume fraction of quartz as high as 20% was determined via quantitative phase analysis. This documented impressively the high abrasive strength of the transformed sialon. We determined the lattice parameter $a_0^I = 7.823 \text{ \AA}$ of the spinel phase. Simultaneous determination of the quartz lattice constants revealed very small deviations from the literature values* (+0.07% and 0.1% for a_0 and c_0 , respectively). To obtain a diffraction pattern free of quartz, another piece of HP-Sial20-I (70 μm in diameter, ca. 20 μm

*PDF Card No. 46 1045

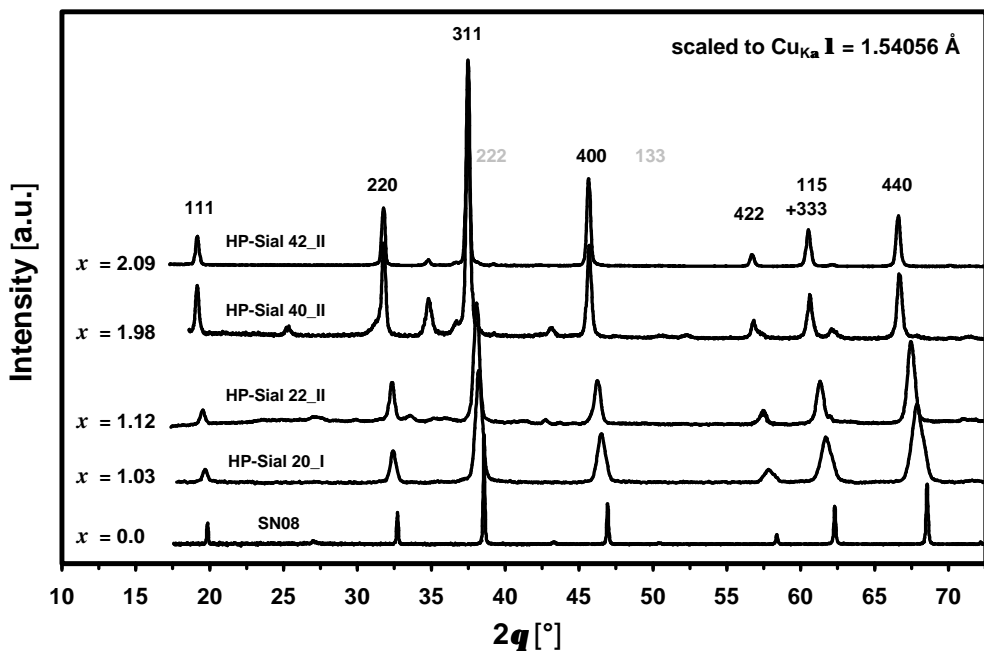


Figure 4.9: Diffractograms of the four successfully synthesized γ -sialons containing some impurity phases. Pattern of γ - Si_3N_4 ($x = 0$) shown as a reference. A systematic shift of the line positions with increasing x (AlO content) is apparent.

thick) was split from the central portion of the cylindrical sample, mounted on a glass capillary and inserted in a Gandolfi camera (**Diffractometer D**). A standard one-dimensional diffraction pattern (data set II) was obtained as outlined in Section 2.5.1 on page 65. It is the one included in Figure 4.9, with the background subtracted and the abscissa adjusted to $\text{Cu } K\alpha_1$ radiation for comparability. Figure 4.15 within the next section shows the pattern in more detail and along with the Rietveld difference plot. In contrast to the other compositions, almost no crystalline impurities are present. This proves the direct conversion of β -sialon into a single-phase spinel and the material of this particular composition is hereafter named γ - Si_2AlON_3 .[†] The geometry of the Gandolfi method causes the corresponding lattice constant (denoted with a_0^{II}) to depend critically on the exact value of the distance between the sample and the X-ray film or imaging plate. Hence a_0^{I} that was derived from data set I and is backed against the lattice parameters of the quartz impurity, is considered the more precise value. In contrast to the line positions, the recorded intensities remain essentially unaffected and data set II was used for a second structure refinement.

[†]Precise composition according to the aforementioned chemical analysis: $\text{Si}_{1.97}\text{Al}_{1.03}\text{O}_{1.03}\text{N}_{2.97}$

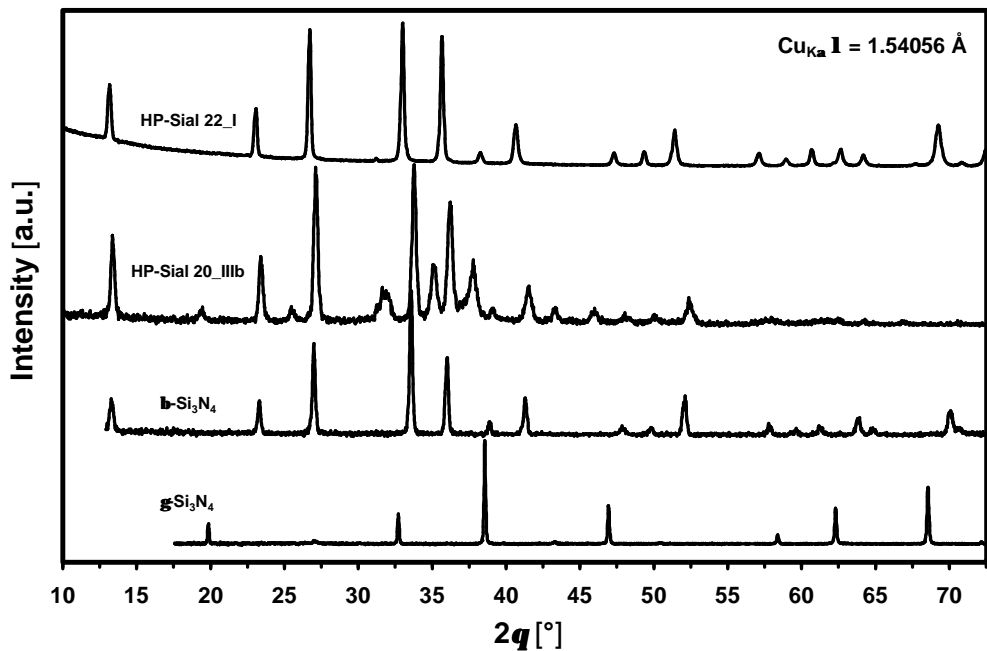


Figure 4.10: X-ray pattern of two untransformed or partially transformed β -sialons. Diffractograms of $\beta\text{-Si}_3\text{N}_4$ and $\gamma\text{-Si}_3\text{N}_4$ shown as a reference.

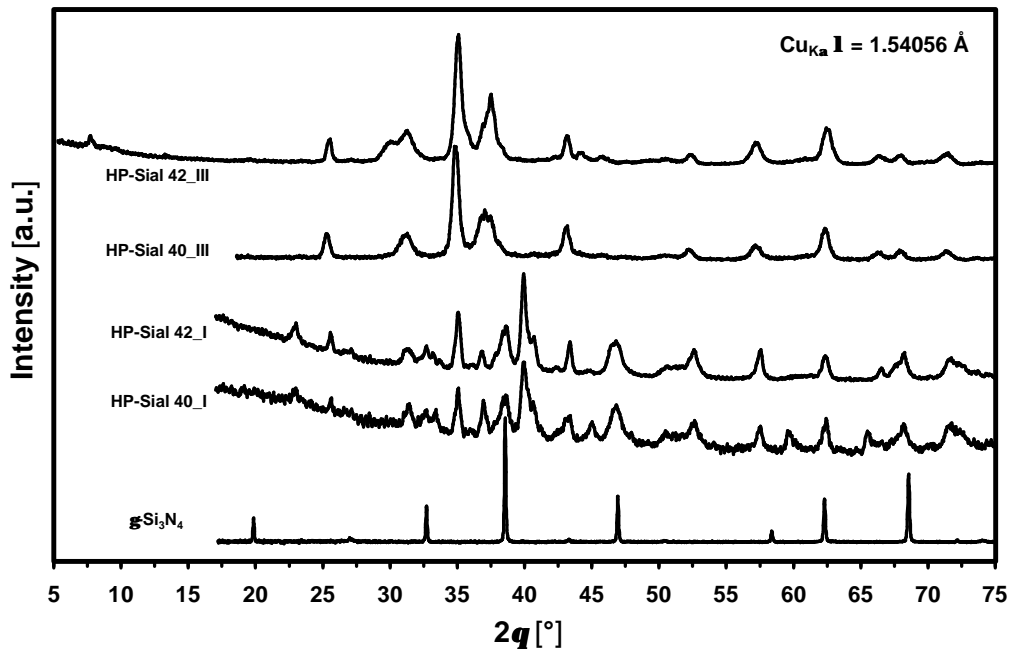


Figure 4.11: X-ray pattern of sialon decomposition products from Series I and III of the HP/HT experiments.

4.4.2 Compositional Dependency of Lattice Parameter

The lattice parameters for the four γ -sialon compositions were obtained by standard least square methods, either within the profile matching mode or during full Rietveld refinement in the case of HP-Sial20-I. In Figure 4.12, the results for both sialon modifications are plotted against the corresponding substitution level x . The cubic lattice constants a_0 of the γ -sialons are shown directly, while for the hexagonal β -structure a characteristic parameter a_β was calculated in order to establish direct comparability:

$$a_\beta = \sqrt[3]{56 \cdot \langle \Omega \rangle} \quad (4.4)$$

Here, $\langle \Omega \rangle$ is the average atomic volume given in Table 4.2 on page 211, and 56 the number of atoms within the unit cell of spinel ($Z = 8$). For pure β - Si_3N_4 , the value from the single crystal analysis of GRÜN [236] has been used, and for γ - Si_3N_4 the own data from SN08 as well as Jiang's result [125] was adopted (cf. Section 3.5 on page 101).

It is immediately apparent from the graph that the lattice size of the γ -sialon solid solution series varies linearly with substitution level, just as it has been established for β -sialon (see [229] and references therein). Moreover, the small deviations from the trend line confirm the correctness of the previously determined compositions (cf. Sect. 4.3.3 on page 4.3.3.) Moreover, it appears that the slope of the trend lines, is almost the same for both phases. Regression analysis of the a - x data yielded the following results:

$$\begin{aligned} a_0 [\text{\AA}] &= 7.7347(9) + 0.0872(17) \cdot x \quad (\gamma\text{-sialon}) \\ R^2 &= 0.9993 \end{aligned} \quad (4.5)$$

$$\begin{aligned} a_\beta [\text{\AA}] &= 8.347(2) + 0.0904(14) \cdot x \quad (\beta\text{-sialon}) \\ R^2 &= 0.9996 \end{aligned} \quad (4.6)$$

The difference in the linear increase is $0.094 - 0.0863 = 0.0041 \text{ \AA}$ or 4.7 %. This can be converted into the corresponding *volume* expansion of 2.39 and 1.96 \AA^3 per AlO-pair for β -sialon and γ -sialon, respectively. This means that substitu-

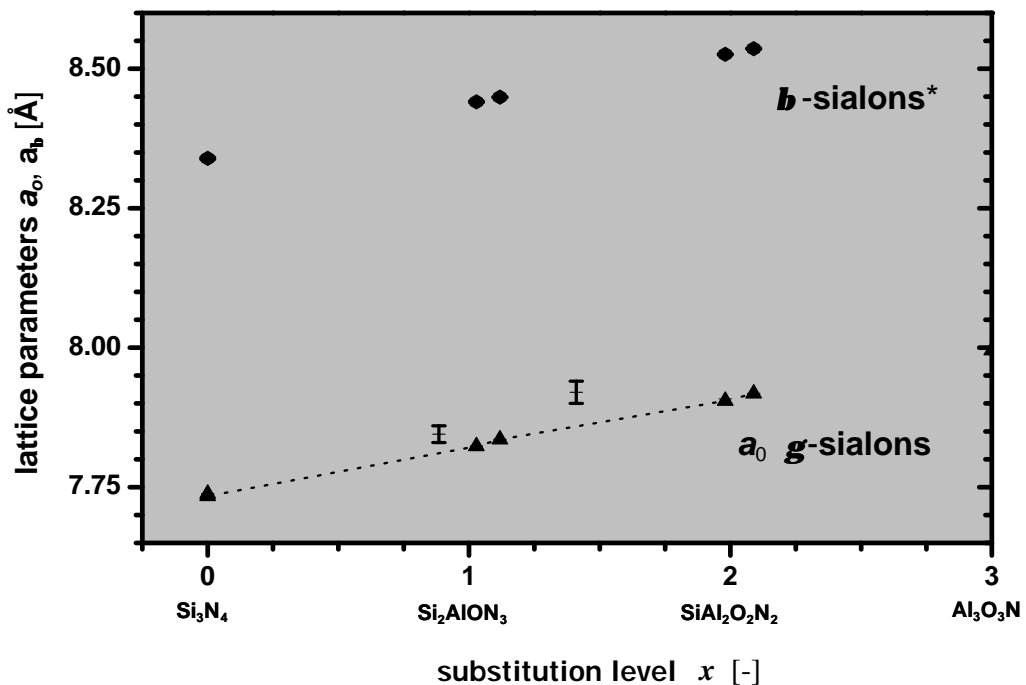


Figure 4.12: Dependency of lattice parameter on AlO substitution level in β - and γ -sialons. At the presented scale, the correlated residuals [235] for both sialon series are smaller than the filled symbols. The error bars above the γ -sialon trend line represent the shock-synthesized material from [112]. The large scatter and positive deviation of lattice parameter is likely due to a very high defect density within the recovered powders.

tion of one SiN versus AlO requires 0.43 \AA^3 (18 %) less space in the dense-packed spinel as compared to the more open structure of $\beta\text{-Si}_3\text{N}_4$. The *relative* volume increase $V^{-1} \cdot \partial V / \partial x$ of the spinel phase is larger: 3.38% versus 3.28% for the β -phase. This shows that the spinel lattice expands more progressively than the phenacite-type $\beta\text{-Si}_3\text{N}_4$. This surplus may therefore be attributed to an increasing population of Al cations in octahedral coordination: Al^{oct} is usually larger than both Al^{tet} and Si^{oct} . Even in the case of a strong preference of aluminum for the *tetrahedral* site, the fraction of Al^{oct} species will inevitably grow for $x > 1$, when all *tetrahedral* sites are already occupied by Al. Determination of the anion parameter \mathbf{u} via Rietveld refinement will provide further information on site preferences in these spinels. SEKINE and coworkers employed ^{29}Si solid state NMR to address this question [112] and at the time of writing also three theoretical publications on γ -sialon and related phases [237, 238, 239] were available. This will be subject of the following sections.

Phase Relationships to the Al–O–N System The present experimental results confirm the hypothesis from the introductory part of this chapter: The existence of a solid solution series $\gamma\text{-Si}_{3-x}\text{Al}_x\text{O}_x\text{N}_{4-x}$ between $\gamma\text{-Si}_3\text{N}_4$ and the aluminum oxide nitride $\text{Al}_3\text{O}_3\text{N}$. Whilst the nitrogen-rich end member of the γ -sialons, $\gamma\text{-Si}_3\text{N}_4$ is now well established and has been treated under various aspects throughout the major part of this thesis, stoichiometric $\text{Al}_3\text{O}_3\text{N} = \text{AlN} \cdot \text{Al}_2\text{O}_3$ has never been observed. Aluminum oxide nitride spinels — the so called γ -alons — are known to exist at the oxygen-rich side of the $\text{AlN}-\text{Al}_2\text{O}_3$ pseudobinary system. According to McCauley, the stoichiometry $\text{Al}_3\text{O}_3\text{N}$ cannot be reached because it lies beyond a threshold, where further AlN insertion into alon causes a local charge imbalance (see [111] and references therein). In addition to experimental work in the 1980s and 1990s, recent ab initio calculations by Fang et al. [231] confirmed the higher stability of the so called “*constant anion model*” originally proposed by McCauley in 1978 [240]. Here the anion sublattice is fully occupied by 32 cations while a part of the cation sites remains vacant in order to maintain charge neutrality. The most stable alon composition, $\text{Al}_{23}\square\text{O}_{27}\text{N}_5$, has one vacancy per unit cell.

Despite $\text{Al}_3\text{O}_3\text{N}$ remains elusive, its would-be lattice constant can now be estimated by extrapolation from ‘two sides’: the γ -alon *and* the γ -sialon system, as illustrated in Fig. 4.13. Here, the compositional scale of the sialons has been extended into the Al–O–N regime by using formula (4.3) on page 204. The alon data has been compiled from publications of McCauley [241] (black triangles) and Willems [103] (black squares) and shows that these two groups obviously obtained different results on the compositional dependence of a_0 in γ -alon which is still subject to some controversy.* The extrapolation of these two series yielded $a_0(x = 3) = 7.971$ and 7.980 \AA , that of the own data 7.997 \AA , respectively. A fourth value of 7.986 \AA was derived from spinels in the Mg–Al–O–N system [175]. The \star symbol at $x = 6$ corresponds to the spinelloid modification of Al_2O_3 .

Apart from the scatter in these extrapolation results due to systematic errors, the values are in a sufficiently small interval to give evidence of the close phase relationship between the γ -sialon and γ -alon solid solution series. It

*J.W. McCauley, personal conversation

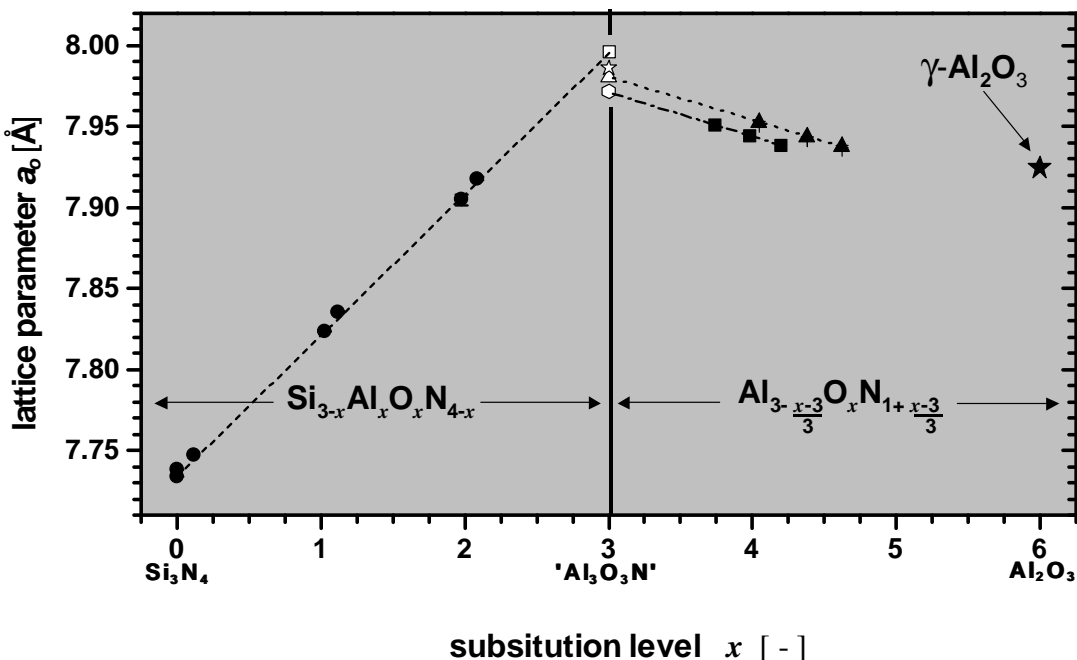


Figure 4.13: Extrapolation to the lattice parameter of the hypothetical spinel $\text{Al}_3\text{O}_3\text{N}$.

is also obvious from the graph that the hypothetical $\text{Al}_3\text{O}_3\text{N}$ would have the largest unit cell volume V in the entire system. As this compound is defined to possess full occupation, this can be converted into an average atomic volume of $\langle \Omega \rangle = V/56 \approx 9 \text{ \AA}/\text{atom}$, which is e.g. to be compared to $\gamma\text{-Si}_3\text{N}_4$ with $8.27 \text{ \AA atom}^{-1}$. Thus, according to Le Chatelier's principle, upon compression, $\text{Al}_3\text{O}_3\text{N}$ and also spinel sialons with a sufficiently high AlO content should be unstable with respect to decomposition into denser phases. This finding will be further traced in Section 4.8 on page 255.

4.4.3 Rietveld Structure Analysis of $\gamma\text{-Si}_2\text{AlON}_3$

The structure of $\gamma\text{-Si}_2\text{AlON}_3$ was published [113] as initially refined directly from the X-ray diffraction data that had been acquired as outlined on page 222. Within the present work, the result of a subsequent structure analysis on data set II is presented. This refinement was carried out after applying further correction in order to convert the integrated intensity from the 2-dimensional image plate (cf. Sect. 2.5.1 on page 65) into the form of a regular Debye-Scherrer diffractogram [84]. The pattern of both data sets, I and II, and their corresponding difference

plots are shown in Figure 4.14 and 4.15 on the following page, respectively. The final R_{Bragg} value was found to be smaller in the case of data set II (see Table 4.7 on page 231). It is therefore assumed that the corresponding refinement yielded the better structure model and will be described in more detail within the following: The 2θ range is $7.6 - 46^\circ$ and the number of theoretical reflections 22. A total of 21 parameters were included in the final refinement. For the spinel phase, 13 parameters were refined: the lattice parameter a_0 , 3 half-width parameters (U, V, W), the Lorentzian isotropic strain parameter, 2 peak asymmetry parameters, three temperature factors, the anion positional parameter \mathbf{u} , and the site occupancy factors of the $8a$ and $32e$ site, $16d$ was left fully occupied to define the intensity scale. The remaining parameters were the zero-point, 6 background polynomial coefficients. For the peak profile, a Thompson-Cox-Hastings pseudo-Voigt function was used.

Using scattering curves for either the neutral atoms or the ions led to nearly the same result. Also, no significant difference could be seen on positioning Al at $8a$ and Si at $16d$, or vice versa or by replacing part of N at $32e$ by O. Table 4.7 on page 231 gives the results for both data sets.

The anion parameter obtained from data set I, \mathbf{u}^I , shows little difference to the value of pure $\gamma\text{-Si}_3\text{N}_4$ ($\mathbf{u} = 0.2597$). The value for \mathbf{u}^{II} as *originally published* was notably smaller (0.2550) [113]. The present value of $\mathbf{u}^{II} = 0.256$ as obtained from the corrected data set II is somewhat closer to \mathbf{u}^I . The difference in these values document the experimental uncertainty, but altogether, a trend towards smaller \mathbf{u} with increasing AlO content is apparent. This means that the deviation δ from the ideal close packing of the anion sublattice ($\mathbf{u} = 0.25$) becomes smaller. In order to exemplify the structural consequences of this, tetrahedral and octahedral bond lengths (d^{tet} , d^{oct}), calculated from \mathbf{u}^{II} , the anion parameter of the better refinement result, and a_0^I , the ‘correct’ lattice parameter that was calibrated against that of the quartz impurity, will be used in the following discussion. The results for d^{tet} and d^{oct} are listed in Table 4.9 on page 232, along with those for pure $\gamma\text{-Si}_3\text{N}_4$ for comparison. As a result of the lower anion parameter, d^{tet} is slightly decreased and d^{oct} increased with respect to the pure nitride. This latter increase is apparently responsible for the increase of the lattice constant from 7.74 to 7.82 Å. The slightly larger size of the octahedral site could be explained by a preferential occupation by Al, which is in general somewhat larger than the

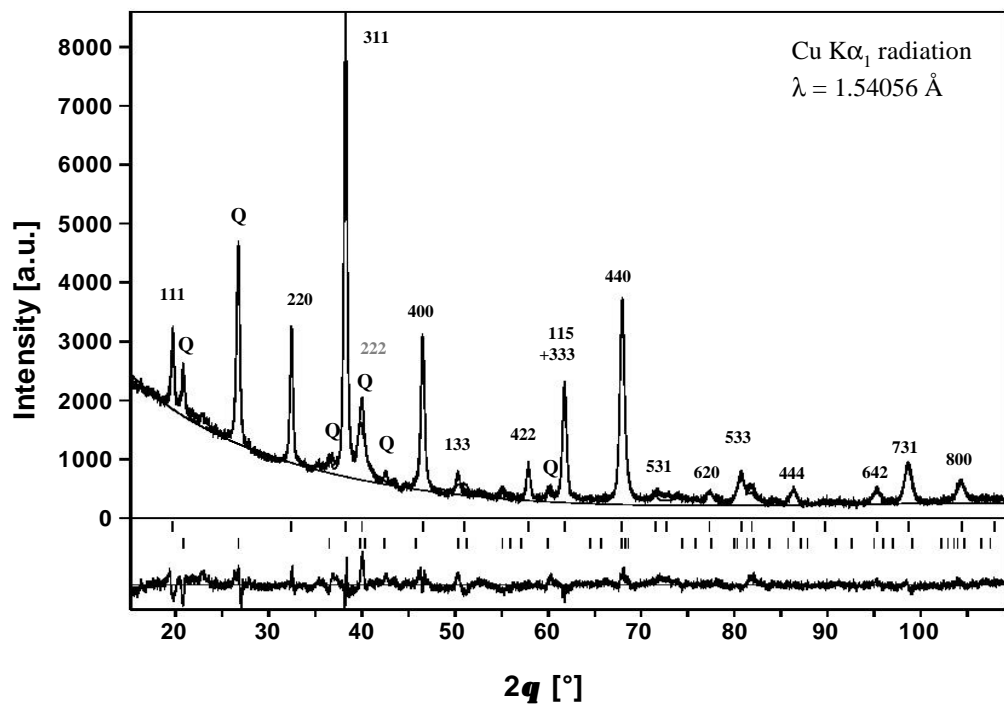


Figure 4.14: XRD powder pattern (data set I) and difference plot of γ - Si_2AlON_3 (sample HP-Sial20-I). Reflections of quartz impurity from the agate mortar are marked with Q

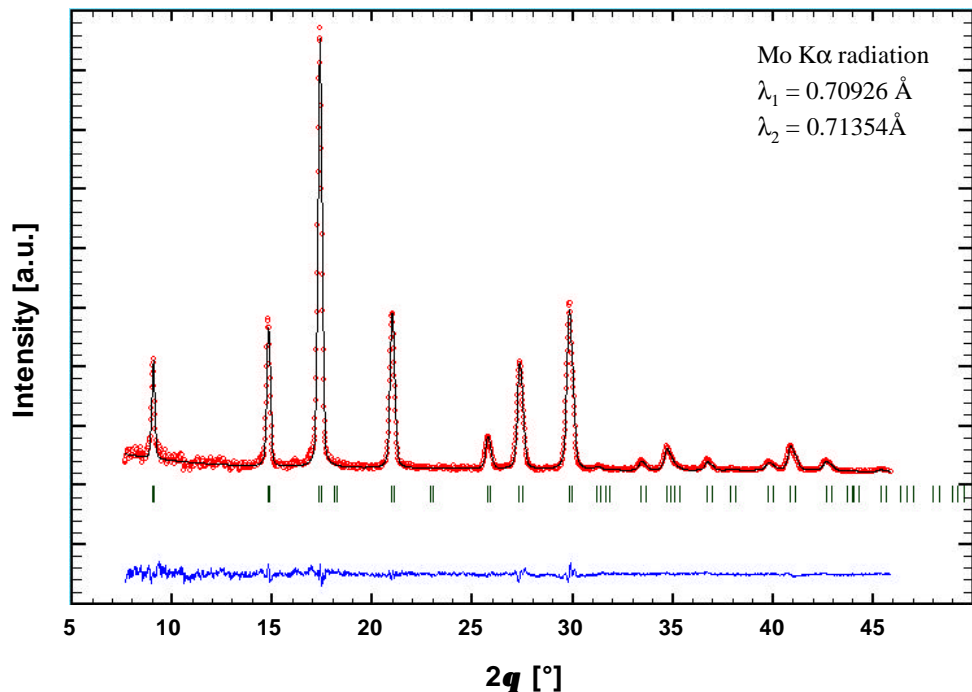


Figure 4.15: XRD powder pattern (data set II, background subtracted) and difference plot of γ - Si_2AlON_3 (sample HP-Sial20-I). Line positions are indicated for Mo $K\alpha_1$ and $K\alpha_2$ radiation, respectively.

Quantity	Symbol	Unit	Data set I	Data set II
Space group	-		$Fd\bar{3}m$ (No. 227)	
Lattice param.	a_0	[Å]	7.8234(3)	7.80(1) ^[a]
Anion param.	\mathbf{u}		0.2591(2)	0.256(1)
Volume	V_0	[Å ³]	478.84	474.45 ^[a]
No. of atoms	Z		8	8
Molecular weight	M	[g mol ⁻¹]	141.17	141.17
Density	$\rho_{calc.}$	[g cm ⁻³]	3.92	3.95 ^[a]
Radiation	λ	[Å]	1.54056 (Cu $K\alpha_1$)	0.7107 (Mo $K\alpha$) ^[b]
Profile range	$2\theta_{min}; 2\theta_{max}$	[°]	18.0 ; 87.9	7.6 ; 45.9
	$d_{max}; d_{min}$	[Å]	4.92 ; 1.11	5.41; 0.92
Step size	$\Delta(2\theta)$	[°]	0.020	0.020
Varied parameters			37 ^[c]	21
Profile function			pseudo-Voigt	pseudo-Voigt ^[d]
R values	R	[%]	4.80	8.31
	R_w	[%]	6.36	13.7
	R_{Bragg}	[%]	6.99	4.48
	χ^2	[-]	2.05	2.67

^[a] Value of a_0 ^{II} not corrected for uncertainties in the sample to imaging plate distance;
^[b]rotating anode; ^[c] includes parameters for quartz; ^[d] Thompson-Cox Hastings

Table 4.7: Crystallographic data for γ -Si₂AlON₃ from two different Rietveld refinements

silicon ion. This would be in agreement to ²⁹Si MAS NMR results from a shock synthesized mixture of γ -sialon and amorphous sialon, published by SEKINE et al. [112]. In contrary to the present multianvil syntheses, the amount of sialon material was sufficient to conduct magnetic resonance measurements. It was found that the Si^{oct}:Si^{tet} signal ratio was smaller than would be expected for a purely random distribution of the Al. The spectrum showed only two sharp signals, corresponding to the SiN₄ and SiN₆ environments in *pure* γ -Si₃N₄ with a

Atom	Position*	site symm.	fractional coordinates			B_{iso} [\AA^2]
			<i>x</i>	<i>y</i>	<i>z</i>	
Data set I						
Al	8 <i>a</i>	$\bar{4}3m$	1/8	1/8	1/8	1.40(6)
Si	16 <i>d</i>	. $\bar{3}m$	1/2	1/2	1/2	-1.8(1) [†]
N/O	32 <i>e</i>	. $3m$	0.2591(2)	0.2591(2)	0.2591(2)	5.2(1) [†]
Data set II						
Al	8 <i>a</i>	$\bar{4}3m$	1/8	1/8	1/8	1.8(2)
Si	16 <i>d</i>	. $\bar{3}m$	1/2	1/2	1/2	2.2(2)
N/O	32 <i>e</i>	. $3m$	0.256(1)	0.256(1)	0.256(1)	3.4(5)

* Wyckoff notation [†] Isotropic equivalents

Table 4.8: Atomic coordinates for $\gamma\text{-Si}_2\text{AlON}_3$ from experiment HP-Sial20-I

Dist./angle	Multiplicity	$\gamma\text{-Si}_3\text{N}_4$	$\gamma\text{-Si}_2\text{AlON}_3$	difference [%]
a_0	-	7.7381(2) \AA	7.8234(3) \AA	+0.6
u	-	0.25968(1)	0.256(1)	-1.4
$d(\text{Si}^{tet}\text{-N})$	4	1.8051(2) \AA	1.77(1) \AA	-1.9
$d(\text{Si}^{oct}\text{-N})$	6	1.8626(1) \AA	1.910(7) \AA	+2.5
$d(\text{Si}^{oct}\text{-Si}^{oct})$	$(= a_0/\sqrt{8})$	2.7358(1) \AA	2.7660(1) \AA	+1.1
$\angle (\text{Si}^{oct}\text{-N-Si}^{oct})$		94.51°	92.78(34)°	-1.8
$\angle (\text{Si}^{tet}\text{-N-Si}^{oct})$		122.00°	123.27(43)°	+1.0

Table 4.9: Selected bond lengths and bond angles of $\gamma\text{-Si}_3\text{N}_4$ (sample SN08) and $\gamma\text{-Si}_2\text{AlON}_3$, the latter calculated from u from data set II and a_0^I from data set I.

signal ratio of 1:5. No peaks from *mixed coordinations* such as SiON_3 etc. could be detected. The authors concluded that almost the entire aluminum occupies octahedral sites within the spinel. It is to be noted however, that this conclusion is regarded as preliminary by the authors themselves and has been drawn on the assumption that the amorphous phase contains solely Si^{tet} species.

Spinel sialons with the lower valent ‘ Al^{3+} ion’ occupying both tetrahedral and octahedral sites may be called ‘partially inverse’ or ‘intermediary’ spinels (cf. Sect. 3.1.3 on page 79). As we shall see from theoretical results discussed within the next section, the site preference is possibly governed by effects other than just the ionicity or size difference between Si^{4+} and Al^{3+} and may moreover change with increasing substitution level x .

Published Theoretical Results on the Structure of γ -Sialon While the structural information acquired by X-ray diffraction does only represent an *average* over the entire sample and solid-state NMR spectra are difficult to deconvolute, theoretical calculations provide direct insights into the *local* bonding structure of the γ -sialons. So far, three theoretical studies explicitly dealing with the spinel modification of sialon have been published: OUYANG and CHING [237] investigated only the composition $\text{Si}_{6-z}\text{Al}_z\text{O}_z\text{N}_{8-z}$ with $z = 1$, while both TATSUMI, TANAKA, and coworkers [238] and LOWTHER [239] investigated γ -sialons at various substitution levels. Moreover, interesting parallels may be drawn to the already mentioned work on γ -alon spinels, published in 2001 by FANG et al. [231]. Insertion of AlO into the $\gamma\text{-Si}_3\text{N}_4$ spinel lattice leads to lowered local symmetries. There is agreement among all three investigations on γ -sialon that this is accompanied by a dispersion of the bond lengths, that are now primarily determined by the individual atom pair, $\text{Al}-\text{O}$, $\text{Si}-\text{N}$, $\text{Si}-\text{O}$ or $\text{Al}-\text{N}$. Similar distortions are also found in γ -alon, where the presence of cation vacancies causes additional relaxation and clustering of oxygen [231]. In agreement to the experimental results, Ching and Lowther find a preference of Al for the octahedral site. The energy difference to configurations with tetrahedral environments is however small, indicating a high probability for random or near-random cation distribution. Also the volume expansion with increasing AlO content is correctly predicted.

TATSUMI and coworkers performed the most elaborate study and considered various bonding configurations for each composition $z = 1, 2, 3, \dots, 6$ in $\text{Si}_{6-z}\text{Al}_z\text{O}_z\text{N}_{8-z}$ for both, γ -sialon as well as the low-pressure β -polymorph [238]. Their results indicate that the site preferences in these spinels are less governed by the size difference between the Al and Si cation (as discussed in the previous section), rather than the *chemical* preference of Al towards oxygen. This means that the energetically most favorable occupation pattern will be always given by those configurations, where the number of Al–O bonds ($N_{\text{Al–O}}$) as well as $N_{\text{Si–N}}$ are maximized. In contrary to the results of Ching, this scheme predicts an *all tetrahedral* environment of Al in the case of Si_5AlON_7 ($z = 1$). By this way, a high Al–O to Al–N bond ratio of 1:3 can be maintained (AlON_3 -units), whereas for the octahedral coordination it would be 1:5 (AlON_5 -units). At higher AlO levels, the fraction of Al^{oct} species is sucessively increased: For $\gamma\text{-Si}_2\text{AlON}_3$, the most stable configuration is predicted to have exactly equal proportions of Al^{tet} and Al^{oct} , i.e. $[\text{Si}_{0.5}\text{Al}_{0.5}]^{tet}[\text{Si}_{1.5}\text{Al}_{0.5}]^{oct}(\text{ON}_3)$ and for $\gamma\text{-Si}_{0.9}\text{Al}_{2.1}\text{O}_{2.1}\text{N}_{1.9}$ the favored configuration $[\text{Si}_{0.75}\text{Al}_{0.25}]^{tet}[\text{Si}_{0.25}\text{Al}_{1.75}]^{oct}(\text{O}_2\text{N}_2)$ is found — governed by the same principle of $N_{\text{Al–O}}$ maximization.

All three theoretical works on γ -sialon also predict interesting details on the electronic structure and the band gap E_{gap} as a function of substitution level of these materials. This will be briefly revised in Section 4.7 on page 252.

Given the predictions of the small energetic differences between individual configurations, there will barely be one unique occupation pattern throughout the entire sialon crystal. Disordering would be paralleled by the situation in oxide spinels, where the cation distribution is known to vary with temperature in order to maximize the configurational entropy [104]. According to Fang's calculations on γ -alon, this entropic contribution is the reason why aluminum oxide nitride spinels are stable with respect to their binary constituents AlN and $\alpha\text{-Al}_2\text{O}_3$ at all. According to experimental results presented in Section 4.8 at the end of this chapter, the same entropical stabilization may be active in the case of the γ -sialons.

4.5 Microstructural Characterization

This section is solely concerned with the samples of Group 1, i.e. those specimen where the sialon spinel phase was formed (cf. Sect. 4.4.1 on page 221). Results on the untransformed and decomposed sialons (Groups 2 and 3) will be presented in Section 4.8 on page 255 at the end of this chapter. The investigations which were mostly carried out with the SEM, but also using EPMA and optical microscopy are presented under two aspects: Firstly, the grain size and grain morphology of the (pure) γ -sialons is documented — important parameters in the interpretation of the micro-mechanical properties of these samples. The second part deals with special features that occurred during the HP/HT treatment: Indications of possible reactions between the sialon and the encapsulation material or the LaCrO_3 heater were investigated by analyzing the recovered samples. Selected results are shown.

4.5.1 Grain Size and Morphology of γ -Sialons

Figures 4.16–4.19 on the following pages show the morphology of γ -sialon fracture surfaces at high magnification. The grain sizes were found to be smaller than those of the starting materials. This is due to the recrystallisation in the course of the phase transformation. The low substituted γ -sialons shown in Figs. 4.16 and 4.5 have small D of less than 1 μm and more irregular grain morphologies than the starting material. Their fracture mode is partially intergranular and partially cleavage. The high substituted sialon samples in contrary exhibit well faceted grains, with a morphology similar to the *low-substituted* β -sialons (compare Fig. 4.19 to the images on page 212). Here, fracture proceeds predominantly along the grain boundaries. The grain sizes are in the range between 1–5 μm which is consistent with the trend for the β -sialons where differences in grain size has been attributed to an increase in ionic bonding with increasing x (Sect. 4.3.3 on page 211). Additionally, grain growth was likely promoted by the longer dwelling times during the HP/HT runs (t_{hold}^T was ten times longer for HP-Sial42-II than for HP-Sial22-II). The different grain sizes of the γ -sialons have important implications for their mechanical properties. The Hall-Petch effect implies higher hardness at smaller grain size. The apparent hardness of the

γ -sialons will therefore contain contributions from both grain size *and* chemical composition, which will be difficult to separate.

After the SEM investigations on the pristine fractured surfaces, some of the specimen were embedded and ground for chemical analysis and hardness testing. Figure 4.17 shows Si, Al, O and N mappings from the center of HP-Sial40-I. Most of the contrast variation is due to residual surface roughness from the grinding, so that there are in fact only small chemical inhomogeneities at this resolution scale.

4.5.2 Reactions between Sialon and the HP/HT-Environment

The occurrence of temperature fluctuations and chemical reactions between the sialon samples and the LaCrO_3 resistance heater during the HP/HT-experiments of Series II has already been anticipated in Section 4.3.4. Evidence for these reactions and partial melting of the octahedron core was especially provided by careful preparation of sample HP-Sial42-II (see Figure 4.20 on page 240). In this cross-section of the octahedral pressure cell, the formerly cylindrical sialon piece now has the shape of an hour glass, the waist of which is roughly one third of the original diameter. A similar double cone shape was also found for sample HP-Sial22-II, which was however less obvious, because in this case the octahedral pressure cell had been broken instead of being cut with a diamond wire saw. Further investigation of sample HP-Sial42-II showed that the reaction did proceed in the molten state: Figure 4.21 is a secondary electron image of the reaction zone at higher magnification. It shows dendritic structures that are typical features of a phase separation during the solidification of a melt. It was already clear from the sample preparation that the reaction zone is softer and less resistant to abrasion than the γ -sialon and no attempts were made to identify the dendritic phase or the surrounding matrix. Investigations of the LaCrO_3 /sialon interface at sample HP-Sial40-II however revealed, that the reaction proceeds under formation of a gas, which is most likely N_2 (Fig. 4.22 on page 241).

Fig. 4.17 on the next page: The diagonal traces in the O and N mappings are artifacts and originate from residual carves of the grinding process. Also the apparent gradient in the Al mapping is caused by variations of detector sensitivity with take-off angle, rather than a real chemical gradient in the material (B. Thybusch, personal communication)

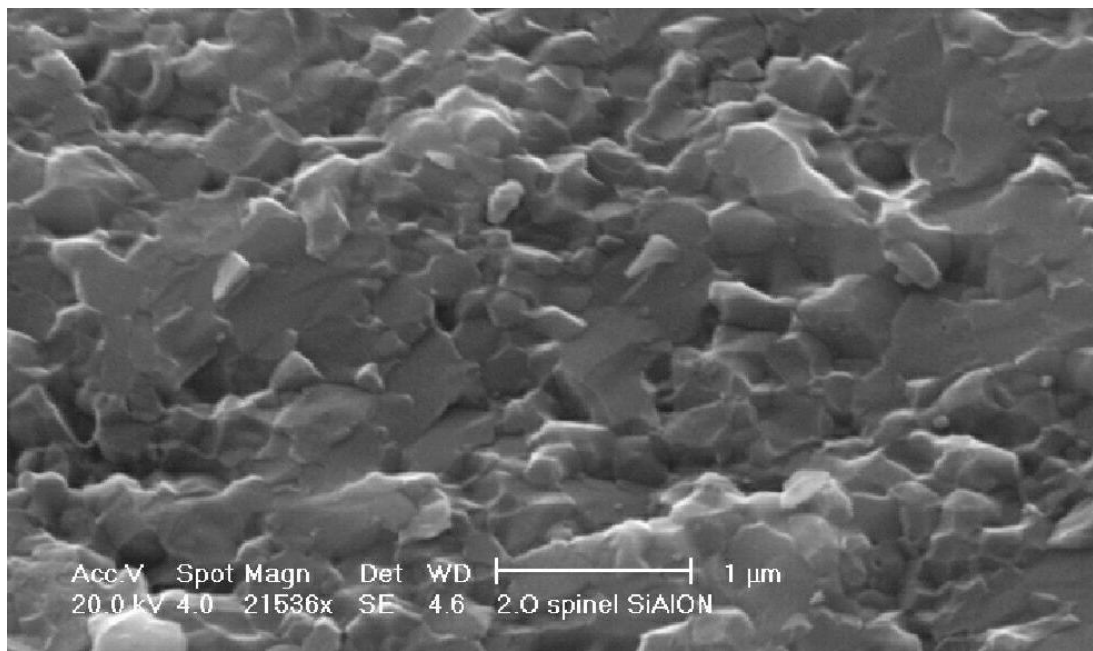


Figure 4.16: Fractured surface of γ - Si_2AlON_3 (sample HP-Sial20-I)

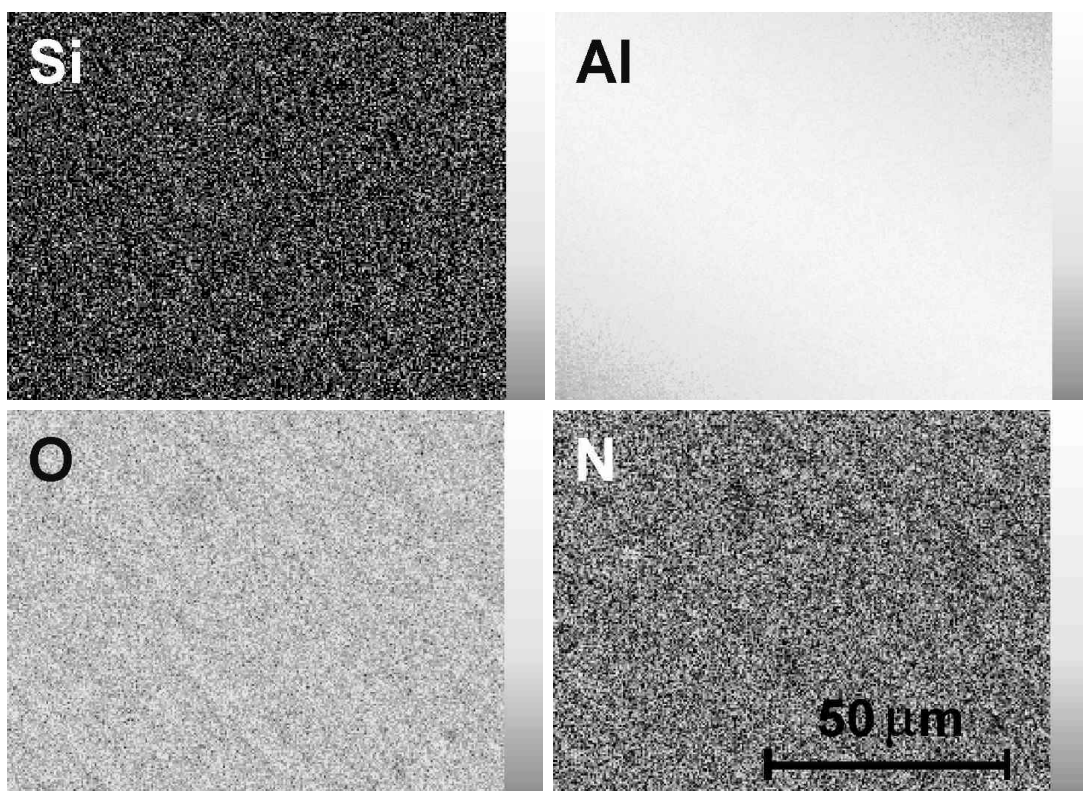


Figure 4.17: EPMA element mappings of the ground surface of HP-Sial40-I, revealing chemical homogeneity at the micrometer scale

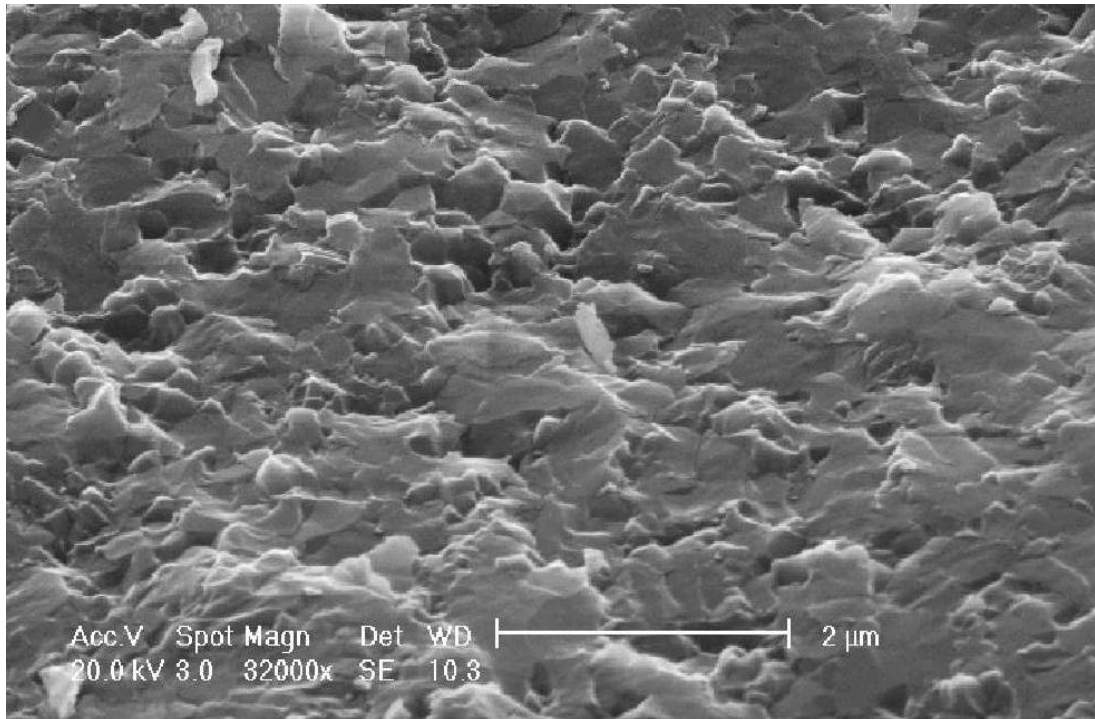


Figure 4.18: Fractured surface of $\gamma\text{-Si}_{1.9}\text{Al}_{1.1}\text{O}_{1.1}\text{N}_{2.9}$ (sample HP-Sial22-II)

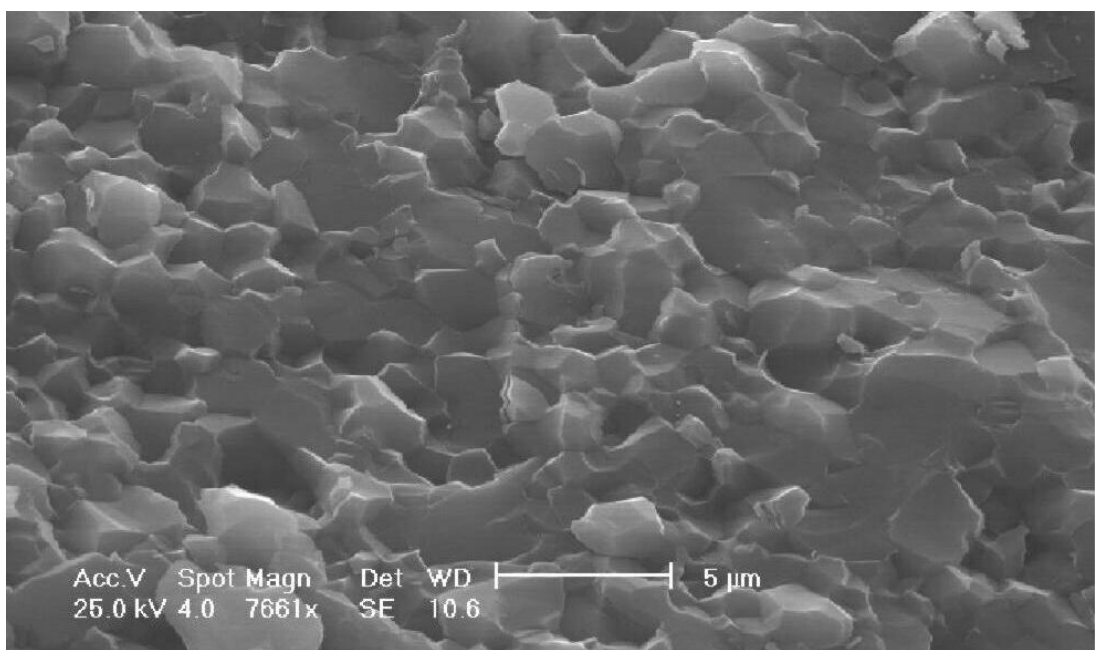


Figure 4.19: Larger and well faceted grains can be seen at higher x , here $\gamma\text{-SiAl}_2\text{O}_2\text{N}_2$ (Sample HP-Sial40-II)

In contrary to the melt-formation with LaCrO_3 , the interface between sialon and the MgO pressure medium* remained sharp but appears to be darker colored than either of the two phases under the optical microscope (Fig. 4.23 on page 241). This indicates a solid state reaction between MgO and γ -sialon. Simultaneous incorporation of Mg, Al and O into $\gamma\text{-Si}_3\text{N}_4$ has already been described for SN13 (cf. Sect. 3.7.3 on page 131). Further investigations, e.g. via transmission electron microscopy on a carefully thinned portion of the interface or via especially designed HP/HT experiments in order to substantiate this hypothesis are planned for the future.

4.6 Micromechanical Properties

4.6.1 Sample Preparation, Testing Methods & Procedure

All samples were hot embedded in either Bakelite with hard mineral filler or a glass-fiber-filled diallylphthalate matrix (Resin 5, Struers) and wet ground down to 4000 mesh SiC paper to give a surface suitable for the indentation measurements. The thus prepared specimen were then subjected to conventional Vickers hardness testing, using **Tester A**. The first hardness imprints were made at 2 kg (HV_2) or 1 kg load (HV_1), which was then decreased until the indentations became undetectable for the optical system. In most cases, this threshold was found to be 5 g. Sample HP-Sial40-I was recovered from the HP/HT experiment in best condition with almost no cracks and a surface area sufficient for four HV_1 and ten $HV_{0.5}$ indentations. Unfortunately the sample had to be sacrificed for X-ray powder diffraction and Rietveld refinement, so that the testing series was not continued to smaller loads. In all other samples coalescence between pre-existent cracks from the HP/HT-synthesis and the crack systems of the Vickers indentations was frequently observed. Consequently, only a few meaningful hardness readings could be obtained at high loads and the data scatter is comparatively high over the entire load range. In some cases, the surface was ground a second time, in order to remove the upper part of the indentations (see Fig. 4.28 on page 245). The γ -sialons of Series II were subjected to instrumented hardness testing, using **Tester D** (load: 100 mN) and **Tester C** (only HP-Sial40-II, load

*i.e. Part (F5) in Figure 2.3 on page 27

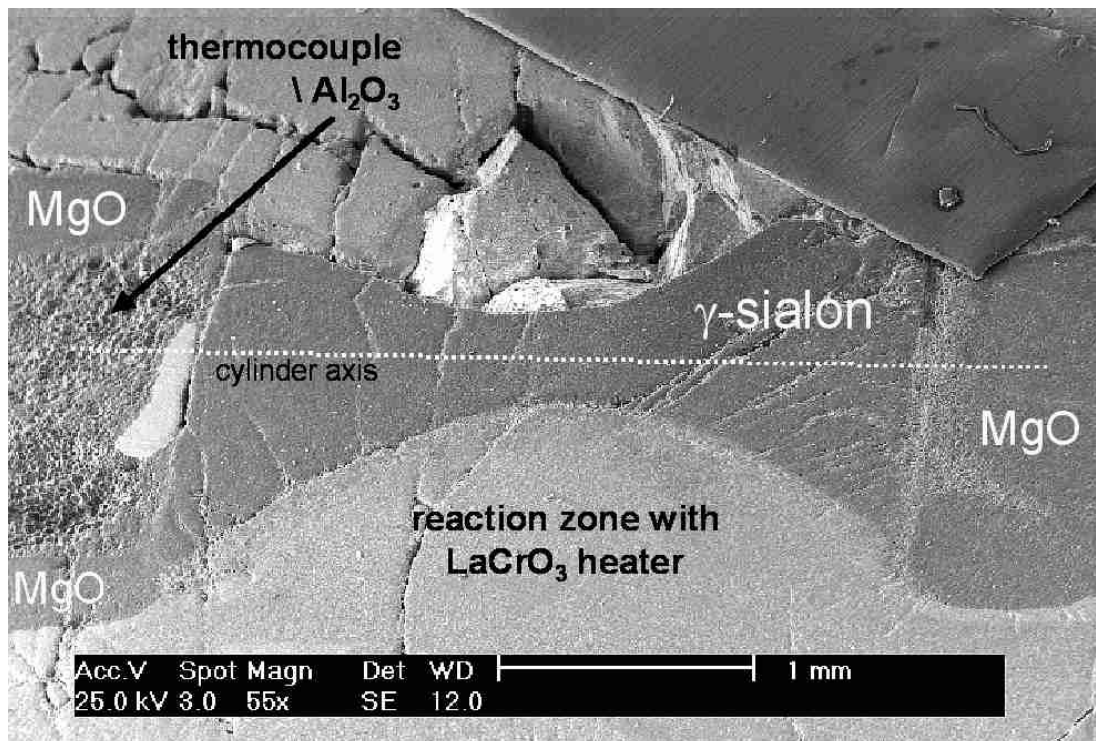


Figure 4.20: Cross section of sample HP-Sial42-II

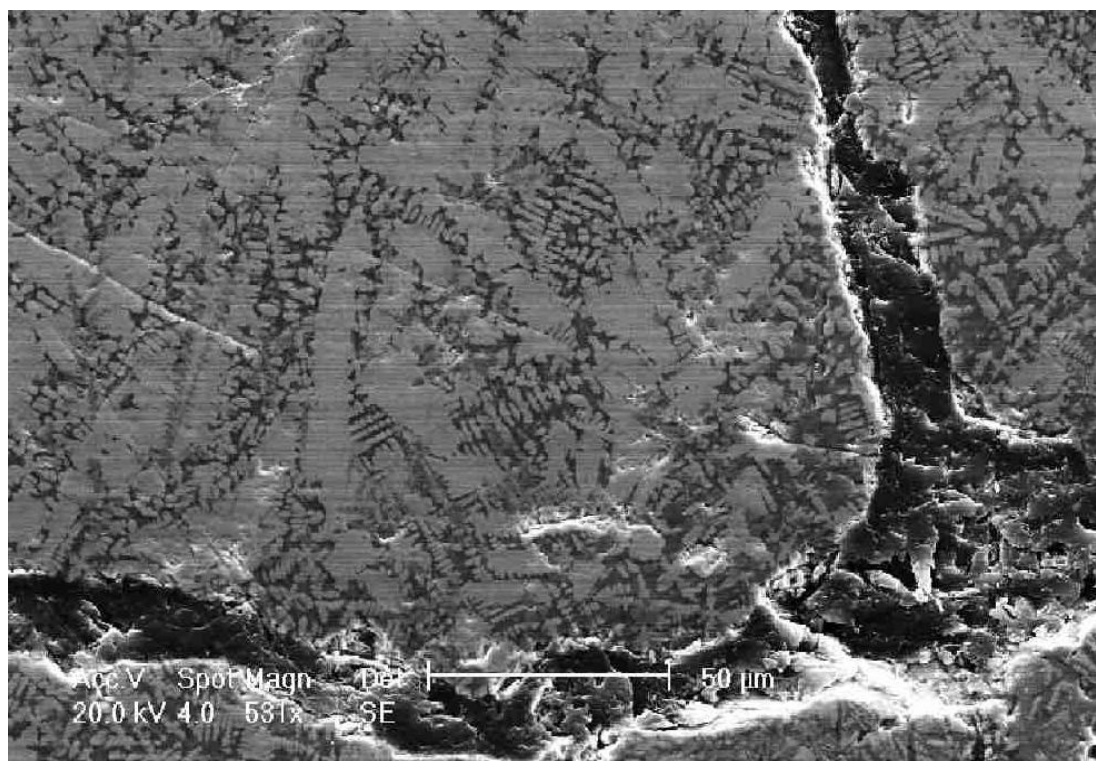


Figure 4.21: Dendritic structures indicate that the reaction zone has solidified from a melt.

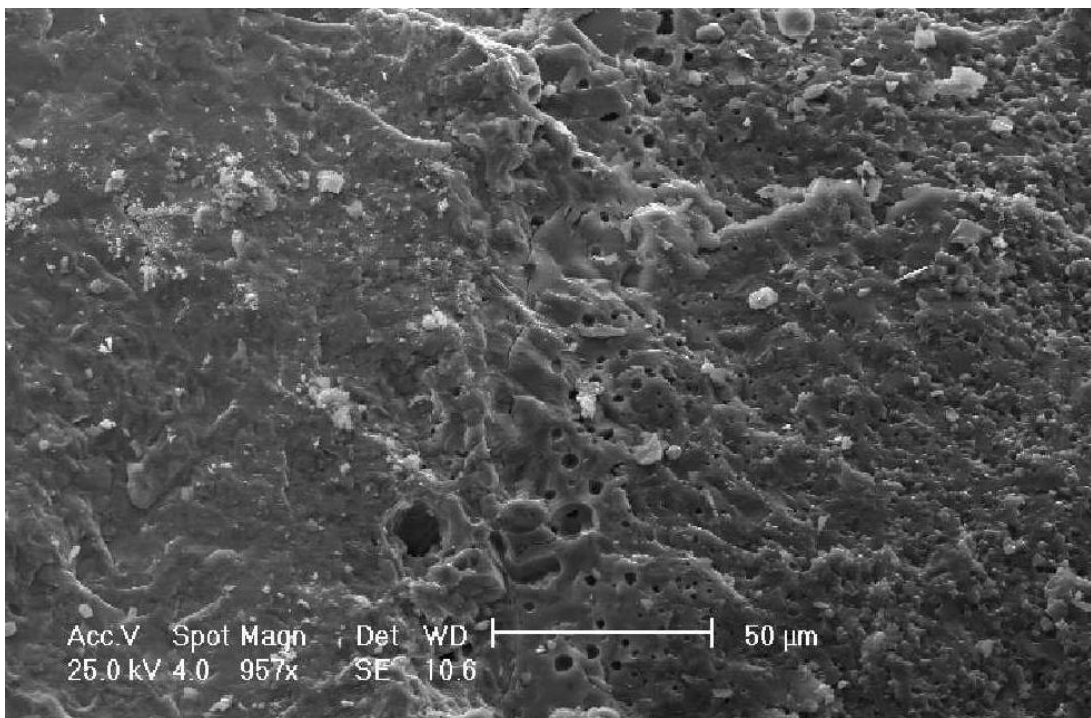


Figure 4.22: Sample HP-Sial40-II: Bubbles at the interface between LaCrO_3 heater (left) and sialon indicate outgassing of N_2

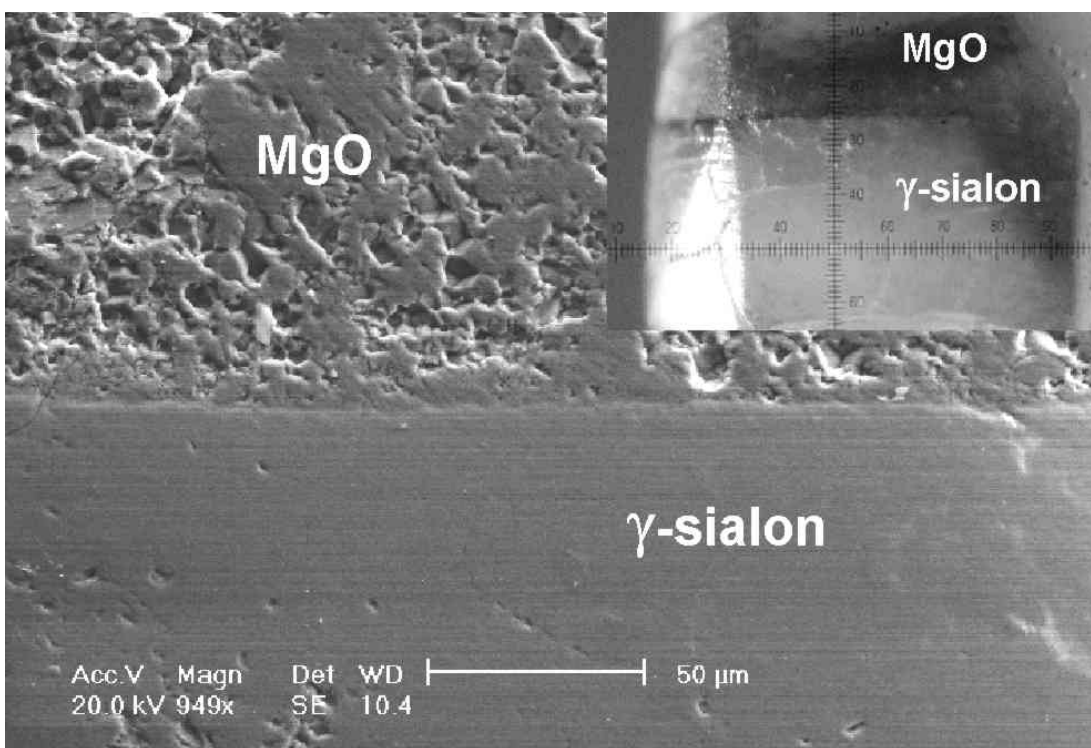


Figure 4.23: Sample HP-Sial40-II: Sharp interface between γ -sialon and the MgO pressure medium. Inset: A dark zone between the two phases is clearly visible under the optical microscope

range: 100–1000 mN). As in the case of the ‘ γ -Si₃N₄ ceramic’ SN13, the first series of indentations gave incorrect and too high values for hardness and indentation modulus, most likely due to the same effect of an anelastic response of the polymeric embedding material (cf. Sect. 3.8.1 on page 144 and Figure 2.15 on page 61). The thus obtained data was discarded. In case of sample HP-Sial40-II three further series of indentations could be made and correct values for the plastic hardness HU_{pl} and reduced modulus E_r could be obtained. Comparable hardness readings were then obtained for samples HP-Sial22-II, 40-II and 42-II, measuring the remanent dimensions of the 100 mN imprints by SEM.

4.6.2 Results: Electron Microscopy of Indentations

For all samples, also the high load indentations and the accompanying crack systems were investigated by scanning electron microscopy. Selected images are shown in Figs. 4.24–4.27.

4.6.3 Results & Discussion: Conventional and Instrumented Hardness Testing

Figures 4.29 and 4.30 on page 247 provide an overview of the entire hardness data as a function of load and measured with different methods. The upper graph represents the nitrogen-rich sialons γ -Si₂AlON₃ (HP-Sial20-I) and HP-Sial22-II (and instrumented hardness data of the ‘ γ -Si₃N₄ ceramic’ SN13 for comparison). In the lower graph, the data for the oxygen-rich SiAl₂O₂N₂ (HP-Sial40-II) and HP-Sial42-II is shown. In the load regime of the conventional testing, between 0.1 and 2 kg, the majority of the hardness readings of both nitrogen- and oxygen-rich sialons are in between 20 and 30 GPa. This is significantly above the hardness reported for single-phase β -sialons by EKSTRÖM et al. [229]. These researchers measured a series of nearly 100% dense β -sialons and found the hardness to decrease from 16.7 to \sim 13.2 GPa HV_{10} with increasing AlO-substitution. For the composition of $x = 0.12$, \sim 19 GPa HV_1 were found. Comparing the two present plots of the γ -sialons, a similar trend is apparent. It can be quantitatively expressed by the HV_1 and normalized hardness (HV_n) values of the four samples given in Table 4.11 on page 252: Both figures drop from about 27 GPa

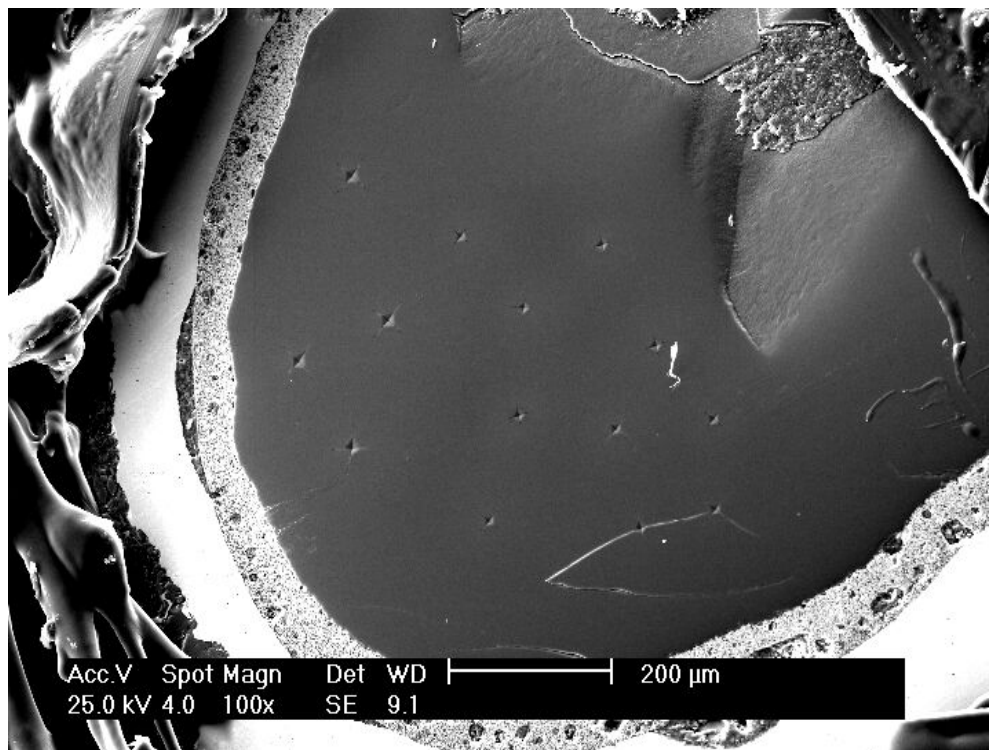


Figure 4.24: Sample HP-Sial20-I with well defined indentations



Figure 4.25: Various indentations and extensive cracking in sample HP-Sial22-II

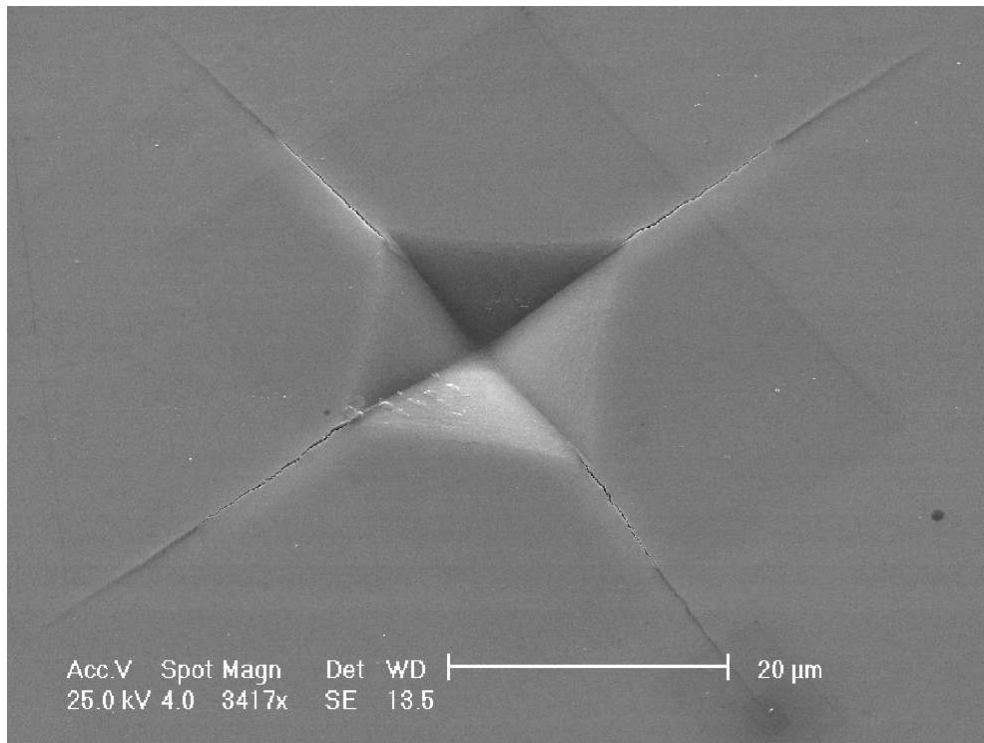


Figure 4.26: A nearly perfect indentation in HP-Sial20-I

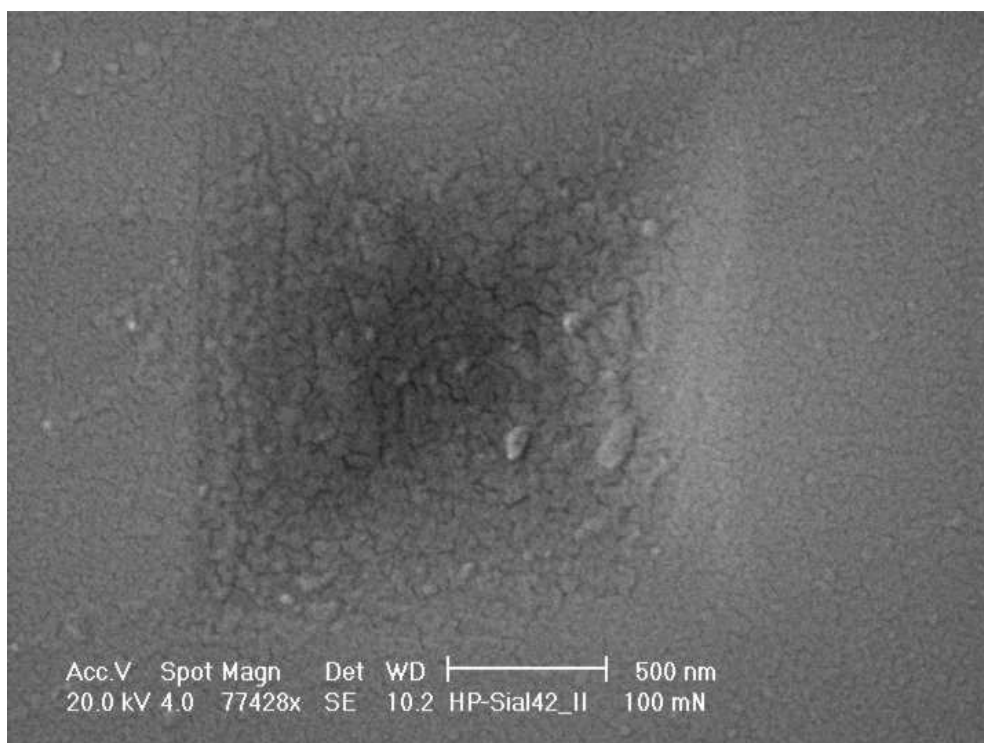


Figure 4.27: HR-SEM image of an indent from instrumented hardness testing in sample HP-Sial42-II. The apparent surface roughness stems from an antistatic Au layer sputtered prior to SEM investigation.

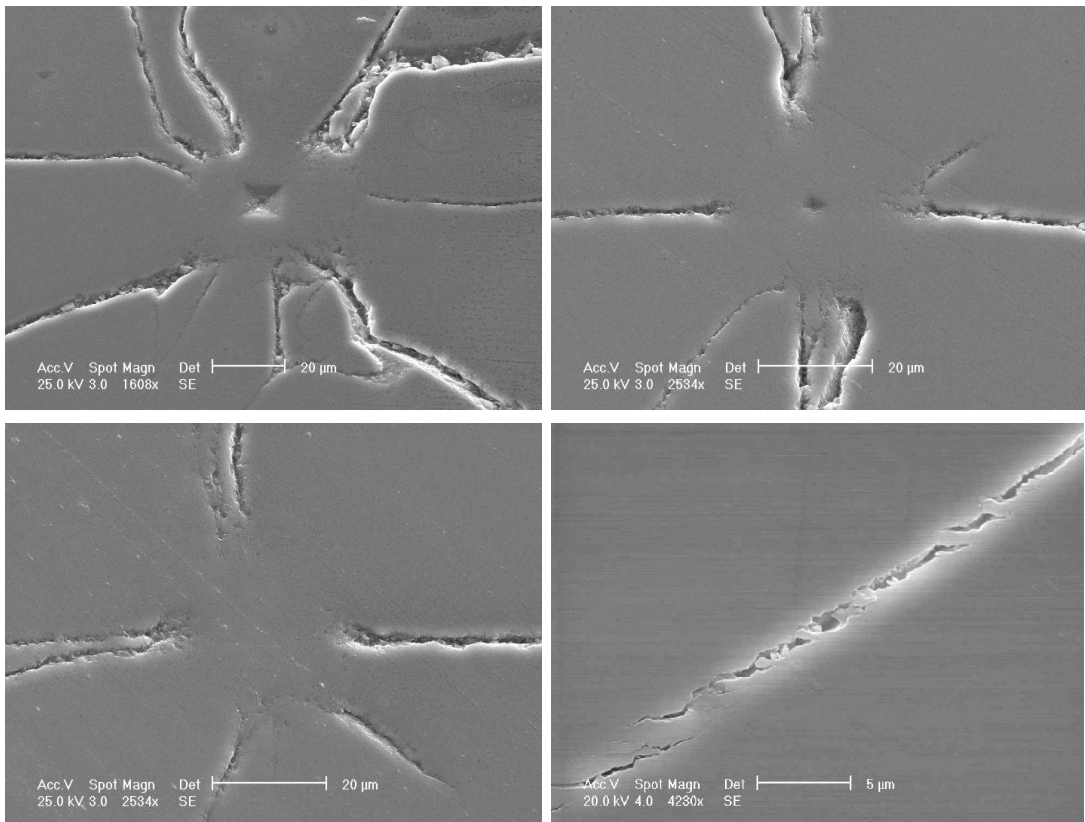


Figure 4.28: Series of partially removed indentations in sample HP-Sial22-II and Palmqvist crack with bridging ligaments in HP-Sial42-II

for $\gamma\text{-Si}_2\text{AlON}_3$ to 18–20 GPa for $\gamma\text{-Si}_{0.9}\text{Al}_{2.1}\text{O}_{2.1}\text{N}_{1.9}$. The low substituted sialon spinels would thus outcompete also the especially designed α -sialon materials with a maximum hardness of $HV = 22$ GPa that have been developed by CHEN and ROSENFLANZ [242]. For $HV_{0.5}$ of coarse grained γ -alon QUINN and coworkers found 15.5 GPa [243]. The observed drop in hardness with substitution level x would be in qualitative agreement to a recent theoretical survey by LOWTHER et al. [239]: Investigating the sialon spinels by techniques of ab-initio density functional plane wave electronic structure theory, a decrease of cohesive energy and bulk modulus with increasing AlO content was predicted. It is to be noted however, that *also the grain size varied with composition*, in the present study as well as in the β -sialon investigation of Ekström et al. In an earlier study of the $\beta\text{-Si}_{3-x}\text{Al}_x\text{O}_x\text{N}_{4-x}$ series, LEWIS and coworkers found only a small difference in hardness of $\sim 10\%$ between the low and high substituted sialons and deduced that the covalent bonding character is retained up to high AlO concentrations [244].

Also in the present case of the γ -sialons, the compositional difference in hardness seems to vanish in the regime of the automated testing between 0.1 and 0.01 kg (1000–100 mN), where the indentation size is approaching the dimensions of a few grains. This means that also only a few grain boundaries are involved so that the grain size effect on hardness is diminished [45]. The hardness values — including those of SN13 — are located between 30 and 35 GPa — close to our previous nanoindentation result on ‘pure’ γ - Si_3N_4 . These results suggest that the observed drop in macroscopic hardness at increased substitution levels could be mainly due to the 2–4 times larger grain size of HP-Sial40-II and HP-Sial42-II as compared to HP-Sial20-I and HP-Sial22-II and that the effect of AlO content on the *intrinsic* hardness would in fact be small. This would be attractive for applications because it means that oxygen-rich γ -sialons with sufficiently small grain size could be equally hard as their nitrogen-rich counterparts, but more chemically resistant due to their inherent oxygen content. On the other hand it must not be forgotten that the SN13 sample which at this microscopic scale seems to be not much harder than HP-Sial22-II, contains \sim 20 vol.% of a weaker glass phase, while in the case of the γ -sialons no indication for such phase was found. A dense sintered γ - Si_3N_4 material with less additives may well be harder.

4.6.4 Indentation Modulus

In order to gain further insight into the dependence of mechanical properties with composition, determination of the elastic response from the load-depth sensing indentation measurements is certainly instructive: As shown in Figure 4.31 on page 248, the reduced modulus E_r of the γ - $\text{SiAl}_2\text{O}_2\text{N}_2$ material (sample HP-Sial40-II) is 18–30% lower than that of the ‘ γ - Si_3N_4 ceramic’ SN13, in spite of the fact that this latter material contains \sim 19 vol.% glass phase. In contrary, the examined portion of the γ -sialon was transparent to visible light which is a strong indicative for single-phase dense sintered microstructure. The indentation elastic response should be mostly independent from grain size and as hardness usually scales with elasticity, a *qualitative* trend towards less high mechanical properties with increasing AlO content can indeed be deduced. However, as outlined in the following, *quantification* of this effect meets difficulties. Using E_r from HP-Sial40-II and a theoretical value for the bulk modulus B_0

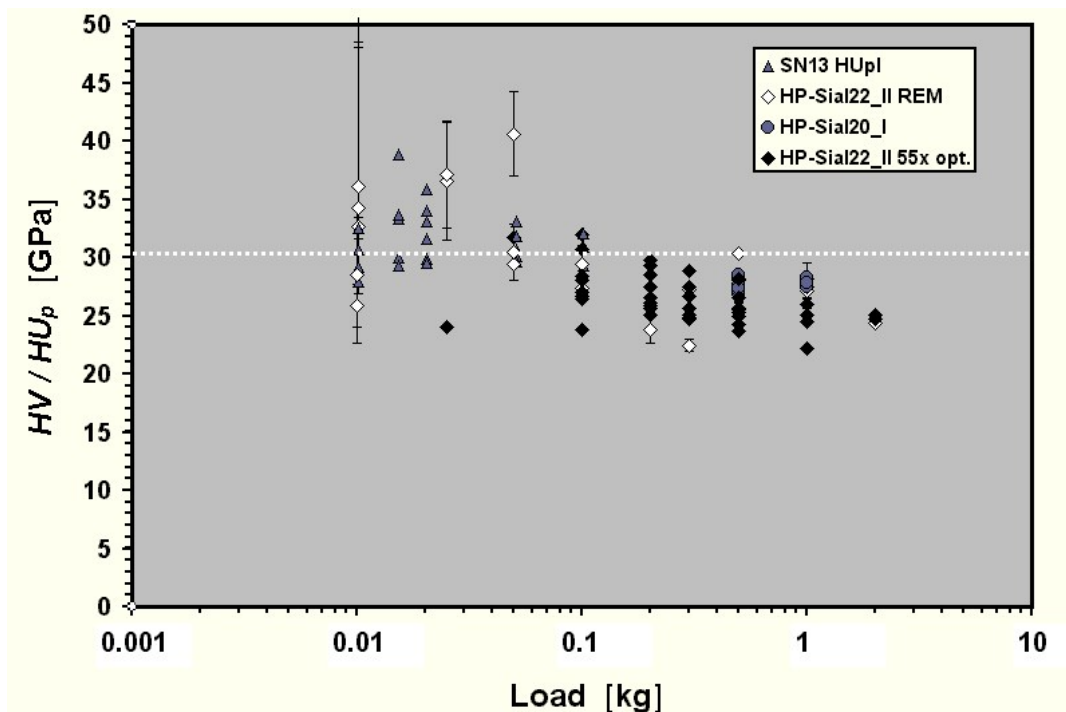


Figure 4.29: Load dependent Vickers hardness of low substituted γ -sialons HP-Sial20-I and HP-Sial22-II. With HU_{pl} of γ - Si_3N_4 'ceramic' SN13 shown for comparison. Error bars denote scatter of multiple measurements of a single indentation.

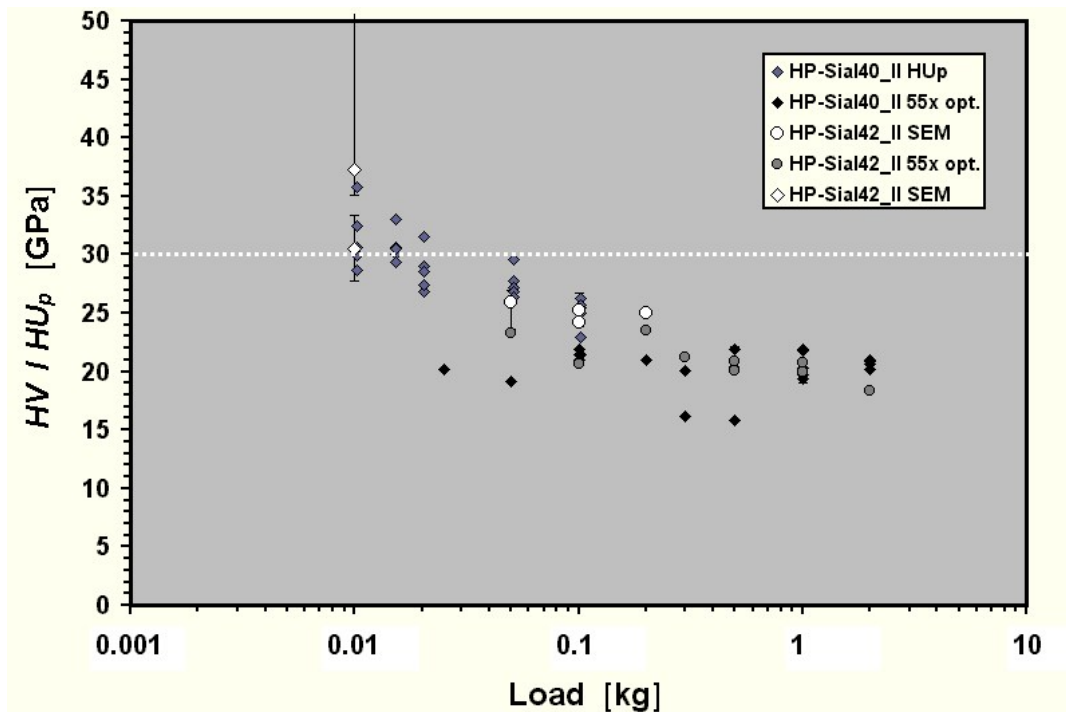


Figure 4.30: Load dependent Vickers hardness of high substituted γ -sialons HP-Sial40-I and HP-Sial42-II. Error bars denote scatter of multiple measurements of a single indentation.

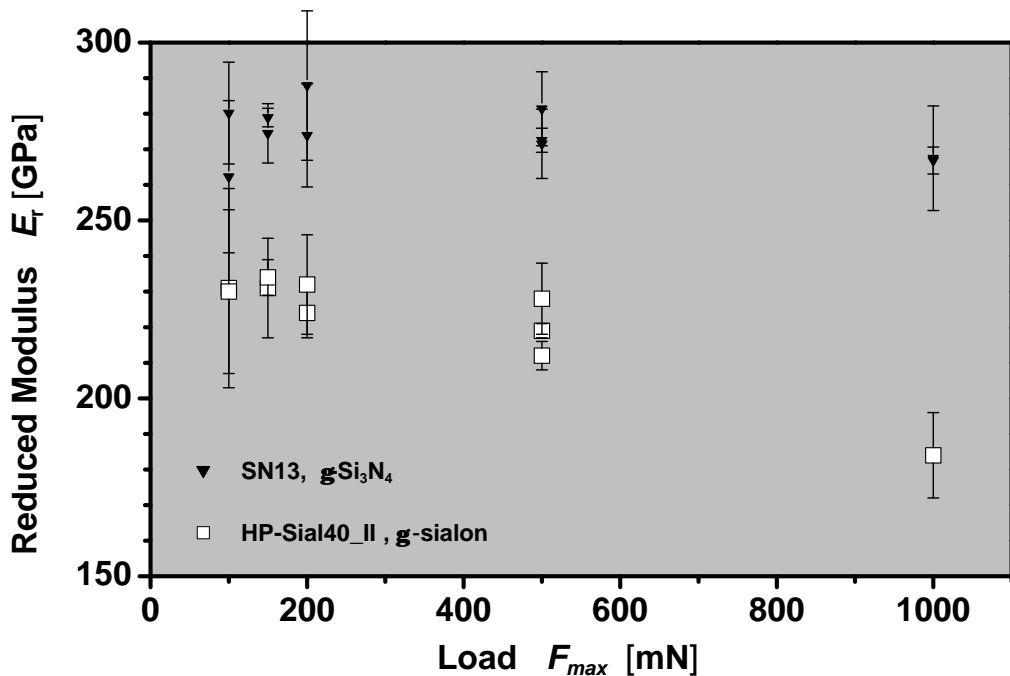


Figure 4.31: Reduced modulus of $\gamma\text{-SiAl}_2\text{O}_2\text{N}_2$ (HP-Sial40-II) and SN13 from load-depth sensing indentation measurements.

from LOWTHER et al. [239], the would-be elastic constants of $\gamma\text{-SiAl}_2\text{O}_2\text{N}_2$ were calculated. The results are provided in Table 4.10 on the next page. Comparison to the elastic properties of related reference materials shows that applying the classical understanding of indentation elasticity to the as-determined E_r values does lead to low elastic constants, which do not resemble the high hardness of the material: The high Poisson ratio of 0.33 would be more common to a metal rather than a covalent hard ceramic material. The Young's modulus of only 257 GPa is lower than that of $\beta\text{-Si}_3\text{N}_4$ and appears not a suitable value to derive the (E/H) ratio for the following fracture toughness analysis. Even if a smaller bulk modulus of 210 GPa (literature value for γ -alon) is assumed, the shear modulus of HP-Sial40-II rises only marginally to 102 GPa. This shows that primarily that the experimentally determined E_r values are too low. Extensive microcracking beneath the indenter tip that increases the compliance of the indented surface could at least explain the further drop of E_r at 1000 mN load, at smaller loads however, usually microplastic deformation that *does not* increase surface compliance becomes the dominant deformation mechanism. The reader should be reminded of the equivalent analysis of indentation elastic data from

SN13 on pages 156–161: In this case the maximum calculated value for the shear modulus that is supported by the experimental data, 205 GPa, is significantly higher compared to HP-Sial40-II, but still below that of stishovite (215 GPa) and well below the theoretical predictions for $\gamma\text{-Si}_3\text{N}_4$ ($G_0^{\text{theo}} \approx 260$ GPa). The low E_r values of HP-Sial40-II could therefore also provide another indicative that the determination of elastic constants from load-depth sensing indentation techniques may have to be revised in the case of very hard materials, as suggested by VEPŘEK (recall Sect. 2.2.6 on page 59).

Material	$\langle E_r \rangle^a$ [GPa]	E_{IT}, E_Y [GPa]	B_0 [GPa]	G_0 [GPa]	ν [-]
$\gamma\text{-SiAl}_2\text{O}_2\text{N}_2$	230(10)	257(20)	257 ^b	96(10)	0.33(1)
$\gamma\text{-alon}^c$	—	314(7)	210(4)	132(6)	0.27
$\beta\text{-Si}_3\text{N}_4^d$	—	316	249(3)	123	0.25-0.35 ^e
$\alpha\text{-Al}_2\text{O}_3^c$	—	416	257	160(10)	0.23

Table 4.10: The would-be elastic constants for sample HP-Sial40-II as calculated from the reduced modulus E_r . Moduli of related materials are given as reference; ^a average from 500 mN measurements, ^b theoretical value from [239], ^c data from [111], ^d references in [245], ^e || and \perp to c axis [196].

4.6.5 Indentation Fracture Toughness

As mentioned previously, many of the indentation crack systems coalesced with pre-existent cracks that must have formed during the HP/HT treatment. These indentations had to be abandoned for the indentation fracture analysis and the remaining ones with well developed radial cracks such as shown in Figure 4.26 on page 244 were rare. In Figures 4.32 and 4.33 on page 251 the available indentation fracture data is plotted for the nitrogen- and oxygen-rich γ -sialons respectively. The inset within the upper graph, shows the identical data plotted as c versus $P^{2/3}$. It indicates that at least the low substituted sialons obey this dependency previously found for the $\beta\text{-Si}_3\text{N}_4$ standard reference material (Section 2.2.5) and the ‘ $\gamma\text{-Si}_3\text{N}_4$ ceramic’ SN13. Plotting the few and scattered data points of the oxygen-rich γ -sialons did not give any definitive trend. Determination of the

indentation fracture toughness according to the ‘Anstis-procedure’ was therefore not attempted, also because of the lack of reliable values on the Young’s moduli of the four sialons. Applying the Shetty formula to the data of HP-Sial20-I, a value of $K_{IC-IF} = 4.6 \text{ MPa m}^{1/2}$ was coincidentally found for the 0.5 and 1 kg indentations [113], and almost the same value was calculated for HP-Sial22-II. This is in the upper range of the toughness values for single-phase, fine-grain β - and α -sialons, with typical values between 3 and $4.5 \text{ MPa m}^{1/2}$ that were also obtained from indentation measurements [224, 229].

The oxygen-rich spinels showed somewhat smaller values of 4.0 and $3.4 \text{ MPa m}^{1/2}$, respectively. Plotting the few K_{IC-IF} values of individual indentations against the mean crack length $\langle \ell \rangle$, as was done previously for SN13 (page 168), yielded no clear trend for none of the four samples. However, the γ -sialons apparently share the trend of a decreased toughness with increasing substitution level with their β -sialon counterparts [229]. It was moreover established for the β -sialons, that the presence of an intergranular phase can significantly increase the toughness [224, 229, 244]. Considering the toughness of the ‘ γ - Si_3N_4 ceramic’ SN13 ($K_{IC-IF} = 6\text{--}7 \text{ MPa m}^{1/2}$ *, this seems also to hold true for the Si_3N_4 high pressure phase and its derivatives. The reason for this increase was however always associated with the formation of grains with higher aspect ratio. This can be definitely ruled out in the present case, where the SEM investigations proved an equi-axed morphology — as expected for cubic crystals in general. Thus, the observed differences in toughness may have to be addressed with methods more precise and more rigorous than the present indentation measurements in future. For the time being, the *potential* of this new class of hard ceramic materials which provides an attractive combination of high hardness and a relatively high toughness, is clearly demonstrated. Table 4.11 on page 252 summarizes the micromechanical properties of the four γ -sialon materials.

*based on the optically determined crack lengths, Fig. 3.46 on page 168

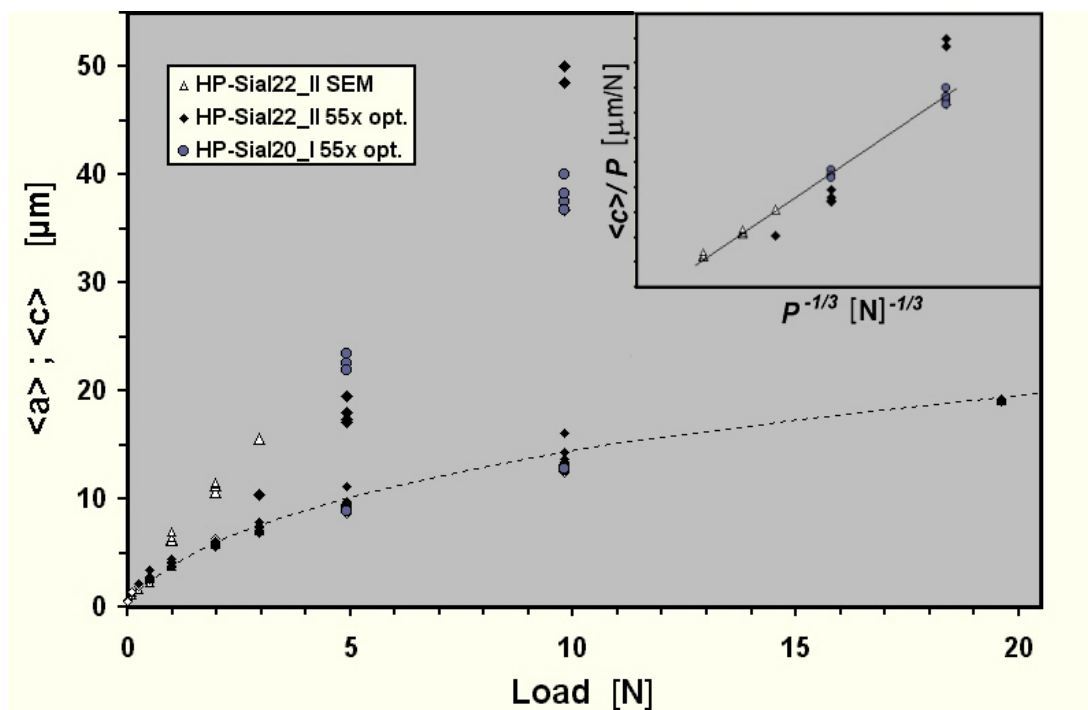


Figure 4.32: Crack radius $\langle c \rangle$ and indentation half-diameter $\langle a \rangle$ plotted versus indentation load of low substituted γ -sialons HP-Sial20-I and HP-Sial22-II. Inset: Normalized plot to check for $c-P^{2/3}$ dependency

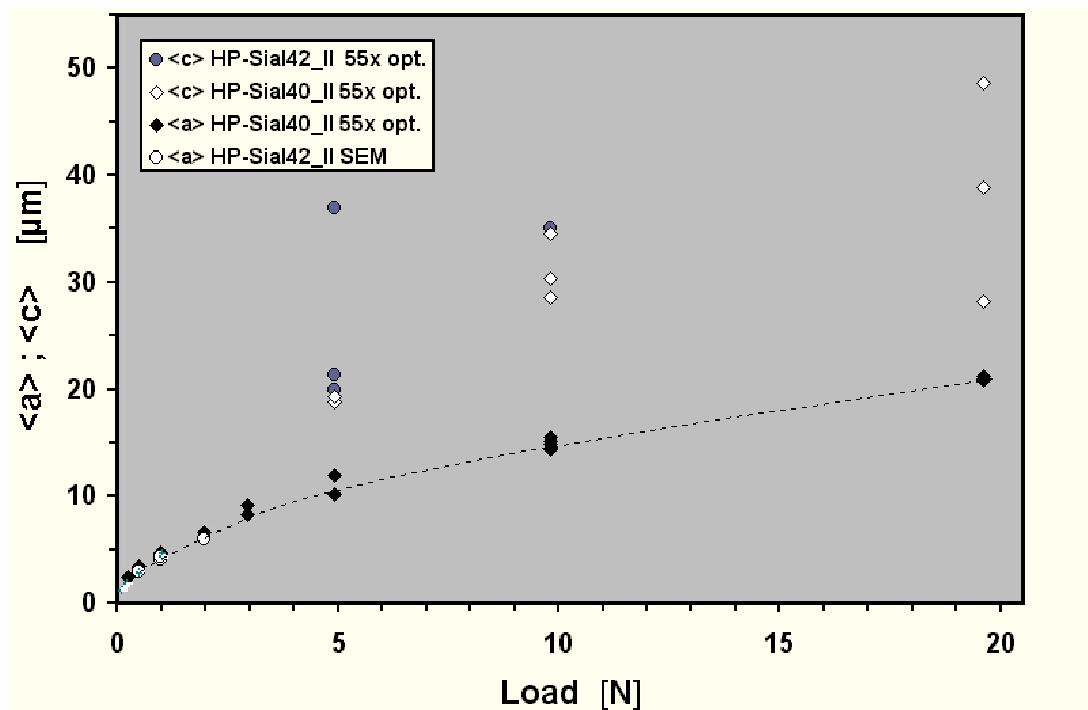


Figure 4.33: Crack radius and $\langle a \rangle$ plotted versus indentation load of high substituted γ -sialons HP-Sial40-I and HP-Sial42-II. Dotted line serves as guide to the eye

Sample		Grain size D	HU_{pl}/HV	HV_1	HV_n	$K_{\text{IC-IF}}^{\text{Shetty}}$
Composition	x	[μm]	[GPa]	[GPa]	[GPa]	[MPa $\text{m}^{1/2}$]
SN13	^a	$\sim 0.5^b$	34	28.2	27.5	6.6
HP-Sial20-I	1.03	≤ 1	n.d.	27.8(4)	n.d.	4.6
HP-Sial22-II	1.12	≤ 1	~ 34	25(1)	24.5(1.0)	4.5(1)
HP-Sial40-II	1.98	1–5	~ 31	20(1)	20.0(8)	4.0(2)
HP-Sial42-II	2.09	1–5	34(8)	20.3(5)	18.2(3)	3.4(5)
Load(range)			100 mN	1 kg	0.01–2 kg	0.5–1 kg
No. of indents	–		3–6	3–5	15–35	3–7

Table 4.11: Micromechanical properties of the four γ -sialon materials. Values in parenthesis give the maximum observed deviation from average.

4.7 Electronic Properties

As previously noted in Section 3.8.10 on page 186, the electronic band gap of $\gamma\text{-Si}_3\text{N}_4$ was predicted in several theoretical works to be within the attractive spectral range for blue solid state emitters. On the basis of ab initio calculations, possible doping elements have been screened [210] and spinel nitride solid solutions e.g. within the system $\text{Si}_{3-x}\text{Ge}_x\text{N}_4$ were suggested [117]. Synthesis of solid solutions like these would allow to adjust the magnitude of the electronic band gap, E_{gap} . While first a experimental study by SOIGNARD et al. indicates that $\gamma\text{-Si}_3\text{N}_4$ and $\gamma\text{-Ge}_3\text{N}_4$ do not mix readily [118], this present work on $\gamma\text{-Si}_{3-x}\text{Al}_x\text{O}_x\text{N}_{4-x}$ proves that $\gamma\text{-Si}_3\text{N}_4$ can be continuously doped with AlO in a wide compositional range. Provided that E_{gap} varies significantly and in a systematic manner with substitution level x , the spinel sialons could not only be used as hard ceramic materials, but also as wide-gap semiconductors.

First Observations To the present date, no experimental work dealing with electronic properties of γ -sialon has been published. First conclusions can be drawn from sample HP-Sial40-II and HP-Sial42-II, that were both found to be transparent to visible light — at least within some sample portions. Figure 4.34 on the facing page shows an optical micrograph of a thin γ -sialon platelet



Figure 4.34: A transparent γ -sialon platelet from sample HP-Sial40-II. Width: ~ 1 mm

that was prepared from sample HP-Sial42-II. The high transparency demonstrates the existence of a single phase material that does not absorb within a major part of the visible spectrum. This is another parallel to the γ -alons that are already in use as window materials in radoms of heat-seeking missiles and transparent armor [111]. The coloration of HP-Sial42-II is slightly yellow, corresponding to an absorption of blue light. This could be either due to the onset of a real absorption edge or due to the presence of defect states within the band gap. The transparent portions of sample HP-Sial40-II with the slightly lower substitution level were found to be colorless. Samples HP-Sial20-I and HP-Sial22-II were opaque, probably due to the submicron grain sizes that cause scattering of the incident light. The appearance of sample HP-Sial40-II and HP-Sial42-II demonstrate that it is possible to fabricate γ -sialon specimen suitable for UV-Vis transmission studies. Determination of E_{gap} of these materials may follow in the near future.

Theoretical Predictions All three theoretical papers on spinel-sialon that have been introduced in Section 4.4.3 on page 233 give predictions on the electronic properties of the γ -sialons. It is generally known that quantum mechanical calculations based on the local density approximation (LDA) do not yield precise qualitative results, but it is assumed that trends are accurately suggested [239]. All authors agree that the direct band gap of $\gamma\text{-Si}_3\text{N}_4$ is retained upon AlO insertion, but discrepancies exist concerning the development of E_{gap} as a function of

AlO content. LOWTHER predicts E_{gap} first to increase to ~ 4 eV for γ -Si₂AlON₃ and then to decrease again to 3.1 eV, when the substitution level is approaching $x = 2$ [239]. In contrary, CHING et al. find a *decreased* band gap for all three configurations of Si₅AlON₇ considered, with E_{gap} of the energetically most favorable form almost 1 eV less than that of pure γ -Si₃N₄ (2.29 versus 3.24 eV). A pronounced dependency of E_{gap} on the individual position of the Al and O atoms at *the same composition* is predicted in all three studies. TATSUMI, TANAKA and coworkers, who investigated several different arrangements for each composition, find that E_{gap} of the lowest-energy configurations decreases with increasing x . This is in agreement with the results of Ching et al. According to Tatsumi's calculations, only SiAl₅O₅N₃, i.e. the most highly substituted sialon, would possess a higher E_{gap} than the γ -Si₃N₄ parent phase. The energetically unfavorable configurations of the γ -sialons have all smaller band gaps than their low-energy counterparts. This is clearly associated with impurity states introduced by the Si–O and Al–N bonds (remember that Si–N and Al–O were predicted to be the preferred bonds). These impurity states were located at the top of the valence band and the bottom of the conduction band, thereby partially closing the band gap.

Resumé In conclusion, two of three theoretical investigations predict a decrease in the electronic band gap of γ -sialon with rising AlO level, so that an adjustment via doping appears possible. Differences between individual bonding configurations at *the same composition* are however found to result in even stronger variations of E_{gap} . The fact that only a small number of configurations were investigated by Lowther et al. may have led to the finding of an opposite compositional dependency of E_{gap} , i.e. an apparent increase of with increasing x .

The fabrication of transparent γ -sialon specimen has been demonstrated within this work. This should facilitate the experimental determination of their electronic properties in the early future. Utilization of the nitride or oxide nitride spinels in special functional/electronical applications appears attractive. In contrary to other large band gap semiconductors such as diamond, SiC or even GaN that only possess fourfold coordination, the structural flexibility of the spinel lattice should admit a large number of doping elements. Due to the high hardness

and structural integrity, devices based on spinel nitrides and oxide nitrides could operate under harsh conditions. Finally, small amounts of these materials may suffice to serve a useful electronic or optoelectronic function. These applications therefore comply better with the small sample amounts available by state-of-the-art equipment. In contrary, massive amounts will be required in the case of industrial abrasive applications.

4.8 Phase Transformation and Phase Stability Aspects

It was noted previously that the experiments of Group 2 and 3 did not yield any spinel phase (recall Sect 4.4.1 on page 221). Accordingly, all investigations on the novel γ -sialons could only be performed using the specimen of Group 1 alone. The small amount and size of these samples therefore prevented the application of several useful analytical methods such as solid state NMR or Vickers hardness testing at loads larger than 2 kg. Apart from these difficulties, the other HP/HT experiments were by no means useless. As will be shown in the following, a comparison of the diffraction pattern of the recovered products with the applied experimental parameters, pressure, temperature and heating time, yields inspiring insights into the phase transformation behavior of the β -sialons and the stability of the sialon spinels.

In Figure 4.35 on the next page, the diffractograms of the Group 3 products and the partially transformed β -sialon from experiment HP-Sial20-IIIb are revisited. The line positions of the β -sialon phase are marked with black triangles. The upper three samples in the graph have been treated at the same pressure, differing mainly in heating time and composition. The patterns of samples HP-Sial40-III and HP-Sial42-III appear to be quite similar and do not contain any more β -sialon. In contrary HP-Sial20-IIIb, which has been subjected to the same treatment (1650 °C for 1 h) still contains β -sialon as a main component. This is indicative for a much slower kinetics / higher stability of the low-substituted sialons. Further reflections at 19.3, 31.8 and 37.7° 2θ within the pattern of this sample coincide with the 111, 220 and 311 lines of a spinel with a lattice constant of 7.88 Å. This would indicate the onset of the $\beta \rightarrow \gamma$

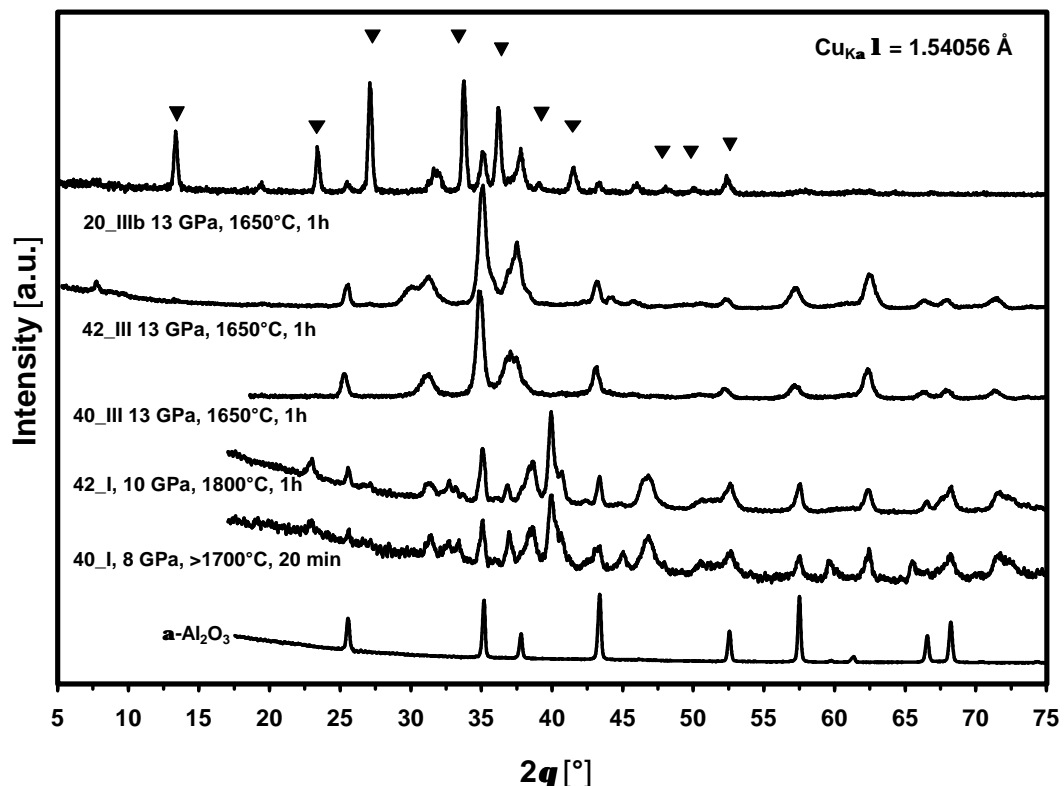


Figure 4.35: X-ray patterns of sialon decomposition products from HP/HT experiments. Coincident line positions with alumina reference pattern (bottom) suggest precipitation of a corundum-type phase, among others

phase transformation, but a clear assignment of the spinel phase is not possible: First the lattice constant determined from the three reflections is *larger* than the 7.823 \AA measured for the pure $\gamma\text{-Si}_2\text{AlON}_3$, secondly the intensity of the 440 reflection at $67^\circ 2\theta$, which is usually half that of the 311 line, is almost zero, and finally, *additional* reflections of a (third) phase are present. These can also be found in the patterns of HP-Sial40-III and HP-Sial42-III, which are higher in AlO content. This indicates that a decomposition occurred in all three samples, with novel phases *precipitating directly* from the β -structure. Given the fact that the applied pressure was the same as in the case of the successful synthesis of $\gamma\text{-Si}_2\text{AlON}_3$ (Experiment HP-Sial20-I, $p_{\text{max}} = 13 \text{ GPa}$), this observation is extremely remarkable. It would mean that the *spinel structure* requires both *high temperatures and high pressures* and that it is not the ground state of the $\text{Si}_{3-x}\text{Al}_x\text{O}_x\text{N}_{4-x}$ system at high pressure and ambient to intermediate tempera-

tures. This would be another analogy to the γ -alons. According to the latest revision of the AlN–Al₂O₃ pseudo-binary phase diagram [246], the alon γ -spinel phase is stable above 1346 °C, while in many other studies, 1700 °C were found to be necessary for the formation [111]. Recent theoretical calculations by FANG et al. confirm that the γ -alons are stabilized by configurational entropy, i.e. that the cation disorder and lattice distortions discussed in Section 4.4.3 are an essential part of their structure [231]. A thermodynamic stability region of the γ -sialons that lies significantly above room temperature would also comply with the observation of a “sluggish” phase transformation during the shock loading experiments by Sekine et al. [112]: The researchers found “*that the transformation from β -sialon to spinel prefers higher shock temperatures*”. The calculated shock temperatures \hat{T} were between 1400 and 2000 °C; In these shock experiments pressure and temperature are applied at extremely short time scales so that virtually no diffusion occurs. Judging from the present results of the static experiments, the shock syntheses could have only been successful in those cases, where the local temperatures reached 1700–1800 °C.

The α -Al₂O₃ reference pattern provided at the bottom of Fig. 4.35 on the facing page suggests that the main decomposition product could be a *corundum-type* structure - possibly α -Al₂O₃ itself. The reflections do also occur in the more complex diffraction patterns of the samples from series I, HP-Sial40-I and HP-Sial42-I.

In order to determine phases other than the corundum-type material, the diffraction patterns were checked for a variety of crystal structures, using the ICCD crystallographic data base. The candidate list included e.g. stishovite, rocksalt-AlN, different sialons and various aluminum oxide nitride phases and polytypes. Some of these latter alon materials showed the best agreement with the present patterns, but an unambiguous assignment was not possible. HP-Sial40-I and HP-Sial42-II were dark grey and extremely brittle, while HP-Sial40-III and HP-Sial42-III were opaque-white and could be prepared for Vickers hardness testing. HV_1 of the multiphase material was around 19.5 GPa — slightly less than that of the corresponding γ -sialons, but significantly more than the values commonly reported for the low substituted β -sialon (\sim 16.7 GPa, recall Sect. 4.6.3 on

page 242). This will be an interesting starting point for future work. For the time being, no further characterization of the samples using e.g. TEM and/or microchemical analysis of these samples has been attempted. Already the *ternary* Al–O–N system shows a very complex phase behavior upon variation of composition and temperature. It inhabits a large number of phases, many structures of which are not clarified to the present date (see e.g. [247, 248, 249]). An even higher degree of complexity is to be expected for the *quaternary* Si–Al–O–N system, especially if not only temperature but also pressure is varied.

Samples HP-Sial40-I and HP-Sial42-I had been heated at 1700–1800 °C, but at pressures *below* 13 GPa, so that in this case γ -sialon has most likely never been present at any instant of the HP/HT experiment. The patterns do not show any residual β -sialon, which therefore must have decomposed *directly* and *completely* into other phases. Unidentified phases in addition to α - and β -sialon were also found in high pressure studies up to 6 GPa, 1800 °C and 1 h dwelling time by HAVIAR et al. ([234], recall Sect. 4.2 on page 204). These researchers pressurized α -sialons as well as stoichiometric mixtures of Si_3N_4 , AlN , and Al_2O_3 corresponding to certain $\text{Si}_{3-x}\text{Al}_x\text{O}_x\text{N}_{4-x}$ compositions. In their experiments, the β -sialon formed up to the highest pressure. The level of maximum AlO insertion, x_{max} , however showed a pronounced decrease with pressure and reached almost zero ($\equiv \beta\text{-Si}_3\text{N}_4$) at 6 GPa. This effect was explained by Le Chatelier's principle: It was argued that if AlO-insertion causes the lattice to expand, the application of pressure would drive the system into the opposite direction — in other words, by applying pressure to a high-substituted β -sialon would 'squeeze out' the AlO-component. The authors omitted to mention that this effect can only take place, if the *total* volume of the system is decreased:

$$V_{(\text{sialon}, x=x_0)} > V_{(\text{sialon}, x=x_0-\delta)} + \sum_{i=1}^n f_i \cdot V_{i \text{ AlO(N)}} \quad (4.7)$$

where V is the specific volume, x refers to $\text{Si}_{3-x}\text{Al}_x\text{O}_x\text{N}_{4-x}$ and the summation denotes the cumulated volume of those phase(s) which exsolute from sialon. These will mainly contain the elements Al, O and N. The volume fraction of each of these phase(s) is expressed by f_i . The exsolution decreases the initial substitution level of the sialon from x_0 to $x - \delta$.

In order to get a deeper understanding of the apparent compositional instability of these sialons, which could pose serious constraints on potential future applications, specific density data of possible reaction products within the Si–Al–O–N system was evaluated. In Figure 4.36 on the next page, the atomic volume $\langle \Omega \rangle$ of various crystalline phases, ranging from stishovite- SiO_2 over $\gamma\text{-Si}_3\text{N}_4$ and $\gamma\text{-alon}$ to $\alpha\text{-Al}_2\text{O}_3$ and the wurtzite (*wz*-) and high-pressure rocksalt (*rs*-) modification of AlN, is plotted versus a compositional scale, that represents an extension of the abscissa previously shown in Fig. 4.13 on page 228. It is apparent that the β -sialons indeed have the largest specific volume of all phases. It is even higher than that of $\beta\text{-Si}_3\text{N}_4$ (or $\alpha\text{-Si}_3\text{N}_4$), *wz*-AlN and Al_2O_3 , the constituents from which they are usually synthesized. Thus, a pressure-driven decomposition into these latter phases would indeed comply with equation (4.7). The overall trend of the atomic volumes is conserved at high pressure: The empty symbols give the volumes of all phases at 20 GPa, calculated from experimental or theoretical values for the bulk modulus B_0 and pressure derivative B'_0 for each phase, and show that even at this comparatively high pressure, none of the substances becomes more dense relative to another (the smaller volume for the white triangle for the low substituted β -sialon in the upper left portion of the graph is likely due to an error in the compressibility data of the β -sialons).

For the spinel-sialons, a similar situation is valid: Due to its all octahedral coordination, regular $\alpha\text{-Al}_2\text{O}_3$ is still more dense than the majority of the γ -sialons and only slightly less dense than $\gamma\text{-Si}_3\text{N}_4$. Therefore, under pressure, an exsolution of Al_2O_3 or AlO-rich phases should be energetically favored for any γ -sialon with a composition $x > \xi$. It should be noted that some of these AlO-rich phases can be *less dense* than either of the other products, as long as their volume fraction f is small enough that (4.7) remains fulfilled. It is also possible, that there are yet unknown phases that possess higher density and could be interesting hard materials themselves. Moreover, some reactions may be *kinetically* prohibited — or favored. Keeping this in mind, it becomes clear that the current experimental results do not suffice to determine the temperature stability range of the γ -sialons: The heating times in the case of the successful γ -sialon syntheses were short compared to those experiments where phase separation was observed: T_{max} was reached within 10–12 min, followed by immediate quenching

in three cases. Thus, the samples were possibly just heated high enough for a rapid, diffusionless transformation into the spinel phase, but also quenched soon enough not to decompose. Only experiment HP-Sial40-II was kept at T_{max} for 10 further minutes. Given the high temperature, one should expect that also this comparatively short time suffices for the onset of a phase separation. However, the fact that sample HP-Sial20-IIIb did still contain β -sialon after 1 h heating, indicates that diffusion is slow. In order to prove the high-temperature stabilization of the γ -phase, re-pressurization and heating of the phase assembly obtained in experiments HP-Sial40-III and HP-Sial42-III would be the most appropriate method: If the spinel is stable, it should form via *re-assembly* of the separated phases.

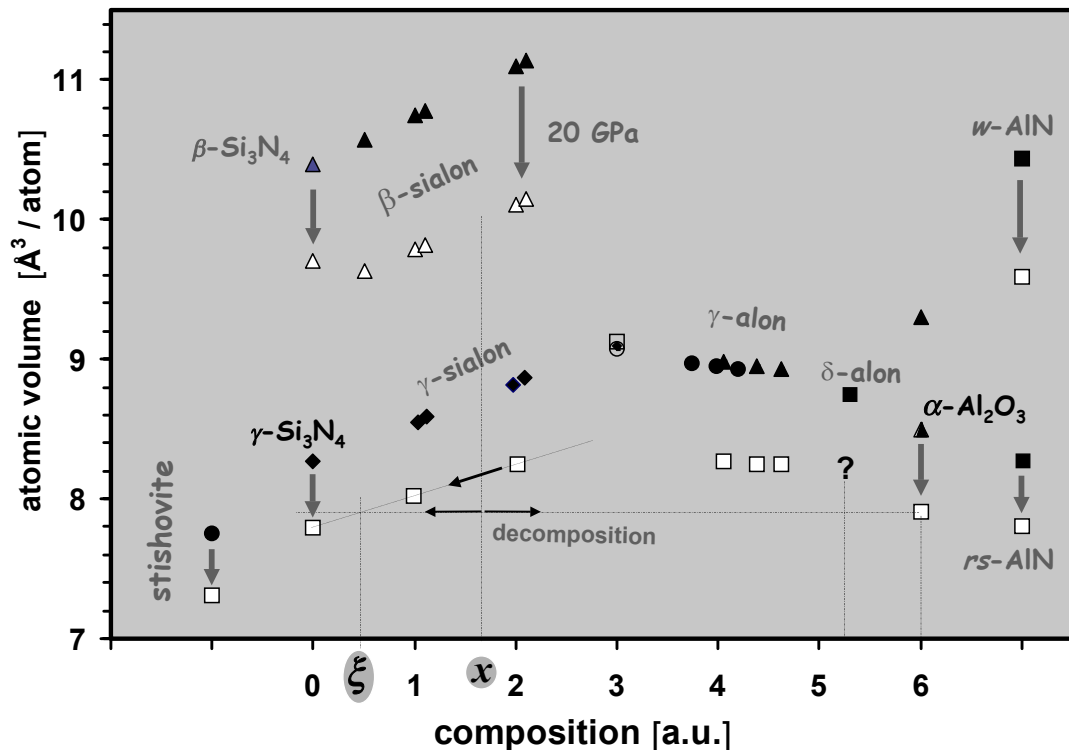


Figure 4.36: Diagram to illustrate the effect of Le Chatelier's principle on the phase stability of sialons: The average atomic volumes $\langle \Omega \rangle$ of important phases within the system Si-Al-O-N are plotted against a composition scale analogous to Fig. 4.13 on page 228. Full symbols correspond to ambient pressure, while the empty ones are volume fits to a pressure of 20 GPa, based on the third order Birch-Murnaghan EoS and theoretical as well as experimental data on B_0 and B_0' . (The ? indicates that the compressibility of δ -alon [248] is not known). The diagram shows that any β - or γ - $\text{Si}_{3-x}\text{Al}_x\text{O}_x\text{N}_{4-x}$ with a composition $x > \xi$ will occupy less volume if it decomposes e.g. into $\alpha\text{-Al}_2\text{O}_3$, $\text{Si}_{3-\xi}\text{Al}_{\xi}\text{O}_{\xi}\text{N}_{4-\xi}$ and an alon phase. This means that it will be unstable under prolonged compression and heating.

4.8.1 Resumé: Formation and Stability of γ -Sialon

(Direct) transformation of γ -sialon from the β -phase so far has only been observed at a static pressure of 13 GPa and temperatures in excess of 1800 °C or upon shock loading of β -sialon/Cu mixtures with peak pressures \hat{p} of at least 33 GPa. The present results from static experiments and the semiempirical considerations of the previous section indicate that sialons with a composition $\text{Si}_{3-x}\text{Al}_x\text{O}_x\text{N}_{4-x}$ show a tendency for phase separation at pressures between 2.5 and at least 10 GPa and temperatures below ~ 1800 °C. This effect is proved for the β -modification and appears not to be forbidden for the γ -spinel phase — at least not by thermodynamic reasons. This sets certain limitations to the manufacture of macroscopic γ -sialon compacts such as cutting tool insets. The decomposition at certain HP/HT conditions is most likely driven by the precipitation of phases that are *more dense* than both the β - and γ -phase at high pressure. The thermal stability of γ -sialon *at ambient pressure* may therefore remain *unaffected*. This highly application-relevant figure is therefore to be assessed in the near future.

Zusammenfassung

Diese Arbeit beschäftigt sich mit der 1998 entdeckten Hochdruckmodifikation des Siliziumnitrids ($\gamma\text{-Si}_3\text{N}_4$) und daraus abgeleiteten Mischkristallen im quaternären System Si–Al–O–N (*Sialone*). Die Niederdruckmodifikationen, $\alpha\text{-Si}_3\text{N}_4$, $\beta\text{-Si}_3\text{N}_4$, sowie die entsprechenden α - und β -Sialone sind die Basis von bereits seit vielen Jahren in der Anwendung befindlichen Hochleistungskeramiken. Das $\gamma\text{-Si}_3\text{N}_4$ und seine Derivate werden daher vor allem unter dem Gesichtspunkt einer möglichen Verwendung als Hartstoffe betrachtet. Ziel der Arbeit war es, ein möglichst umfassendes Profil dieser Materialien zu erstellen, um deren Eignung für abrasive oder alternative Anwendungen beurteilen zu können. Dieses Profil schließt deren Synthese, Struktur und Eigenschaften ein.

Spinell- Si_3N_4

Die vorliegende Dissertation zeichnet zunächst die gleich zweifache Entdeckung von $\gamma\text{-Si}_3\text{N}_4$ nach, die aus einer Zusammenarbeit zwischen dem Fachgebiet Disperse Feststoffe der Technischen Universität Darmstadt, Fachbereich Materialwissenschaft, und der Abteilung für Hochdruckmineralphysik am Max-Planck Institut für Chemie in Mainz hervorging. In beiden Fällen wurde $\gamma\text{-Si}_3\text{N}_4$ in Diamantstempelzellen (DACs), bei Drücken von zwischen 30 und 40 bzw. bei 15 Gigapascal (GPa) und Temperaturen über 2000 K synthetisiert.

Die Kristallstruktur von $\gamma\text{-Si}_3\text{N}_4$ konnte mittels Transmissionselektronenmikroskopie (TEM) an den so erzeugten Proben aufgeklärt werden. Das Siliziumnitrid ist der erste Vertreter der *Spinell-Nitride* $\gamma\text{-E}_3\text{N}_4$ (E = Si, Ge, Sn), Raumgruppe $Fd\bar{3}m$, deren schwerere Homologe ebenfalls im Zeitraum 1997/1998 von anderen

Zusammenfassung

Forschergruppen entdeckt wurden. Eine strukturelle Besonderheit dieser Materialien ist die — insbesondere für Silizium erstmals zweifelsfrei nachgewiesene — 6-fache Koordination durch Stickstoff in einem Festkörper (SiN_6 -Einheiten).

Unter Verwendung von amorphen Ausgangssubstanzen (“*Precursoren*”), wie dem Siliziumnitrid-imid, $\text{Si}_2\text{N}_2(\text{NH})$, und einem hieraus durch Kalzination bei $1200\text{ }^\circ\text{C}$ gewonnenen amorphen Si_3N_4 , konnten mittels Vielstempel-Hochdruckapparaten (“**multianvil press**”, MAP) zunächst größere, und nach Anwendung einer speziellen Kapselungstechnik auch weitgehend sauerstofffreie $\gamma\text{-Si}_3\text{N}_4$ -Proben im Milligramm-Maßstab erzeugt werden. Die Verwendung von amorphen Ausgangssubstanzen erwies sich als vorteilhaft, da deren Umwandlung in die jeweils thermodynamisch stabile Phase kaum einer kinetischen Hemmung unterliegt. Das Auftreten von reinem $\beta\text{-Si}_3\text{N}_4$ bei 10 GPa und reinem $\gamma\text{-Si}_3\text{N}_4$ bei 13 GPa ermöglichte somit eine Eingrenzung der thermodynamischen β/γ -Phasengrenze zwischen diese beiden Drücke. Mittels der eigenen, wie auch Literaturdaten konnte ein vorläufiges $p\text{-}T$ Phasenzustandsdiagramm von Si_3N_4 erstellt werden. In diesem Zusammenhang werden auch die durch die Entdeckung der Spinell-Nitride motivierten theoretischen Arbeiten zu möglichen “*post-spinell*”-Phasen des Siliziumnitrids kritisch diskutiert. Ebenfalls vorgestellt werden die $\gamma\text{-Si}_3\text{N}_4$ Synthesen anderer Arbeitsgruppen, bei denen von den *kristallinen* Niederdruckmodifikationen $\alpha\text{-Si}_3\text{N}_4$ und/oder $\beta\text{-Si}_3\text{N}_4$ ausgegangen wurde. Zur Erzeugung der erforderlichen Umwandlungsbedingungen kamen hierbei entweder ebenfalls DACs, MAPs oder Schockwellenmethoden zum Einsatz.

Die mit der MAP-Methode hergestellten Mengen an $\gamma\text{-Si}_3\text{N}_4$ ermöglichten eine Vielzahl weiterer Untersuchungen an dem Material. So wurden der Gitterparameter a_0 und der Stickstofflageparameter \mathbf{u} von Spinell- Si_3N_4 durch Strukturverfeinerung eines konventionellen Röntgenpulverdiffraktogramms ermittelt [154]. Die erhaltenen Werte von $a_0 = 7,7381\text{ \AA}$ und $\mathbf{u} = 0,2597$ stimmen auf $0,05$ bzw. $0,5\%$ genau mit denen an einer aus $\beta\text{-Si}_3\text{N}_4$ hergestellten und am Synchrotron gemessenen Probe [125] überein. Die Kenntnis dieser Strukturparameter — auch die der schwereren Spinell-Nitride $\gamma\text{-Ge}_3\text{N}_4$ und $\gamma\text{-Sn}_3\text{N}_4$ aus der Literatur — ermöglichte einen umfassenden Vergleich sowohl innerhalb der homologen Reihe, als auch mit bekannten binären (z.B. Fe_3O_4) - oder siliziumhaltigen Spinellen wie z.B. Mg_2SiO_4 . Auch ließen sich Rückschlüsse auf die bislang nicht beobach-

teten und vermutlich nicht existenten Spinelle ‘ γ -C₃N₄’ und ‘ γ -Pb₃N₄’ ziehen. Der strukturelle Vergleich wurde schließlich auch auf die in der Kochsalzstruktur kristallisierenden Hochdruckmodifikationen der benachbarten Nitride AlN, GaN und InN ausgeweitet.

Mit dem γ -Si₃N₄-Material aus den MAP-Synthesen gelang ebenfalls die Bestimmung physikalischer Eigenschaften, wie dem Kompressionsmodul B_0 [82] und dem linearen thermischen Ausdehnungskoeffizienten α_{th} . Die aus den eigenen Proben ermittelten Werte werden jeweils mit im gleichen Zeitraum veröffentlichten theoretischen Vorhersagen und experimentellen Arbeiten anderer Forscher verglichen. Mit einem experimentell verifizierten Kompressionsmodul zwischen 290 und 310 GPa liegt γ -Si₃N₄ in Übereinstimmung mit theoretischen Berechnungen im Bereich anderer (Super)hartstoffe. Offenbar verursacht die oktaedrische Koordination des Siliziums eine stärkere Anharmonizität des interatomaren Potentials, weshalb γ -Si₃N₄ mit einem — wiederum durch andere Gruppen bestätigten — α_{th} zwischen 3,5 und $5,5 \cdot 10^{-6} \text{K}^{-1}$ eine signifikant höhere thermische Ausdehnung als die Niederdruckmodifikationen besitzt { $\alpha_{\text{th}}(\beta\text{-Si}_3\text{N}_4) = 1-2,5 \cdot 10^{-6} \text{K}^{-1}$ }. Im Zusammenhang mit diesen temperaturabhängigen Röntgenmessungen wurde auch eine Bestimmung der thermischen Beständigkeit von γ -Si₃N₄, also seiner Rückumwandlungstemperatur in α - oder β -Si₃N₄ versucht. Eine solche Phasenreaktion konnte jedoch bis zu einer Temperatur von 1000 K, dem gerätetechnischen Limit, nicht beobachtet werden. Auslagerungsversuche von JIANG et al. [88], sowie thermogravimetrische und kalorimetrische Messungen von SEKINE et al. [186] ergaben eine Zersetzungstemperatur um 1400 °C. Damit wäre γ -Si₃N₄ in seiner thermischen Beständigkeit dem kubischen Boronitrid *c*-BN als dem derzeit besten kommerziellen Schneidstoff ebenbürtig und deutlich metastabiler als Stishovit, der ebenfalls sehr harten Hochdruckphase des SiO₂.

In einem nachfolgenden Abschnitt werden kurz die noch überwiegend auf theoretischen Berechnungen basierenden Literaturdaten zu weiteren thermischen und thermodynamischen Eigenschaften von γ -Si₃N₄, wie z.B. die spezifische Wärmekapazität zusammengestellt. Die vorhergesagte Wärmeleitfähigkeit von γ -Si₃N₄ ist mit 60–70 W/mK geringer als diejenige von β -Si₃N₄.

Zusammenfassung

Die schwingungsspektroskopische Zuordnung der experimentell gemessenen Raman- und Infrarotabsorptionsbanden von $\gamma\text{-Si}_3\text{N}_4$ erfolgt anhand gruppentheoretischer Vorhersagen aus der Literatur und wird mit einem Vergleich mit den Bandenlagen der schwereren Spinell-Nitride $\gamma\text{-Ge}_3\text{N}_4$ und $\gamma\text{-Sn}_3\text{N}_4$ vervollständigt. Wichtiges Erkennungsmerkmal von $\gamma\text{-Si}_3\text{N}_4$ sind zwei starke Raman-Banden bei 522 und 850 cm^{-1} .

Eine Bestimmung der Härte von $\gamma\text{-Si}_3\text{N}_4$ blieb zunächst aufgrund der Porosität der aus den amorphen Precursoren erzeugten Proben auf sog. "Nanoindentation" — Messungen mit sehr kleinen Eindrucklasten (wenigen Millinewton) — beschränkt. Diese Messungen ergaben eine "Nano-Härte" um 36 GPa [82], andere Autoren berichteten von Werten bis über 40 GPa [120], dem willkürlich definierten Schwellwert für "superharte" Materialien [9].

Härtemessungen mit Eindrucklasten von bis zu 2 kg wurden mit Realisierung eines dichtgesinterten $\gamma\text{-Si}_3\text{N}_4$ -Körpers möglich, bei dessen Herstellung von einer kommerziellen $\beta\text{-Si}_3\text{N}_4$ -Keramik mit Sinteradditiven ausgegangen worden war. Konventionelle Vickers- und Knoophärtemessungen ergaben Härtewerte von $HV_2 = 27,8$ GPa und $HK_2 = 22$ GPa; eine durchschnittliche Vickershärte von 34 ± 3 GPa wurden mittels Ultramikrohärtemessung bei 100 mN bestimmt. Diese Werte liegen deutlich über denen des $\beta\text{-Si}_3\text{N}_4$ Ausgangsmaterials mit $HV_2 = 15$ GPa, reichen jedoch nicht ganz an diejenigen einer kommerziellen Wendeschneidplatte mit einem *c*-BN Gehalt von 80% heran ($HV_2 = 32$ GPa, $HK_2 = 26$ GPa). Die an den die Vickers-Eindrücke begleitenden Rißsystemen ermittelte Eindruck-Rißzähigkeit ist mit $K_{\text{IC-IF}} = 6\text{--}7 \text{ MPa m}^{1/2}$ mit der des *c*-BN Materials vergleichbar. Wie rasterelektronenmikroskopische Studien an der ' $\gamma\text{-Si}_3\text{N}_4$ -Keramik' zeigten, sind verschiedene Rißüberbrückungsmechanismen aktiv.

Genau wie ihre konventionellen Pendants auf $\beta\text{-Si}_3\text{N}_4$ -Basis, besteht die $\gamma\text{-Si}_3\text{N}_4$ -Keramik aus Si_3N_4 -Körnern die durch eine amorphe Glasphase zusammengehalten werden. Die Körner sind im vorliegenden Fall equiaxial und durchschnittlich 0,5 μm groß. Da sich Menge und Volumen der Y–Si–Al–O–N Glasphase offenbar kaum verändert haben, $\gamma\text{-Si}_3\text{N}_4$ aber 25% dichter ist als $\beta\text{-Si}_3\text{N}_4$, beträgt deren Anteil nach der Hochdruckbehandlung ca. 19 vol.%. Die Probe wurde weiterhin

mittels XRD und TEM untersucht. Aus einer geringfügig größeren Gitterkonstante und lokalen Elementanalysen mittels EDX ergaben sich Anhaltspunkte für die Einlagerung von Al, Mg, O und eventuell Y in das Spinellgitter.

Bei den vorgenannten Ultramikrohärtemessungen waren Last–Eindringkurven aufgezeichnet worden, aus denen der *reduzierte elastische (Eindring-)Modul* E_r der Probe zu ca. 275 GPa bestimmt wurde. Unter Berücksichtigung des Fremdphasenanteils wurde auf die Elastizität von *reinem* γ -Si₃N₄ zurückgeschlossen und Werte für G_0 (Schermodul), E_Y (Elastizitätsmodul) und ν (Querkontraktionszahl) berechnet. Danach beträgt der maximale, durch die vorliegenden Daten abgesicherte Wert für G_0 205 GPa, konservative Abschätzungen ergaben ~ 175 GPa. Beide Werte sind höher als der zuvor von Zerr et al. durch Nanoindentation an den Precursor-abgeleiteten γ -Si₃N₄-Proben gemessene (148 ± 16 GPa), aber geringer als die theoretischen Vorhersagen (~ 260 GPa).

Durch Verringerung des Glasphasenanteils lässt sich für die Zukunft eine weitere Steigerung der mechanischen Eigenschaften γ -Si₃N₄-basierter Materialien erwarten. Es kann jedoch als unwahrscheinlich angenommen werden, daß γ -Si₃N₄ an die Härte von mit vergleichbaren Aufwand herstellbaren, binderfreien *c*-BN Körnern [36] heranreichen wird. Diese weisen makroskopische Härtewerte von über 50 GPa auf und sind als Nischenprodukte für spezielle Anwendungen bereits kommerziell erhältlich.* Eine industrielle Verwendung γ -Si₃N₄-basierter Materialien müßte folglich auf anderen Vorzügen als einer hohen Härte allein basieren.

Mit einer theoretisch vorhergesagten elektronischen Bandlücke $E_{gap} \approx 3,4$ eV liegt γ -Si₃N₄ in einem für optoelektronische Anwendungen interessanten Bereich. Die publizierten Vorhersagen der elektronischen und dielektrischen Eigenschaften von γ -Si₃N₄ und hypothetischen ternären Spinellen wie SiTi₂N₄ werden zusammengefaßt, und bislang erfolgte Versuche zur experimentellen Bestimmung von E_{gap} an eigenen Proben vorgestellt.

*<http://www.sei.co.jp/sn/0009/p1.html>

Zusammenfassung

Im dem letzten Abschnitt des γ -Si₃N₄-Kapitels werden zwei Schockwellenexperimente an amorphem Si₃N₄ beschrieben. Mit ihnen sollte die Darstellbarkeit größerer Mengen des Spinell-Nitrids durch dynamische Hochdruckverfahren erkundet werden. Aus der Literatur sind zahlreiche Schockversuche aus der Zeit *vor* und *nach* der Entdeckung von γ -Si₃N₄ bekannt, die im Rahmen dieser Arbeit gesichtet und evaluiert werden. Erstere zielen auf die Schockkompaktierung von Siliziumnitrid-Keramiken ab. Dabei wurde häufig eine schockinduzierte Umwandlung von α -Si₃N₄ nach β -Si₃N₄ beobachtet. Vom Auftreten einer unbekannten Phase, die im Nachhinein γ -Si₃N₄ zugeordnet werden könnte, wird jedoch in keinem Fall berichtet. Im Jahr 2000 gelangen der Gruppe um T. SEKINE Schocksynthesen von nanokristallinem γ -Si₃N₄ [112]. Alle Autoren berichten ausschließlich von *kristallinen* Ausgangsmaterialien. Die Umwandlung in γ -Si₃N₄ erfolgt nach Sekine meist unvollständig und erfordert eine nachgeschaltete naßchemische Aufreinigung des Produkts. In den im Rahmen der vorliegenden Dissertation unternommenen Versuchen wurde wegen der bereits aus den statischen Versuchen bekannten geringen kinetischen Umwandlungsbarriere auf *amorphes* Si₃N₄ zurückgegriffen. Die unter Schutzgasatmosphäre versiegelten Proben wurden mit dynamischen Drücken von 61 und 71 GPa in einer sog. "Flyer-Plate" Apparatur beaufschlagt. Während bei 71 GPa offenbar eine Zersetzung des Siliziumnitrids auftritt, konnten in der 61 GPa-Probe neben β -Si₃N₄ nennenswerte Anteile an γ -Si₃N₄ nachgewiesen werden. Eine halbquantitative Auswertung der Röntgenpulverdiffraktogramme von verschiedenen Stellen der Probenkapsel deutet darauf hin, daß sich der amorphe Precursor nahezu vollständig in γ -Si₃N₄ umwandelt und bei zu hohen post-shock Temperaturen in β -Si₃N₄ übergeht. Durch die Gewährleistung hoher Abkühlraten im gesamten Probenvolumen sollten sich daher praktisch quantitative Ausbeuten an γ -Si₃N₄ erzielen lassen. Die Untersuchungen wurden durch raster- und transmissionselektronenmikroskopische Untersuchungen vervollständigt. Die etwa 50 nm großen γ -Si₃N₄-Kristallite zeigten unter dem TEM Ansätze von Facettierung und eine angesichts der gewaltsamen Synthesbedingungen erstaunlich geringe Dichte an Defekten wie Verzwillingung oder remanenter Gitterverzerrungen.

Spinell-Sialone

Hinweisen über im Spinellgitter enthaltene Fremdelemente aus den Untersuchungen der vorgenannten ‘ γ -Si₃N₄-Keramik’ folgend, wurde im zweiten Teil dieser Arbeit eine Reihe von γ -Si₃N₄-Derivaten synthetisiert. Es zeigte sich, daß das Spinell-Siliziumnitrid ganz analog zur β -Si₃N₄ Modifikation in der Lage ist, mit den Elementen Al und O eine Festkörperlösung der allgemeinen Zusammensetzung Si_{3-x}Al_xO_xN_{4-x} einzugehen. Vier nahezu phasenreine β -Sialone mit den Zusammensetzungen $x = 1,03; 1,12; 1,98$ und $2,09$ wurden bei 13 GPa und 1800 °C und Gesamtheizdauern von ca. 20 min in die entsprechenden ‘ γ -Sialone’ gleicher Stöchiometrie umgewandelt. Dies zeigt, daß der Löslichkeitsbereich von AlO im Spinell mindestens genauso groß ist wie in der β -Si₃N₄-Struktur. Eine weitere Analogie ergab sich bei der Bestimmung der kubischen Gitterkonstante, die, wie auch die Gitterparameter des hexagonalen β -Sialon *linear* mit dem Substitutionsgrad x in Si_{3-x}Al_xO_xN_{4-x} zunimmt. Eine Auftragung des Gitterparameters a_0 gegen x ergab die quantitative Abhängigkeit

$$a_0 [\text{\AA}] = 7.7347(9) + 0.0872(17) \cdot x$$

Ein Vergleich der relativen *Volumenzunahme* der beiden Phasen ergab, daß γ -Sialon 0,1% pro AlO-paar und Formeleinheit stärker expandiert als β -Sialon. Unter der Annahme, daß die Substitution Si^{tet} → Al^{tet} der *tetraedrisch* koordinierten Kationen in beiden Strukturen gleich viel Platz erfordert, wurde dieser *zusätzliche* Volumenzuwachs im Spinell der Anwesenheit oktaedrisch koordinierter Aluminium-Spezies (Al^{oct}) zugeschrieben. Weitere Anhaltspunkte für die Bevorzugung der oktaedrischen Koordination von Al ergaben sich aus der für die Zusammensetzung Si₂AlON₃ durchgeführten Rietveld-Verfeinerung, bei der eine Abnahme des Anionenlageparameters u von 0,2597 für reines γ -Si₃N₄ auf 0,256 (γ -Si₂AlON₃) festgestellt wurde. Zusammen mit der Vergrößerung des Gitterparameters a_0 bedeutet dies, daß der tetraedrische Anion-Kation Bindungsabstand d^{tet} weitgehend konstant bleibt, während d^{oct} sich vergrößert und damit für die gesamte Volumenexpansion verantwortlich ist.

Bei der HP/HT Unwandlung der Sialon-Proben traten häufiger Fluktuationen in der gemessenen Probentemperatur und der Heizleistung auf, woraufhin die

Zusammenfassung

Beheizung der Probe vorzeitig abgebrochen werden musste. Dies deutete auf Reaktionen zwischen der Probe und den zur Heizung und Kapselung verwendeten Materialien hin. Um dem nachzugehen, wurden Anschlüsse der noch im keramischen Druckübertragungsbehälter befindlichen Proben angefertigt. Dabei zeigte sich, daß Sialon ohne zusätzlichen Schutz gegen die LaCrO_3 -Widerstandsheizung mit dieser reagiert und bei den angewandten Heizströmen und Temperaturen von über 1800°C eine Schmelze bildet. An der Grenzfläche zu dem als Kapselungsmaterial verwendeten MgO war im optischen Mikroskop eine dunkle Zone sichtbar, was die Entstehung neuer Phasen andeutet. Dem wurde bislang nicht weiter nachgegangen. Gefügeuntersuchungen mit dem REM ergaben, daß die niedrig substituierten Sialone Si_2AlON_3 und $\text{Si}_{1.9}\text{Al}_{1.1}\text{O}_{1.1}\text{N}_{2.9}$ überwiegend transgranular brechen. Die an der Bruchfläche erkennbaren Körner hatten keine ausgeprägten Facetten und waren im Durchschnitt etwa $0,5\text{ }\mu\text{m}$ groß. Anders die Sialone mit hohem AlO -Gehalt. Hier zeigten die Körner der Bruchfläche eine ausgeprägte Facettierung und die Korngrößen betrugen bis zu $5\text{ }\mu\text{m}$. Da alle Proben etwa eine ähnliche Zeitspanne geheizt worden waren, deutet dies auf eine erhöhte Diffusivität und einen stärker ionischen Bindungscharakter bei hohen AlO -Konzentrationen hin. Gleiches war für die β -Sialone beobachtet worden.

Trotz der oben beschriebenen Reaktion zwischen dem Sialon und der LaCrO_3 -Widerstandsheizung während der HP/HT-Synthese waren Vickershärtemessungen an allen vier Proben mit Lasten von 10 g bis 2 kg möglich. Dabei ergab sich eine Mikrohärte $HV \approx 20\text{ GPa}$ für die sauerstoffreichen (hohes x) und $HV \approx 25\text{--}27\text{ GPa}$ für die stickstoffreichen (kleines x) γ -Sialone. Diese Werte liegen über denen der β -Sialone mit einer maximalen Härte von ca. 19 GPa HV_1 für $x = 0,12$ und typischen Werten von $14\text{--}17\text{ GPa}$ [229]. Die niedrig substituierten Spinell-Sialone sind auch härter als speziell entwickelte α -Sialone, für die bis zu 22 GPa erzielt wurden [242]. Sowohl β - [229] als auch die neuen γ -Sialone zeigen einen scheinbaren Abfall der Härte mit steigendem AlO -Gehalt. Ultramikrohärtemessungen an $\gamma\text{-SiAl}_2\text{O}_2\text{N}_2$ bei kleinen Lasten von $10\text{--}100\text{ g}$ ergaben jedoch Härtewerte zwischen 30 und 35 GPa , die damit nur wenig unter denen der ‘ $\gamma\text{-Si}_3\text{N}_4$ -Keramik’ liegen. Dies zeigt, daß der Härteabfall überwiegend durch die größeren Korndurchmesser der hochsubstituierten Sialone hervorgerufen wird, während sich die intrinsische Härte des Kristallgitters mit steigendem x nur wenig zu ändern scheint.

Aus den mittleren Rißlängen $\langle 2c \rangle$ der Vickers-Eindrücke wurden Zähigkeitswerte K_{IC-IF} von $\sim 4,5 \text{ MPa m}^{1/2}$ für die niedrig substituierten und $3,4\text{--}4,0 \text{ MPa m}^{1/2}$ für die AlO-reichen γ -Sialone bestimmt. Dies liegt im oberen Bereich von einphasigen, feinkörnigen α - und β -Sialonen, die typischerweise 3 bis $4,5 \text{ MPa m}^{1/2}$ aufweisen [224, 229]. Untersuchungen der Rißpfade zeigten, daß Rißüberbrückungsmechanismen in den γ -Sialonen aktiv sind. Vor dem Hintergrund der hohen Rißzähigkeit von Probe SN13 ($6\text{--}7 \text{ MPa m}^{1/2}$), die aus einem zweiphasigen Verbund von $\gamma\text{-Si}_3\text{N}_4$ Körnern und einer Y-Si-Al-O-N Matrix besteht, lässt sich eine weitere Steigerung der mechanischen Eigenschaften durch Zugabe von Sinteradditiven erwarten.

Wie auch im Falle von SN13 wurden bei den Ultramikrohärtemessungen an $\gamma\text{-SiAl}_2\text{O}_2\text{N}_2$ Last-Eindringkurven aufgezeichnet, aus denen zunächst ein reduzierter elastischer Modul von $E_r = 230 \pm 10 \text{ GPa}$ ermittelt wurde. Um daraus die elastischen Konstanten E_Y , G_0 , ν zu berechnen, wurde ein theoretisch berechneter Wert für den Kompressionsmodul B_0 von 257 GPa zugrunde gelegt [239]. Die hierdurch ermittelten Werte fielen unrealistisch gering aus. So lag z.B. der Wert des Young'schen Moduls (E-Modul) mit $E_Y = 257 \pm 20 \text{ GPa}$ noch unter dem der $\beta\text{-Si}_3\text{N}_4$ Niederdruckmodifikation (316 GPa). Dies deutet auf die bereits von mehreren Autoren in Zweifel gezogene Anwendbarkeit des bislang praktizierten Auswertungsverfahrens von Last-Eindringdaten zur Bestimmung der elastischen Konstanten im Fall von sehr harten Materialien hin [80, 78].

In einem weiteren Abschnitt dieser Arbeit werden die Erkenntnisse über Phasenzustandsänderungen des $\text{Si}_{3-x}\text{Al}_x\text{O}_x\text{N}_{4-x}$ -Systems bei hohen Drücken und Temperaturen behandelt. Unter anderen p - T - t Bedingungen als den zur Bildung von γ -Sialon notwendigen $p_{max} = 13 \text{ GPa}$ und $T \geq 1800 \text{ }^\circ\text{C}$, wurde entweder keine Umwandlung oder eine Zersetzung in mehrere Phasen beobachtet. Eines der Zersetzungsprodukte hat wahrscheinlich $\alpha\text{-Al}_2\text{O}_3$ Korundstruktur, bei einer anderen Phase wurden Übereinstimmungen mit dem Beugungsmuster von sog. δ -Alon gefunden. Aus dem Vergleich der mittleren Atomvolumina $\langle \Omega \rangle$ prominenter binärer, ternärer und quaternärer Phasen im System Si-Al-O-N, darunter β -Sialon, γ -Sialon, $\gamma\text{-Si}_3\text{N}_4$ und $\alpha\text{-Al}_2\text{O}_3$, ergab sich, daß die Verringerung des Gesamtvolumens eine wichtige Triebkraft für die beobachtete Phasenseparati-

Zusammenfassung

on unter hohem Druck darstellt (Le Chatelier'sches Prinzip). Die thermische Stabilität der γ -Sialone bei Atmosphärendruck ist hiervon jedoch nicht notwendigerweise betroffen. Die bislang durchgeführten Hochdruckexperimente lassen noch offen, ob die γ -Sialone oberhalb einer Temperatur von 1700–1800 °C und $p > 13$ GPa *thermodynamisch* stabil sind oder als metastabile Zwischenstufe aus den β -Sialonen durch eine topotaktische Phasenumwandlung mit geringer Aktivierungsbarriere hervorgehen. Aus der bei geringeren Drücken beobachteten Zersetzung ergeben sich ernsthafte Konsequenzen für die zukünftige Anwendbarkeit der γ -Sialone: Zum einen wird die Herstellung monolithischer Körper durch statische Verdichtung von Pulvern — analog zur Herstellung von polykristallinem Diamant und c -BN — erheblich erschwert sein, zum andern sind Anwendungen, bei denen hohe Drücke und Temperaturen simultan auftreten, nicht mehr als ein naheliegendes Einsatzgebiet dieser Materialien zu betrachten.

Interessante Alternativen zur Nutzung von γ -Sialon als Abrasivstoff ergeben sich aus der erfolgreichen Darstellung optisch transparenter Proben (Experimente HP-Sial40-II und HP-Sial42-II). Dadurch sollte die experimentelle Bestimmung der elektronischen Bandlücke E_{gap} in naher Zukunft möglich sein. In Verbindung mit den exzellenten mechanischen Eigenschaften wäre die Verwendung von γ -Sialon als hochbelastbares Fenstermaterial in der Sensorik oder Spektroskopie denkbar. Mögliche optoelektronische Anwendungen erschließen sich aus theoretischen Vorhersagen über die Variation von E_{gap} im System $\text{Si}_{3-x}\text{Al}_x\text{O}_x\text{N}_{4-x}$ [237, 238, 239]. Zwei dieser Arbeiten sagen übereinstimmend eine Abnahme von E_{gap} , einerseits mit zunehmendem Substitutionsgrad x voraus. Einen fast noch stärkeren Einfluß auf E_{gap} scheint jedoch die Verteilung der Si- und Al-Ionen auf die tetraedrischen und oktaedrischen Gitterplätze zu haben.

Bibliography

- [1] E.G. Acheson. “Production of Artificial Crystalline Carbonaceous Materials”. *US Pat. 492 767 (28 Feb. 1893), DE 76629 (1894), DE 85195 (1896)*.
- [2] J.J. Berzelius. *Am. Phys. Chem.*, 1, pp. 169–230, 1824.
- [3] C.M. Despretz. *Compt. Rend.*, 29, pp. 709–724, 1849.
- [4] M.W. Bailey. “Superabrasive tools: A Brief Introduction”. In R. Riedel, editor, *Handbook of Ceramic Hard Materials, Part II*, pages 481–482. Wiley-VCH, Weinheim, 2000.
- [5] S. Ozbayarktar. “Polycrystalline Diamond and Cubic Boron Nitride”. In R. Riedel, editor, *Handbook of Ceramic Hard Materials, Part II*, pages 512–520. Wiley-VCH, Weinheim, 2000.
- [6] J. Haines, J.M. Léger and G. Bocquillon. “Synthesis and Design of Superhard Materials”. *Annu. Rev. Mater. Res.*, 31, pp. 1–23, 2001.
- [7] S. Vepřek and A.S. Argon. “Towards the understanding of mechanical properties of super- and ultrahard nanocomposites”. *J. Vac. Sci. Technol. B*, 20[2], pp. 650–664, 2002.
- [8] D.M. Teter. “Computational Alchemy: The Search for New Superhard Materials”. *MRS. Bull.*, pages 22–27, January 1998.
- [9] S. Vepřek. “The search for novel, superhard materials”. *J. Vac. Sci. Technol. A*, 17[5], pp. 2401–2420, 1999.

Bibliography

- [10] C.-M. Sung and M. Sung. “Carbon nitride and other speculative superhard materials”. *Mater. Chem. Phys.*, 43, pp. 1–18, 1996.
- [11] M.L. Cohen. “Predicting new solids and superconductors”. *Science*, 234[4776], pp. 549–553, 1986.
- [12] M.L. Cohen. “Novel Materials from Theory”. *Nature*, 338, pp. 291–292, 1989.
- [13] H. Cynn, J.E. Klepeis, C.-S. Yoo and D.A. Young. “Osmium has the Lowest Experimentally Determined Compressibility”. *Phys. Rev. Lett.*, 88[13], pp. 135701(1–4), 2002.
- [14] T. Malkow. “Critical observation in the research of carbon nitride”. *Adv. Eng. Mater.*, A292, pp. 112–124, 2000.
- [15] E. Kroke and M. Schwarz. “Novel group 14 nitrides”. *Coord. Chem. Rev.*, 248[5-6], pp. 493–532, 2004.
- [16] A. Szymansky and J.M. Szymansky. “Hardness Estimation of Minerals, Rocks and Ceramic Materials”. *Elsevier, Amsterdam*, 1989.
- [17] W.A. Harrison. *Electronic Structure and the Properties of Solids*. W.H. Freeman and Co., San Francisco, 1980.
- [18] M.J.P. Musgrave and J.A. Pople. “A general valence force field for diamond”. *Proc. R.Soc.*, A 268[1335], pp. 474–484, 1962.
- [19] W. Kleber and K.-Th. Wilke. “Synthese und Kristallchemie anorganischer Stoffe bei hohen Drücken und Temperaturen”. *Kristall und Technik*, 4[2], pp. 165–199, 1969.
- [20] J. Haines, J.M. Léger, F. Gorelli and M. Hanfland. “Crystalline Post-Quartz Phase in Silica at High Pressure”. *Phys. Rev. Lett.*, 87[15], pp. 155503(1–4), 2001.
- [21] A. Putnis. *Introduction to Mineral Sciences*. Cambridge University Press, Cambridge, U.K., 1992.

- [22] E.O. Hall. “The deformation and ageing of mild steel: III Discussion of results”. *Proc. Phys. Soc. Lond. B*, 64, pp. 747–753, 1951.
- [23] N.J. Petch. “The cleavage strength of polycrystals”. *J. Iron Steel Inst.*, 174, pp. 25–28, 1953.
- [24] D. Hull and D.J. Bacon. “Introduction to Dislocations”. In *Internat. Series on Mater. Sci. and Technol.*, page 16. Butterworth Heinemann, 1984.
- [25] T.G. Nieh and Wadsworth. “Hall-Petch Relation in nanocrystalline Solids”. *Scripta Metall. Mater.*, 25, pp. 955–958, 1991.
- [26] J. Schiøtz, F.D. Di Tolla and K.W. Jacobsen. “Softening of nanocrystalline metals at very small grain sizes”. *Nature*, 391, pp. 561–563, 1998.
- [27] J. Patscheider. “Nanocomposite Hard Coatings for Wear Protection”. *MRS. Bull.*, 28[3], pp. 180–183, 2003.
- [28] S.A. Barnett, A. Madan, I. Kim and K. Martin. “Stability of Nanometer-Thick Layers in Hard Coatings”. *MRS. Bull.*, 28[3], pp. 169–172, 2003.
- [29] H.-D. Männling, D.S. Patil, K. Moto, M. Jilek and S. Vepřek. “Thermal stability of superhard nanocomposite coatings consisting of immiscible nitrides”. *Surf. Coat. Technol.*, 146–147, pp. 263–267, 2001.
- [30] P. Karvánková, H.-D. Männling, C. Eggs and S. Vepřek. “Thermal stability of ZrN–Ni and CrN–Ni superhard nanocomposite coatings”. *Surf. Coat. Technol.*, 146–147, pp. 280–285, 2001.
- [31] A. Niederhofer, T. Bolom, P. Nesladek, K. Moto, C. Eggs, D.S. Patil and S. Vepřek. “The role of percolation threshold for the control of the hardness and thermal stability of super- and ultrahard nanocomposites”. *Surf. Coat. Technol.*, 146–147, pp. 183–188, 2001.
- [32] S. Vepřek and A.S. Argon. “Mechanical properties of superhard nanocomposites”. *Surf. Coat. Technol.*, [146–147], pp. 175–182, 2001.

Bibliography

- [33] M.V. Swain. “Structure and properties of ceramics”. In R.W. Cahn, P. Haasen and E.J. Kramer, editors, *Mater. Sci. and Technol. Vol. 11*. VCH, New York, Basel, Cambridge, Tokyo, 1994.
- [34] E. Mitchell. “Dislocations and Mechanical Properties of MgO–Al₂O₃ Spinel Single Crystals”. *J. Am. Ceram. Soc.*, 82[12], pp. 3305–3316, 1999.
- [35] M. Akaishi, T. Satoh, M. Ishii, T. Taniguchi and S. Yamaoka. “Synthesis of translucent sintered boron nitride”. *J. Mater. Sci. Lett.*, 12, pp. 1883–1885, 1993.
- [36] T. Taniguchi, M. Akaishi and S. Yamaoka. “Mechanical Properties of Polycrystalline Translucent Cubic Boron Nitride as Characterized by the Vickers Indentation Method”. *J. Am. Ceram. Soc.*, 79[2], pp. 547–549, 1996.
- [37] M. Grimsditch, S. Popova, V.V. Brazhkin and R.N. Voloshin. “Temperature-induced amorphization of SiO₂ stishovite”. *Phys. Rev. B*, 50[17], pp. 12984–12986, 1994.
- [38] L.S. Dubrovinsky, N.A. Dubrovinskaia, V. Swamy, J. Muscat, N.M. Harrison, R. Ahuja, B. Holm and B. Johansson. “The hardest known oxide”. *Nature*, 410, pp. 653–654, 2001.
- [39] T. Evans and P.F. James. “A Study of the Transformation of Diamond to Graphite”. *Proc. Roy. Soc. London*, A277, pp. 260, 1964.
- [40] V.L. Solozhenko, V.Z. Turkevich and W.B. Holzapfel. “Refined Phase Diagram of Boron Nitride”. *J. Phys. Chem. Solids*, 103, pp. 2903–2905, 1999.
- [41] M. Kalin and J. Vizintin. “A tentative explanation for the tribochemical effects in fretting wear”. *Wear*, 250, pp. 681–689, 2001.
- [42] T.G. Dawson. *Machining Hardened Steel with Polycrystalline Cubic Boron Nitride Cutting Tools*. PhD thesis, Georgia Institute of Technology, http://www.hardinge.com/hardturn/PDF/Dawson_PhD_Dissertation.pdf, 2001.

- [43] M. Kalin, J. Vizintin, J. Vleugels and O. Van Der Biest. “Chemical reactivity of silicon nitride with steel and oxidized steel between 500 and 1200 °C”. *Mater. Sci. Eng.*, A281, pp. 28–36, 2000.
- [44] M. Kalin, J. Vizintin, J. Vleugels and O. Van Der Biest. “Influence of mechanical pressure and temperature on the chemical interaction between steel and silicon nitride ceramics”. *J. Mater. Res.*, 15[6], pp. 1367–1377, 2000.
- [45] A. Krell. “Ceramics Based on Alumina: Increasing the Hardness for Tool Applications”. In R. Riedel, editor, *Handbook of Ceramic Hard Materials, Part II*, pages 649–682. Wiley-VCH, Weinheim, 2000.
- [46] J.H. Wijngaard. “PVD Coatings in High Speed Cutting Operations (HSC)”. http://www.balzers.fr/docs/Pdf/Metz_en.pdf, pages 1–10, 2003.
- [47] R.F. Cook and G.M. Pharr. “Direct Observation and Analysis of Indentation Cracking in Glasses and Ceramics”. *J. Am. Ceram. Soc.*, 73[4], pp. 787–817, 1990.
- [48] E. Kroke. “High-Pressure Syntheses of Novel Binary Nitrogen Compounds of Main Group Elements”. *Angew. Chem. Int. Ed.*, 41[1], pp. 77–82, 2002.
- [49] A. Zerr, G. Serghiou and R. Boehler. “Phase Transitions and Material Synthesis using the CO₂-Laser Heating Technique in a Diamond Cell”. In *Handbook of Ceramic Hard Materials, Part I*, pages 41–49. Wiley-VCH, Weinheim, 2000.
- [50] J. Jayaraman. “Diamond anvil cell and high-pressure investigations”. *Review of Modern Physics*, 55[1], 1983.
- [51] A. Chopelas and R. Boehler. “MgO:V²⁺ Pressure Scale for Diamond Anvil Cells”. *Mat. Res. Soc. Symp. Proc.*, 22, pp. 275–280, 1984.
- [52] H.K. Mao, J. Xu and P.M. Bell. “Calibration of the ruby pressure gauge to 800 kbar under quasi-hydrostatic conditions”. *J. Geophys. Res.*, 91, pp. 4673–4676, 1986.

Bibliography

- [53] D.C. Rubie. “Characterising the sample environment in multianvil high-pressure experiments”. *Phase Transitions*, 68, pp. 431–451, 1999.
- [54] M.J. Walter, Y. Thibault, K. Wei and R.W. Luth. “Characterizing experimental pressure and temperature conditions in multi-anvil apparatus”. *Can. J. Phys.*, 73, pp. 273–286, 1995.
- [55] T. Sekine. “Shock wave chemical synthesis”. *Eur. J. Solid State Inorg. Chem.*, 34, pp. 823–883, 1997.
- [56] F. Langenhorst, M. Boustie, A. Deutsch, U. Hornemann, Ch. Matignon, A. Migault and J.P. Romain. “Experimental techniques for the simulation of shock metamorphism: A case study on calcite”. In L. Davison, Y. Horie and Sekine T., editors, *Shock compression of solids V: Shock Chemistry with applications to meteorite impacts*, page 8 ff. Springer-Verlag, New York, 2003.
- [57] H. Blumenauer (ed.). *Werkstoffprüfung*. VEB Deutscher Verlag für Grundstoffindustrie, Leipzig, 1984.
- [58] D.B. Marshall, T. Noma and A.G. Evans. “A Simple Method for Determining Elastic-Modulus-to-Hardness Ratios using Knoop Indentation Measurements”. *J. Am. Ceram. Soc.*, pages C 175–176, 1982.
- [59] S.J. Bull, T.F. Page and E.H. Yoffe. “An explanation of the indentation size effect in ceramics”. *Phil. Mag. Lett.*, 59[6], pp. 281–288, 1989.
- [60] J.B. Quinn and G.D. Quinn. “Indentation brittleness of ceramics: a fresh approach”. *J. Mater. Sci.*, 32, pp. 4331–4346, 1997.
- [61] M. Kaji, M.E. Stevenson and R.C. Bradt. “Knoop Microhardness Anisotropy and the Indentation Size Effect on the Basal Plane of Single-Crystal Alumina (Sapphire)”. *J. Am. Ceram. Soc.*, 85[2], pp. 415–422, 2002.
- [62] J. Gong and Z. Guan. “Effect of microcracking on the energy-balance relationship for hardness testing of ceramics”. *Mater. Lett.*, 49[3-4], pp. 180–184, 2001.

- [63] Heinrich Hertz. “On the contact of elastic solids”. *J. Reine Angew. Math.*, 92, pp. 156–171, 1882.
- [64] Heinrich Hertz. “On the Contact of Rigid Elastic Solids and on Hardness”. *Verhandlungen des Vereins zur Beförderung des Gewerbefleisses*, 61, pp. 449, 1882.
- [65] S. Palmqvist. “A Method to Determine the Toughness of Brittle Materials, Especially Hard Metals”. *Jernkontorets Ann. (in Swedish)*, 141, pp. 303–307, 1957.
- [66] S. Palmqvist. “The Work for the Formation of a Crack During Vickers indentation as a Measure of the Toughness of Hard Materials”. *Arch. Eisenhüttenwes. (in German)*, 33, pp. 629–634, 1962.
- [67] S. Palmqvist. “The Work for the Formation of a Crack During Vickers indentation as a Measure of the Toughness of Hard Materials”. *Jernkontorets Ann. (in German)*, 147, pp. 107–110, 1963.
- [68] B.R. Lawn, A.G. Evans and D.B. Marshall. “Elastic/Plastic Indentation Damage in Ceramics: The Median/Radial Crack System”. *J. Am. Ceram. Soc.*, 63[9–10], pp. 574–581, 1980.
- [69] K. Niihara, R. Morena and P.H. Hasselmann. “Evaluation of K_{IC} of Brittle Solids by the Indentation Method With Low Crack-to-Indent Ratios”. *J. Mater. Sci. Lett.*, 1[1], pp. 13–16, 1982.
- [70] G.R. Anstis, P Chantikul, B.R. Lawn and D.B. Marshall. “A Critical Evaluation of Indentation Techniques for Measuring Fracture Toughness: I, Direct Crack Measurements”. *J. Am. Ceram. Soc.*, 64, pp. 533–538, 1981.
- [71] D.K. Shetty, I.G. Wright, P.N. Mincer and A.H. Clauer. “Indentation fracture of WC-Co cermets”. *J. Mater. Sci.*, 20, pp. 1873–1882, 1985.
- [72] J. Dusza. “Comparison of Fracture Toughness Testing Methods Applied to $\text{Si}_3\text{N}_4 + \text{SiC}$ -Whisker System”. *Scripta Metall Mater*, 26, pp. 337–324, 1992.

Bibliography

- [73] M.F. and Doerner. “A method for interpreting the data from depth-sensing indentation instruments”. *J. Mater. Res.*, 1[4], pp. 601–609, 1986.
- [74] ASTM C 1259. *Standard Test Method for Dynamic Young’s Modulus, and Poisson’s Ratio for Advanced Ceramics by Impulse Excitation of Vibration.*
- [75] DIN 50359. *Universalhärteprüfung, Teil 1: Prüfverfahren.* Beuth-Verlag, Berlin, 1997.
- [76] DIN EN ISO 14577-1. *Metallische Werkstoffe - Instrumentierte Eindringprüfung zur Bestimmung der Härte und anderer Werkstoffparameter - Teil 1: Prüfverfahren.* Beuth-Verlag, Berlin, 2002.
- [77] H.-R. Wilde and A. Wehrstedt. “Martens Hardness HM - an international accepted designation for “Hardness under Test Force””. *Mat.-wiss. u. Werkstofftech.*, 31, pp. 937–940, 2000.
- [78] S. Vepřek S. Mukherjee, P. Karvankova, H.-D. Männling, J.L. He, J. Xu, J. Prochazka, A.S. Argon, A.S. Li, Q.F. Fang, S.Z. Li, M.H. Manghnani and S. Tkachev. “Possible Artefacts in Measurement of Hardness and Elastic Modulus on Superhard Coatings and the Verification of the Correctness of the Data”. *Mater. Res. Soc. Symp. Proc.*, 750, Symposium Y, Surface Engineering 2002 — Synthesis, Characterization and Applications, 2002.
- [79] W.C. Oliver and G.M. Pharr. “An Improved Technique for Determining Hardness and Elastic Modulus Using Load and Displacement Sensing Indentation Experiments”. *J. Mater. Res.*, 7, pp. 1564–1583, 1992.
- [80] M.M. and Chaudhri. “A note on a common mistake in the analysis of nanoindentation data”. *J. Mater. Res.*, 16[2], pp. 336–339, 2001.
- [81] I.N. Sneddon. “The relation between load and penetration in the axisymmetric Bousinnesq problem for a punch of arbitrary profile”. *Int. J. Engng. Sci.*, 3, pp. 47–57, 1965.

[82] A. Zerr, M. Kempf, M. Schwarz, E. Kroke, M Göken and R. Riedel. “Elastic Moduli and Hardness of Cubic Silicon Nitride”. *J. Am. Ceram. Soc.*, 85[1], pp. 86–90, 2002.

[83] S. Vepřek, S. Mukherjee, P. Karvankova, H.-D. Männling, J.L. He, K. Moto, J. Prochazka and A.S. Argon. “The Limits to the Strength of Super- and Ultra-Hard Nanocomposite Coatings”. *J. Vac. Sci. Technol. A*, 21[3], pp. 532–544, 2003.

[84] A. Zerr, G. Miehe and R. Riedel. “Synthesis of zirconium and hafnium nitride having Th_3P_4 structure”. *Nature Materials*, [2], pp. 185–189, 2003.

[85] A. Zerr, G. Miehe, G. Serghiou, M. Schwarz, E. Kroke, R. Riedel, H. Fueß, P. Kroll and R. Boehler. “Synthesis of cubic silicon nitride”. *Nature*, 400, pp. 340–342, 1999.

[86] S-D Mo, L. Ouyang, W.Y. Ching, I. Tanaka and R. Riedel. “Interesting Physical Properties of the New Spinel Phase of Si_3N_4 and C_3N_4 ”. *Phys. Rev. Lett.*, 83[24], pp. 5046–5049, 1999.

[87] T. Sekine, H.L. He, T. Kobayashi, Zhang. M. and F.F. Xu. “Shock-induced transformation of $\beta\text{-Si}_3\text{N}_4$ to a high pressure cubic-spinel phase”. *Appl. Phys. Lett.*, 76[25], pp. 3706–3708, 2000.

[88] J.Z. Jiang, F. Kragh, D.J. Frost, K. Ståhl and H. Lindelov. “Hardness and thermal stability of cubic silicon nitride”. *J. Phys.: Condens. Matter*, 13, pp. L515–519, 2001.

[89] K. Leinenweber, M. O’Keeffe, M. Somayazulu, H. Hubert, P.F. McMillan and G.H. Wolf. “Synthesis and Structure Refinement of the Spinel, $\gamma\text{-Ge}_3\text{N}_4$ ”. *Chem. Eur. J.*, 5[10], pp. 3076–3078, 1999.

[90] N. Scotti, W. Kockelmann, J. Senker, St. Traßel and H. Jacobs. “ Sn_3N_4 , ein Zinn(IV)-nitrid – Synthese und erste Strukturbestimmung einer binären Zinn–Stickstoff-Verbindung”. *Z. Anorg. Allg. Chem.*, 625, pp. 1435–1439, 1999.

Bibliography

- [91] W. Schnick. “Die ersten Nitrid-Spinelle - neue Synthesewege für binäre Nitride der 4. Hauptgruppe”. *Angew. Chem.*, 111[22], pp. 3511–3512, 1999.
- [92] W. Schnick. “The First Nitride Spinels - New Synthetic Approaches to Binary Group 14 Nitrides”. *Angew. Chem. Int. Ed.*, 38[22], pp. 3309–3310, 1999.,
- [93] P.F. McMillan. “New materials from high pressure experiments”. *Nature Materials*, 1, pp. 19–25, 2002.
- [94] S. Saha, M.A. Hossian and M.A. Quader. “X-Ray Powder Diffraction Studies of Reaction Bonded Silicon Nitride”. *J. Bangladesh. Acad. Sci.*, 10[1], pp. 13–16, 1986.
- [95] D.M. Teter and R.J. Hemley. “Low Compressibility Carbon-Nitrides”. *Science*, 271, pp. 53–55, 1996.
- [96] W. Dawei, F. Djun, G. Huaixi, Z. Zhihong, M. Xianquan and F. Xiangung. “Structure and characteristics of C_3N_4 thin films prepared by rf plasma-enhanced chemical vapor deposition”. *Phys. Rev. B*, 56, pp. 4949–4954, 1997.
- [97] L.C. Chen, C.Y. Yang, D.M. Bhusari, K.H. Chen, M.C. Lin and T.J. Chuang. “Formation of crystalline silicon carbon nitride films by microwave plasma-enhanced chemical vapor deposition”. *Diamond Rel. Mater.*, 5, pp. 514–518, 1996.
- [98] E. Ott and E. Ohse. “Zur Kenntnis einfacher Cyan- und Cyanurverbindungen II. Über das Cyanurtriazid (C_3N_{12})”. *Chem. Ber.*, 54, pp. 179–186, 1921.
- [99] T. Hahn (editor). *International Tables for Crystallography*, volume A. Kluwer Academic Publishers, Dordrecht, the Netherlands, 5th edition, 2002.
- [100] W. Heininger, K. Polborn and G. Nagorsen. “A further silicate anion - $[\text{Si}(\text{NCSe})_6]^{2-}$ ”. *Z. Naturforsch. B*, 43[7], pp. 875–861, 1988.

[101] K. Köllisch and W. Schnick. “Ce₁₆Si₁₅O₆N₃₂ – ein Oxonitridosilicat mit Silicium in oktaedrischer Stickstoff-Koordination”. *Angew. Chem.*, 111[3], pp. 368–370, 1999.

[102] T. Sekine, M. Tansho and S. Kanzaki. “²⁹Si magic-angle-spinning nuclear-magnetic-resonance study of spinel-type Si₃N₄”. *Appl. Phys. Lett.*, 78[20], pp. 3050–3051, 2001.

[103] H.X. Willems, G. de With, R. Metselaar, R.B. Helmholdt and K.K. Petersen. “Neutron diffraction of γ -aluminium oxynitride”. *J. Mater. Sci. Lett.*, 12, pp. 1470–1473, 1993.

[104] K.E. Sickafus and J.M. Wills. “Structure of Spinel”. *J. Am. Ceram. Soc.*, 82[12], pp. 3279–3292, 1999.

[105] R. Dronskowski. “The Little Maghemite Story: A Classic Functional Material”. *Adv. Funct. Mater.*, 11[1], pp. 27–29, 2001.

[106] K.E. Sickafus and R. Hughes. “Spinel Compounds: Structure and Property Relations”. *J. Am. Ceram. Soc.*, 82[12], pp. 3277–3278, 1999.

[107] Yu. P. Vorob’ev, V. G. Bamburov, N. I. Lobachevskaya, A. N. Men and G. I. Chufarov. “Structure and ferrimagnetism of spinel solid solutions R₁-cIRcII₂O₄, R = rare earth elements and yttrium”. *Dokl. Akad. Nauk SSSR*, 250[6], pp. 1406–1409, 1980.

[108] E.G. Moshopoulou. “Superconductivity in the Spinel Compound LiTi₂O₄”. *J. Am. Ceram. Soc.*, 82[12], pp. 3317–3320, 1999.

[109] D. Brasen, J.M. Vandenberg, M. Robbins, R.H. Willens, W.A. Reed, R.C. Sherwood and X.J. Pinder. “Magnetic and Crystallographic Properties of Spinels of the Type A_xB₂S₄ Where A = Al, Ga, and B = Mo, V, Cr”. *J. Solid. State. Chem.*, 13, pp. 298–303, 1975.

[110] J. Grins, P.-O. Käll and G. Svensson. “Synthesis, Structure and Magnetic Susceptibility of the Oxynitride Spinel Mn₂(MnTa₃)N_{6- δ} O_{2+ δ} , 0 \leq δ \leq 1”. *J. Solid. State. Chem.*, 117, pp. 48–54, 1995.

Bibliography

[111] J.W. McCauley. “Aluminum Nitride and AlON Ceramics, Structure and Properties of”. In K. H. J. Buschow, R.W. Cahn, M. C. Flemmings, B. J. Schmer, E. J. Kramer and S. Mahajan, editors, *Encyclopedia of Materials: Science and Technology*, pages 127–132. Elsevier, Amsterdam, 2001.

[112] T. Sekine, H.L. He, T. Kobayashi, M. Tansho and K. Kimoto. “Cubic $\text{Si}_{6-z}\text{Al}_z\text{O}_z\text{N}_{8-z}$ ($z=1.8$ and 2.8) spinels formed by shock compression”. *Chem. Phys. Lett.*, 344, pp. 395–399, 2001.

[113] M. Schwarz, A. Zerr, E. Kroke, G. Miehe, I.-W. Chen, M. Heck, B. Thybusch, B.T. Poe and R. Riedel. “Spinell-Sialone”. *Angew. Chem.,* 114[5], pp. 804–808, 2002.

[114] G. Serghiou, G. Miehe, O. Tschauner, A. Zerr and R. Boehler. “Synthesis of a cubic Ge_3N_4 phase at high pressures and temperatures”. *J. Chem. Phys.*, 111, pp. 4659–4661, 1999.

[115] J.-J. Dong, J. Deslippe, O.F. Sankey, E. Soignard and P.F. McMillan. “Theoretical study of the ternary spinel nitride system $\text{Si}_3\text{N}_4\text{-Ge}_3\text{N}_4$ ”. *Phys. Rev.*, 67[094104], pp. 1–7, 2003.

[116] W.Y. Ching, S-D. Mo, I. Tanaka and M. Yoshida. “Prediction of spinel structure and properties of single and double nitrides”. *Phys. Rev. B*, 63, pp. 064102(1–4), 2001.

[117] W.Y. Ching, S-D. Mo and L. Ouyang. “Electronic and optical properties of the cubic spinel phase of c- Si_3N_4 , c- Ge_3N_4 , c- SiGe_2N_4 , and c- GeSi_2N_4 ”. *Phys. Rev. B*, 64[24], pp. 245110(1–7), 2001.

[118] E. Soignard, M. Somayazulu, H.K. Mao, J.-J. Dong, O.F. Sankey and P.F. McMillan. “High pressure-high temperature investigation of the stability of nitride spinels in the systems $\text{Si}_3\text{N}_4\text{-Ge}_3\text{N}_4$ ”. *Solid State Commun.*, 120, pp. 237–242, 2001.

[119] J.M. Léger, J. Haines, M. Schmidt, J.P. Petitet, A.S. Pereira and J.A.H. da Jomada. “Discovery of the hardest known oxide”. *Nature*, 383, pp. 400–401, 1996.

- [120] I. Tanaka, F. Oba, T. Sekine, E. Ito and A. Kubo. “Hardness of cubic silicon nitride”. *J. Mater. Res.*, 17[4], pp. 731–733, 2002.
- [121] A. Rosenflanz. “Silicon nitride and sialon ceramics”. *Curr. Opin. Solid. St. M.*, 4[5], pp. 453–459, 1999.
- [122] H.L. He, T. Sekine, T. Kobayashi and H. Hirosaki. “Shock-induced phase transition of β -Si₃N₄ to c -Si₃N₄”. *Phys. Rev. B*, 62[17], pp. 11412–11471, 2000.
- [123] S.K. Deb, J. Dong, H. Hubert, P.F. McMillan and O.F. Sankey. “The Raman spectra of the hexagonal and cubic (spinel) forms of Ge₃N₄: an experimental and theoretical study”. *Solid State Commun.*, 114, pp. 137–142, 2000.
- [124] E. Soignard, M. Somayazulu, J.-J. Dong, O.F. Sankey and P.F. McMillan. “High pressure-high temperature synthesis and elasticity of the cubic nitride spinel γ -Si₃N₄”. *J. Phys.-Condens. Mat.*, 13[4], pp. 557–563, 2001.
- [125] J.Z. Jiang, K. Ståhl, R.W. Berg, D.J. Frost, T.J. Zhou and P.X. Shi. “Structural characterisation of cubic silicon nitride”. *Europhys. Lett.*, 51[1], pp. 62–67, 2000.
- [126] W.Y. Ching, S-D. Mo and L. Ouyang. “Prediction of the new spinel phase of Ti₃N₄, and SiTi₂N₄ and the metal-insulator transition”. *Phys. Rev. B*, 61[16], pp. 10609–10614, 2000.
- [127] W.Y. Ching, S-D Mo, L. Ouyang and P. Rulis. “Theoretical Prediction of the Structure and Properties of Cubic Spinel Nitrides”. *J. Am. Ceram. Soc.*, 85[1], pp. 75–80, 2002.
- [128] P. Kroll. “Hafnium Nitride, Hf₃N₄, with Thorium Phosphide Structure: Physical Properties and an Assessment of the Hf-N, Zr-N, and Ti-N Phase Diagrams at High Pressures and Temperatures”. *Phys. Rev. Lett.*, 90, pp. 125501, 2003.
- [129] H. Vollstädt, E. Ito, M. Akaishi, S. Akimoto and O. Fukunaga. “High Pressure Synthesis of Rocksalt Type of AlN”. *Proc. Japan Acad.*, 66 B, pp. 7–9, 1990.

Bibliography

- [130] P.E. Van Camp, V.E. Van Doren and J.T. Devreese. “High-pressure properties of wurtzite- and rocksalt-type aluminium nitride”. *Phys. Rev. B*, 44[16], pp. 9056–9059, 1992.
- [131] M. Ueno, A. Onodera, O. Shimomura and K. Takemura. “X-ray observation of the structural phase transition of aluminum nitride under high pressure”. *Phys. Rev. B*, 45[17], pp. 10123–10126, 1992.
- [132] M. Ueno, M. Yoshida, A. Onodera, O. Shimomura and K. Takemura. “Stability of the wurtzite-type structure under high pressure: GaN and InN”. *Phys. Rev. B*, 49[1], pp. 14–21, 1994.
- [133] A. Muñoz and K. Kunc. “Structure and static properties of indium nitride at low and moderate pressures”. *J. Phys.: Condens. Matter*, 5, pp. 6015–6022, 1993.
- [134] J.L. Corkill, A. Rubio and M.L. Cohen. “Cation dependence of the electronic structure of III-V nitrides”. *J. Phys.: Condens. Matter*, 6, pp. 963–976, 1994.
- [135] Q. Xia, H. Xia and A.L. Ruoff. “Pressure-induced rocksalt phase of aluminum nitride: A metastable structure at ambient condition”. *J. Appl. Phys.*, 73[12], pp. 8198–8200, 1993.
- [136] D.P. Dandekar, A. Abbate and J. Frankel. “Equation of state of aluminum nitride and its shock response”. *J. Appl. Phys.*, 76[7], pp. 4077–4085, 1994.
- [137] S. Limpijumnong and R.L. Lambrecht. “Homogeneous Strain Deformation Path for the Wurtzite to Rocksalt High-Pressure Phase Transition in GaN”. *Phys. Rev. Lett.*, 86, 2001.
- [138] S. Uehara, T. Masamoto, A. Onodera, M. Ueno, O. Shimomura and K. Takemura. “Equation of state of the rocksalt phase of III-V nitrides to 72 GPa or higher”. *J. Phys. Chem. Solids*, 58[12], pp. 2093–2099, 1997.
- [139] G.J. Davies. “The Crystallization of Diamond”. In R. Riedel, editor, *Handbook of Ceramic Hard Materials, Part II*, pages 485–496. Wiley-VCH, Weinheim, 2000.

[140] M.B. Kruger, J.H. Nguyen, Y.M. Li, W.A. Caldwell, M.H. Manghnani and R. Jeanloz. “Equation of state of α -Si₃N₄”. *Phys. Rev. B*, 55[6], pp. 3456–3460, 1997.

[141] Y. Cerenius. “Melting-Temperature Measurements on α -Silicon Nitride to a Pressure of 37 GPa”. *J. Am. Ceram. Soc.*, 82[2], pp. 380–386, 1999.

[142] A. Zerr, M. Schwarz, G. Serghiou, E. Kroke, G. Miehe, R. Riedel and R. Boehler. “Kubisches Siliciumnitrid, Verfahren zu dessen Herstellung und Anwendungen”. *German Pat. DE 198 55 514 A1*, 2000.

[143] G.M. Crosbie. “Liquid phase reaction processes”. In A. W. Weimer, editor, *Carbide, Nitride and Boride Materials Synthesis and Processing*, pages 392–401. Chapman & Hall, London, 1997.

[144] T. Sekine, G. Koryo and T. Kobayashi. “Synthetic Method for Spinel Type Silicon Nitride Powder”. *Japanese Patent JP 2001199714*, 2001.

[145] M. Zhang, H.L. He, F.F. Xu, T. Sekine, T. Kobayashi and Y. Bando. “Cubic silicon nitride embedded in amorphous silicon dioxide”. *J. Mater. Res.*, 16[8], 2001.

[146] T. Sekine. “Shock Synthesis of Cubic Silicon Nitride”. *J. Am. Ceram. Soc.*, 85[1], pp. 113–116, 2002.

[147] F.L. Riley. “Silicon Nitride and Related Materials”. *J. Am. Ceram. Soc.*, 83[2], pp. 246–265, 2000.

[148] J.W. McCauley and N.D. Corbin. “High Temperature Reactions and Microstructure in the Al₂O₃–AlN System”. *Nato ASi ser. E*, [65], pp. 111–118, 1983.

[149] P. Kroll. “High-Pressure Phases of Silicon Oxynitride”. At the 104th Annual Meeting of the American Ceramic Society, Session AMA.4-B-04, St. Louis, MO, U.S.A., 2002.

[150] P. Kroll. “A Theoretical Study of the High-Pressure Phase Diagram of Silicon Oxynitrides: Balancing between Spinel, Stishovite and

Bibliography

Corundum". At the *First International Workshop on Spinel Nitrides and Related Materials*, Rüdesheim, Germany, 02.–04. Sept. 2002.
www.hotmaterials.com.

[151] P. Kroll and M. Milko. "A Theoretical Investigation of the Solid State Reaction of Silicon Nitride and Silicon Dioxide forming Silicon Oxynitride ($\text{Si}_2\text{N}_2\text{O}$) under Pressure". *Z. Anorg. Allg. Chem.*, 629[10], pp. 1737–1750, 2003.

[152] P.F. McMillan and A.M. Hofmeister. "Infrared and Raman Spectroscopy". In F.C. Hawthorne, editor, *Reviews in Mineralogy Vol. 18, Spectroscopic Methods in Mineralogy and Geology*, chapter 4, page 100 ff. Mineralogical Society of America, 1988.

[153] C.M. Fang, G.A. Wijs, H.T. Hintzen and G. de With. "Phonon spectrum and thermal properties of cubic Si_3N_4 from first principles calculations". *J. Appl. Phys.*, 2003.

[154] M. Schwarz, G. Miehe, A. Zerr, E. Kroke, B. Poe, H. Fuess and R. Riedel. "Spinel- Si_3N_4 : Multi-Anvil Press Synthesis and Structural Refinement". *Advanced Materials*, 12, pp. 883–887, 2000.

[155] R. J. Hill and C. J. Howard. "A computer program for Rietveld analysis of fixed wavelength X-ray and neutron powder diffraction patterns". In *AAEC Report*, number M112, Sydney, 1986. Australian Atomic Energy Commission.

[156] W.Y. Ching, L. Ouyang and J.D. Gale. "Full ab initio geometry optimization of all known crystalline phases of Si_3N_4 ". *Phys. Rev. B*, 61[13], pp. 8696–8700, 2000.

[157] H. Huppertz and W. Schnick. " $\text{BaYbSi}_4\text{N}_7$ - Unexpected Structural Possibilities in Nitridosilicates". *Angew. Chem. Int. Ed.*, 35[17], pp. 1983–1984, 1996.

[158] M. Schwarz. "The Homologous Series of the Group 14-Element Spinel Nitrides". *Silicates Industriels*, 69[7–8], pp. 333–340, 2004.

[159] M.P. Shemkunas, G.H. Wolf, K. Leinenweber and W.T. Petuskey. “Rapid Synthesis of Crystalline Spinel Tin Nitride by a Solid-State Metathesis Reaction”. *J. Am. Ceram. Soc.*, 85[1], pp. 101–104, 2002.

[160] H. Stanjek and J. Schneider. “Anisotropic peak broadening analysis of a biogenic soil greigite (Fe_3S_4) with Rietveld analysis and single peak fitting”. *Am. Mineral.*, 85, pp. 839–846, 2000.

[161] B. Kiefer, L. Stixrude and R. Wentzcovitch. “Normal and inverse ringwoodite at high pressures”. *Am. Mineral.*, 84, pp. 288–293, 1999.

[162] R.D. Shannon. “Revised Effective Ionic Radii and Systematic Studies of Interatomic Distances in Halides and Chalcogenides”. *Acta Crystallogr., Sect. A: Found. Crystallogr.*, A32, pp. 751–767, 1976.

[163] P. Kroll. “Pathways to metastable nitride structures”. *J. Solid. State. Chem.*, 176, pp. 530–537, 2003.

[164] J.-J. Dong, O.F. Sankey, S.K. Deb, G.H. Wolf and P.F. McMillan. “Theoretical study of β - Ge_3N_4 and its high-pressure spinel γ phase”. *Phys. Rev. B*, 61[18], pp. 11979–11992, 2000.

[165] Y. Xie, Y. Quian, W. Wang, S. Zhang and Y. Zhang. “A Benzene-Thermal Synthetic Route to Nanocrystalline GaN”. *Science*, 272, pp. 1926–1927, 1996.

[166] C.S. Choi, E. Prince and W.L. Garrett. “Refinement of α -Lead Azide by Neutron Diffraction”. *Acta Cryst.*, B33, pp. 3536–3537, 1977.

[167] H. Suematsu, M. Mitomo, T.E. Mitchell, J.J. Petrovic, O. Fukunaga and N. Ohashi. “The α – β Transformation in Silicon Nitride Single Crystals”. *J. Am. Ceram. Soc.*, 80[3], pp. 615–620, 1997.

[168] J.J. Liang, A. Navrotsky, V.J. Leppert, M.J. Paskowitz, S.H. Risbud, T. Ludwig, H.J. Seifert, F. Aldinger and M. Mitomo. “Thermochemistry of $Si_{6-z}Al_zO_zN_{8-z}$ ($z = 0$ to 3.6) Materials”. *J. Mater. Res.*, 14[12], pp. 4630–4636, 1999.

Bibliography

[169] A. Zerr. “A New High-Pressure δ -Phase of Si_3N_4 ”. *phys. stat. sol. (b)*, 227[2], pp. R4–R6, 2001.

[170] E. Soignard, P.F. McMillan, C. Hejny and K. Leinenweber. “Pressure-induced transformations in α - and β - Ge_3N_4 : in situ studies by synchrotron X-ray diffraction”. *J. Solid. State. Chem.*, 177[1], pp. 299–311, 2004.

[171] M.T. Yin and M.L. Cohen. “Theory of static structural properties, crystal stability, and phase transformations: Applications to Si and Ge”. *Phys. Rev. B*, 26, pp. 5668–5687, 1982.

[172] M. Kitayama, K. Hirao, A. Tsuge, M. Toriyama and S. Kanzaki. “Oxygen Content in β - Si_3N_4 Crystal Lattice”. *J. Am. Ceram. Soc.*, 82[11], pp. 3263–3265, 1999.

[173] P. Kroll and J. von Appen. “Post-Spinel Phases of Silicon Nitride”. *phys. stat. sol. (b)*, 226[1], pp. R6–R7, 2001.

[174] K. Tatsumi, I. Tanaka, H. Adachi, F. Oba and T. Sekine. “Theoretical Predictiton of Post-Spinel Phases of Silicon Nitride”. *J. Am. Ceram. Soc.*, 85[1], pp. 7–10, 2002.

[175] J. Weiss, P. Greil and L.J. Gauckler. “The System Mg-Al-O-N”. *J. Am. Ceram. Soc.*, C, pp. 68–69, 1982.

[176] S. Wild, G. Leng-Ward and M.H. Lewis. “Nucleation and growth of β' -magnesium sialons and their composition limits”. *J. Mater. Sci.*, 16, pp. 1815–1828, 1981.

[177] K.J.D. MacKenzie, G.J. Gainsford and M.J. Ryan. “Rietveld Refinement of the Crystal Structures of the Yttrium Silicon Oxynitrides $\text{Y}_2\text{Si}_3\text{N}_4\text{O}_3$ (N-Melilite) and $\text{Y}_4\text{Si}_2\text{O}_7\text{N}_2$ (J-Phase)”. *J. Eur. Ceram. Soc.*, [16], pp. 553–560, 1996.

[178] V.A. Izhevskiy, L.A. Genova, J.C. Bressiani and F. Aldinger. “Progress in SiAlON ceramics”. *J. Eur. Ceram. Soc.*, 20, pp. 2275–2295, 2000.

[179] I-W. Chen and R. Shuba. “Sialon Ceramics, Structure and Properties of”. In K. H. J. Buschow, R.W. Cahn, M. C. Flemmings, B. J. Schmer, E. J. Kramer and S. Mahajan, editors, *Encyclopedia of Materials: Science and Technology*, pages 8471–8476. Elsevier, Amsterdam, 2001.

[180] L.W. Yin, Z.D. Zou, M.S. Li, G.L. Geng, D.S. Sun, Z.Y. Hao and Z.Y. Yao. “TEM Investigation on Micro-Inclusions and Dislocations on a HPHT-Grown Diamond Single Crystal from Ni-C System”. *Cryst. Res. Technol.*, 35[11-12], pp. 1289–1294, 2000.

[181] P. Kroll, B. Eck and R. Dronskowski. “First-Principles Studies of Extended Nitride Materials”. *Adv. Mater.*, 12[4], pp. 307–310, 2000.

[182] E. Knittle. In T.J. Ahrens, editor, *Mineral Physics and Crystallography: a Handbook of Physical Constants*, pages 98–142. Am. Geophys. Union, Washington D.C., 1995.

[183] W.Y. Ching, S-D Mo and Y. Chen. “Calculation of XANES/ELNES Spectra of All Edges in Si_3N_4 and $\text{Si}_2\text{N}_2\text{O}$ ”. *J. Am. Ceram. Soc.*, 85[1], pp. 11–15, 2002.

[184] C. Kocer, N. Hirosaki and S. Ogata. “Ab initio calculation of the ideal tensile and shear strength of cubic silicon nitride”. *Phys. Rev.*, B 67[035210], pp. 1–4, 2003.

[185] D. Tromans and J. A. Meech. “Fracture toughness and surface energies of covalent minerals: theoretical estimates”. *Miner. Eng.*, 17, pp. 1–15, 2004.

[186] T. Sekine and T. Mitsuhashi. “High-temperature metastability of cubic spinel Si_3N_4 ”. *Appl. Phys. Lett.*, 79[17], pp. 2719–2721, 2001.

[187] B. Li, S.M. Rigden and R.C. Liebermann. “Elasticity of stishovite at high pressure”. *Phys. Earth Planet. Interiors*, 96, pp. 113–127, 1996.

[188] A. Zerr, H. Reichmann, H. Euler and R. Boehler. “Hydrostatic Compression of γ -($\text{Mg}_{0.6}\text{Fe}_{0.4}$)₂ SiO_4 to 50 GPa”. *Phys. Chem. Miner.*, 19, pp. 507–509, 1993.

Bibliography

[189] J.Z. Jiang, H. Lindelov, L. Gerward, K. Ståhl, J.M. Recio, P. Mori-Sanchez, S. Carlson, M. Mezouar, E. Dooryhee, A. Fitch and D.J. Frost. “Compressibility and thermal expansion of cubic silicon nitride”. *Phys. Rev. B*, 65, pp. 16202(1–4), 2002.

[190] L.W. Finger, R.M. Hazen and A. Hofmeister. “High-Pressure Crystal-Chemistry of Spinel ($MgAl_2O_4$) and Magnetite (Fe_3O_4) - Comparisons with Silicate Spinel”. *Phys. Chem. Miner.*, 215-220, pp. 13, 1986.

[191] J.M. Recio, R. Franco, A. Martín Pendás, M.A. Blanco and L. Pueyo. “Theoretical explanation of the uniform compressibility behaviour observed in oxide spinels”. *Phys. Rev. B*, 63, pp. 184101(1–7), 2001.

[192] T. Mashimoto, M. Uchino, A. Nakamura, T. Kobayashi, E. Takawasa, T. Sekine, Y. Noguchi, H. Hikosaka, K. Fukuoka and Y. Syono. “Yield properties, phase transition, and equation of state of aluminum nitride (AlN) under shock compression up to 150 GPa”. *J. Appl. Phys.*, 86[12], pp. 6710–6716, 1999.

[193] Z. Wang, Y. Zhao, D. Schiferl, C.S. Zha, R.T. Downs and T. Sekine. “Critical pressure for weakening of size-induced stiffness in spinel-structure Si_3N_4 nanocrystals”. *Appl. Phys. Lett.*, 83[15], pp. 3174–3176, 2003.

[194] S.R. Shieh, T.S. Duffy and B. Li. “Strength and Elasticity of SiO_2 across the Stishovite– $CaCl_2$ Structural Phase Boundary”. *Phys. Rev. Lett.*, 89[25], pp. 255507/1–4, 2002.

[195] H. Lemercier, T. Rouxel, D. Fargeot, J.-L. Besson and B. Piriou. “Yttrium SiAlON glasses: structure and mechanical properties — elasticity and viscosity”. *J. Non-Cryst. Solids*, 201, pp. 128–145, 1996.

[196] J.C. Hay, E.Y. Sun, G.M. Pharr, P.F. Becher and K.B. Alexander. “Elastic Anisotropy of β -Silicon Nitride Whiskers”. *J. Am. Ceram. Soc.*, 81[10], pp. 2661–2669, 1998.

[197] M.S. Somayazulu, K. Leinenweber, H. Hubert and P.F. Mc Millan. “High pressure-high temperature synthesis of spinel Ge_3N_4 ”. In M. H. Manghnani, W. J. Nellis and M. F. Nicol, editors, *Science and Technology of High Pressure, Proceedings of AIRAPT-17*, pages 663–666. Universities Press, Hyderabad, India, 2000.

[198] M. P. Shemkunas, W. T. Petuskey, A. V. G. Chizmeshya, K. Leinenweber and G. H. Wolf. “Hardness, elasticity, and fracture toughness of polycrystalline spinel germanium nitride and tin nitride”. *J. Mater. Res.*, 19[5], pp. 1392–1399, 2004.

[199] J.E. Lowther. “High-pressure phases and structural bonding of Ge_3N_4 ”. *Phys. Rev. B*, 62[1], pp. 5–8, 2000.

[200] T. Taniguchi and M.P. D'Evelyn. “Elastic properties of translucent polycrystalline cubic boron nitride as characterized by the dynamic resonance method”. *Diamond Relat. Mater.*, 8, pp. 1522–1526, 1999.

[201] A.D. Kounga Njiwa, T. Fett, J. Rödel and G.D. Quinn. “Crack-Tip Toughness Measurements on Sintered Reaction Bonded Si_3N_4 ”. *J. Am. Ceram. Soc.*, 87[8], pp. 1502–1508, 2004.

[202] A.R. De Arellano-Lopez, M.A. Mcmann, J.P. Singh and J. Martinez-Fernandez. “Microstructure and room-temperature mechanical properties of Si_3N_4 with various α/β ratios”. *J. Mater. Sci.*, 33[24], pp. 5803–5810, 1998.

[203] W. Paszkowicz, R. Minikayev, P. Piszora, M. Knapp, C. Bähtz, J. M. Recio, M. Marques, P. Mori-Sanchez, L. Gerward and J. Z. Jiang. “Thermal expansion of spinel-type Si_3N_4 ”. *Phys. Rev. B*, 69[5], pp. 052103/1–052103/4, 2004.

[204] H.T. Hintzen, M.R.M.M. Hendrix, H. Wondergem, C.M. Fanga, T. Sekine and G. de With. “Thermal expansion of cubic Si_3N_4 with the spinel structure”. *J. Alloy. Compd.*, 351[1-2], pp. 40–42, 2003.

[205] R. Larson and R.B. Von Dreele. *General Structure Analysis System GSAS*. Manual, Los Alamos, 1994.

Bibliography

- [206] R.J. Bruls, H.T. Hintzen, G. de With, R. Metselaar and J.C. van Miltenburg. “The temperature dependence of the Grüneisen parameters of MgSiN_2 , AlN and $\beta\text{-Si}_3\text{N}_4$ ”. *J. Phys. Chem. Solids*, 62, pp. 783–792, 2001.
- [207] E. Soignard and P.F. McMillan. “Raman Spectroscopy of $\gamma\text{-Si}_3\text{N}_4$ and $\gamma\text{-Ge}_3\text{N}_4$ Nitride Spinel Phases Formed at High Pressure and High Temperature: Evidence for Defect Formation in Nitride Spinels”. *Chem. Mater.*, 16[18], pp. 3533–3542, 2004.
- [208] A. de Pablos, M. Osendi and P. Miranzo. “Effect of Microstructure on the Thermal Conductivity of Hot-Pressed Silicon Nitride Materials”. *J. Am. Ceram. Soc.*, 85[1], pp. 200–206, 2002.
- [209] D. Bagayoko and G. L. Zhao. “Predicted electronic properties of cubic Si_3N_4 ”. *Physica C*, 364–365, pp. 261–264, 2001.
- [210] F. Oba, K. Tatsumi, H. Adachi and I. Tanaka. “*n*- and *p*-type dopants for cubic silicon nitride”. *Appl. Phys. Lett.*, 78[11], pp. 1577–1579, 2001.
- [211] F. Oba, K. Tatsumi, I. Tanaka and H. Adachi. “Effective Doping in Cubic Si_3N_4 and Ge_3N_4 : A First-Principles Study”. *J. Am. Ceram. Soc.*, 85[1], pp. 97–100, 2002.
- [212] I. Tanaka, K. Tatsumi, M. Nakano and H. Adachi. “First-Principles Calculations of Anion Vacancies in Oxides and Nitrides”. *J. Am. Ceram. Soc.*, 85[1], pp. 68–74, 2002.
- [213] Y.-N. Xu and W.Y. Ching. “Electronic structure and optical properties of α and β phases of silicon nitride, silicon oxynitride and with comparison to silicon dioxide”. *Phys. Rev. B*, 51[24], pp. 17379–17389, 1995.
- [214] A. Zerr, M. Schwarz, R. Schmeichel, R. Kolb, H. von Seggern and R. Riedel. “New High Pressure Nitrides”. *Acta Cryst.*, A 58 (Supplement), pp. C47, 2002.
- [215] W.T. Petuskey, G.H. Wolf, M.P. Shemkunas, A.V. Chizmeshya and K. Leinenweber. “Physical and Chemical Properties of Group IV Nitrides

and Their Derivatives”. At the *104th Annual Meeting of the American Ceramic Society, Session AMA.4-B-04*, St. Louis, MO, U.S.A., 2002.

- [216] R. G. Egdell, V. E. Henrich, R. Bowdler and T. Sekine. “On the difference in valence electron plasmon energy and density of states between beta- and cubic-Si₃N₄”. *J. Appl. Phys.*, 94[10], pp. 6611–6615, 2003.
- [217] G.J. Davies. “Cubic Boron Nitride Crystallization”. In R. Riedel, editor, *Handbook of Ceramic Hard Materials, Part II*, pages 510–512. Wiley-VCH, Weinheim, 2000.
- [218] M. Mitomo and N. Setaka. “Consolidation of Si₃N₄ by shock compression”. *J. Mater. Sci. Lett.*, 16, pp. 851–852, 1981.
- [219] J.J. Petrovic, B.W. Olinger and R.B. Roof. “Explosive shock loading of alpha-Si₃N₄ powder”. *J. Mater. Sci.*, 20, pp. 391–398, 1985.
- [220] H. Hirai and K. Kondo. “Shock-Compacted Si₃N₄ Nanocrystalline Ceramics: Mechanisms of Consolidation and of Transition from alfa- to beta-form”. *J. Am. Ceram. Soc.*, 77[2], pp. 487–492, 1994.
- [221] B.L. Turner-Adomatis and N.N. Thadhani. “Shock-enhanced alfa to beta phase transformation in Si₃N₄ powders”. *Mater. Sci. Eng.*, A 256, pp. 289–300, 1998.
- [222] R. Metselaar. “Terminology for Compounds in the Si-Al-O-N System”. *J. Eur. Ceram. Soc.*, 18, pp. 183–184, 1998.
- [223] R. Riedel (transl.). “Zur Benennung von Verbindungen im Si-Al-O-N System”. *Angew. Chem.*, 114, pp. 2721–2723, 2002.
- [224] T. Ekström and M. Nygren. “SiAlON Ceramics”. *J. Am. Ceram. Soc.*, 75[2], pp. 259–276, 1992.
- [225] C.B. Raju, S. Verma, M.N. Sahu, P.K. Jain and S. Choudary. “Silicon nitride/SiAlON ceramics - A review”. *Indian J. Eng. Mater. S.*, 8, pp. 36–45, 2001.

Bibliography

- [226] L.J. Gauckler, H.L. Lukas and G. Petzow. “Contribution to the phase diagram Si_3N_4 – AlN – SiN_2 – Al_2N_3 ”. *J. Am. Ceram. Soc.*, 58, pp. 346–347, 1975.
- [227] K.H. Jack. “Review: Sialons and Related nitrogen ceramics”. *J. Mater. Sci.*, 11, pp. 1135–1158, 1976.
- [228] R. Dupree, M.H. Lewis and M.E. Smith. “Structural Characterisation of Ceramic Phases with High-Resolution ^{27}Al NMR”. *J. Appl. Cryst.*, 21, pp. 109–116, 1988.
- [229] T Ekström, P.O. Käll, M. Nygren and P.O. Olsson. “Dense single-phase β -sialon ceramics by glass encapsulated hot isostatic pressing”. *J. Mater. Sci. Lett.*, 24, pp. 1853–1861, 1989.
- [230] W. Rafaniello and I.B. Cutler. “Preparation of Sinterable Cubic Aluminium Oxynitride by Carbothermal Nitridation of Aluminium Oxide”. *J. Am. Ceram. Soc.*, C-128, 1981.
- [231] C.M. Fang, R. Metselaar, H.T. Hintzen and G. de With. “Structure Models for γ -Aluminum Oxynitride from *Ab Initio* Calculations”. *J. Am. Ceram. Soc.*, 84[11], pp. 2633–2637, 2001.
- [232] M. Haviar and H. Herbertsson. “The pressure stability of β -sialons”. *J. Mater. Sci. Lett.*, 11, pp. 179–180, 1992.
- [233] M. Haviar and H. Herbertsson. “The stability of yttrium α -sialon under high pressure”. *J. Mater. Sci. Lett.*, 12, pp. 1888–1890, 1993.
- [234] M. Haviar, Z. Lences and H. Herbertsson. “The stability of yttrium γ -SiAlON and β -SiAlON at high pressure and high temperature”. *J. Mater. Sci. Lett.*, 16, pp. 236–238, 1997.
- [235] J.F. Berar and P. Lelann. “ESDs and estimated probable-error obtained in rietveld refinements with local correlations”. *J. Appl. Cryst.*, 24, pp. 1–5, 1991.

[236] R. Grün. “The Crystal Structure of β - Si_3N_4 ; Structural and Stability Considerations Between α - and β - Si_3N_4 ”. *Acta Crystallogr.*, B 35, pp. 800–804, 1979.

[237] L. Ouyang and W.Y. and Ching. “Structure and bonding in a cubic phase of SiAlON derived from the cubic spinel phase of Si_3N_4 ”. *Appl. Phys. Lett.*, 81[2], pp. 229–231, 2002.

[238] K. Tatsumi, I. Tanaka, H. Adachi and M. Yoshida. “Atomic structures and bondings of β - and spinel- $\text{Si}_{6-z}\text{Al}_z\text{O}_z\text{N}_{8-z}$ by first principles calculations”. *Phys. Rev. B*, 66, pp. 165210(1–8), 2002.

[239] J.E. Lowther, M. Schwarz, E. Kroke and R. Riedel. “Electronic Structure Calculation of Cohesive Properties of some $\text{Si}_{6-z}\text{Al}_z\text{O}_z\text{N}_{8-z}$ Spinels”. *J. Solid. State. Chem.*, 176[2], 2003.

[240] J.W. McCauley. “A Simple Model for Aluminum Oxynitride Spinels”. *J. Am. Ceram. Soc.*, 61, pp. 372–373, 1978.

[241] J.W. McCauley and N.D. Corbin. “Phase Relations and Reaction Sintering of Transparent Cubic Aluminium Oxynitride Spinel (AlON)”. *J. Am. Ceram. Soc.*, 62[9-10], pp. 476–469, 1979.

[242] I-W. Chen and A. Rosenflanz. “A tough SiAlON ceramic based on α - Si_3N_4 with a whisker-like microstructure”. *Nature*, 389, pp. 701–704, 1997.

[243] G.D. Quinn, P.J. Patel and I. Lloyd. “Effect of Loading Rate Upon Conventional Ceramic Microindentation Hardness”. *J. Res. Natl. Inst. Stand. Technol.*, 107[3], pp. 299–306, 2002.

[244] M.H. Lewis, R. Fung and D.M.R. Taplin. “Indentation plasticity and fracture of Si_3N_4 ceramic alloys”. *J. Mater. Sci.*, 16, pp. 3437–3446, 1981.

[245] V.V. Brazhkin, A.G. Lyapin, and R.J. Hemley. “Harder than diamond: dreams and reality”. *Phil. Mag. A*, 82[2], pp. 231–253, 2002.

[246] P. Tabary and C. Servant. “Thermodynamic reassessment of the AlN-Al₂O₃ system”. *Calphad.*, 22[2], pp. 179–201, 1998.

Bibliography

- [247] P. Tabary and C. Servant. “Crystalline and microstructure of the AlN–Al₂O₃ section in the Al–N–O system. I. Polytypes and γ -AlON spinel phase”. *J. Appl. Cryst.*, 32, pp. 241–252, 1999.
- [248] P. Tabary and C. Servant. “Crystalline and microstructure of the AlN–Al₂O₃ section in the Al–N–O system. II. ϕ' - and δ - Polytypes and γ -AlON spinel phases”. *J. Appl. Cryst.*, 32, pp. 253–272, 1999.
- [249] P. Tabary, C. Servant and J.A. Alary. “Microstructure and phase transformation in the AlN–Al₂O₃ pseudo-binary system”. *J. Eur. Ceram. Soc.*, 20, pp. 913–926, 2000.

This bibliography was created using the L^AT_EX package `natbib` Version 7a, and the literature database program `TinyBib` v1.5 by Sergio Luis dos Santos e Lucato, Darmstadt Technical University, Materials Science Dept., Ceramics Group. (http://www.tu-darmstadt.de/fb/ms/fg/naw/soft/f_soft.html)

Danksagung

Diese Arbeit entstand in der Zeit von November 1998 bis Oktober 2003 innerhalb des Fachgebietes **Disperse Feststoffe** (DF) im Fachbereich Materialwissenschaft der Technischen Universität Darmstadt. Ein herzliches Dankeschön an alle, die zum Entstehen dieser Arbeit beigetragen haben.

Herrn Professor Ralf Riedel danke ich für die Annahme als Doktorand, die Betreuung dieser Arbeit und die vielfältige Förderung, seien es Auslandsaufenthalte, die Partizipation an Tagungen u.v.a.m. Edwin Kroke danke ich für die fortwährende, harmonische und erfolgreiche Zusammenarbeit und den regen Ideenaustausch — angefangen von meiner Diplomarbeit, deren Betreuer er war, bis hin zur Rezension von Teilen dieser Dissertation. Besten Dank auch an Prof. Arlan Norman, der mich während meines sechsmonatigen Aufenthaltes an der University of Colorado at Boulder betreut hat, sowie allen Mitgliedern seiner Arbeitsgruppe. Herrn Gerhard Miehe vom Fachgebiet **Strukturforschung** (SF) im Fachbereich Materialwissenschaft haben wir die Strukturaufklärung von $\gamma\text{-Si}_3\text{N}_4$ zu verdanken. Ich danke ihm außerdem für zahlreiche TEM-Untersuchungen und Rietveld-Verfeinerungen meiner Proben und viele spannende Gespräche — nicht nur über deren Auswertung. Als weiteren Mitarbeitern von SF danke ich insbesondere Carsten Bähtz, Michael Knapp und Helmut Ehrenberg für Synchrotronmessungen. Helmut sei auch für die geduldige Hilfestellung bei meinen Versuchen das ‘Rietvelden’ zu erlernen und anderen kristallographischen Problemen, sowie für die Rezension von Teilen dieser Arbeit gedankt. Für letzteres, sowie für die Aufmunterungen und Ratschläge danke ich auch Isabel Kinski (DF). Claudia Fasel, ebenfalls DF, danke ich u.a. für zahlreiche Verbrennungsanalysen. Andreas Zerr danke ich unter anderem für gemeinsame Hochdruckexperimente — am MPI in Mainz wie auch am Geoinstitut in Bayreuth — und für zahlreiche Diskussionen mit wertvoller, konstruktiver Kritik an meiner Arbeit. George Serghiou danke ich für die Durchführung der Diamantstempel-Versuche an $\text{C}_3\text{N}_{12}/\text{Si}_3\text{N}_4$ und die gute Zusammenarbeit am Beginn meiner Forschungen. Brent Poe, damals am Bayerischen Geoinstitut Bayreuth, war ein hervorragender und geduldiger Lehrmeister in allen Belangen der Multianvil-Hochdruckversuche. Herrn Ulrich Hornemann vom Fraunhoferinstitut für Kurzzeitdynamik in Freiburg

Danksagung

und seinen Mitarbeitern sei für die Durchführung der Schockwellenexperimente an Si_3N_4 und Sialon gedankt. Martin Heck und insbesondere Brunhilde Thybusch vom Fachgebiet Chemische Analytik danke ich für die Mikrosondenuntersuchungen. Peter Kroll danke ich für eine spannende und aufschlussreiche elektronische Korrespondenz über Eigenschaften, Struktur- und Phasenbeziehungen der (Oxid-) Nitrid Spinelle und für die kritische Rezension von Teilen dieser Arbeit. Prof. I-Wei Chen von der University of Pennsylvania hat die Sache mit den Spinell-Sialonen ins rollen gebracht. Ihm und seinem Mitarbeiter M. Zenotchkine herzlichen Dank für das β -Sialon Ausgangsmaterial, sowie für wichtige Anregungen zu meiner Arbeit. Mein Dank gilt auch Prof. Stan Vepřek und Pavla Karvankova vom Institut für Chemie Anorganischer Materialien der TU München, für die Ultramikrohärteprüfungen an den dichten $\gamma\text{-Si}_3\text{N}_4$ - und Sialon-Proben sowie für den interessanten Austausch über die Neuinterpretation des Eindruck-elastischen Moduls E_{IT} . Herrn Kilian Friederich von CeramTec danke ich für Referenzdaten zur SL200-Schneidkeramik. Stefan Lauterbach hat das Wunder vollbracht, meinen Tee-geschädigten Laptop binnen zwei Tagen wieder zum Laufen zu bekommen und mich so vor einer jähnen, langwierigen und teuren Unterbrechung meiner Schreibarbeit bewahrt. Michael Nimz und Sergio Lucato sei herzlich für die Bereitstellung von Formatierungsvorlagen und weitere Hilfestellung beim Erlernen von L^AT_EX gedankt. Ich danke außerdem den Gastwissenschaftlern K. Rama Subrahmanyam und Mila Chibusova für die Zusammenarbeit auf dem Gebiet der Spinell-Nitride, sowie allen andern Kollegen von DF. Weiterer Dank geht an Jochen Korzer, Harry Wedel, Roland Schmeichel, Holger Hoche und Bettina Ströbel, Jim McCauley, Bert Hintzen und Chang-Ming Fang, Derek Thompson, Hans-Joachim Kleebe, Vladimir Solozhenko, Toshimori Sekine, Günter Engling, Ted Lowther und Jack Sigalas von der Firma *Element6* (vormals DeBeers Industrial), die hochinteressante Projekte innerhalb dieser Arbeit auch finanziell unterstützt hat.

Ganz besonder Dank gilt meiner Mutter und Juan Gil, für ihren Zuspruch, ihre Unterstützung und Hilfe, die mir vielfach den Rücken für meine Forschungs- und Promotionsarbeit freigehalten haben. Neben allem andern gedenke ich der guten Schulausbildung und der finanziellen Unterstützung während des Studiums, die mir mein Vater und meine Mutter haben zukommen lassen. Sie bildeten die Basis für eine kurze Diplomstudienzeit und die anschließenden Erfolge.

Curriculum Vitae

Marcus Rolf Schwarz

Marckus.Schwarz@web.de

geboren am: 25. Jan. 1974

in: Offenbach/Main, Deutschland

Schulbildung: 1980 – 1985 Grundschule in Offenbach

1985 – 1993 Gymnasium, Anna-Schmidt-Schule in Frankfurt/Main

Studien: 1993 – 1997 Diplomstudiengang
Materialwissenschaften, Technische
Hochschule bzw. Technische Universität
Darmstadt (TUD)

1997 – 1998 Diplomarbeit im Fachgebiet Disperse
Feststoffe am Fachbereich
Materialwissenschaften der TUD,
Thema: “*Neue Materialien aus
s-Triazinderivaten*”

1998 – 2003 Promotion im FG Disperse Feststoffe
bei Prof. Dr. R. Riedel

2004 – Wissenschaftlicher Mitarbeiter bei
Prof. Dr. E. Kroke, Fachgebiet
“Chemische Materialwissenschaften”,
Fachbereich Chemie, Universität
Konstanz

Konstanz, Januar 2005

Curriculum Vitae

Index

A

Al₃O₃N
introduction, 206
lattice parameter, 230
instability under pressure, 230
phase relation to γ -sialon, 229

AlN, GaN
 $wz \rightarrow rs$ transition, 114

alon, *see* γ -alon

α -Si₃N₄
average coordination number, 76
resilience to static pressure, 113
shock loading results, 190, 201

anelastic effect (indentation), 61

archimedian density, 67
of β -sialons, 213

automated hardness testing
 γ -Si₃N₄, 144
 γ -sialons, 249

average atomic volume $\langle \Omega \rangle$, 107

c -BN, rs -AlN ..., 110
diamond, 110
spinel nitrides, 110

average coordination number \bar{N}_c , 9
 α -, β - and γ -Si₃N₄, 76

B

B₄C
oxidation stability, 15

B_0 , bulk modulus, 7
see also elastic moduli

band gap
 γ -Si₃N₄, 186
 γ -sialon, 254

Baysinid, 85

β -Si₃N₄
average coordination number, 76
crystallites, 93, 121
 E - V curve, 115
phase stability field, 112
seed crystals, 71

β -sialon, 204
chemical composition, 210
lattice constants, 205
measured densities, 213
microstructure, 213
sample size, 217

BGI, Bayerisches Geoinstitut, 84

bond angles
in γ -Si₃N₄, 103
in γ -Si₂AlON₃, 234

bond bending, 8
bond length ratio
 spinels, 105
bond lengths
 in hard materials, 7
 in $\gamma\text{-Si}_2\text{AlON}_3$, 234
 in $\gamma\text{-Si}_3\text{N}_4$, 103
 $\gamma\text{-Si}_3\text{N}_4$ ‘ceramic’, 125
bond strength, 7
boron nitride, *see also* $c\text{-BN}$ and $w\text{-BN}$
 sample capsules, 29
 wurtzite and sphalerite type, 69
bulk modulus, B_0 , 7
 see also elastic moduli

C

C_3N_{12} , 73
 C_3N_4
 $c\text{-C}_3\text{N}_4$, $w_{II}\text{-C}_3\text{N}_4$, 70
 review articles, 5
cation disorder
 in spinels, 79
 in $\gamma\text{-sialon}$, 228, 231
 $c\text{-BN}$, 69
 atomic volume, 110
 fracture toughness, 168
 hardness, 168
 thermal stability, 14
coefficient of thermal expansion
 β - and $\gamma\text{-Si}_3\text{N}_4$, 177
 formula, 176
coordination number, *see* average coordination number
 $cottunite\text{-TiO}_2$, 15
 $c\text{-}P$ curve

$\gamma\text{-Si}_3\text{N}_4$ ‘ceramic’, 163
 $\gamma\text{-sialon}$, 253
SRM 2100, 51
crack bridging
 in $\gamma\text{-Si}_3\text{N}_4$ ‘ceramic’, 163
 in $\gamma\text{-sialons}$, 247
crack length ℓ , 41
crack radius c , 41
creep resistance, 13
crystal structure
 of spinel, 77
crystallographic data
 $\gamma\text{-Si}_3\text{N}_4$, 103
 $\gamma\text{-Si}_3\text{N}_4$ ‘ceramic’, 125
 $\gamma\text{-Si}_2\text{AlON}_3$, 233
 $c\text{-Si}_3\text{N}_4$, 69
 Cu powder
 for shock synthesis, 35, 191

D

DAC
 sample heating, 22
 Si_3N_4 experiments, 73, 112
DAC diamond anvil cell, 20
defects in $\gamma\text{-Si}_3\text{N}_4$
 anion vacancies, 183
 cation vacancies, 97
 in post-shock $\gamma\text{-Si}_3\text{N}_4$, 200
 $\delta\text{-Si}_3\text{N}_4$, 114
diamond
 atomic volume, 110
 thermal stability, 14
diamond anvil cell, *see* DAC
diamond wire saw
 manufacturer, 32

sample preparation, 33
Druck-Homogenregel, 114

E

E_{IT} , *see* indentation modulus
elastic moduli
equations, 59
 γ - Si_3N_4 , 163
 γ - Si_3N_4 ‘ceramic’, 155
 γ -sialon etc., 251
oxide spinels, 163
electron diffraction pattern
 γ - Si_3N_4 , 75
electroneutrality, 76
electronic properties
 γ - Si_3N_4 , 186
 γ -sialon, 254
element mappings
 γ - Si_3N_4 , 96
 γ - Si_3N_4 ‘ceramic’, 130
 γ - $\text{SiAl}_2\text{O}_2\text{N}_2$, 239
elemental analysis EA, 67
EMI Ernst Mach Institut, 34
 E_r reduced modulus, 57
 E - V curves
 Si_3N_4 phases, 115
extrinsic hardness, 10

F

Fe_3O_4 , Fe_3S_4 , 106
flyer-plate apparatus, 35
fracture toughness, *see also* indentation
fracture toughness
of cutting tool materials, 16

free structural parameters \bar{N}_f , 9
FT-IR, *see also* IR-spectra
spectrometer, 63

G

γ -alon
introduction, 206
lattice parameter, 230
phase relations, 262
constant anion model, 229
phase relations, 97
 γ - C_3N_4 , 109
 γ - Ge_3N_4 and γ - Sn_3N_4
 HV , E_Y and K_{IC-IF} , 170
 γ - Si_3N_4
average coordination number, 76
bond lengths and angles, 103
crystallites, 93
crystallographic data, 103
crystallographic settings, 75
DAC synthesis, 73
 E - V curve, 115
HP/HT syntheses, 72
ideal strength, 148
IR and Raman spectra, 99
nanoparticles, 198
nomenclature, 69
oxide layer, 94
published syntheses, 90
recovered sample, 88
seed crystals, 86
shear modulus, 159
shear strength, 148, 151
summary, 265
 γ - Si_3N_4 ‘ceramic’, 120

Al, Mg, O content, 130
crystallographic data, 125
hardness, 141
microstructure, 128

γ -sialon
solid soln. series, 205
chemical composition, 211
crystallographic data, 233
decomposition at high pressure, 262
electronic band gap, 254
HP/HT-experiments, 223
lattice parameter, 227
summary, 271

γ -Sn₃N₄
 HV , E_Y and K_{IC-IF} , 170

γ -Ti₃N₄, Zr₃N₄..., 82

γ -(Si_xGe_{1-x})₃N₄, 111

GaN
abnormal B_0 , 114

H

half penny crack, 41
hardness
definition, 6
intrinsic, 6
extrinsic, 10
 c -BN, 168
cottunite-TiO₂, 15
 γ -Ge₃N₄ and γ -Sn₃N₄, 170
 γ -Si₃N₄
automated measurement, 144
conventional testing, 140
 γ -Si₃N₄ ‘ceramic’, 141
nanoindentation, 135
published data, 137

γ -sialons, 249, 254
polycryst. c -BN, 168
stishovite r -SiO₂, 14

H/E -ratio, 38
 γ -Si₃N₄ ‘ceramic’, 166
reference SRM 2100, 50

heating
in DAC, 22
in MAP, 30

high pressure synthesis
 γ -Si₃N₄, overview own work, 72
 γ -Si₃N₄, published work, 90
 γ -sialon, overview own work, 223
of hard materials, 10

hkl indices, 232

hot hardness, 13

HU universal hardness, 56

HU_{pl} plastic hardness
definition, 56
 γ -Si₃N₄ ‘ceramic’, 145
 γ -sialon, 249

HV_n , HK_n , *see* normalized hardness

hybrid orbitals, 8

I

indent size
in pure γ -Si₃N₄, 136
in γ -Si₃N₄ ‘ceramic’, 143
in γ -Si₂AlON₃, 246
in γ -sialons, 253

indentation curve, 56

indentation elastic modulus, *see* indentation modulus

indentation fracture, 41

indentation fracture toughness

γ -Ge₃N₄ and γ -Sn₃N₄, 170
 γ -Si₃N₄ ‘ceramic’, 163
 γ -Si₃N₄ vs. *c*-BN, 168
 γ -sialons, 254
SRM 2100, 51
indentation modulus
 formula, 58
 γ -Si₃N₄, 154
 γ -Si₃N₄ ‘ceramic’, 159
 γ -SiAl₂O₂N₂, 250
possible artifacts, 61
indentation process, 56
indentation size effect ISE, 38
indenter
 ideal stiff, 58
inversion parameter, 79, *see also* site preference
IR spectra
 γ -Si₃N₄, 99
ISE indentation size effect, 38

K

Knoop hardness
 formula, 38
 γ -Si₃N₄ ‘ceramic’, 141
Kröger-Vink Notation, 97

L

ℓ crack length, 41
lattice parameter
 γ -Si₃N₄, 102
 Al₃O₃N, 230
 β -sialon, 205
 γ -sialon, 227

Lince, 120
load-displacement curve, 56
lonsdaleite, 69

M

magnetite Fe₃O₄, 106
MAP multianvil press
 schematic drawing, 24
 accessible pressures, 25
 temperature measurement, 30
 ceramic pressure medium, 27
 inert encapsulation, 29
 p-T-t parameters, 32
 XRD sample preparation, 66
MAP synthesis
 γ -Si₃N₄ ‘ceramic’, 120
 γ -Si₃N₄, overview own work, 72
 γ -Si₃N₄, published work, 90
 recovered γ -Si₃N₄ sample, 88
Mg₂SiO₄, 104
MgO-octahedron, *see* octahedral pressure cell
microstructure
 β -Si₃N₄ ceramic, 121
 β -Si₃N₄(HP/HT-synthesized), 93
 β -sialon, 213
 γ -Si₃N₄ ‘ceramic’, 128
 γ -sialon, 240
 post-shock Si₃N₄, 195
multianvil apparatus, *see* MAP

N

nanoindentation, 56
natbib, 274

\bar{N}_c , *see* average coordination number
NIST, 48
NMR, ^{29}Si chemical shifts, 78
normalized hardness, 38
 $\gamma\text{-Si}_3\text{N}_4$ 'ceramic', 143
 γ -sialons, 254
 reference SRM 2100, 49

O _____

octahedral crystallites, 94, 127
octahedral pressure cell
 schematic drawing, 27
 size after experiment, 33
 $\langle\Omega\rangle$, *see* average atomic volume
oxidation stability
 B_4C , 15
 $\gamma\text{-Si}_3\text{N}_4$, 171
 hard materials, 15
oxide layer
 on $\gamma\text{-Si}_3\text{N}_4$, 94
oxide nitride spinels, 80
oxygen content
 in $\gamma\text{-Si}_3\text{N}_4$, 95

P _____

Palmqvist crack, 41
penetration depth, 56
phase diagram
 Si_3N_4 , 112
plane wave impact, 35
plasma etching, 63
plastic zone, 41
 p_{\max} max. pressure, 32
Poisson's ratio ν , 59

post-spinel Si_3N_4 phases, 118

Q _____

quartz impurity, 232

R _____

R-curve

$\gamma\text{-Si}_3\text{N}_4$ 'ceramic', 168
 reference SRM 2100, 54

Raman

$\gamma\text{-Si}_3\text{N}_4$, 99
 spectrometer, 62
 spinel nitrides, 182
reduced modulus
 formula, 57
 $\gamma\text{-Si}_3\text{N}_4$, $f(\text{load})$, 154
 $\gamma\text{-SiAl}_2\text{O}_2\text{N}_2$, 250
 of a composite, 156

Rietveld refinement

$\gamma\text{-Si}_3\text{N}_4$, 101
 $\gamma\text{-Si}_3\text{N}_4$ 'ceramic', 124
 $\gamma\text{-Si}_2\text{AlON}_3$, 232
ringwoodite $\gamma\text{-Mg}_2\text{SiO}_4$, 104, 149
rocksalt-AlN, GaN, InN, *see* rs-AlN...
rs-AlN, GaN, InN, 82
 average atomic volume, 110

S _____

seed crystals

$\beta\text{-Si}_3\text{N}_4$, 71
 $\gamma\text{-Si}_3\text{N}_4$, 86
shear modulus G
 $G = f(\nu, B)$, 59

γ -Si₃N₄, 159
 shock synthesis
 copper powder, 35, 191
 defects in γ -Si₃N₄, 200
 experimental parameters, 192
 experiments before γ -Si₃N₄, 190
 microstructure of Si₃N₄, 195
 recovered samples, 193
 shock wave apparatus, 35
 Si^{tet}, Si^{oct}, 76, 77
 NMR chemical shifts, 78
 Si₂N₃H, 85
 Si-Al-O-N
 phase diagram, 204
 Si-O-N system
 high pressure behavior, 97
 sialon, *see also* β -sialon and γ -sialon
 HP/HT-exp. published, 206
 HP/HT-experiments, 223
 SiC
 discovery, 3
 tribochemical stability, 15
 spinel
 anion positional parameter, 78
 bond length ratio, 106
 crystal structure, 77
 crystallographic settings, 75
 elasticity data, 163
 inversion parameter, 79
 selected compounds, 80
 Si-Ge-N system, 111
 slip systems, 14
 spinel nitrides, 82, 108
 assignment of Raman modes, 184
 atomic volume, 110
 elasticity data, 163
 Raman shifts, 182
 structural comparison, 110
 split-sphere, 24
 SRM 2100, 48
 stishovite, 72
 crystallites, 98
 hardness and thermal stability, 14
 multianvil experim., 72
 pressure derivative B'_0 , 149
 sulfide spinels, 80
 Summary (in German)
 γ -Si₃N₄ part, 265
 γ -sialon part, 271
 superhard, definition, 4

T
 thermal expansion
 coefficient of, 17, 176
 γ -Si₃N₄, *a-T* curves, 175
 thermal stability
 c-BN, diamond..., 14
 thermodynamic properties
 γ -Si₃N₄, 181
 thiospinels, 80
 TinyBib
 literature database, 274
 T_{max} max. temperature, 32
 toughness, *see also* indentation fracture
 toughness
 cutting tool materials, 16
 $t_{raise}^p, t_{raise}^T \dots$ definition, 32
 tribochemical stability
 c-BN, 15
 SiC, 15

U _____

ultrahard, 4
universal hardness, 56

Y _____

Young's modulus E_Y
 $E_Y = f(B, G)$, 59

V _____

vibrational modes, *see* Raman
Vickers hardness
formula, 37
 γ -Si₃N₄ 'ceramic', 141
 γ -sialons, 249

Z _____

Zusammenfassung, 265

W _____

w-BN, 69
wear resistance, 16
 w_{II} -C₃N₄, 109
 w_{II} -Si₃N₄
definition, 70
 E - V curve, 115
willemite, 70
C₃N₄, Si₃N₄, *see* w_{II} -C₃N₄... etc.

X _____

XPS
 γ -Si₃N₄, 188
XRD
diffractometers, 65
 γ -Si₃N₄, 101
 γ -Si₃N₄ 'ceramic', 124
 γ -sialon, 225
post-shock γ -Si₃N₄, 196
sample preparation, 66